Title
Discrete Element Analysis of Surface Fault Rupture through Granular Media

Author
Garcia, Fernando Estéfan Thibodeaux

Publication Date
2018

Peer reviewed|Thesis/dissertation

Discrete Element Analysis of Surface Fault Rupture through Granular Media

By

Fernando Estéfan Thibodeaux Garcia

A dissertation submitted in partial satisfaction of the

requirements for the degree of

Doctor of Philosophy

in

Engineering – Civil and Environmental Engineering

in the

Graduate Division

of the

University of California, Berkeley

Committee in charge:

Professor Jonathan D. Bray, Chair
Professor Nicholas Sitar
Professor Douglas S. Dreger

Fall 2018

Abstract

Discrete Element Analysis of Surface Fault Rupture through Granular Media

by

Fernando Estéfan Thibodeaux Garcia

Doctor of Philosophy in Engineering – Civil and Environmental Engineering

University of California, Berkeley

Professor Jonathan D. Bray, Chair

Earthquake surface fault rupture can cause substantial structural damage and loss of life in near-fault regions. Active fault traces cannot always be avoided, especially by linear infrastructure such as lifelines. With effective design the damaging effects of surface fault rupture can be mitigated. The development of effective mitigation techniques warrants investigation of the fundamental mechanisms of earthquake fault rupture propagation through granular media. The discrete element method (DEM) provides an avenue for analyzing the micromechanics of fault rupture propagation and its interactions with the built environment. In this dissertation, DEM is used to simulate reverse and normal fault rupture in three-dimensions (3D) with assemblages of irregularly shaped sphere-clusters that capture the non-spherical nature of real sand grains.

Simulated dip-slip fault rupture surfaces delineated by particle rotations, frictional dissipation, and strains compare favorably with the results of sandbox-style experiments at various fault dip angles. Reverse fault rupture surfaces become less curved and more linear as the fault dip angle decreases from 90° to 30°, and normal fault rupture simulations successfully capture graben development at shallow fault dip angles. Arched distributions of strong contact forces show a stress arching phenomenon in normal fault rupture that is also seen in trapdoor simulations, and the mechanism of graben formation in shallow normal fault rupture is shown through the collapse of the arched distribution of strong contact forces. Steep reverse fault rupture produces half-arched patterns of strong contact forces that are also present in anchor pull-out simulations, and a widespread distribution of strong contact forces develops over the entire hanging wall during shallow reverse fault rupture. Significant out-of-plane particle rotations highlight the need for 3D DEM even in scenarios of plane-strain shearing.

Simulations with a wide range of void ratio distributions capture the transition from distinct localization to broadly distributed shearing as the void ratio increases, which also produces a smaller gradient of the deformed ground surface. Contractive and dilatant volumetric changes during shearing are associated with increases and decreases in the coordination number of individual particles. In assemblages with the same stress distribution but different relative densities, the inter-particle contact forces are higher on average in looser assemblages because the total force in the system is distributed across fewer contacts. The higher contact forces and more widespread distribution of shear deformation in loose particle assemblages dissipate more friction during fault rupture than in denser particle assemblages. In all particle assemblages, reverse fault

rupture increases the number of horizontally oriented inter-particle contacts; whereas, normal fault rupture produces a slight decrease in the number of horizontally oriented inter-particle contacts.

The LIGGGHTS DEM code is modified and used to perform a large suite of direct shear test simulations with different particle shapes, relative densities, and applied pressures. High-performance computing facilitates the simulation of over 100,000 sphere-clusters containing approximately 250,000 constituent spheres. Through homogenization techniques, the mobilized friction angles measured at the rigid-wall boundaries of the test are shown to reflect accurately those that develop along the mid-plane of each specimen, and the angles of dilation measured at the boundaries slightly underestimate those along the mid-plane due to partial absorption of the volumetric expansion through the rest of the specimen. Densely packed particle assemblages exhibit strain-softening, volumetric dilation, and distinctive shear bands seen through localized particle rotations; whereas loosely packed particle assemblages exhibit contraction, no distinct peak strength, and broadly distributed particle rotations throughout the specimen. The shear bands through densely packed sphere-clusters are thicker than those through spheres due to the inability of spheres to interlock. The inability of the particles to crush in the simulations produces little stress dependency in the critical state void ratio, but stress dependency is observed through the coordination number at the critical state and in the initial stiffness of each particle assemblage. Fluid-like characteristics such as vortex structures within the shear bands of densely packed sphere-clusters are seen in the velocity fields of the particle assemblages.

The interaction between a propagating fault rupture surface and a rigid building foundation is simulated for the first time with 3D DEM. High-performance computing with a modified version of the LIGGGHTS DEM code is used to efficiently simulate 400,000 to 1.7 million sphere-clusters containing up to approximately 4.3 million constituent spheres. Physically observed influences of the contact pressure, position, and width of the foundation on fault rupture propagation are captured satisfactorily with high-performance DEM simulations containing hundreds of thousands of sphere-clusters. Micromechanical analyses of particle rotations, void ratios, and contact forces provide valuable insight into mechanisms of reverse and normal fault-foundation interaction. The reverse fault rupture surface is shown to deflect systematically towards the hanging wall edge of the foundation as the foundation contact pressure increases, because higher foundation contact pressures increase the forces between particles and essentially create a barrier to shear rupture beneath the foundation. If the foundation is located sufficiently away from the projected surface fault trace on the footwall during normal fault rupture, a complex sequence of fault rupture propagation develops in which shear activity ceases along one rupture surface propagating towards the hanging wall edge of the foundation and migrates towards a second rupture surface that ultimately outcrops on the footwall edge of the foundation. DEM has great potential for understanding the fundamental granular influences on earthquake surface fault rupture.

To Mamee, Papee, Astrid, Rafael, Inez, and Luis.

TABLE OF CONTENTS

LIST OF FIGURES

ACKNOWLEDGEMENTS

This dissertation is based upon work supported by the National Science Foundation (NSF) Graduate Research Fellowship under Grant No. DGE 1106400. Any opinion, findings, and conclusions or recommendations expressed in this dissertation are those of the author and do not necessarily reflect the views of the NSF. Additional financial support was provided by the Faculty Chair in Earthquake Engineering Excellence in the College of Engineering at UC Berkeley. The Savio computational cluster resource was provided by the Berkeley Research Computing program at UC Berkeley. The Extreme Science and Engineering Discovery Environment (XSEDE), which is supported by NSF grant number ACI-1548562, provided Bridges, Comet, SuperMIC, and Stampede2 computational cluster resources under allocations TG-BCS170013 and TG-TRA150025. The Particle Flow Code software was provided by Itasca Consulting Group through the Itasca Education Partnership.

First and foremost, I want to thank my PhD advisor Prof. Jonathan Bray for his guidance, support, and mentorship throughout this research. Prof. Bray challenged me to always aim higher than I initially thought I could, and his unfaltering faith in my capabilities gave me the necessary confidence to overcome all challenges in the research process. I am forever grateful for his positivity and for the knowledge and wisdom he instilled in me for both my life and my career.

I would like to thank the many brilliant scientists and engineers who graciously lent their time to provide helpful feedback and insight throughout the preparation of this dissertation. My many conversations with my dissertation committee members Prof. Nicholas Sitar and Prof. Douglas Dreger always left me with new ideas and considerations for this research, and I thank them for their thorough reviews of this dissertation and their constructive comments. I thank Dr. David Potyondy and Dr. Varun of Itasca Consulting Group for their many online meetings that helped me become proficient with the Particle Flow Code, and I thank Prof. Catherine O'Sullivan and Dr. John O'Donovan of Imperial College London for taking the time to answer many of my questions in the early stages of this research. Prof. O'Sullivan provided her strain homogenization code for use in Chapters 3 and 4. Dr. Nicolas Oettle shared results and helpful insights for Chapter 6, and Drs. George Gazetas and Ioannis Anastasopoulos shared the results of centrifuge experiments conducted by Dr. Mark Bransby and others as part of their collaborative research project. Chapters 3, 4, and 5 were further improved with comments and feedback by anonymous journal reviewers.

I am grateful to the geotechnical engineering, structural engineering, seismology, and mathematics faculty at UC Berkeley who educated me in the background and skills needed to even begin the work of this dissertation. Prof. Michael Riemer, Prof. Juan Pestana, Prof. Raymond Seed, Prof. Kenichi Soga, and Prof. Rob Kayen all at different times offered their expertise on specific topics relevant to this dissertation or offered sage advice on the research process in general, and I thank them all for opening their doors to me. The Berkeley Research Computing staff were extremely helpful to me as I first learned to use high-performance computing systems. I also want to thank Shelley Okimoto and the rest of the Davis Hall staff for helping me navigate the administrative side of graduate school. Furthermore, I thank Dr. Swaminathan Krishnan, Dr. Ramses Mourhatch, Dr. Robert Nigbor, and the faculty of the Department of Civil & Environmental Engineering at UCLA for preparing me to enter graduate school in the first place.

My friends in Davis Hall truly made my graduate school experience unforgettable. For all the good times shared, I would like to thank my fellow PhD students, in no particular order, Jorge Macedo, Christine Beyzaei, Chukwuebuka Nweke, Michael Gardner, Grigorios Lavrentiadis,

Nella Pierre Louis, Robert Lanzafame, Ezra Setiasabda, Daniel Hutabarat, Christie Hale, Julien Cohen-Waeber, Maggie Parks, Roberto Luque, Chris Markham, Mike George, Nathaniel Wagner, Khaled Chowdhury, Heyder Carlosama, Zhishuai Zhang, Regan Patterson, Brad Harken, Jiang Jun Lee, and Zhen Yang, as well as the "It Depends..." crew of my master's classmates. I am fortunate to have met so many visiting scholars and post-doctoral fellows who joined the Davis Hall community, and I thank Dr. E. James Fern, Dr. Krishna Kumar, and Dr. Xingyue Li for sharing with me their own insight on topics related to my research during their stays in Berkeley. In addition, I thank my friends and colleagues outside of Davis Hall for their moral support, especially Sean Ahdi for his many visits and random conversations from UCLA.

I cannot overstate how important the encouragement of my entire family has been to me during my time at UC Berkeley. I especially thank my parents Amber and Fernando for being my role models and for supporting all of my endeavors my whole life. To my siblings Adrianna, Vince, Tyler, and Jaymi and my cousins Nicque, Rena, Tiahnna, Phillip, Isela, Xavier, and Wyatt: You have always been my inspiration.

Finally, I owe a most profound thanks to my partner in life, Kelly, for giving me the courage to embark on this journey, even though it meant moving hundreds of miles away from her. I am always amazed by her incredible strength and patience as we strive to achieve our goals together. Her love, support, and encouragement were truly instrumental in the completion of this dissertation.

CHAPTER 1: INTRODUCTION

1.1 Research Motivation and Objective

Earthquake surface fault rupture is the natural phenomenon in which subsurface fault rupture manifests in some form at the ground surface. Much of modern earthquake engineering research focuses on hazardous effects related to the seismically induced ground motions felt over a broad area of several kilometers or tens of kilometers. Surface fault rupture, on the other hand, is the static component of fault offset that results in local permanent ground surface deformation. This permanent ground surface deformation takes many forms, including but not limited to broad warping in ductile soils and distinct, localized offsets in stiff, brittle soils as demonstrated for dip-slip fault rupture in Fig. 1.1 (Bray et al. 1994a). The emergence of fault rupture at the ground surface can induce devastating and catastrophic damage when it collides with the built environment, as demonstrated in Fig. 1.2 from the 1999 Kocaeli, Turkey, earthquake.

The potential for devastating damage and loss of life due to earthquake surface fault rupture warrants extreme scrutiny of this phenomenon by the modern civil engineering research community. Since as far back as the 1906 San Francisco earthquake and fire (Lawson 1908), earthquake engineers, particularly in near-fault regions, have been forced to consider the potential for this hazard in design guidelines. One of the principal design guidelines for siting structures near active faults centers around avoidance. The Alquist-Priolo Earthquake Fault Zoning Act[1] of 1972, or A-P Act, formally passed this avoidance guideline into law in California by requiring that "no structure for human occupancy…be permitted to be placed across the trace of an active fault" and that "the area within fifty (50) feet of such active faults shall be presumed to be underlain by active branches of that fault unless proven otherwise…" (Anderson et al. 2018). The choice of 50 feet in the A-P Act may be under-conservative if the fault zone includes secondary faulting over distances of hundreds of feet, as was observed following the 1906 San Francisco earthquake (Lawson 1908, Bray & Kelson 2006), or overconservative if the fault zone is confined to a narrow, localized trace. Field reconnaissance following past earthquakes such as the 1999 Kocaeli, Turkey, earthquake has shown that buildings located well within 50 feet of a normal fault trace may actually incur negligible damage when located on the footwall side of the surface fault trace (e.g., Lettis et al. 2000). Enforcing avoidance is only a partial solution to the surface fault rupture hazard.

Reasons for needing to build new structures near or across active fault traces may arise due to growing urban populations. As the populations continues to grow in major cities, demand will rise for new space in which people can reside. Linear infrastructure such as lifelines, railways, and highways that connect these population centers are especially vulnerable to damage related to surface fault rupture in near-fault regions. Active faults such as the San Andreas Fault may extend for long distances, which makes them extremely difficult to circumnavigate. Complete avoidance of the surface fault rupture hazard is economically impractical. Even if all efforts are made to adequately set structures back from known active fault traces, there is still an ever-present possibility of the existence of unknown faults. The 1994 Northridge earthquake in southern California highlights the hazard of unknown subsurface faults, because its mainshock and aftershock sequence revealed a previously unmapped thrust fault beneath the San Fernando Valley (Hauksson et al. 1995). The location of this fault beneath such a heavily populated area further exacerbated its damaging effects and increases its future risk. Undetected, unknown, or unmapped

1 http://www.conservation.ca.gov/cgs/rghm/ap

faults can become even more damaging if their rupture reaches the ground surface, especially if a structure situated at its outcrop location is designed without consideration of surface fault rupture. Uncertainty in the presence or lack thereof of an active fault is a principal reason why avoidance is not always a complete solution to the surface fault rupture hazard.

The A-P Act does not protect the many structures that were sited across an active fault trace prior to 1972. Such buildings may be retrofit to accommodate fault displacement in a way that maintains serviceability and life safety, as was done for the California Memorial Stadium, which is directly intersected by the Hayward Fault in Berkeley (Friedman et al. 2012). Furthermore, other types of ground movement including mining subsidence, landslides, and lateral-spreading have warranted strategic structural design to accommodate the ground movement instead of avoiding the hazard entirely (Bray 2001). Since retrofit schemes are permissible for existing structures sited across active fault traces and structures have been designed to accommodate other forms of ground movement, then structures may be designed to accommodate fault movement following a thorough geologic investigation to characterize the magnitude and frequency of activity on the fault trace.

Case studies of surface fault rupture interaction with structures shows that mitigation of this hazard is possible. Heavily reinforced concrete structures that induce large contact pressures on the soil, for example, may incur very little damage by actually deflecting the path of fault rupture. This was demonstrated by the bunkers diagrammed in Fig. 1.3 during the 1999 Düzce, Turkey, earthquake (Lettis et al. 2000, Bray 2001) and by the underground basement housing the bank vault of the Banco Central building in downtown Managua during the 1972 Managua, Nicaragua, earthquake (Niccum et al. 1976). The improvement of mitigation techniques based on these and other case studies begins with a fundamental understanding of the surface fault rupture phenomenon. Such an understanding informs the development of new design or retrofit guidelines for structures near active faults.

Engineers, geologists, and seismologists use a variety of methods to fundamentally understand the process and mechanisms of surface fault rupture propagation and its effects on structures. Case studies of real surface fault rupture events are the first tool used to study this phenomenon. Case studies may involve observations of structural damage, ground deformations, trench investigations, and other geologic observations to understand the characteristics of a specific event. Regression analyses may pool together data from a large suite of case studies to gather statistical variations and relations between different variables involved in fault rupture. Wells & Coppersmith (1994), for example, gathered data from over 400 earthquakes to develop empirical relations linking subsurface rupture length, surface rupture length, subsurface rupture width, rupture area, maximum and average surface displacement, moment magnitude, and seismic moment for reverse, normal, and strike-slip faults. These empirical relationships are useful for predicting future fault rupture variables based on past observations. The drawback to case studies and regression analyses is that large earthquakes, e.g., $M_w > 4.5$ in Wells & Coppersmith (1994), are relatively infrequent. Years may pass before a new earthquake occurs that can improve a given data set, and, without enough data, statistical variation could be very high.

Experimentation is useful for studying surface fault rupture in a controlled laboratory environment. Laboratory experiments of fault rupture are much smaller in scale than real case studies and are sometimes referred to as "sandbox" style tests given the relatively small size of the soil container. They may be performed at 1g or up to several hundred g's if performed with a centrifuge. The main advantage of centrifuge testing over 1g testing is that the stress distribution present in the field (i.e. in a real, natural soil deposit) can be replicated at the laboratory scale.

Given that the stress state, soil characteristics, and type of deformation in the field are the same as those controlled in the laboratory, a given soil will respond in the laboratory similarly to how it responds in the field.

Experimental results are gathered observationally at the visible boundaries of an experiment or inferred from measurements at select locations such as through precisely located load cells. Fully quantitative information throughout the experimental domain, particularly within the domain instead of at the boundaries, is difficult to obtain physically. Numerical and computational methods, on the other hand, do provide fully quantitative information throughout the model domain. Numerical methods fall into two general categories for studying surface fault rupture: continuum methods and discrete methods. The most common continuum methods, the finite element method (FEM) and finite difference method (FDM), calculate the stresses and strains in each element of a mesh through the forces and displacements calculated at the nodal points of the mesh. Discrete methods, on the other hand, track the motions of individual particles and the interactions of pairs of particles. Continuum methods are computationally efficient and can provide valuable insight for geotechnical design. Stress dependency and dilational responses of the soil are captured through constitutive models that relate stresses and strains utilizing theories of elasticity and plasticity applied to soils. The input parameters for constitutive models are typically determined through laboratory testing of soil specimens or through field testing, and then the model may be subsequently applied to large-scale design projects to evaluate potential failure mechanisms and factors of safety. The efficiency of continuum modeling and the ease of constitutive model calibration makes continuum modeling quite attractive for engineering practice. However, the calibration procedure for constitutive models is for the behavior of a *mass* of soil, and the applications of most continuum modeling are strictly macroscopic. The characteristics, interactions, and kinematics of individual soil grains are only incorporated in how they relate to observed behaviors of the soil mass. Treatment of particles as individual entities with real pore space between them requires discrete methods. Since particles are tracked individually and no meshes are involved, discrete methods are particularly well-suited for large strain problems, whereas continuum modeling may require re-meshing techniques or meshfree methods such as the material point method (MPM) to effectively analyze large-strain problems. Unlike in physical experiments, discrete methods can track quantitative information about the kinematics and interactions of individual particles throughout the entire model domain instead of just at select locations.

A significant hindrance for discrete methods is their high computational demand. Field-scale soil masses include billions or trillions of individual soil grains, and even laboratory soil specimens may have millions of individual grains. Many simplifications, such as increasing the size of particles or using idealized grain shapes, must be made for discrete models to be practical for surface fault rupture problems. Simplification is inherent to all experimental and numerical methods for studying surface fault rupture, but even with notable simplifications, discrete methods can provide valuable insight into the shear characteristics and localization behavior of masses of particles when the interactions and kinematics of the individual particles are closely scrutinized. In-depth analysis of how macroscopic observations relate to grain-scale phenomena in numerical simulations provides significant insight into how real field-scale phenomena relate to inter-granular interactions. This insight can be useful in developing and evaluating mitigation measures against natural hazards.

All methods used for studying earthquake surface fault rupture have notable advantages over one another, and each method has some notable drawbacks. No one method is any better than

another except in how it answers a specific question. The specific question asked in this study of earthquake surface fault rupture is *how do the granular kinematics and inter-granular interactions inform the process of fault rupture propagation from the bedrock to the ground surface?* Earthquake surface fault rupture is fundamentally a discontinuity problem involving shear rupture through a mass of individual particles. It is fundamentally a granular phenomenon. Hence, the question asked in this study must be answered through a method that addresses the fundamental granular nature of soil. Furthermore, full knowledge of how granular phenomena relate to the mechanisms of fault rupture propagation from the bedrock to the ground surface at the macroscopic level requires a fully quantitative approach. Of all the research methods available, discrete methods are the only methods that can achieve both of these goals simultaneously.

The simulations in this dissertation utilize the discrete element method (DEM), also commonly referred to as the distinct element method, originally developed by Cundall & Strack (1979). DEM is a viable alternative to continuum modeling and an effective complementary tool to be used in conjunction with experimentation, continuum modeling, and investigations of real surface fault rupture events. The most in-depth study of surface fault rupture requires insightful contributions from all available research techniques, and this study provides contributions that can only be gained using discrete methods.

1.2 Scope of Research

The scope of this dissertation is limited to dip-slip fault rupture and similar plane-strain boundary-displacement problems involving cohesionless, dry, granular materials. Cohesive, clayey materials are not considered, because the sizes of clay particles are so small and the effects of chemical cohesion so strong that their mass is effectively a continuum that is better suited for continuum-based numerical analyses. Furthermore, many laboratory dip-slip fault experiments using dry, cohesionless sands are described in the literature that may serve as effective validation studies for the simulations presented in this dissertation. Other boundary-displacement problems analyzed in this dissertation are anchor pull-out, trapdoor displacement, and the direct shear test. Strike-slip fault rupture, while recognized as a significant natural hazard, is not considered in the suite of simulations presented in this dissertation. Significant attention is given to the analysis of reverse and normal fault rupture in the free-field and with a rigid mat foundation located atop the ground surface. Mechanisms of quasi-static fault rupture propagation are analyzed without considerations of dynamic effects. The effects of saturation or partial saturation are not considered, because the materials would be considered drained during quasi-static rupture.

1.3 Research Outline

This dissertation is organized into 7 chapters including this introduction. Chapter 2 presents a review of the literature on earthquake surface fault rupture with a focus on recent case studies, experimental studies, and numerical modeling of earthquake surface fault rupture and related boundary-displacement problems. A very brief overview of relevant DEM concepts is presented, and the significant findings of previous discrete element studies of surface fault rupture and related boundary-displacement problems are presented. Chapter 3 presents an analysis of surface fault rupture through dilatant, granular material and other boundary-value problems. Chapter 4 presents analyses of surface fault rupture through materials of varying density to show how DEM captures the effects of soil ductility through varying void ratio on fault rupture propagation. The analyses

in Chapters 3 and 4 are performed using the Particle Flow Code in three dimensions (PFC3D; Itasca 2014). Chapter 5 presents analyses from a suite of direct shear test simulations using a high-performance parallel computing code called LIGGGHTS (Kloss et al. 2012). These analyses show the effects of particle shape and void ratio on the shear characteristics of three-dimensional (3D) particle assemblages. Chapter 6 presents analyses and findings from simulations of fault rupture interaction with rigid mat foundations using the LIGGGHTS DEM code. At the time of this writing, no other author has shown the influence of a heavy, rigid foundation on the path of rupture propagation during dip-slip fault rupture using DEM. In Chapter 7, the summary of this dissertation, the principal findings, and suggestions for future research are presented.

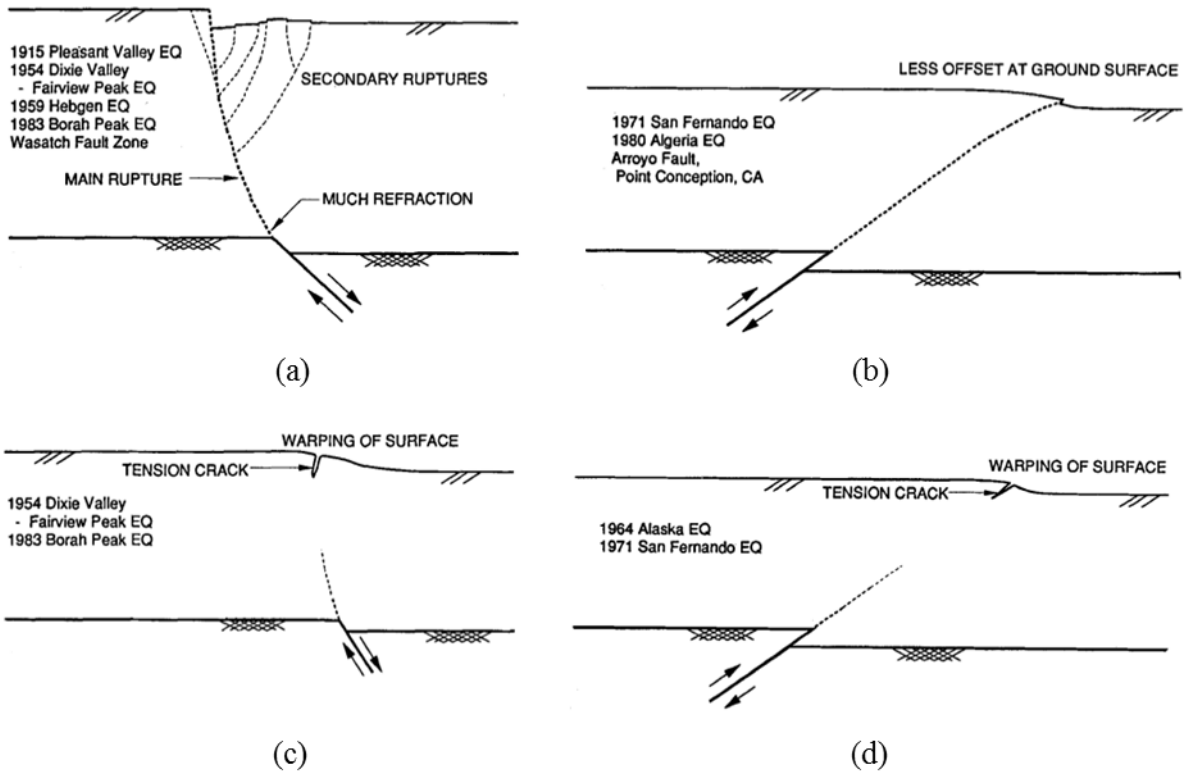

Fig. 1.1. Idealized schematics of (a) distinct fault scarp formation during normal fault rupture through stiff soil, (b) distinct fault scarp formation during reverse fault rupture through stiff soil, (c) warping of the ground surface during normal fault rupture through ductile soil, and (d) warping of the ground surface during reverse fault rupture through ductile soil (figures from Bray et al. 1994a, with permission from ASCE).

Fig. 1.2. Damage to a primary school building in the village of Kullar due to rupture on the Sapanca fault segment during the 1999 Kocaeli, Turkey, earthquake (Photo by L.S. Cluff; from Lettis et al. 2000, reproduced with permission of the Earthquake Engineering Research Institute). Lettis et al. (2000) report approximately 2 m of lateral offset and 0.5 m of vertical offset at this location.

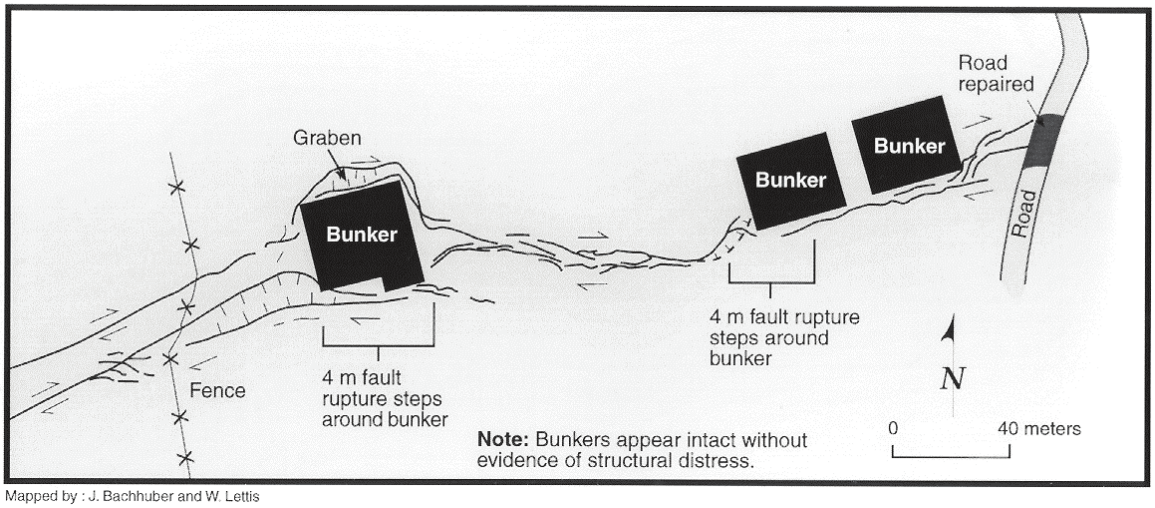

Fig. 1.3. Heavy concrete bunkers located at the Gölcük Naval Base. The bunkers incurred no structural damage from 4 m of strike-slip offset on the Gölcük fault segment during the 1999 Kocaeli, Turkey, earthquake (Lettis et al. 2000, reproduced with permission of the Earthquake Engineering Research Institute; figure modified by Bray 2001).

CHAPTER 2: LITERATURE REVIEW

2.1 Introduction

This section presents relevant advances in discrete element modeling as well as recent findings from earthquake surface fault rupture studies. Surface fault rupture case studies from 2014 to 2016 are presented, and the significance of these events based on the information gathered by different reconnaissance teams are discussed. Relevant experimental and numerical continuum studies of surface fault rupture are then summarized and discussed. This literature review of surface fault rupture builds upon the literature reviews of Bray (1990), Lazarte (1996), and Oettle (2013). A brief overview of relevant discrete element modeling concepts is provided as well as recommendations for aspiring researchers to begin learning about discrete element modeling. The discrete element modeling review builds upon the previous literature reviews of Thomas (1997) and O'Sullivan (2003) and focuses on those aspects that are relevant to the analyses of surface fault rupture in this dissertation. A comprehensive overview of discrete element studies of surface fault rupture, soil-structure interaction, and similar boundary-displacement problems is presented as well. The needs for on-going research on earthquake surface fault rupture using DEM are discussed based on the review of the literature.

2.2 Overview of Recent Surface Fault Rupture Cases

Field studies of surface fault rupture are critical to understanding this phenomenon and for validating physical and numerical models. The dissertations of Bray (1990), Lazarte (1996), and Oettle (2013) together present a comprehensive overview of all major surface fault rupture case histories up until the aftershocks of the 2011 Tohoku, Japan, earthquake. In the time since that event, several more major earthquakes occurred around the world, many of which caused significant damage to infrastructure and loss of life. The findings from the investigations of surface fault rupture produced by major earthquakes since 2014 are summarized below. More complete descriptions of the case studies below may be found at the website for the Geotechnical Extreme Events Reconnaissance (GEER) Association (www.geerassociation.org).

2014 South Napa, California Earthquake (M_w6.0)

The 2014 M_w6.0 South Napa, California, earthquake occurred on August 24, 2014. Rupture initiated in the West Napa Fault Zone approximately 8 km southwest of Napa, California, at a focal depth of approximately 10 km (Bray et al. 2014). Not since the 1906 San Francisco earthquake has an earthquake of this magnitude struck Northern California, and no other earthquake has produced expressions of surface fault rupture within a densely populated region of Northern California (Bray et al. 2014). Significant findings from this event are documented in GEER Report #GEER-37 (Bray et al. 2014). The GEER reconnaissance team observed right-lateral expressions of surface fault rupture at different parts of the West Napa Fault zone over a distance of 12-15 km. They report surface offsets on the order of 20-25 cm in most areas with some offsets up to 45 cm and en echelon left-stepping fractures along the surface fault trace as shown in Fig. 2.1 The en echelon fractures varied in width from less than 1 m to several tens of meters (Bray et al. 2014), and this magnitude of variation in fracture width is consistent with similar observations from the 1906 San Francisco earthquake (Lawson 1908, Bray & Kelson 2006). As shown in Fig. 2.2, surface rupture

traces were much more localized across paved roads than in unpaved granular soils as in Fig. 2.1 (Bray et al. 2014). Compressional ground movement coupled with strike-slip offset also caused buckling of sidewalks and pavement, as shown in Fig. 2.3 (Bray et al. 2014). As discussed in Bray et al. (2014), the reconnaissance team observed latent surface fault rupture that did not appear until 36-48 hours following the August 24 mainshock.

The types of structural damage resulting from surface fault rupture fell into 3 categories described by Cohen-Waeber et al. (2015) as:

- Type I: *"Cracking of reinforced concrete and concrete masonry components within structures."*
- Type II: *"Displacement between structures and adjacent ground or structures."*
- Type III: *"Cracking of paved and unpaved areas at the ground level."*

Bray (2009), in a summary of surface fault rupture design recommendations, advises against anchoring structures into the ground with piles or piers and instead recommends the use of unanchored foundations such as thick, reinforced mat foundations. The damage observations of Cohen-Waeber et al. (2015) support these recommendations. Cohen-Waeber et al. (2015) observed that structures founded on strip footings tended to have a "decoupling" effect from the ground surface and thus exhibited only Type II damage due to sliding, whereas structures founded on pier and grade-beam foundations exhibited much Type I cracking due to differential ground settlement. In two specific examples of stiff, seismically retrofit structures founded atop strip footings described by Cohen-Waeber et al. (2015), surface fault rupture did not cause significant damage even though the fault trace directly traversed these structures. Other more flexible structures founded atop strip footings in Cohen-Waeber et al. (2015) showed more Type I cracking. These observations of both anchored, flexible structures incurring significant damage and stiff structures on reinforced strip footings exhibiting negligible damage support the defensive measures for accommodating surface fault rupture outlined in Bray (2009).

2015 Gorkha, Nepal Earthquake (M_w7.8)

The M_w7.8 Gorkha, Nepal, earthquake occurred on April 25, 2015, followed by 5 aftershocks of magnitude greater than 6.0 (Hashash et al. 2015). The mainshock occurred at a depth of 15 km approximately 80 km northwest of the city of Kathmandu on the Main Himalayan Thrust fault, a blind thrust fault which separates the Indian Plate from the Eurasian Plate (Hashash et al. 2015). Although surface fault rupture did not actually occur during this event, Hashash et al. (2015) note that previous earthquakes along branches of the Main Himalayan Thrust fault, typically of magnitude 8.0 or greater, did produce surface fault rupture expressions in the past. This suggests a threshold for full surface fault rupture propagation along this particular fault.

2016 Kumamoto, Japan Earthquakes (M_w6.0, M_w6.2, M_w7.0)

The 2016 Kumamoto, Japan, earthquakes are a series of 3 earthquakes including 2 foreshocks and 1 mainshock. The first foreshock of M_w6.2 occurred on April 14 on the Hinagu Fault, the second foreshock of M_w6.0 occurred on April 15 on the Hinagu Fault, and the mainshock of M_w7.0 occurred on April 16 on the Futagawa Fault beneath Kumamoto City in the Kumamoto Prefecture on Kyushu, Japan (Kayen et al. 2016). The GEER reconnaissance team, as documented

in GEER Report #GEER-048 by Kayen et al. (2016), observed surface fault rupture traces over a distance of 28 km along the Futagawa Fault and over a distance of 6 km on the Hinagu Fault. Right-lateral strike-slip movement of up to 2.2 m occurred with up to 0.35 m of associated vertical offset on the Futagawa Fault (Kayen et al. 2016). Unlike in the Napa earthquake, no latent fault rupture was reported.

Three notable case histories of surface fault rupture damage are detailed in Kayen et al. (2016). The first is that of the Oh-Kirihata Dam. The Futagawa fault crossed the reservoir of this dam along the flank of the reservoir and through the intersection between its spillway and spillway outlet channel, as shown in Fig. 2.4 (Kayen et al. 2016). The highway in Fig. 2.4 also shows right-lateral strike-slip offset with significant cracking damage to the pavement. Kayen et al. (2016) briefly mentions a pipeline failure that caused water to flow out of the dam, leading downstream residents to evacuate in fear of a dam break. The LIDAR (Light Detection and Ranging) image shown in Fig. 2.5 shows the fault zone through the Oh-Kirihata Dam. The width of rupture was approximately 9 m wide where it entered the southwest side of the dam and 25 m wide on the northeastern side of the dam near the embankment and spillway (Kayen et al. 2016). Reconnaissance team members estimated lateral movement of approximately 50 cm with little vertical movement. Surface fault movement caused one of the spillway retaining walls to fail, displacing soil into the spillway as shown in Fig. 2.6. Kayen et al. (2016) suggests that a catastrophic breach could have occurred during the Kumamoto earthquake if the reservoir overtopped its spillway and eroded the soil exposed behind an opened gap in the spillway. A larger vertical offset of 9 m underneath the Shihkang Dam during the 1999 Chi-Chi, Taiwan, earthquake did cause a significant breach that prohibited the Shihkang Dam from continuing to divert water to the city of Taichung (Bray 2001). These two cases in Japan and Taiwan highlight the vulnerability of dams traversed by active faults.

The second case study is that of the Aso Caldera Depression Zone. The Aso Caldera is a region of active volcanism, and the depression zone is a 10 km-long graben-like feature produced by the earthquake (Kayen et al. 2016). The image in Fig. 2.7 shows a view of this depression zone as it cuts through a rice field. Fig. 2.8a shows a structure on the upthrown block of the depression zone that shows very little damage to its outer façade and no cracking in its windows. The lack of damage in this building is recognizant of a similar case from the 1999 Kocaeli, Turkey, earthquake in which a house within a few meters of a normal fault trace exhibited almost no damage due to its location on the footwall, as shown in Fig. 2.8b. Kayen et al. (2016) interprets the primary fault trace of the depression zone as being caused by nearly vertical normal fault movement of 0.5-2.5 m on the ring fault of the Aso Caldera, which may be interpreted as a type of trapdoor movement. The second rupture trace that forms the graben-like structure is interpreted by Kayen et al. (2016) as either secondary, antithetic fault rupture in the caldera or a result of interaction with a ring dike or other geologic feature. Numerical finite element analyses by Oettle et al. (2017) suggest an alternative interpretation of the depression zone as being caused by flat or extremely shallow normal faulting that produces primary and secondary rupture surfaces dipping in opposite directions. As shown in Fig. 2.9, a bridge that crossed this depression zone did not settle with the rest of the ground surface, which suggests that the depression zone may have resulted from consolidation of sediment or a similar mechanism as opposed to normal fault rupture (Kayen et al. 2016). However, if the bridge piles resisted damage from the fault rupture and rested on the footwall of the fault, then the bridge may still not have settled with the rest of the surrounding soil.

The third surface fault rupture case study from Kayen et al. (2016) is of the Shimojin-Cho River Canal. Kayen et al. (2016) reports that at this site, two separate strands of the Futagawa Fault

converged and ruptured through the canal. Right-lateral strike-slip rupture consistent with the rupture mechanism in the previous two case studies occurred along a northeastern-trending strand, but another northwest-trending strand exhibited left-lateral strike-slip rupture (Kayen et al. 2016). Kayen et al. (2016) interprets this second strand as a link between a northern strand of the Futagawa Fault located 0.6 km north of where the Futagawa Fault intersects the canal.

2016 Central Italy Earthquake Sequence (M_w6.0, M_w5.9, M_w6.5)

The 2016 Central Italy earthquake sequence consisted of 3 earthquakes that are documented in GEER Report #GEER-050 (Zimmaro & Stewart 2016a,b, 2017a,b). The first earthquake of M_w6.0 occurred at a focal depth of 8 km on August 24 in a stepover zone between the Mt. Vettore Fault and the Amatrice Fault within a seismic gap between the epicenters of the 1997 M_w6.1 Umbria-Marche earthquake and the 2009 M_w6.1 L'Aquila earthquake (Zimmaro & Stewart 2016b). The GEER reconnaissance team notes in Zimmaro & Stewart (2016b) that this seismic gap was recognized and designated as a zone of elevated risk prior to the August 24 event. Strong ground shaking during this event caused significant damage to unreinforced masonry structures and 299 fatalities in the towns of Arquata del Tronto, Accumoli, Amatrice, and Pescara del Tronto (Zimmaro & Stewart 2016b). The next two earthquakes of M_w5.9 and M_w6.5 occurred on the Mt. Vettore fault within the seismic gap on October 26 and October 30, respectively. The latter two events caused significant damage to the villages of Visso, Ussita, and Norcia but did not cause additional loss of life in part due to evacuations (Zimmaro & Stewart 2017b). Zimmaro & Stewart (2016b) note that the length of surface rupture and the amount of surface displacement are consistent with the statistical findings of Wells & Coppersmith (1994) for an earthquake of this magnitude.

The August 24 event produced downward surface displacements of up to 35 cm with an average of 12 cm over a 5 km stretch of the Mt. Vettore fault (Gori et al. 2018, Zimmaro & Stewart 2016b). Oettle & Bray (2013a) showed numerically that fault rupture tends to follow paths of least resistance through existing, pre-ruptured shear zones, and the rupture patterns from the October 30 event support those numerical findings. Zimmaro & Stewart (2017a) state that the October 30 earthquake re-ruptured the previously ruptured stretch of the Mt. Vettore fault from the August 24 event and brought the total length of the surface fault rupture to 15-20 km. Zimmaro & Stewart (2017a) also report vertical surface displacements from the October 30 event as high as 1.6 m even in some of the same areas where the August 24 event only produced displacements of 10-25 cm. Two examples of the October 30 event producing even more offset along the same fault scarp produced by the August 24 event are shown in Figs. 2.10 and 2.11. The October 30 event did not only produce rupture along pre-ruptured fault traces; Zimmaro & Stewart (2017a) also report new displacements from the October 30 earthquake of "several tens of cm" in two areas that did not displace during the August 24 event.

2016 Kaikoura, New Zealand Earthquake (M_w7.8)

The Kaikoura, New Zealand, earthquake of M_w7.8 occurred on November 14, 2016, at a focal depth of approximately 15 km on a strand of the Humps Fault Zone underneath the north Culverden Basin (Cubrinovski & Bray 2017). The rupture propagated approximately 180 km, inducing discontinuous rupture on at least 21 faults, both mapped and unmapped (Stirling et al. 2017, Cubrinovski & Bray 2017). Cubrinovski & Bray (2017) report several examples of large

surface fault offsets including vertical and horizontal displacements of up to 2 m near Waiau, vertical displacements of up to 5 m on the North Leader oblique thrust fault, and 10 m of horizontal offset with 7-8 m of vertical offset on the Kekerengu Fault. The Kaikoura Earthquake also produced significant coastal uplift, especially along the Papatea Fault, which exposed seabed off the Kaikoura coast (Clark et al. 2017). Cubrinovski & Bray (2017) report that the most coastal uplift of approximately 6 m occurred where two strands of the Papatea Fault intersected the coast. An example of this coastal uplift is visible in Fig. 2.12. Combined with low-tide conditions, the coastal uplift actually helped reduce the impact of subsequent tsunami run-up (Bradley et al. 2017). On land, such significant uplift caused significant damage to homes and infrastructure. As shown in Fig. 2.12, the rupture crossing through State Highway 1 produced significant vertical uplift that rendered this particular stretch of highway impassable (Stirling et al. 2017). Another example of significant damage is shown in Fig. 2.13 where reverse fault rupture outcrops directly beneath a single-story house (Stirling et al. 2017). Since many of the faults that ruptured during the Kaikoura earthquake were unmapped, the type of damage shown in Figs. 2.12 and Figs. 2.13 may not be fully avoidable if the active fault traces in the region are not known prior to construction of new roadways, lifelines, and residences.

2.3 Overview of Relevant Experimental Studies

The dissertations of Bray (1990), Lazarte (1996), and Oettle (2013) together present a thorough overview and critical evaluation of previous experimental studies of surface fault rupture completed prior to the year 2013. The key points of those studies that are particularly relevant to this dissertation are reiterated in this section, and more comprehensive summaries may be found in the previous reviews. In addition to surface fault rupture studies, experimental studies of problems with similar boundary conditions including direct shear testing, anchor pull-out, and trapdoor displacement are also discussed.

The study of Tchalenko (1970) highlights why direct shear testing should be included in the same category of boundary-displacement problems as surface fault rupture. Tchalenko (1970) observed that very similar patterns of shear rupture through stiff, clayey soils develop at different scales. The scales discussed by Tchalenko (1970) are shown in Fig. 2.14 and include the microscale with the direct shear box dimensions being on the order of centimeters, the intermediate scale with the Riedel experiment dimensions being on the order of tens of centimeters, and the regional scale on the order of kilometers. The similarity of the shear structures at each of the scales in Tchalenko (1970) suggests that the mechanisms of shear rupture development can be reliably studied in the laboratory setting. These findings are most relevant for strike-slip fault rupture, but local shear structures along the rupture surface in dip-slip fault rupture should be similar to those seen locally along a strike-slip rupture surface. In addition to the scales shown in Fig. 2.14, this dissertation also defines the "field scale" as the scale of tens of meters at which local fault rupture propagation may interact with an individual foundation or structure.

The direct shear test is particularly convenient for studying surface fault rupture numerically. The rigid walls of this experiment make numerical implementation of the displacement boundary conditions computationally simple. One issue with direct shear testing is that the stress state within the shear band is not necessarily reflected by the stresses inferred from the boundaries of the direct shear box via axial load cells. Jewell (1989) and Shibuya et al. (1997) both note that the vertical stresses applied through the loading platen of the direct shear test are unevenly distributed along the shear zone in the horizontal direction, which creates a less

distinctive peak stress measurement resulting from progressive failure in shear. While both Jewell (1989) and Shibuya et al. (1997) suggest different kinematic conditions for the upper shear box and loading platen that would allow more uniform stress development and hence a distinctive peak stress during shearing, the recommendation of Shibuya et al. (1997) is preferred in this dissertation. Shibuya et al. (1997) give 3 requirements for the direct shear test arrangement that allow the results to be interpreted as "quasi-simple shear," i.e., interpreted such that the stresses inferred from forces at the boundaries reflect those present along the mid-plane within the shear zone. These requirements are (Shibuya et al. 1997):

1. The lateral walls be made frictionless (or friction minimized) so that the vertical loads can be measured through the lower shear box that does not contain the loading platen.
2. The loading platen be prevented from rotating and the vertical walls be prevented from moving in the vertical direction.
3. The gap between the upper and lower shear boxes be maintained at 10-20D_{50}, where D_{50} is the median grain diameter.

These conditions are shown schematically in Fig. 2.15. If these conditions are met, Shibuya et al. (1997) argue that the boundary-measured strengths and dilatancy are characteristic of those in a simple shear test.

The studies of Tchalenko (1970) and Shibuya et al. (1997) address the issues of scale and interpretation of results when using the direct shear test as an analogy for fault rupture, but they do not address the material itself. If a granular material is used in the direct shear test, particle size effects must be taken into consideration. Dense granular materials will tend to localize during shearing, and the width of the shear band is directly proportional to the particle size. Roscoe (1970) observed that shear bands are approximately 10 grain diameters in thickness. Scarpelli & Wood (1982) also found the shear band width to be approximately 10 times the median grain diameter (D_{50}) at the critical state. Oda & Kazama (1998) observed that the width of the shear band may be as low as 7-8D_{50}. The largest shear band width in an overview by Wood (2002) is 18.5D_{50} based on the results of Mülhaus & Vardoulakis (1987) for fine sands. Overwhelming evidence exists in the literature to state that shear band thickness is primarily a function of grain size and typically on the order of 10D_{50}.

Particle size is also important for the development of rupture surfaces towards the ground surface in other boundary-displacement problems. However, particle size is mainly important in relation to the dimensions of the experiment, or a characteristic length. The base displacement experiments of Stone & Wood (1992) showed that the patterns of shear rupture propagation toward the ground surface vary with dense sands having different median grain sizes. Multiple rupture surfaces developed in the finest sand having a D_{50} of 0.4 mm. In this fine sand, the initial rupture surface propagated upward and curved over the trapdoor until the sand ceased to dilate. According to Stone & Wood (1992), when the sand ceased dilating, continued rupture along the initial rupture surface became kinematically inadmissible, and a second rupture surface began to propagate at an even steeper angle than the initial rupture surface. This process repeats until a final rupture surface breaks through to the ground surface. In their experiment with the coarsest sand having a D_{50} of 1.6 mm, the initial rupture surface did reach the ground surface, and no additional rupture surfaces developed. This does not necessarily suggest that more complex rupture surfaces develop in finer sands. Stone & Wood (1992) observed that, when the amount of base displacement was normalized by a characteristic length represented by D_{50}, similar patterns of shear rupture were apparent at

nearly the same stages of *normalized* base displacement as shown in Fig. 2.16. Hence, the same patterns of shear rupture are expected to develop in the coarse sand as in the fine sand if the particle sizes in each experiment are proportional to the characteristic length. The grain size as it relates to the dimensions of the experiment is significantly more important than absolute grain size.

Several studies suggest that the dilatancy of a material is more important than its strength in the propagation of a rupture surface towards the ground surface. When Stone & Wood (1992) performed trapdoor-style experiments under a gravitational acceleration of 100g instead of 1g, they calculated a drop in the peak angle of dilation from approximately 25° to 19° based on the relation of Bolton (1986). These calculated angles of dilation were consistent with the initial orientation of the rupture surface in each experiment. Cole & Lade (1984) argue that the dilatancy of the soil is the only material property that effects the path of rupture propagation. They developed a closed-form, log-spiral solution for the shape and outcrop location of the rupture surface through cohesionless soil that takes the fault dip angle, the soil height, and the soil angle of dilation as inputs. The different cases for their solution are shown in Fig. 2.17. With the dependence of the Cole & Lade (1984) solution on angle of dilation, particle size should not affect the path of fault rupture propagation. As shown in Fig. 2.18 from Stone & Wood (1992), coarser particles will exhibit greater total dilation than finer particles, but the rate of dilation, i.e., the slope in Fig. 2.18, is equivalent amongst all particle sizes. This slope angle is the angle of dilation on which Cole & Lade (1984) base their solution.

Shear rupture development depends systematically on soil ductility. The solution of Cole & Lade (1984) is primarily applicable to sands that are dense enough for shear to sufficiently localize along a distinct rupture surface. It is far less applicable in looser materials that tend to bifurcate during shear and reveal broader zones of deformation instead of distinct shear localizations. The parametric study of Lazarte & Bray (1996) showed the effects of soil ductility on the development of shear rupture during strike-slip fault rupture. Their study showed that as the failure strain of the soil increases, or as ductility increases, the amount of relative fault displacement for subsurface rupture to reach the ground surface increases. The width of the shear zone as viewed along the strike direction also tends to increase with soil ductility, as shown in Fig. 2.19 (Lazarte & Bray 1996). Johansson & Konagai (2006) analyzed the effect of soil ductility with dry and wet sands. They performed 1g vertical displacement experiments similar to those of Stone & Wood (1992) with dense dry sands and dense wet sands with approximately 80% saturation. This amount of saturation increased the failure strain of their sands, which they show produced more ductile shear behavior such as a wider zone of shear-induced deformation in their wet sand experiments than in their dry sand experiments. Bray et al. (1994b) similarly related soil ductility to its failure strain and concluded that the height of the fault scarp in cohesive soil increases with decreasing failure strain. The results of these latter studies used different clay mixtures or saturation levels, respectively, to alter the ductility of the soil. Similar findings are expected with sandy or gravelly soils having different void ratios. The centrifuge experiments of Roth et al. (1981) showed more distinctive soil offset along the rupture surface in dense sands than in loose sands as demonstrated in Fig. 2.20.

The work of Ahmadi et al. (2018a,b) suggests an optimum amount of saturation or clay content that minimizes the ductility of a sand in dip-slip fault rupture. They performed sandbox model experiments in 1g conditions to analyze the influence of pore-water pressure and clay content in free-field reverse fault rupture through sand. Ahmadi et al. (2018a) explain that pore-water pressure up to a water content of 15% creates an apparent cohesion in the soil that causes it to deform in a more brittle manner than when dry. For example, they observed the formation of

tension cracks on the hanging wall in wet sands as well as thinner shear bands in the wet sands. The data presented by Ahmadi et al. (2018a) show the lowest fault displacement at which fault rupture emerges at the ground surface, the widest zone of ground surface deformation including tension cracks, the shallowest inclination of the rupture surface at the ground surface, and the furthest fault rupture propagation distance at a water content of 5%. Thus, a water content of 5% may be interpreted as the water content that creates the most apparent cohesion, and Ahmadi et al. (2018a) state that at this water content the sand is most brittle. Ahmadi et al. (2018a) further argue that 1g experiments with different water contents are an effective means of mimicking the shear behavior of cemented granular soils. Replication of natural cementation in sands in a laboratory setting is otherwise a difficult task. Ahmadi et al. (2018b) similarly found that, in clay-sand mixtures, those with 5% clay content also required the lowest amount of fault displacement for fault rupture to emerge at the ground surface, but higher clay contents tended to make the mixture more ductile than with 0% clay content. They note that the stress conditions in 1g experiments are not fully representative of field conditions in which the behavior of soil under much higher stresses would be dominated by frictional behavior.

Rate of rupture also has some effect on the rupture surface. Faster rates of rupture produced less distinctive surface offsets and steeper, more inclined rupture surfaces than slower rates of rupture in the experiments of Roth et al. (1981) as seen in Fig. 2.20. Lin et al. (2006) found through physical experiments that faster rates of rupture produce narrower zones of surface deformation. Subsequent numerical analyses by Lin et al. (2006), however, showed angle of dilation and Young's modulus to be more critical parameters than rate of rupture on surface deformation.

Trapdoor and anchor pull-out represent other boundary-displacement problems that are very similar to surface fault rupture, and the literature review of Bray (1990) is recommended for an overview of trapdoor and anchor pull-out experiments. Two more recent studies by Costa et al. (2009) and Iglesia et al. (2013) are summarized here. These two studies provide further insight into the soil arching phenomenon associated with load transfer from a trapdoor to the surrounding soil originally explained by Terzaghi (1936, 1943). Costa et al. (2009) performed single gravity and centrifuge experiments of trapdoor displacement in dense and loose sands with and without a pipe embedded above the trapdoor. They describe the development of "internal failure surfaces" emanating inward and becoming "gradually more inclined toward the vertical" as trapdoor displacement proceeds, as shown in Fig. 2.21 (Costa et al. 2009). Costa et al. (2009) also found that the initial angle from the vertical direction of these internal failure surfaces tended to decrease under higher gravitational accelerations and with looser soils due to reductions in the dilatancy of the soil under these conditions. This dependence of failure surface inclination on soil dilatancy is further supported by the observation by Costa et al. (2009) that the internal failure surfaces are vertical at the critical state when the soil ceases dilating. When the soil above the trapdoor began displacing downward and producing settlement at the ground surface, external failure surfaces emanated outward and gradually declined towards the horizontal until ultimately reaching the angle of repose at large trapdoor displacements (Costa et al. 2009). The external failure surfaces are also shown schematically in Fig. 2.21. Costa et al. (2009) further observed larger ground surface settlement for soils with lower relative densities.

Iglesia et al. (2013) present a similar perspective on the soil arching phenomenon and relate different stages of soil arching to the loads that develop on the trapdoor. The typical load development on the trapdoor in their centrifuge experiments is shown in Fig. 2.22. Iglesia et al. (2013) observed an initial rapid drop to a minimum load on the trapdoor at early stages of trapdoor displacement. This early stage of trapdoor displacement associated with the rapid drop in load

shown in Fig. 2.22 is equivalent to the early stages of internal failure surface development in Costa et al. (2009). The rapid drop in trapdoor load is balanced by a rapid increase in load on the surrounding stationary material at the outer edges of the trapdoor. The load on the trapdoor then increases at a relatively low rate with continued trapdoor displacement and approaches a constant value at a similar stage at which Costa et al. (2009) observed nearly vertical internal failure surfaces. At even larger amounts of trapdoor displacement, the external failure surfaces observed by Costa et al. (2009) could reasonably be expected to develop as well. The soil arching phenomenon described in these two trapdoor studies can be summarized as an arched pattern of shear deformation characterized by the dilatancy of the soil and representing load transfer between the trapdoor and the surrounding stationary soil.

The results of centrifuge experiments of surface fault rupture presented by Bransby et al. (2008a,b) and Ahmed & Bransby (2009) provide a large suite of data with which to validate numerical models of surface fault rupture due to dip-slip faulting and its interaction with foundations of different widths, contact pressures, positions, and flexibilities. The arrangement of their sandbox-style centrifuge model is shown in Fig. 2.23 for normal fault rupture. The experiments include free-field fault rupture experiments and fault rupture-soil-foundation interaction (FR-SFI) experiments for both normal and reverse fault rupture. Bransby et al. (2008b) describe 3 different mechanisms of reverse FR-SFI shown in Fig. 2.24 that are similarly described by Ahmed & Bransby (2009). The first mechanism in Fig. 2.24a occurs when the stresses imposed by the foundation to the soil are sufficiently large for the fault rupture surface to be unable to continue along its preferred path in the free-field, i.e., with no foundation. In this case, the rupture surface outcrops on the hanging wall side of the foundation, because too much energy is required for fault rupture to propagate underneath and uplift the foundation. In the second mechanism in Fig. 2.24b, the foundation is light enough for the fault rupture surface to continue along its free-field path and emerge beneath the foundation. In this mechanism, the fault rupture surface requires more energy to change path than to uplift the foundation, so it follows the lower-energy route. This imposes stresses on the foundation due its cantilevering over the empty space beneath its footwall side. In the third mechanism in Fig. 2.24c, the foundation may be offset towards the hanging wall and too heavy for the fault rupture surface to continue along its free-field path. In this case, the fault rupture surface deflects and outcrops towards the footwall side of the foundation. Another summary of these experiments is provided in the literature review of Oettle (2013).

A similar centrifuge-based reverse fault study was carried out by Ashtiani et al. (2016) to analyze the effect of embedment depth on reverse fault rupture interaction with shallow foundations. They concluded that embedment, in general, has a detrimental effect on the foundation during reverse fault rupture. Bransby et al. (2007) also applied centrifuge testing to model the interaction of reverse fault rupture with a flexible, embedded pipeline, and Tsatsis et al. (2015) later modeled soil-pipeline interaction during normal fault rupture with both 1g experiments and numerical modeling.

2.4 Overview of Relevant Continuum-Based Numerical Studies

Continuum-based simulations have provided much insight into the processes and mechanics of earthquake surface fault rupture and its associated hazards. Bray et al. (1994b) and Bray (2001) used the finite element method (FEM) with the Duncan Hyperbolic constitutive model (Duncan et al. 1980) to numerically analyze free-field surface fault rupture. The Duncan Hyperbolic model captures the nonlinear stress-strain behavior of soil during shearing and

incorporates the failure strain of a soil, but it does not capture post-peak strain softening in dilatant soils. Lazarte (1996) reviewed several numerical boundary-displacement studies between 1981 and 1995 and concluded that strain localization in numerical studies of surface fault rupture can only develop satisfactorily if post-peak strain softening is incorporated into the constitutive model. The inclusion of strain softening in constitutive models is now routine in more recent numerical continuum studies of surface fault rupture (e.g., Anastasopoulos et al. 2007, Loukidis et al. 2009, Oettle & Bray 2013a, Thebian et al. 2018). Anastasopoulos et al. (2007) incorporated post-peak strain softening in their modified Mohr-Coulomb model by reducing the mobilized friction angle and mobilized angle of dilation linearly with the increase in octahedral plastic shear strain. Loukidis et al. (2009) and Thebian et al. (2018) similarly decreased these values linearly with plastic shear strain to study surface fault rupture with different fault dip angles and soil densities. Oettle & Bray (2013a) used the finite-difference code FLAC (Itasca 2016) to incorporate strain softening into a modified version of the UBCSAND model (Byrne et al. 2004). In continuum models that analyze subsurface faulting features and folding features on the regional scale, the inclusion of strain softening is not necessary. Instead, a stick-slip model using Coulombic friction along the fault surface may be sufficient (e.g., Sanz et al. 2007).

The shear band that develops in a mesh containing the most basic 4-node elements cannot be any smaller than the mesh size and is therefore dependent on the mesh size (Anastasopoulos et al. 2007). Anastasopoulos et al. (2007) note that, while the mesh size can be made the same size as the expected shear band width, such a small mesh size is computationally expensive. Anastasopoulos et al. (2007) and Oettle & Bray (2013a,b) both removed mesh dependency from shear strain by normalizing it by mesh size, but Anastasopoulos et al. (2007) showed that the shear band width is still dependent on the mesh size, as shown in Fig. 2.25. This mesh dependency for the shear band width is consistent with physical observations of shear band width being dependent on particle size (e.g., Wood 2002). Mesh size did not, according to Anastasopoulos et al. (2007), appear to significantly affect the path of fault rupture propagation or its outcrop location.

The numerical analyses associated with the QUAKER project, a 3-year project funded by the European Commission focused on surface fault rupture (Pecker 2008), present a large suite of numerical analyses of surface fault rupture based on the centrifuge experiments of Bransby et al. (2008a,b). The analyses associated with the QUAKER project centrifuge experiments include development of a simplified FR-SFI design approach through continuum modeling coupled with upper and lower bound limit analysis (Tolga Yilmaz & Paolucci 2007), free-field fault rupture simulations (Anastasopoulos et al. 2007), comparisons between different constitutive models and FEM codes (Anastasopoulos et al. 2008a), FR-SFI simulations with strip foundations during dip-slip fault rupture (Anastasopoulos et al. 2009, 2010), and back-analyses of case studies from recent earthquakes (Anastasopoulos & Gazetas 2007b, Faccioli et al. 2008). Gazetas et al. (2008) summarize the main findings of the QUAKER project and provide a list of preliminary design recommendations, many of which generally focus on enforcing rigid-body rotation of the structure during fault rupture to reduce the development of internal stresses within the structure. The key findings for the DEM simulations of this dissertation are worth noting. Anastasopoulos et al. (2007) showed that the fault scarp is higher in denser soils than in looser soils at the same amount of fault displacement and that looser soils require greater fault displacements for surface fault rupture to outcrop at the ground surface. These findings are consistent with the well-known link between failure strain and soil ductility (e.g., Bray 1994b, Lazarte & Bray 1996, Johansson & Konagai 2006). Anastasopoulos et al. (2009) showed that the bending stiffness (*EI*) of a solid foundation does not have a significant effect on the path of fault rupture propagation during normal

fault rupture or on the foundation response, although Bransby et al. (2008) showed that completely flexible foundations are significantly less effective in altering the path of fault rupture propagation than rigid foundations. Anastasopoulos et al. (2009) also demonstrated systematic effects of foundation load and foundation location on the path of normal fault rupture propagation, as shown in Fig. 2.26, and Anastasopoulos et al. (2010) demonstrated the influence of these parameters in addition to soil compliance, or density, in reverse fault rupture. The calibration procedure described in Anastasopoulos et al. (2007) is also suitable for other numerical analyses. They used laboratory direct shear test results on Fontainebleau sand by Gaudin (2002) to calibrate their constitutive model to actually predict the fault-foundation interaction without knowing the physical FR-SFI test results beforehand.

The coupling of physical and numerical modeling is now commonplace in earthquake surface fault rupture studies, and the aforementioned examples associated with the QUAKER project highlight the benefits of using experimental data to validate analogous numerical simulations. Loli et al. (2011, 2012) performed centrifuge experiments of normal and reverse fault rupture interaction with caisson foundations and validated the capability of their FEM methodology to capture the mechanisms of this interaction. Their simulations were necessarily three-dimensional since caissons cannot be adequately represented with plane-strain modeling. They state that the capability of FEM to capture the physically observed mechanisms of fault rupture interaction with caisson foundations highlights its potential effectiveness for future design applications. The successful validation of the 3D FEM methodology by Loli et al. (2011, 2012) justifies its extension to the interaction of normal fault rupture with 2x4 pile foundations by Anastasopoulos et al. (2013). The conclusion by Anastasopoulos et al. (2013) that pile performance is worst when fault rupture propagates in between the two rows of piles justifies the recommendation of Bray (2009) against pile foundations when traversing active fault traces. Numerical comparison of pile and caisson foundations by Gazetas et al. (2007) showed that the more massive caisson foundations are superior to pile foundations in terms of limiting fault-induced damage to structures. Loli et al. (2015) later used their 3D FEM approach to model the interaction of normal fault rupture with masonry structures atop different foundations. Their analyses support the use of continuous foundations to mitigate structural damage and, unlike the physical reverse fault experiments of Ashtiani et al. (2016), actually showed a beneficial effect of foundation embedment when interacting with normal fault rupture. Analytical design methodologies for shallow foundations sited near dip-slip faults (Anastasopoulos et al. 2008b,c) and bridges founded on pile or caisson foundations (Anastasopoulos et al. 2008d) were also calibrated against the QUAKER project centrifuge experiments and analogous numerical models. Moss et al. (2018) most recently used physical experimentation and finite element modeling to supplement their previous statistical model (Moss et al. 2011, 2013) that uses shear wave velocity in the upper 30 meters of sediment (V_{s30}) as a proxy for shear stiffness that predicts whether or not reverse fault rupture will emerge at the ground surface. In general, physical models should necessarily validate analogous numerical models for the reliance on numerical models in analyses of earthquake surface fault rupture.

The QUAKER project analyses focused on homogenous sands in the free-field and with a foundation atop the ground surface. Oettle & Bray (2013a) recognized that faults may re-rupture and most likely follow the same path of existing shear zones that essentially provide a path of least resistance. They analyzed the influence of pre-ruptured soil with the finite-difference method (FDM) by simulating FR-SFI and fault rupture-soil-foundation-structure interaction (FR-SFSI) with an existing rupture surface in the soil. Their analyses showed that existing rupture surfaces

act as a plane of weakness through which new ruptures will tend to propagate, sometimes even in the presence of a structure that would otherwise deflect the path of fault rupture propagation. The influence of this pre-ruptured zone was significant in dense material but not in loose material due to the higher strength contrast between the dense soil and the fully softened shear zone. However, the influence of pre-ruptured soil and whether it is beneficial or detrimental to a structure depends on the type of structure, the contact pressure, and the location of the structure (Oettle & Bray 2013a). Oettle & Bray (2015) analyzed the influence of pre-ruptured soil with more rapid rates of hanging wall displacement and observed little difference with the results of quasi-static analyses. These findings suggest that the kinematic constraints imposed by an existing, fully softened rupture zone control the surface fault rupture process more than dynamic effects.

Oettle & Bray (2016) describe two different modifications to the UBCSAND constitutive model (Byrne et al. 2004) that they call the Modified-UBCSAND-I and Modified-UBCSAND-II models. Both of their models incorporate non-linear stress-strain behavior, stress-dependent strength, strain softening, and the failure strain of the soil. One of the key differences between their two models is that the Modified-UBCSAND-II model includes an additional parameter that changes "the stress ratio at which contractive response transitions to dilative behavior" (Oettle & Bray 2016). Changing this onset of dilation effectively facilitates refinement of the constitutive model when calibrating to match experimental results. Thus, Oettle & Bray (2016) achieved a better match to the experimental results of Bransby et al. (2008a,b) by adjusting the onset of dilation in the Modified-UBCSAND-II model for each loading condition in reverse and normal fault rupture, as shown in the free-field surface deformations in Fig. 2.27. Oettle & Bray (2013a) describe the loading condition in reverse fault rupture as extensional loading and in normal fault rupture as compressional unloading, as shown in Fig. 2.28. The adjustment of model parameters to match different loading conditions, however, is akin to changing the intrinsic properties of the soil. While the friction angle and dilatancy may be considered extrinsic properties since they do depend on such things as the type of loading and the intermediate principal stress (e.g., Kulhawy & Mayne 1990), the intrinsic nature of individual grains remains constant in all loading conditions. Capturing experimental results most satisfactorily with the same set of model parameters in all loading conditions remains a numerical challenge.

Mortazavi Zanjani & Soroush (2017) analyzed layered soil systems using FEM simulations with a Mohr-Coulomb constitutive model that incorporates post-peak strain softening. As might be expected based on the closed-form solution of Cole & Lade (1984), the rupture surfaces in their study propagated further in dense soil than in loose soil during reverse fault rupture at all dip angles. During normal fault rupture, they observed greater reversal of the rupture surface towards the hanging wall in denser soils. The existence of a thin layer of loose soil located at any depth amongst dense soil did not measurably affect the path of fault rupture propagation, but the inclusion of wider layers of loose to medium soil above or between dense soil resulted in a more complex propagation process consisting of shear activity migrating from one propagation path to another (Mortazavi Zanjani & Soroush 2017). They performed simulations with homogeneously loose and dense soil to provide bounds to the fault outcrop location and the width of the shear band, and they showed that the outcrop locations and shear band widths in layered soil simulations tended to fall within these bounds.

Loukidis et al. (2009) studied surface fault rupture using a wide range of fault dip angles ranging from 45° to 135° in 15° increments, with dip angles greater than 90° representing reverse fault rupture (reverse fault dip angles of 45°, 60°, and 75°), as shown in Fig. 2.29. They modeled dense sand as a strain softening material with peak and residual friction angles of 45° and 30°,

respectively, and a dilation angle that decreases from 15° to 0° during strain softening. The friction angle and dilation angle remained constant in the loose sand at 30° and 0°, respectively. Overconsolidated and normally consolidated clays were modeled with total stress parameters using undrained shear strengths in a SHANSEP framework. As shown in Fig. 2.29 for dense sand, the rupture surface in the reverse fault simulations of Loukidis et al. (2009) tended to curve downward over the footwall as it approached the ground surface, which is consistent with the experiments of Cole & Lade (1984). In their normal fault rupture simulations with a dip angle of 45°-60°, an antithetic shear band developed in the opposite direction of the primary shear band, indicating the formation of a graben in between the two shear bands. A graben also formed in their loose sand simulation with a dip angle of 45°. No grabens developed in any of their clay simulations. Sharper shear bands developed in the dense sand simulations than in the loose sand and normally consolidated clay simulations. This is consistent with observations of fault rupture absorption in ductile materials by Bray et al. (1994a). Fault absorption has the effect of reducing the distinctness of shear localization and spreading the rupture over a broader area. The data from Loukidis et al. (2009) in Fig. 2.30 shows that reverse fault rupture requires greater hanging wall displacement than normal fault rupture to reach the ground surface in all soil types. This is consistent with Oettle & Bray (2013a), who related normal fault rupture to the development of Rankine active earth pressures and reverse fault rupture to the development of Rankine passive earth pressures. In each simulation, Loukidis et al. (2009) measured the width of "significant ground distortion" as the width over which "surface inclinations exceed 1/500 or 0.2%". Soil type did not appear to affect the width of significant ground distortion, but fault type did; reverse fault rupture tended to produce wider zones of significant ground distortion than normal fault rupture. The results in the study of Loukidis et al. (2009) showed that during the process of fault rupture propagation, the width of significant ground distortion tended to increase at a high rate after an initial short-lived period of little ground distortion. After a hanging wall displacement of approximately 1% of the soil height in all fault rupture cases, the width of significant ground distortion in their simulations widened at a slower rate or leveled out completely. Loukidis et al. (2009) showed that for both reverse and normal fault rupture, higher fault dip angles caused the center of the zone of significant ground distortion to be located further away from the bedrock fault location.

Thebian et al. (2018) expanded upon the work of Anastasopoulos et al. (2007) and Loukidis et al. (2009) by incorporating stress dependency into their constitutive model. Stress-dependency tends to affect fault rupture through denser soils more than through looser soils due to higher peak strengths than critical state strengths in dense soil. The results of Thebian et al. (2018) were qualitatively similar to those of the previous studies. For example, their simulations with dense soils produced thinner shear zones than with loose soils. However, they found that, when incorporating a stress dependent friction angle and angle of dilation, the fault rupture surface tended to propagate at a higher dip angle in normal fault rupture and a lower dip angle in reverse fault rupture. Their incorporation of stress dependency essentially caused the fault rupture surface to deviate towards the downthrown block compared to when constant properties are used. Thebian et al. (2018) also emphasize the strong influence of soil depth independent of other factors such as fault dip angle and soil type by showing that trends in the width of the ground surface deformation and the bedrock fault displacement required for the fault rupture surface to outcrop at the ground surface cannot be consistently normalized by soil depth, especially during reverse fault rupture and as the magnitude of fault displacement increases. This suggests that these features are nonlinearly related to soil depth, and it further highlights the complex interplay between soil depth, soil properties, fault type, and fault dip angle during earthquake surface fault rupture.

Nollet et al. (2012) also analyzed normal fault rupture through uniform soil with a wide range of dip angles ranging from 0° to 90°. They captured shear band formation in their FEM model using strain softening and an adaptive remeshing technique. The patterns of shear band formation during propagation of the fault rupture surface in their simulations are shown in Fig. 2.31. Nollet et al. (2012) categorize these shear band patterns into 3 different structural domains: 1. Graben domain, 2. Precursor domain, and 3. Transitional domain. Nollet et al. (2012) associate the graben domain with normal faults dipping between 0° and 60°. In this domain, according to Nollet et al. (2012), a synthetic shear band first develops from the bedrock fault and dips at a steeper angle typically of 60°-67°. The steeper dip of the fault rupture surface through soil in the graben domain is consistent with observations of refraction at the soil-bedrock interface by Bray et al. (1994a). Further base displacement in the simulations of Nollet et al. (2012) resulted in the development of one or more antithetic shear bands dipping in the opposite direction of the initial synthetic shear band, as seen in Fig. 2.31a-g. Through contours of incremental displacements, Nollet et al. (2012) showed that the antithetic and synthetic shear bands bound grabens that displace at a faster rate than the hanging wall. In the precursor domain, according to Nollet et al. (2012), the initial shear band actually changes direction towards the hanging wall as it approaches the ground surface, as shown in Fig. 2.31h-j. The simulation results of Nollet et al. (2012) in the precursor domain were consistent with the experimental results of Stone & Wood (1992) in that new, shallower-dipping shear bands developed in succession when dilation ceased along the previous shear bands until a final shear band finally reached the ground surface. However, the purely vertical bedrock displacement in Fig. 2.31j did not produce the consecutive shear band development observed by Stone & Wood (1992). Nollet et al. (2012) describe the transitional domain as including components of both the precursor domain and the graben domain when the bedrock fault dips 60°-70°.

Continuum models are useful in developing and evaluating design strategies. Oettle & Bray (2013b) analyzed different surface fault rupture mitigation strategies after validating the capability of the Modified-UBCSAND-I model to effectively replicate the centrifuge test results of Bransby et al. (2008a,b). Fig. 2.32 shows an example of this validation through comparisons of normal fault rupture in the presence of a foundation in both centrifuge experiment and numerical simulation. Oettle & Bray (2013b) placed their design strategies into 3 categories: 1. Diffusion of fault rupture, 2. Rigid body movement, and 3. Diversion of fault rupture. Their diffusion strategies included using ductile engineered fill to spread the induced shear deformation over a broad zone and thus reduce the angular distortion of the ground surface. Their strategies for rigid body movement included founding the structure on a thick mat foundation and decoupling the foundation from the soil. Their simulations showed that decoupling interfaces such as geosynthetics, while certainly beneficial, are not nearly as effective as the use of a thick mat foundation that effectively prevents the strains induced at the ground surface from transferring to the structural elements. Their strategies for diverting the path of fault rupture propagation include ground improvement through soil densification, installation of a diaphragm wall between the fault and structure, construction of a strong basement, installation of a seismic gap, and installation of ground anchors to lock the structure to the footwall side of a fault. Bray (2009) advises against anchoring the structure to the soil because this can produce significant damage if it is anchored on both sides of the fault, and Oettle & Bray (2016) also note the risks involved with anchoring structures. Oettle & Bray (2013b) ultimately recommend a combined strategy of diffusion of the fault rupture and rigid body movement with a thick mat foundation.

Other researchers analyzed methods of deflecting fault rupture away from a structure or blocking its impact on a structure. Loli et al. (2018) used 1g experiments followed by 2D finite element modeling to evaluate a "rocking isolation" method of reducing the adverse effects of reverse fault rupture on a shallow foundation by installing a cofferdam or skirt wall around the foundation to limit the amount of rigid-body rocking and displacement induced to the foundation. Fadaee et al. (2013, 2016) used a coupled physical and numerical modeling approach to analyze the use of a sacrificial wall, which they propose as a soil-bentonite wall, that will act as a weak region that constrains the path of reverse fault rupture.

Wang et al. (2017) performed 1530 finite element simulations to develop design charts for the maximum load ratio on an active and passive trapdoor using upper bound and lower bound limit analysis. The passive trapdoor case is essentially the anchor pullout problem, and the active trapdoor case is the classic trapdoor problem initially described by Terzaghi (1936, 1943). The maximum load ratio (P/P_0) refers to the load on the trapdoor at collapse normalized by its initial load, and the developed design charts in Wang et al. (2017) show dependence of P/P_0 on soil height normalized by trapdoor width (H/B), soil friction, and soil cohesion. Their analyses demonstrated that as the ratio H/B increases, P/P_0 increases in the passive case due to increasing frictional resistance from the surrounding soil and decreases in the active case due to increasing frictional support from the surrounding soil. For the same reasons of greater support or resistance from the surrounding soil, their analyses also showed that increases in soil friction and cohesion also decreased P/P_0 in the active case and increased P/P_0 in the passive case. As in Costa et al. (2009), Wang et al. (2017) observed failure mechanisms involving internal and external failure surfaces. As shown in Fig. 2.33, the collapse mechanism for the passive trapdoor, or anchor pull-out, simulations in Wang et al. (2017) was typically through external failure surfaces regardless of the shear strength of the soil. Shear strength had a more significant effect on the collapse mechanism of the active trapdoor. Wang et al. (2017) observed that increasing the frictional strength in deep, active trapdoors tended to change the collapse mechanism from external to internal, the latter of which is more indicative of the soil arching phenomenon. They also observed that the soil arching phenomenon may not develop above a shallow active trapdoor because the internal failure surfaces might reach the ground surface before intersecting each other, as shown in Fig. 2.33. Wang et al. (2017) state that when H/B is greater than 2, however, the yield surface may transition from an internal arch to an external mechanism. They note that the initial yield surface is still an internal arch in what Wang et al. (2017) call "active arching".

The above surface fault rupture analyses made a point to minimize dynamic effects by allowing the hanging wall to displace quasi-statically. In reality, earthquake surface fault rupture is a dynamic phenomenon involving vibrational wave propagation in addition to fault rupture propagation. Lin et al. (2006) performed physical experiments and finite element simulations of surface fault rupture and found that the rate of rupture is not as significant as other parameters, particularly Young's modulus and angle of dilation. Oettle et al. (2015) compared dynamic and quasi-static surface fault rupture simulations with and without a structure at the ground surface. As shown in Fig. 2.34, most of their dynamic results using realistic slip velocities between 0.4-1.0 m/s were similar to their quasi-static results. However, dynamic free-field analyses showed wider, less distinct zones of shear strain. This is similar to the findings from centrifuge experiments by Roth et al. (1981). In the dynamic analyses of Oettle et al. (2015), some shear strains tended to develop at the rigid boundaries of the hanging wall. Hence, the presence of strains or other signs of disturbance at the boundaries may be used as an indicator of quasi-static or dynamic rupture. Simulations by Oettle et al. (2015) with a structure on the footwall side of a normal fault and on

the hanging wall side of a reverse fault showed very little difference between dynamic and quasi-static analyses, but simulations with a structure on the hanging wall side of a normal fault and on the footwall side of a reverse fault showed some slight to moderate differences between dynamic and quasi-static analyses. This suggests that dynamic effects may be more important to consider if a structure is located on the downthrown block.

2.5 Introduction to DEM

2.5.1 A Note on Learning DEM for Aspiring Researchers

At the time of this writing, it is almost 40 years since the formulation of the original distinct element method was introduced by Cundall & Strack (1979), yet formal university classes on discrete element modeling are still not as widespread as those focusing on finite element modeling. It is the experience of the author of this dissertation that the basics and fundamentals of DEM ought to be learned through trial-and-error practice with a particular DEM code and through disciplined reading of informative texts on the subject (in no particular order). Many such texts as well as concise overviews of DEM are now available for aspiring researchers seeking to use DEM to study their problem of interest, and the minute details in these texts need not be repeated here. Instead, select texts are recommended as a starting point. Cundall & Strack (1979) must always be read by beginning DEM researchers so they may see the original DEM formulation. In that text, readers may see that, at its core, DEM is simply solving the equation of motion for every particle at every consecutive time step. A concise overview of key DEM concepts, recent advancements, and applications is presented in O'Sullivan (2011a). Bardet (1998) presents a concise overview of numerical implementations and early homogenization schemes in discrete element modeling. These three texts are highly recommended as an initial reading of discrete element modeling. The dissertation of Cui (2006) is also recommended, because it presents another overview of notable advances in DEM as well as a thorough description of popular techniques for preparing a particle assemblage for simulation. The textbook *Particulate Discrete Element Modeling: a Geomechanics Perspective* by Catherine O'Sullivan (2011b) is recommended for those researchers who are ready to move beyond brief overviews and learn in greater depth the concepts, techniques, and applications of discrete element modeling.

Many DEM codes are available both commercially and open-source. The author of this dissertation has first-hand experience with 3 codes in particular: the Particle Flow Code (Itasca 2014), LIGGGHTS (Kloss et al. 2012), and YADE (Šmilauer et al. 2015). The Particle Flow Code (PFC) contains many built-in features that allow much flexibility in simulations. Servo-controlled walls, creation of clumped particles or sphere-clusters, and monitoring of unbalanced forces are just a few of the features that are already incorporated. PFC is widely used amongst researchers in geomechanics. The drawbacks to PFC are that it is a commercial software, and more advanced researchers in DEM are unable to modify the underlying source code. YADE is very similar to PFC while also being open-source, so YADE users may freely obtain the source code and modify it. Many of the same built-in features in PFC are also built into YADE. Both YADE and PFC also include a graphical user interface through which users can view their simulation in real time. YADE requires users to have some familiarity with the Python programming language; whereas, PFC users must learn the FISH programming language developed by Itasca. PFC only runs on Windows operating systems, and YADE only runs on Linux operating systems. It is the opinion of the author of this dissertation that the choice between YADE and PFC is mostly a matter of

financial restrictions. Either of these codes may be used by beginning DEM researchers to gain familiarity with how to run DEM simulations.

When researchers move on to larger-scale simulations containing hundreds of thousands or millions of particles, they may quickly find themselves needing to use high-performance computing. YADE uses Open Multiprocessing (OpenMP), which allows all the processors to share memory. YADE still runs in parallel but only on a single computing node, such as your standard desktop computer. PFC also will only work on a single node. LIGGGHTS, on the other hand, uses the Message Passing Interface (MPI), which distributes the memory across multiple computing nodes. LIGGGHTS is fully optimized for high-performance computing clusters. One principal drawback to LIGGGHTS is that it does not have the same flexibility as YADE and PFC, although it was developed to be easily modifiable for those familiar with basic C++ programming. Some features that were convenient for geomechanics researchers in YADE and PFC must be added separately in LIGGGHTS. LIGGGHTS also does not have a graphical user interface, so visualization of results requires extra post-processing. In general, simulation schemes may be tested or verified on small scales using YADE or PFC, and then LIGGGHTS can be used when the user is ready to perform a full-scale simulation with a much greater number of particles.

2.5.2 Review of DEM Concepts

DEM uses a "soft-sphere" approach, as shown in Fig. 2.35, in which particles are permitted to overlap slightly at the boundaries. The shear and normal contact forces (F_t and F_n) are calculated between two overlapping, or contacting, particles using a rheological contact law. Fig. 2.36 shows an example rheological model for the calculation of inter-particle contact forces using a penalty-spring approach. Penalty-springs impose equal and opposite repulsive forces onto the two particles in contact. Cohesionless granular materials cannot have tensile forces between the particles, so the inclusion of no-tension joints in the contact law ensures that the force between two granular particles is zero when they no longer overlap. The normal contact force is most commonly related to the amount of inter-particle overlap (δ_n) through the normal spring stiffness K_n, which should be chosen such that particle overlaps remain relatively small. Huang et al. (2014a) defines the *overlap ratio* as "the ratio between the interparticle overlap and the diameter of the smaller particle in the contact" and suggests that it not exceed 0.05 at any contact. As with the normal force, the tangential force is calculated as the product of relative tangential displacement (δ_t) and the tangential spring stiffness K_t. Viscous dashpots may be included to calculate an additional contact force as the product of normal or tangential viscosity coefficients (C_n, C_t) and the normal or tangential rate of displacement, or velocity. The equations for the shear and normal contact forces acting at a contact are summarized as

$$F_n = K_n\delta_n + C_n\dot{\delta_n} \tag{2.1a}$$

$$F_t = K_t\delta_t + C_t\dot{\delta_t} \tag{2.1b}$$

Tangential slip is typically incorporated into the contact law by enforcing the condition

$$|F_t| \leq \mu F_n \tag{2.2}$$

where μ is the coefficient of friction at the particle surface. A reasonable value of μ is 0.5, because this is equivalent to the coefficient of friction for a quartz mineral surface, which is one of the most common minerals in sands (Mitchell & Soga 2005). If F_t reaches its upper limit μN, then the particles may slide relative to one another at a constant shear force.

The total force acting on a particle is summed as the resultant of all contact forces acting on the particle plus any additional body forces or externally applied forces not resulting from inter-particle contacts, e.g., forces resulting from gravitational acceleration. Equilibrium is never fully reached in a simulation, but the total out-of-balance force in the system may be small enough for the system to be considered in quasi-equilibrium. A local non-viscous damping force can be applied in the opposite direction to the resultant force of accelerating particles in order to bring the system to equilibrium more quickly (Cundall 1987, Itasca 2014). This type of damping is incorporated in PFC and is applied individually to each particle as (Itasca 2014):

$$F_d = -\alpha |F| \frac{v}{|v|} \tag{2.3}$$

where $\boldsymbol{F}$ is the out-of-balance force acting on the particle, $\boldsymbol{v}$ is the velocity of the particle, and α is a damping coefficient. Potyondy & Cundall (2004) suggest an α value of 0.7 for quasi-static simulations.

The most basic contact law is a linear model that uses constant values of K_n, K_t, C_n, and C_t. Constant values of the stiffness and viscosity coefficients do not account for changes in stiffness when two contacting particles have different radii. If particle radius is not accounted for in a contact law, then the inter-particle stiffness will not be compatible with the stiffness of the entire assemblage (Yan & Dong 2011). The elastic Young's modulus (E) of uniformly sized spheres packed in a hexagonal close-packed or rectangular arrangement should theoretically be the same for the entire assemblage as between individual particles, although irregular particle arrangements may have slight variations in E due to their randomness. Yan & Dong (2011) demonstrated that the E for the assemblage is compatible with E at the inter-particle contacts if K_n is directly proportional to particle radius, i.e., $E \propto \frac{K_n}{r}$. PFC incorporates this principle with a "deformability" method for the linear contact law. The deformability method calculates inter-particle spring stiffness for 3D spheres in contact as (Itasca 2014):

$$K_n = \frac{\pi \min(R_1^2, R_2^2) E}{R_1 + R_2} \tag{2.4}$$

where R_1 and R_2 are the radii of the contacting spheres. A ratio between K_n and K_t is also specified by the user. More detail about this contact model is available in the PFC documentation (Itasca 2014).

Contact force may be a non-linear function of particle overlap as well. The Hertz-Mindlin contact model based on the work of Mindlin & Deresiewicz (1953) is a very common non-linear model. LIGGGHTS implements a Hertz-Mindlin contact model that uses the same relationship in Eqn. 2.1 but makes K_n and K_t functions of δ_n. The spring stiffnesses and viscosity coefficients for this model are calculated as follows (Kloss et al. 2012):

$$K_n = \frac{4}{3} E^* \sqrt{R^* \delta_n} \tag{2.5a}$$

$$C_n = -2\sqrt{\frac{5}{6}}\beta\sqrt{S_n m^*} \geq 0 \tag{2.5b}$$

$$K_t = 8G^*\sqrt{R^*\delta_n} \tag{2.5c}$$

$$C_t = -2\sqrt{\frac{5}{6}}\beta\sqrt{S_t m^*} \geq 0 \tag{2.5d}$$

$$S_n = 2E^*\sqrt{R^*\delta_n} \tag{2.5e}$$

$$S_t = 8G^*\sqrt{R^*\delta_n} \tag{2.5f}$$

$$\beta = \frac{ln(e)}{\sqrt{ln^2(e)+\pi^2}} \tag{2.5g}$$

$$\frac{1}{E^*} = \frac{(1-\nu_1^2)}{E_1} + \frac{(1-\nu_2^2)}{E_2} \tag{2.5h}$$

$$\frac{1}{G^*} = \frac{2(2-\nu_1)(1+\nu_1)}{E_1} + \frac{2(2-\nu_2)(1+\nu_2)}{E_2} \tag{2.5i}$$

$$\frac{1}{R^*} = \frac{1}{R_1} + \frac{1}{R_2} \tag{2.5j}$$

$$\frac{1}{m^*} = \frac{1}{m_1} + \frac{1}{m_2} \tag{2.5k}$$

where G is the elastic shear modulus of the inter-particle contact, m is the particle mass, e is the coefficient of restitution at the inter-particle contact, and ν is the Poisson's ratio of the inter-particle contact. More details about this contact model are available in the LIGGGHTS documentation. The Hertz-Mindlin model also incorporates the effect of particle radius on the spring stiffness. Whether a linear or non-linear contact law is employed, the contact law should at least account for differences in the radii of the contacting particles in the calculation of spring stiffnesses.

The motions of particles in a DEM simulation are calculated explicitly using a Verlet central-difference formulation with a predefined time-step (Δt). When the forces acting on the particles are calculated, their resulting accelerations are calculated and integrated to obtain the linear and angular velocities of the particles. Then the positions and rotations of the particles are updated using Δt. The new overlaps between particles following their movement over the previous time-step are used to re-calculate the inter-particle contact forces, and the calculation cycle repeats. The general overview of this calculation cycle as presented in O'Sullivan (2011a) is shown in Fig. 2.37. The solution scheme is conditionally stable, so Δt must be less than a critical time-step (Δt_{crit}) that is dependent on the mass and contact stiffness of the particles. Itasca (2014) gives Δt_{crit} as the smallest value of $\sqrt{\frac{m}{K}}$ over all degrees of freedom for all particles in the system, and they recommend $\Delta t \leq 0.8\Delta t_{crit}$. For 3D assemblages of uniformly sized particles, O'Sullivan & Bray (2004) recommend $\Delta t \leq 0.17\Delta t_{crit}$ using $\Delta t_{crit} = \sqrt{\frac{m}{K}}$. Li et al. (2005) point out that this form of

Δt_{crit} is inappropriate with the non-linear Hertz-Mindlin contact law, because K_n and K_t change with δ_n . They instead use the Rayleigh time-step for the critical time-step, which is based on the Rayleigh wave speed. Li et al. (2005) give the Rayleigh time-step as:

$$\Delta t_R = \frac{\pi \bar{R}}{0.8766+0.163\nu}\sqrt{\frac{\rho}{G}} \tag{2.6}$$

where ρ is the particle density and $\bar{R}$ is the average particle radius. A review of the literature by Otsubo et al. (2017) suggests that the simulation time-step be 0.2 Δt_R, and they recommend that a "conservative estimate of Δt_{crit}" be $0.05\sqrt{\frac{m_{mean}}{K_{max}}}$ or $0.1\sqrt{\frac{m_{min}}{K_{max}}}$ in lieu of Δt_R. The addition of a safety factor to Δt_{crit} is a general recommendation from all of these studies.

Larger time-steps may be used if the density or masses of the particles are increased. This density scaling is useful for quasi-static simulations that do not involve gravitational acceleration (e.g., Thornton 2000, Cui & O'Sullivan 2006). However, the velocity of any moving boundaries may also have to be adjusted if the densities are scaled and the time-step increased. The inter-particle spring stiffnesses could also be reduced to increase Δt, but the applied forces in a system would have to correspondingly decrease for the overlap ratios to not then increase. These adjustments may affect the stability of the system, so measures of stability are often employed based on the total out-of-balance, or unbalanced, forces in the system. Ng (2006) measures stability with an index of unbalanced forces:

$$I_{uf} = \sqrt{\frac{\sum_1^{n_b}(unbalanced forces)^2/n_b}{\sum_1^{c}(contact forces)^2/n_c}} \tag{2.7}$$

When I_{uf} is less than 0.01, Ng (2006) considers the system to be quasi-static, meaning that dynamic influences are negligible. In other words, the system is in quasi-equilibrium if it is quasi-static. Itasca (2014) uses a similar index, R_{avg}, given as:

$$R_{avg} = \frac{\langle \boldsymbol{U}_b \rangle_{b\in B}}{\langle \boldsymbol{F}_b^* \rangle_{b\in B}} \tag{2.8a}$$

$$\boldsymbol{U}_b = \left\| \sum_{\boldsymbol{F}/b} \boldsymbol{F} \cdot \boldsymbol{\delta} \right\| \tag{2.8b}$$

$$\boldsymbol{F}_b^* = \sum_{\boldsymbol{F}/b} \|\boldsymbol{F} \cdot \boldsymbol{\delta}\| \tag{2.8c}$$

If an index of unbalanced forces is not used, quasi-static behavior or equilibrium could also be monitored by verifying that the forces measured across opposite boundaries in a simulation are approximately equal. For example, in a direct shear test simulation, the forces on the upper and lower boxes should be nearly equal during quasi-static shear in the absence of gravity and boundary friction. Another method of checking quasi-static behavior is simply to run the same simulation with lower velocities, or with a lower shear rate, and check if the measured results are significantly different (e.g., Härtl & Ooi 2011). In a quasi-static system, the simulation results should not be significantly affected by any imposed velocities on boundaries or on particles, and

all of these methods may be used to ensure that the results of a simulation are not significantly affected by any imposed velocities in the system.

The most realistic simulations of granular soil generally make the fewest simplification, yet simplification is inevitable in any numerical model. In discrete element modeling, simplifications are primarily made with respect to particle shape, degrees of freedom (2D or 3D), and relative particle size. The original formulation of DEM (Cundall & Strack 1979) used 2D disks as particles. Since then, 3D simulations have become more practical, and different methods are available to generate non-spherical particles. Fundamentally, granular particles are three-dimensional, non-spherical objects with an inherent resistance to rolling and rotation. Iwashita & Oda (1998, 2000) introduced a rheological rolling resistance contact model as shown in Fig. 2.36. This model uses a rotational spring to prevent a disc or spherical particle from rolling freely when in contact with another particle. When the moment in the rotational spring exceeds a certain threshold of the same form as in Eqn. 2.2, the particle then rolls against a constant moment resistance until it loses contact with the particle against which it is rolling (Iwashita & Oda 1998). Other variations of rolling or rotational resistance contact models are also available (e.g., Jiang et al. 2005).

Rolling resistance contact models do not account for the effect of particle shape on dilatancy. Dilatancy is a geometric granular phenomenon that occurs along sliding planes (e.g., Bolton 1986), and these sliding planes within the soil are affected by particle shape and angularity. Salazar et al. (2015) succeeded in calibrating their sphere assemblages in direct shear test simulations to match the frictional strength of a real sand, but they were less successful in matching the dilatancy characteristics of the sand. Increases in the coefficient of rolling resistance tended to increase the total amount of dilation in their simulations, but it had little effect on the *rate* of dilation, i.e., the angle of dilation. Rheological rolling resistance may change the strength in terms of friction angle for a particle assemblage, but its inability to change the rate of dilation makes it ineffective for studying surface fault rupture due to the dependence of fault rupture on the dilation angle of the soil (Cole & Lade 1984). Zhou et al. (2013) showed that assemblages of non-circular disk clusters do not show the final form of their shear bands in their strain fields until after the peak state during biaxial shear simulations. Their simulations with disks having rolling resistance, however, did show the final form of the shear bands prior to the peak state. This finding highlights a fundamental difference in the shearing behavior and process of shear band formation in spherical particle assemblages having rheological resistance to rotation as opposed to inherent resistance to rotation directly through non-spherical particle shape.

Making non-spherical particles is rather trivial with modern discrete element codes. Clumped particles, or sphere-clusters, in which spheres are rigidly connected to make one non-spherical particle are commonly employed to study shape effects. Fig. 2.38 shows examples of sphere-clusters with varying degrees of complexity. Modeling the extremely complex shapes of real sand grains may require hundreds of constituent spheres within a single sphere-cluster (e.g., Ferellec & McDowell 2010). Such a large number of constituent spheres in a single sphere-cluster may not be necessary to capture the important effects of non-spherical particle shape. Yan (2009) performed direct shear test simulations with elongated sphere-clusters containing 2 to 3 constituent spheres and showed that these simply-shaped sphere-clusters capture the dependence of the assemblage strength on depositional direction, which is important for showing the effects of bedding orientation in a field-scale simulation. Yan (2009) further showed that when particles are oriented with their long axis parallel to the direction of shear, the assemblage tends to exhibit lower shear strengths than when particles are oriented randomly or with their long axis perpendicular to

the direction of shear. Yan (2009) and O'Sullivan (2011b) both note that sphere-clusters are also concave and may have multiple points of contact with a single other particle, whereas ellipsoidal particles can only form one contact with another particle. The contact forces in spheres and ellipsoids act through the centroid of the particle, but the contact forces acting on sphere-clusters do not act through the particle centroid and thus impart a torque on the particle (O'Sullivan 2011b). Sphere-clusters generally tend to exhibit higher strengths and rates of dilation than spheres (e.g., Thomas & Bray 1999, O'Sullivan & Bray 2002), and assemblages of sphere-clusters with higher aspect ratios tend to exhibit even higher strengths (Härtl & Ooi 2011). Other methods of creating non-spherical particles include use of superquadrics, polyhedrons, and, more recently, level sets (Kawamoto et al. 2016).

Dimensionality greatly affects the shearing behavior of an assemblage of particles. Deluzarche & Cambou (2006) point out that the restriction of movement to a single plane of motion in 2D simulations creates artificially high rates of dilation. Soil strength is essentially a function of the difficulty for particles to rearrange, and restriction to two dimensions artificially constrains particle rearrangement (Deluzarche & Cambou 2006). Deluzarche & Cambou (2006) also note that grain size distributions are fundamentally 3D and do not have a 2D equivalent. Hazzard & Mair (2003) and Cui & O'Sullivan (2006) demonstrated that even plane-strain simulations of 3D particle systems exhibit myriad out-of-plane motions. 2D simulations are essentially simulations of parallel rods, and O'Sullivan et al. (2002) verified that 2D DEM simulations of hexagonally arranged, uniformly sized disks having the properties of steel rods do mimic the shearing mechanisms in physical biaxial shear tests on steel rods in the same hexagonal arrangement with the same dimensions. O'Sullivan et al. (2004) similarly verified that 3D DEM triaxial test simulations of uniformly sized steel spheres in face centered cubic and rhombic arrangements closely mimic the stress-strain results of equivalent physical tests. These latter two studies also showed that slight variations in particle size can have a notable effect on the stress-strain behavior of the entire assemblage, which highlights the importance of capturing the correct grain size distribution when trying to represent real materials. Uniformly sized particles may naturally fall into regular hexagonal arrangements whose shear behavior is predominantly controlled by geometric planes through the particle assemblage. Where the grain size distribution is well-distributed, the smallest particles may be neglected as they may essentially "float" within the system if they have less than 3 points of contact (Potyondy & Cundall 2004, Huang et al. 2014b). These floating particles do not contribute to the overall mechanical response.

Arguably the greatest computational hurdle in discrete element modeling is capturing the size of real sand grains. Even the smallest laboratory test specimens may contain several million individual sand grains (O'Sullivan 2011b). When sphere-clusters are used, the number of nodes to track is scaled by the number of constituent spheres per sphere-cluster. Simulating a realistic number of sphere-clusters close in size to a real sand grain in a laboratory test is beyond the capacity of most desktop workstations and requires high-performance computing. Advances in parallel computing and high-performance computing (e.g., Gardner et al. 2017) will allow researchers to simulate greater numbers of smaller particles in field-scale simulations.

Within unchanging model dimensions and when maintaining a consistent void ratio, decreasing particle size is equivalent to increasing the number of particles. As with determining what imposed velocities maintain quasi-static conditions, though, multiple simulations with different numbers of particles within the same boundary dimensions may be performed to evaluate how many particles are required for the macroscopic simulation results to not be affected by particle size. Ni et al. (2000) showed that when direct shear test simulations contain at least 30,000

sphere-clusters having 2 constituent spheres, the macroscopically measured angles of dilation and friction are not significantly affected by further increases in the number of particles within the same test dimensions. Bernhardt et al. (2016) performed 3D direct simple shear test simulations that were analogous to physical experiments with steel spheres. Their simulation results were much closer to their experimental results in terms of volumetric dilation and frictional strength when using 60,000 total spheres instead of 7,500 total spheres. Bernhardt et al. (2016) explain that larger sample sizes tend to be more homogeneous and are less influenced by boundary effects. The minimization of boundary effects requires that particles be made small enough relative to a characteristic length, which Bernhardt et al. (2016) suggest as the minimum boundary dimension. The notion of a minimum total number of particles for physically accurate results applies to macroscopic friction angles and *rates* of dilation. Total dilation will inevitably increase with particle size (e.g., Stone & Wood 1992). Fortunately, most DEM applications do not require particles to be equivalent in size to real sands for them to provide valuable insight into granular behavior.

2.6 Previous DEM Studies of Boundary-Displacement Problems and Soil-Structure Interaction

Discrete numerical methods such as DEM are particularly well-suited for analyses of large-strain problems, because their solution scheme follows a Lagrangian approach in which the particle paths are tracked individually. Such a scheme does not involve a mesh and hence does not have issues related to mesh locking or mesh distortion as discussed by Lazarte (1996). Multiple authors studying earthquake surface fault rupture such as Bray (2001) and Oettle & Bray (2016) have recommended that future studies of this phenomenon utilize DEM. Bray (2001) states that discrete element modeling may offer a "revolutionary way to investigate the particulate nature of soil." The need for discrete element modeling in the study of earthquake surface fault rupture is well established but has until recently been hindered by significant computational challenges. Given the recent advances in DEM and parallel processing, DEM is now ready to be used for grain-scale analyses of earthquake surface fault rupture. This section presents previous discrete element studies of surface fault rupture, soil-structure interaction, and other relevant boundary-displacement problems. The findings and notable contributions from these studies are briefly summarized and discussed.

2.6.1 Review of Discrete Element Studies of Surface Fault Rupture and Related Boundary-Displacement Problems

Saltzer (1992), Saltzer & Pollard (1992)

DEM gained early popularity amongst researchers in geology and tectonics well before its more widespread use amongst researchers in earthquake engineering. Saltzer & Pollard (1992) used DEM to investigate the development of fault-induced folding features in sedimentary overburden resulting from normal fault bedrock offset. They used a linear contact model derived from Hertz theory with a constant contact area, and they used a coefficient of friction of 0.5 at the inter-particle contacts. The simulations in their study are essentially 2D versions of the sandbox models typically used in surface fault rupture studies (e.g., Cole & Lade 1984, Bransby et al. 2008a,b). Saltzer & Pollard (1992) modeled 3 material types: Type A material with particles

varying in radii by 40%, Type B material with particles varying in radii by 30%, and Type C material with particles varying in radii by 10%. They performed normal fault rupture simulations with dip angles of 30°, 60°, and 80° as well as simulations of lateral wall extension and base rotation. The computational restrictions at the time of their study limited the number of particles to approximately 900. As seen in Fig. 2.39 for their 30°-dip normal fault simulations, the shear behavior is highly dependent on size gradation. The more uniformly sized Type C material behaved like a dense, brittle soil with distinct localization; whereas, the more well-distributed Type A material behaved more like a loose, ductile soil with broadly distributed shearing. The approximately hexagonal arrangement of the Type C material, however, appears to largely control the faulting patterns. In the Type C material, Saltzer & Pollard (1992) showed that the fault rupture surface propagates linearly at an angle of approximately 60°, and the shear band at the end of fault rupture contained only 1 to 2 particles. At such a shallow bedrock dip angle, a graben is expected to form that displaces more than the particles overlying the hanging wall and footwall (Cole & Lade 1984, Lade et al. 1984). However, Fig. 2.39 shows that a graben does not form at all in the Type C material, yet in the Types A and B materials antithetic shear surfaces do develop over the hanging wall. The material bounded by the synthetic and antithetic shear surfaces does not displace more than the surrounding material, so it is not considered a graben. These shear mechanisms are not consistent with those observed by Cole & Lade (1984) and Lade et al. (1984), but the study of Saltzer & Pollard (1992) does highlight the influence of particle gradation.

Saltzer (1992) used DEM to explain mechanisms of crustal extension observed via sandbox models and geophysical surveys. This study is an early application of DEM towards the explanation of physical soil behavior through numerical replication of a physical experiment. Such verification with physical models allows researchers to explain physical phenomena in more depth through quantitative numerical analysis. Saltzer (1992) showed that the formation of grabens and antithetically dipping shear rupture surfaces depends on the uniformity of basal extension. In simulations where only the lateral walls extended outward, Saltzer (1992) observed that single "half-grabens" developed only at the boundaries of the particle assemblage. When Saltzer (1992) distributed an extensional gradient across the base of the assemblage with greater extension near the simulation boundaries than near the center, as shown in Fig. 2.40, then successive grabens formed throughout the horizontal length of the particle assemblage. The failure surfaces in the study of Saltzer (1992) also tended to orient at 60° to the horizontal due to the hexagonal arrangement of uniformly sized disks.

Thomas (1997)

The dissertation of Thomas (1997) presents a suite of 2D surface fault rupture simulations using discrete deformation analysis (DDA) and DEM. Amongst the principal findings of this dissertation with respect to simulating surface fault rupture is that fewer numbers of disk-clusters than disks are required to obtain satisfactory fault rupture patterns through a particulate medium. Thomas (1997) reports that simulations with 1700 disks did not produce physically realistic patterns of surface fault rupture, but simulations with 5651 or more disks did produce satisfactory fault rupture patterns. When Thomas (1997) used disk-clusters containing 2-4 constituent disks instead of single disks, as few as 2270 disk-clusters produced satisfactory fault rupture patterns. This many disk-clusters will still contain upwards of 6000 constituent disks. The minimum number of particles needed for a fault rupture simulation to produce informative results depends on the

total number of spheres or disks, whether they are single particles or constituents of larger cluster particles.

Using more disk clusters increases the run-time of DEM simulations. Thomas (1997) recognized that the shear zone is primarily confined to the center of the simulation while the particles near the lateral boundaries of the simulation have little influence on the shear zone. Hence, Thomas (1997) reduced the sizes of the particles near the center of the simulation while making the particles near the boundaries coarser. This use of larger boundary particles is similar to the practice of mesh refinement in finite element and finite difference modeling in that it significantly reduces the computational demands of a simulation focused on the shearing behavior of relatively fine particles.

Fault Gouge: Morgan (1999), Morgan & Boettcher (1999), Morgan (2001), Morgan (2004), Guo & Morgan (2004, 2007), Fournier & Morgan (2012)

The findings from DEM simulations of shear deformation in fault gouge have important implications towards the granular mechanics prevalent within fault-induced shear zones. The companion studies of Morgan (1999) and Morgan & Boettcher (1999), described herein, demonstrated the different shearing mechanisms present in disk assemblages having low to high coefficients of friction and low to high fines contents. Morgan (1999) showed that as the coefficient of friction increases, the dominant mechanism of shearing transitions from inter-particle sliding at the contacts to particles rolling in response to shear displacement. As shown in Fig. 2.41 and explained by Morgan (1999), rolling, unlike sliding, involves a coupling effect between particles that increases the amount of dilation and in turn increases the macroscopic strength of the assemblage. The latter also results in greater strain-softening behavior in assemblages of particles having higher inter-particle friction coefficients (Morgan 1999). Morgan & Boettcher (1999) demonstrated how a matrix of fine particles has a "lubricating" effect that reduces the macroscopic strength of a gouge zone containing scattered coarse particles mixed within the fines. As shown in Fig. 2.42 and explained by Morgan & Boettcher (1999), the coarse particles in assemblages containing relatively few fines directly interact with each other, and this direct interaction produces high frictional resistance to rolling when contacting particles roll in the same direction, or synthetically, with each other. Morgan & Boettcher (1999) further explain how a matrix of fines can decouple the coarse particles from each other in a manner analogous to roller bearings that roll in the opposite direction, or antithetically, to the coarse particles and facilitate more distinctive localization through the granular assemblage. Morgan (2001) notes that shear-induced particle crushing can create such a fine-grained particle matrix within a gouge zone. Morgan (1999) also observed that the number of particles sliding relative to each other is initially high due to "unfavorable" contact orientations with higher shear stresses than normal stresses. Morgan (1999) explains that more contacts reorient toward the major principal stress direction during shearing, creating more favorably oriented contacts and a reduction in overall inter-particle sliding.

Subsequent studies built upon the work of Morgan (1999) and Morgan & Boettcher (1999). Morgan (2004) performed similar simulations using the Particle Dynamics Method (PDM) to restrict the rotational motion of particles as a proxy for the true three-dimensional, non-spherical shapes of real sand grains. Assemblages in the PDM simulations showed higher macroscopic frictional strengths than free-rolling particle assemblages in DEM simulations. Guo & Morgan (2004) explicitly analyzed the effect of grain shape by comparing the shear behaviors of disks, rounded disk-clusters, and triangular disk-clusters. They observed that triangular disk-clusters, as

compared to the more rounded particle shapes, exhibit significantly more interlocking due to their greater angularity, which restricts their ability to roll and forces them to instead slide relative to one another. Thus, as in Morgan (1999), Guo & Morgan (2004) also observed higher rates of dilation in the assemblages of triangular sphere-clusters. This suggests dilation rates can be increased in DEM simulations by using more angular sphere-clusters, which is preferred over the rheological restriction of particle rolling to account for the interlocking effects of non-spherical grains. Guo & Morgan (2007) examined the influence of uniaxial compressive strength on the development of gouge zones by inserting tensile bonds in between contacting particles. Fournier & Morgan (2012) also inserted bonds between particles except along a pre-defined fault plane. They observed "stick-slip" shearing behavior under high stresses and "stable sliding" under low stresses. This may be expected given the dependence of tangential shear resistance on applied normal stress in contact models that incorporate frictional slip. The use of tensile bonds between particles is not consistent with the properties of cohesionless granular materials, but it does present an avenue for exploring the effects of aging and cementation on granular shear behavior as well as the influence of clayey infills within a granular soil matrix.

Finch et al. (2003, 2004), Hardy & Finch (2006, 2007), Finch & Gawthorpe (2017), Deng et al. (2017)

Finch et al. (2003) used 2D assemblages of frictionless, bonded disks to study the influence of cover strength and fault dip angle on the development of contractional faulting and folding features within regional-scale sediment overlying a blind bedrock fault. They treated a total of 5925 disks as representative of geologic blocks of diameter 250-500 m. The boundary conditions, however, are still equivalent to those for reverse fault rupture on a smaller scale. The particulate medium is undisturbed and intact with no predetermined rupture path prior to the initiation of fault rupture to capture the effects of a blind bedrock fault. Their model shown in Fig. 2.43 has similar boundary conditions to the centrifuge sandbox experiments of Bransby et al. (2008a,b). They generated frictionless disks with different bond strengths and a tensile cut-off, and the bonds were not allowed to "heal" when coming back into contact after the bond breaks. Thus, their assemblage is purely cohesive. Their contractional faulting simulations with more ductile cover having weaker inter-particle bond strengths displayed broad zones of deformation with "upward-widening monoclines", as shown in Fig. 2.44; whereas, their simulations with brittle cover having stronger inter-particle bond strengths exhibited more distinctive localization along the rupture path as shown in Fig. 2.45. Finch et al. (2004) report nearly identical findings for extensional, normal fault rupture simulations as well as wider zones of deformation for shallower fault dip angles. Finch et al. (2003, 2004) quantified the strength of their sedimentary cover using a ratio of fault rupture propagation to base displacement and showed that fault rupture reached the ground surface at lower base displacements in stronger covers with higher inter-particle bond strengths than in weaker covers with lower inter-particle bond strengths.

Finch et al. (2004) also performed extensional faulting simulations with alternating layers of strongly and weakly bonded disks. They showed that the weaker layers tend to distribute the deformation over a broader zone than in the stronger layers that rupture more brittlely. These observations are consistent with those of Bray et al. (1994a) in that more ductile soils tend to distribute the distinct bedrock offset into wider zones of deformation. Hardy & Finch (2006) further investigated the influence of layer strength in heterogeneous, interbedded strata. In their 2-layer stratigraphies in which the lower half of disks were strongly bonded and the upper half of

disks were weakly bonded, the fault brittlely ruptured through the strong lower layer but did not produce distinctive offsets in the upper weak layer. When a strong layer overlay a weak layer, no rupture extended through to the strong layer. Instead, they observed that the strong layer folded into a monocline with unchanged thickness. In their 3-layer models with a strong layer in between 2 weak layers or a weak layer in between 2 strong layers shown in Fig. 2.46, the strong layers directly overlying the bedrock fault again exhibited brittle fault rupture whereas strong layers overlying weak layers again tended to fold without distinctly rupturing. Distinctive localization easily continued directly through the strong layers, but distinctive localization would not reemerge through a strong layer once it was diminished within a weak layer. Hardy & Finch (2006) further observed that the distribution of broken bonds in weak layers tends to widen over a triangular zone referred to as the "trishear model" of fault-related folding. Hardy & Finch (2007) showed that in sequences of thinly interbedded layers of strongly and weakly bonded particles, the bond breakage spreads widely and parallel to bedding in the weak layers. This further highlights the capability of weak soil to distribute the shear due to fault rupture over a broad zone and inhibit localization.

Finch & Gawthorpe (2017) and Deng et al. (2017) extended the methodology of using frictionless DEM particles to three dimensions using 1,080,000 spheres and 1,830,000 spheres, respectively. They note that the exclusion of shear forces greatly speeds up simulation times while still informing regional-scale observations of fault nucleation, growth, and linkage in an extensional regime containing a preexisting plane of weakness. Their models represented a depth of 30 km through both brittle and ductile crust. These two studies highlight the capability of DEM to not only inform researchers of micro-mechanical and grain-scale phenomena during fault rupture but to also provide insight into the formation of major geophysical structures on the regional scale.

Strayer & Suppe (2002)

Strayer & Suppe (2002) used PFC3D in one of the earlier applications of 3D DEM towards earthquake fault rupture. They generated 83,000 spherical particles within a 3D sandbox-style domain of dimensions 7.5 km x 10 km x 1 km, with the 10 km length being the strike direction. The average sphere diameter was 50 m with a maximum to minimum diameter ratio of 1.33 to prevent the spheres from self-organizing into a hexagonal close-packed arrangement. The boundary conditions in this model are different from those of experimental sandbox models of dip-slip fault rupture (e.g., Bransby et al. 2008a,b). The entire base layer in their simulation remains stationary while one wall running parallel to the strike direction moves inward perpendicular to the strike direction. The particles were bonded using tensile and shear bonds, and Strayer & Suppe (2002) determined the macroscopic properties of the bonded assemblage using biaxial shear test simulations. Strayer & Suppe (2002) "seeded" a fault rupture surface by reducing the bond strength between pairs of particles located on opposite sides of a 25°-dip planar fault projection. Seeding the fault constrains rupture to occur along a distinct, predetermined plane and serves as an early demonstration of the influence of pre-ruptured soil discussed in Oettle & Bray (2013a). Strayer & Suppe (2002) also varied the inter-particle friction coefficient in the strike direction from 0.0 to 0.4, which produced more distinctive rupture along the strike as friction decreased.

Strayer & Suppe (2002) address some of the issues related to the use of single spheres to represent 50 m diameter rock masses. They recognized that, due to the preponderance of defects over larger sized rocks, the elasticity of the particles could justifiably be smaller than elasticity measurements made on intact rock. They also addressed the dependence of the results on particle

size by performing simulations with smaller and larger particles to show that the overall macroscopic response is virtually the same with each set of particle sizes. However, Strayer & Suppe (2002) state that further refinement of particle size would allow smaller-scale features to develop. This is analogous to using a finer mesh in a continuum model where finer details must be observed.

Growth Faults: Strayer et al. (2004), Chu et al. (2014)

Growth faults form when soil sediment deposits atop a ruptured fault outcrop and masks its surface expression. This makes field investigations of the underlying rupture surface difficult (Chu et al. 2014). Strayer et al. (2004) and Chu et al. (2014) used DEM to study the influence of growth strata on fault rupture and fault-related folding in assemblages of bonded disks and frictional disks, respectively. Strayer et al. (2004) modeled growth strata by topping the ground surface with new layers of variable thickness after successive growth stages. They modeled the fault as a ramped wall boundary in 2D and induced fault rupture by moving inward a lateral boundary similar to the way Strayer & Suppe (2002) induced fault rupture. The initial layer in their simulation contained only 5000 disks, and the disks of the growth layers in later stages were made smaller in diameter. Strayer et al. (2004) state that their methodology and analyses are useful in understanding the subsurface conditions that influence geologic structures and may provide guidance for field investigations. This is a notable value of discrete element modeling towards understanding the development of many natural geologic features.

The results of Chu et al. (2014) highlight a significant hazard associated with growth faults. Through comparative DEM simulations and sandbox experimentation, they showed that the fault rupture surface outcrops at the ground surface at a lower increment of hanging wall displacement for growth normal fault as opposed to a standard normal fault with no growth features or pre-ruptured zones. Chu et al. (2014) estimate that fault outcrop in growth faults requires about one-third of the amount of hanging wall displacement as non-growth normal faults. Furthermore, they showed that the rupture surface that outcrops in a growth fault is a continuation of the previous rupture surface, which is consistent with the findings of Oettle & Bray (2013a) on pre-ruptured soils. This suggests that avoidance of the growth fault outcrop location is relatively straight-forward if the original fault is located, but this avoidance also requires that the presence of the growth fault be known in the first place. Where growth strata hide the signs of surface fault rupture, structures situated near the potential fault outcrop location may actually incur damage at a lower amount of hanging wall displacement than in the presence of a standard normal fault that has yet to rupture.

Cardozo et al. (2005)

Cardozo et al. (2005) used DEM to analyze the mechanics of folding in the Rip Van Winkle Anticline in eastern New York and La Zeta Anticline in Argentina. Their model domain represents a horizontal distance of 6000 m and a vertical distance of 1000 m. It contained 5080 rotationally-restricted particles with diameters of 15 m, 20 m, and 25 m. As shown by Morgan (2004), the restriction or prevention of particle rotations increases dilatancy and shear strength for the assemblage. The large scaling of the particles means each particle essentially represents a homogeneous block of geologic material. Any faults, fissures, or joints inherent to geologic strata are coalesced into a single rigid disk that interacts with other disks. This is a major simplification

to the complexities of geologic phenomena, but such a simplification is very often necessary for practical analyses of such phenomena using DEM. Cardozo et al. (2005) settled the particle assemblages under a gravitational acceleration of 10 m/s^2 and 30 m/s^2. The assemblage settled under 10 m/s^2 behaved like a normally consolidated soil, and the assemblage settled under 30 m/s^2 and then equilibrated under 10 m/s^2 behaved like an overconsolidated soil with an earth pressure coefficient greater than 1.0 (Cardozo et al. 2005). Their use of high and low gravitational accelerations to create overconsolidated or normally consolidated materials highlights the sensitivity of discrete element assemblages to stress history by showing that locked-in stresses may still be present when unloading from a higher gravitational load. As shown in Fig. 2.47, the overconsolidated particle assemblage in Cardozo et al. (2005) exhibited more distinctive localization than the normally consolidated assemblage. Cardozo et al. (2005) also analyzed the effects of layer strength on the folding characteristics of the particle assemblages by creating layers with lower inter-particle friction overlying layers of higher inter-particle friction. The rupture surface tended to spread widely when transitioning from a highly frictional layer to a less frictional layer. This effect of weaker layers distributing shear more broadly is consistent with observations of looser sand or more ductile clay with lower shear strength locally absorbing shear and inhibiting distinct localization (e.g., Bray et al. 1994, Lazarte & Bray 1996).

Schöpfer et al. (2006, 2007a, 2007b. 2009), Schöpfer et al. (2016, 2017)

Schöpfer et al. (2006, 2007a, 2007b) performed DEM simulations containing over 23,000 disks using PFC2D to study the mechanisms of fault linkage in alternating strong and weak layers during normal fault rupture. The weak layers consisted of unbonded particles interacting through a linear elastic contact model, and the strong layers were bonded using the parallel bond contact model of Potyondy & Cundall (2004). Schöpfer et al. (2007a) describe their numerical calibration procedure using biaxial shear test simulations for unbonded particles and direct tension, Brazilian disk, unconfined compression, and confined compression test simulations for bonded particles. They note that the bonded particle properties were strongly dependent on the sample size relative to the test dimensions, but the macroscopic unbonded particle properties were relatively independent of sample size as long as the biaxial test width was at least 32 times the average particle diameter. This notion of a threshold for sample-size independence of macroscopic properties in cohesionless particles is consistent with similar findings from direct shear test simulations by Ni et al. (2000). In their fault rupture model, Schöpfer et al. (2006, 2007a,b) obtained their desired at-depth stress state in the assemblage by applying a confining pressure through the uppermost layer of particles. As shown in Fig. 2.48, Schöpfer et al. (2007b) observed that the fault rupture mechanism, whether through shearing or tension between particles, depended heavily on the applied confining pressure. Under high confining pressures, the shear mode of failure dominated in the bonded particle layers, especially when the bonds between particles were relatively weak. At lower confining pressures and with higher bond strengths, the bonded layers tended to fail more in tension, which produced a "staircase geometry" of fault rupture propagation through the alternating bonded and unbonded layers. The staircase structure resulted from the rupture surface dipping at a steeper angle in the stronger bonded layers and more shallowly in the unbonded layers (Schöpfer et al. 2007b). Tensile fracturing in the bonded layers produced intact blocks that tended to rotate in the sense of shear induced by normal fault rupture, and larger asperities due to this tensile failure developed as bond strength and confining pressure decreased. Schöpfer et al. (2007b) describe this block rotation as a drag feature of normal fault rupture. The

tensile mode of failure in the bonded layers under low confining stresses and the shear mode of failure under high confining stresses is consistent with experimental observations by Roth et al. (1981), who also found that cohesive strength controls the failure mode at low stresses but frictional strength controls at high stresses. Schöpfer et al. (2009) furthered their work with 2D DEM and showed that the relative thickness of strong and weak layers significantly influences the manner of fault rupture propagation and fracture through the bonded layers.

Schöpfer et al. (2016, 2017) extended their previous fault rupture geometry to three dimensions. They used a "shining-lamp" algorithm to apply a confining pressure through the uppermost layer of particles. Schöpfer et al. (2017) monitored quasi-static rupture through the development of stresses on the rigid hanging wall and footwall, which, given frictionless boundary walls, should have approximately equal and opposite changes in force during quasi-static movement of the hanging wall. Schöpfer et al. (2017) judged their quasi-static rupture velocity to be 0.1 m/s. The model of Schöpfer et al. (2016) had a homogeneous particle size distribution with approximately 250,000 total spheres, but Schöpfer et al. (2017) used up to 380,000 total spheres with finer particle sizes at the center of the model where fault rupture occurs. As was shown by Thomas (1997) in two dimensions, this refinement of particle sizes solely within a region of interest significantly reduces simulation run-times. The simulation results of Schöpfer et al. (2017) demonstrated how higher stresses and larger hanging wall displacements enhance the localization of fault rupture through cohesionless, granular soil deposits.

Egholm et al. (2007), Egholm et al. (2008)

Egholm et al. (2007) used a modified formulation of DEM called the stress-based discrete element method (SDEM), which was developed by Egholm (2007), with additional tensile bonding and rolling resistance at the inter-particle contacts. SDEM stores a strain-rate tensor for each particle, which is then used to obtain the inter-particle contact forces via a constitutive law that converts the strain-rate tensor to a stress tensor (Egholm et al. 2007). The tracking of strain-rate tensors for each particle gives SDEM an advantage in that displacement rates may be easily calculated along a shear band. This allowed Egholm et al. (2007) to visualize shear activity along existing rupture surfaces and see when shear displacement discontinued along one shear band and transferred to another shear band, as shown in the lateral extension simulations in Fig. 2.49. The macroscopic Mohr-Coulomb strength parameters are direct inputs to the SDEM contact formulation, which greatly simplifies the calibration process with SDEM. In a separate study on clay smearing during fault rupture, Egholm et al. (2008) states that "SDEM parameterization is therefore better suited for simulations where rules governing the microphysical grain interactions are poorly known..." Inter-particle contact stiffnesses are rarely known except in the case of man-made materials such as steel (e.g., O'Sullivan et al. 2002, 2004, Cui & O'Sullivan 2006), but the macroscopic properties of a geologic material are easily obtained through laboratory testing. Thus, SDEM is advantageous in that it can take these laboratory results as direct inputs for its contact model.

Egholm et al. (2007) quasi-statically performed their lateral extension simulations in Fig. 2.49 with 110,000 disks. These lateral extension simulations are essentially the extreme case of 0°-dip normal fault rupture. As extension continued from the velocity discontinuity (VD) in their model, new graben structures developed near the edges of the weak particle layer at the bottom of their model. This weak layer is simply a layer of particles having a friction angle of 1° as opposed to 36° for the rest of the assemblage. Egholm et al. (2007) note that the frictional properties of the

lateral walls, however, did not affect their extension simulations. As new grabens formed near the edges of the weak layer, Egholm et al. (2007) showed that displacement rates gradually reduced along the shear bands bounding the previously formed grabens, indicating a cessation of shear activity along those shear bands.

Egholm et al. (2007) further assessed the applicability of SDEM to fault rupture and folding by reproducing the boundary conditions of the extensional faulting simulations performed by Finch et al. (2004). Egholm et al. (2007) used 62,000 disks of radii 0.05-0.5 mm and base dip angles of 30°, 45°, and 60°. As in Finch et al. (2004), Egholm et al. (2007) also describe an "upward-widening" rupture surface propagating over the footwall at an angle of 60°-65° to the horizontal in each of their simulations. Egholm et al. (2007) explain that an antithetic rupture surface propagates over the hanging wall to form a graben when the horizontal component of hanging wall displacement is greater than or equal to the vertical component (e.g., when the fault dip angle was 45° or lower). They showed that in the case of purely extensional base displacement, the resulting graben structures were nearly symmetric, but the graben structures grew increasingly more asymmetric as the relative magnitude of the vertical component of hanging wall displacement increased until no antithetic rupture surface developed at all.

Hardy (2008, 2011, 2013)

Hardy (2008, 2011, 2013) describes a suite of 2D simulations of normal fault rupture and trapdoor-style displacement representative of caldera formation using assemblages of disks. Hardy (2008) performed trapdoor-style simulations with 12,000 purely frictional disks and showed that the sequence of shear surface development in trapdoor-style scenarios is dependent on the width of the subsiding base relative to the depth of soil. Hardy (2008) found that wider trapdoor regions tend to produce a pair of inward curving shear bands that emerge at the ground surface followed by the formation of nearly vertically propagating shear bands. These findings are consistent with the experimental trapdoor results of Iglesia et al. (2013). When the trapdoor width is thin enough for the initial pair of inward curving shear bands to meet at their apex before reaching the ground surface, successive pairs of inward curving shear bands may continuously form at steeper angles until a final pair reaches the ground surface (Hardy 2008). These inward curving shear bands that meet below the ground surface support the weight of the uppermost soil and, as explained by Hardy (2008), produce less displacement at the ground surface than occurs at depth immediately above the trapdoor.

Hardy (2011) performed DEM simulations with 12,000 frictional disks to model steep normal fault rupture with a dip angle of 70° through a 5.5 km x 12.5 km section of idealized crustal material. The results in Fig. 2.50 show two zones of shear localization in the assemblage, which Hardy (2011) describes as a zone of reverse faulting (Zone R) following by a zone of normal faulting (Zone N). The zone of reverse faulting, however, is not strictly a reverse fault, because the sense of shear in this zone is consistent with that of the base fault. Zone R in Fig. 2.50 is similar to the inward curving shear bands from Hardy (2008), whereas Zone N is more consistent with the shear localization above a shallow-dipping normal fault as observed by Bray et al. (1994a). This suggests that fault dip angles near 70° represent a transitional case between the shear mechanisms in shallow-dipping normal fault rupture and nearly vertical base displacement. Nollet et al. (2012) similarly describe fault dip angles around 70° as a transitional case of normal fault rupture. Hardy (2013) then performed similar simulations of steep normal fault rupture using 47,000 frictional disks with additional bond strength to represent cohesion. Hardy (2013) notes that these

simulations were completed in under 24 hours using parallel computing, whereas earlier simulations by Finch et al. (2003, 2004) that contained 5925 disks took approximately 90 hours. The simulations of Hardy (2013) produced different stress-dependent mechanisms of rupture consistent with the failure modes shown by Schöpfer et al. (2007a,b). The failure mode in the soil near the ground surface tended to be that of tensile fracture, which is consistent with materials dominated by cohesion under low stresses. At greater depths, the mode of deformation was in shear, which is consistent with frictional materials.

Abe et al. (2011)

Abe et al. (2011) modeled normal surface fault rupture propagation through homogeneous cohesive material using the parallel DEM code ESyS-Particle (https://launchpad.net/esys-particle/) in 2D with approximately 56,000 bonded disks. They checked that their rate of rupture was sufficiently quasi-static over a range of rupture velocities from 0.5 mm/s to 20 mm/s to reduce the run-time of their simulations and noted that rupture velocities in comparative physical experiments were actually over an order of magnitude slower. Their findings were consistent with those of Schöpfer et al. (2007b) in that assemblages with lower cohesive strengths tended to fail in shear whereas those with higher cohesive strengths tended to fail in tension. As in Hardy (2013), Abe et al. (2011) also showed the mode of failure in highly cohesive assemblages change from tensile failure near the top of the assemblage to shear failure near the bottom due to the increasing stress with depth. As the fault dip angle increased, the rupture surfaces in the simulations of Abe et al. (2011) tended to bend more over the downthrown block, and tension cracks tended to develop at the ground surface of the upthrown block at all dip angles.

Taniyama (2011, 2017)

The work of Taniyama (2011, 2017) shows the extreme computational speedups that may be gained with high-performance computing. Taniyama (2011) modeled strike-slip fault rupture using over 2.3 million spheres with radii of 9-12 cm, and Taniyama (2017) modeled oblique-slip fault rupture using over 12.8 million spheres with radii of 3-5 cm. The contacts between the spheres included rheological rolling resistance to account for the non-spherical shapes of real sand grains. The height of each model was approximately 4.9-5.2 m, and the width perpendicular to the strike was 10.9 m for strike-slip fault rupture and 15.5 m for oblique-slip fault rupture. The along-strike lengths were 34.6-37.4 m with periodic boundaries that approximate an infinitely long strike. Taniyama (2011) observed similar en-echelon shear structures in the high-performance DEM simulations that were also observed in strike-slip fault case studies such as the 2014 Napa, California, earthquake (see Fig. 2.1). Taniyama (2011) further described the formation of Riedel shears and secondary shear structures as resulting from the buckling of column-like structures oriented in the direction of the major principal stress. This type of shear mechanism was also described by Iwashita et al. (1998, 2000) in 2D biaxial compression simulations. The reverse oblique-slip fault movement in the model of Taniyama (2017) produced similar features that developed more above the footwall. Similar en-echelon shears developed near the ground surface, and Taniyama (2017) report that these shears were convex-upward as a result of the dip-slip component of fault movement. The fine particle sizes used by Taniyama (2011, 2017) allow complex shear patterns and mechanisms of shear development to be viewed in extreme detail.

Widuliński et al. (2011)

Although not a surface fault rupture study, the findings in the boundary-displacement simulations of Widuliński et al. (2011) have notable implications for shear band formation in all boundary value problems including surface fault rupture. Widuliński et al. (2011) used YADE to perform 2D simulations of different types of retaining wall displacement including horizontal wall translation, wall rotation about its top, and wall rotation about its bottom. YADE is actually a three-dimensional code, but the simulations can be made effectively two-dimensional by restricting out-of-plane movement. The wall translation simulations of Widuliński et al. (2011) were performed with 5,000 particles, 31,000 particles, and 110,000 particles within the same domain, i.e., with different particle sizes. They found that the overall geometries of the shear bands were relatively independent of particle size but that the width of the shear band did depend on D_{50}. In the 5,000-particle simulation with D_{50} = 5.0 mm, Widuliński et al. (2011) measured the shear band thickness as $7D_{50}$. In the simulations having 31,000 particles (D_{50} = 1.0 mm) and 110,000 particles (D_{50} = 0.5 mm), they measured shear band thicknesses of $22D_{50}$ and $36D_{50}$, respectively. Widuliński et al. (2011) also report simulation times of 1 day using the fewest particles and 24 days using the most particles with a personal computer. This dependence of shear zone thickness on particle size and the dramatic increase in computational time when using a larger number of particles highlights the need for more advanced computing methods in discrete element modeling.

Chevalier et al. (2012)

The stress distributions and shear surfaces resulting from trapdoor boundary movement have notable parallels to the surface fault rupture problem. Chevalier et al. (2012) used physical sandbox experiments and analogous 3D DEM simulations to study the mechanisms of load transfer in granular soils overlying a trapdoor. They observed three distinct phases of load transfer between the soil grains and the trapdoor: the maximum transfer phase, the transitional phase, and the critical phase. As described by Chevalier et al. (2012), these phases represent a rapid load drop (maximum transfer phase) on the trapdoor followed by a steady increase in load on the trapdoor (transitional phase) until the load eventually asymptotes at a stable value (critical phase). The descriptions of these phases in Chevalier et al. (2012) are very similar to the sequence of load transfer described by Iglesia et al. (2013). Chevalier et al. (2012) followed their experimental tests with a series of DEM simulations with assemblages of spheres and sphere-clusters. They prepared their trapdoor simulations using a radius expansion procedure with 23,000 particles, and the resulting earth pressure coefficient (K_0) was approximately 0.4 through most of the assemblage except near the ground surface where the stresses were nearly isotropic. The contact normal orientations resulting from this radius expansion procedure were also nearly isotropic. Micro-mechanical analyses revealed an arch-like pattern of strong contact forces above the trapdoor, as shown in Fig. 2.51, which is consistent with the soil arching phenomenon described by Terzaghi (1943). Chevalier et al. (2012) observed an inverse relationship between the peak friction angle of the particle assemblage and the width and height of the arched zone of contact forces, and they observed that assemblages with different particle shapes having similar peak friction angles exhibited very similar arch shapes. This finding suggests that the characteristics of soil arching are primarily a function of the frictional strength of the material, although the influence of dilatancy was not explicitly discussed in their study. The results from the simulations of Chevalier et al. (2012) are qualitatively informative, but the inter-particle friction coefficient of 1.466 used in these

simulations is extremely high. Regardless, this study does show with DEM that the process of load transfer in the soil is related to the expansion of the developing soil wedge above the trapdoor as shear surfaces develop from the trapdoor edges.

Chang et al. (2013)

Chang et al. (2013) performed a series of sandbox model experiments of surface fault rupture through dense, cohesionless, quartz-based sand under 1g laboratory conditions and with a centrifuge at 40g and 80g. The boundary conditions of their model were similar to the reverse fault rupture experiments performed by Bransby et al. (2008b). They attempted to replicate their physical test results using analogous DEM simulations with 28,759 disks scaled up in diameter by a factor of 20 relative to the sand used in their physical experiments. They calibrated the contact properties of the disks through comparisons of numerically simulated settlements under varying gravitational accelerations with settlements of the physical sand under the same range of gravitational accelerations. Calibrations based on shearing behavior are more appropriate given the dependence of surface fault rupture on the characteristics of soil in shear. Although the comparisons between physical model and numerical model of surface fault rupture were in close qualitative agreement, the study of Chang et al. (2013) is overly simplified. The use of 2D disks ignores the influence of out-of-plane contacts and kinematics present in real scenarios of plane-strain shear. The inter-particle friction coefficient of the disks was 0.73, which is higher than the widely accepted value of 0.5 for the surface friction of quartz sand grains (Mitchell & Soga 2005). The inability of the disks in capturing the non-spherical shape of real sand grains and the high inter-particle friction coefficient may result in grain-scale behavior that is not representative of real sands, but the results do succeed in showing that DEM simulations of surface fault rupture can provide qualitatively accurate results on the macroscopic level even with such notable simplifications.

Zhang et al. (2013)

Zhang et al. (2013) performed comparative analyses of regional-scale thrust faulting and folding features using both 2D DEM and plane-strain FEM. The DEM assemblage contained approximately 50,000 disks with diameters of 15 m, 20 m, and 30 m within a domain of size 26,854 m by 3,481 m. They divided the particles into 9 layers of variable inter-particle bond strength to represent variable stratigraphic units in Sheep Mountain, Wyoming. The FEM model was similarly organized into 9 stratigraphic units and contained approximately 35,000 rectangular elements. The boundary displacements in their study are not the same as a typical surface fault rupture simulation with a simple displacement of the hanging wall along the dip direction; instead, Zhang et al. (2013) imposed a more complex sequence of boundary displacements to represent different stages of thrust faulting in the basin beneath the Sheep Mountain region. Zhang et al. (2013) reports that the two continuum and discrete simulations both yielded "similar kinematic and mechanical results" with some tension cracks present in the surface of the DEM simulation that are not present in the FEM simulation, as shown in Fig. 2.52. The continuity of a standard FEM mesh typically does not allow gaps to form between elements without more sophisticated formulations, but the discontinuous nature of DEM easily facilitates formation of gaps in bonded particle assemblages. The overall similarity between the main faulting features between the FEM and DEM simulations shows that these two methods complement each other, and the differences in the deformations at

the ground surface suggests that key features not shown through continuum-based analyses may be captured with DEM.

Detachment Folding: Hardy & Finch (2005), Hardy et al. (2009), Dean et al. (2013), Morgan (2015)

Several researchers used DEM to analyze detachment folding through layered strata or homogeneous media. The types of folding and thrusting features in these analyses are not directly applicable to surface fault rupture except in the extreme case of 0°-dip reverse fault rupture. These analyses typically focus on the influence of a weak décollement layer that acts as a decoupling interface between the rigid base boundary and the overlying particulate medium. Hardy & Finch (2005) modeled the décollement as a bottom layer of particles with extremely low bond strengths compared to within the overlying layers. Their analyses focused on the influence of layer thickness in alternating strong and weak layers. Dean et al. (2013) and Morgan (2015) modeled a single vertical wall that only extends to the top of the lowest particulate layer and moves laterally inward at constant velocity. They located a décollement layer at the bottom position of the laterally moving wall. Dean et al. (2013) included a second décollement at shallower depth. The inward-moving vertical wall and non-displacing lowermost particle layer produced compressional wedge structures whose formation was dependent on the cohesive strength of the particle assemblage (Morgan 2015) and the stratigraphic changes through alternating strong and weak layers (Dean et al. 2013).

Hardy et al. (2009) used a set of boundary conditions that is most consistent with those of traditional sandbox models of surface fault rupture, albeit with a dip angle of 0°. In their simulations, the base and lateral boundary of only one side of a velocity discontinuity moved inward. They demonstrated that the wedge patterns of faulting in their DEM model are consistent with those observed in sandbox experiments having equivalent boundary conditions. Their results with different friction coefficients for the décollement are particularly informative for the surface fault rupture simulations in this dissertation. When Hardy et al. (2009) set the inter-particle friction coefficient of the décollement particles equal to that between the particles in the overburden, the particles on the right side of the velocity discontinuity uniformly displaced inward. As shown in Fig. 2.53a, this resulted in a single wedge zone above the velocity discontinuity. If the décollement friction coefficient was lower than that in the overburden, the overburden decoupled from the décollement, which produced multiple wedge zones throughout the entire right boundary as shown in Fig. 2.53b. These results suggest that the friction coefficient of the horizontal basal boundary should be set equal to that in the overlying particulate medium if shear deformations are to concentrate above the distinct discontinuity at the bedrock level in a simulation of surface fault rupture through sedimentary overburden.

Botter et al. (2014)

Botter et al. (2014) generated two separate particle assemblages, one with fine particles and one with coarse particles, to assess a seismic imaging technique using 2D DEM. The particle assemblages contained two thin layers of low-friction granular material representing shale mixed between higher-friction layers representing sandstone. In both assemblages, 60°-dip normal fault rupture produced an initial rupture surface at low amounts of hanging wall displacement followed by a second, shallower dipping rupture surface at higher amounts of hanging wall displacement.

The shear zones were thinner in the finer particle assemblage, which is consistent with observations of the dependence of shear band thickness on particle size (e.g., Wood 2002). Furthermore, the development of the second rupture surface at a lower amount of hanging wall displacement in the finer particle assemblage than in the coarser particle assemblage in their study is consistent with the dependence of rupture formation on the characteristic length of the model as discussed in Stone & Wood (1992). Botter et al. (2014) note that the "resolution of the fine model is higher than that of the coarse model, allowing capturing more details of fault formation..." This statement supports the notion that particle size may be refined to capture more complex details and features in a manner similar to mesh refinement in continuum modeling.

Hazeghian & Soroush (2015, 2016, 2017, 2018)

A series of studies by Hazeghian & Soroush (2015, 2016, 2017, 2018) demonstrates the significant advantages of advanced computing toward the study of earthquake surface fault rupture propagation. These studies utilized a 3D DEM code that runs on a graphics processing unit, which Hazeghian & Soroush (2015) claim sped up their simulations by a factor of 20 compared to serial simulations performed using the YADE DEM code. The simulations in their studies were still 2D since the spheres used were restricted to in-plane motion. The spheres themselves had a rheological resistance to rolling (e.g., Iwashita & Oda 2000) that indirectly accounts for the non-spherical shapes of real sand grains. Hazeghian & Soroush (2015) describe a material calibration process using direct shear test simulations as was done by Anastasopoulos et al. (2007) with FEM simulations. Following the direct shear test calibrations, they prepared their assemblages for fault rupture by quasi-statically increasing the gravitational acceleration on the particle assemblage until achieving a desired centrifuge scaling factor. They deposited looser specimens with an initial inter-particle friction coefficient of 0.5 and denser specimens with an initial inter-particle friction coefficient of 0.05. Although a DEM specimen prepared with a friction coefficient of 0.5 may be expected to exhibit contractive behavior in shear, both assemblages exhibited volumetric dilation in the direct shear test simulations of Hazeghian & Soroush (2015). This is likely a consequence of the 2D particle motion, which tends to make assemblages excessively dilatant (Deluzarche & Cambou 2006).

Hazeghian & Soroush (2015) performed select fault rupture simulations with over 700,000 spheres under a gravitational acceleration of 115*g*. The simulations were quasi-static with a rupture velocity of 0.01 m/s, and Hazeghian & Soroush (2015) monitored the quasi-static nature of their simulations using an index of unbalanced forces as in Ng (2006). The simulation results compared satisfactorily overall with results from the QUAKER project centrifuge experiments of Bransby et al. (2008a,b). A principal difference between the simulations and the experiments was that the simulated reverse fault rupture surfaces outcropped further out on the footwall in Hazeghian & Soroush (2015) than in the experiments. Hazeghian & Soroush (2016) further showed that the fault rupture surfaces in normal and reverse fault rupture simulations with a wide range of fault dip angles are consistent with the rupture surfaces predicted by the closed-form solution of Cole & Lade (1984), and Hazeghian & Soroush (2017) describe how the fault rupture surfaces align with zero-extension directions within the ruptured assemblage. The gradients of the ground surface in response to surface fault rupture tended to increase with decreasing soil ductility, or decreasing void ratio (Hazeghian & Soroush 2015). As Hazeghian & Soroush (2015) also note, this suggests that rupture-induced structural damage may be worse atop denser soils since higher surface

gradients can produce larger differential surface displacements that can damage structures (Bray 2001, 2009).

The capability of DEM to show the micromechanics of fault rupture propagation was thoroughly demonstrated by Hazeghian & Soroush (2016). They showed that shear rupture propagation in dense, dilatant soil is associated with decreases in coordination number amongst the particles and increases in void ratio. Hazeghian & Soroush (2016) also quantified the bedrock offset at which the fault rupture surface emerges at the ground surface by connecting it to the peak stress state within the developing shear band at the ground surface. Hazeghian & Soroush (2017) used peak stress states to show that the fault rupture surface requires less hanging wall displacement during normal fault rupture than reverse fault rupture to emerge at the ground surface, and they found that more ductile, higher void ratio assemblages require greater amounts of hanging wall displacement to reach the ground surface than brittle, low void ratio assemblages. The hanging wall displacements that produced surface outcropping in their study compared well with those in previous continuum model studies and physical experiments. The broad suite of reverse and normal fault rupture simulations with loose and dense materials over a wide range of fault dip angles allowed Hazeghian & Soroush (2017) to produce preliminary design criteria for setback distances from the fault outcrop location based on the width of the zone of significant ground surface distortion.

Hazeghian & Soroush (2018) extended their discrete element methodology to sloping, as opposed to flat, ground surfaces. Their sloped geometries included a trapezoidal geometry and one-sided upward and downward sloping geometries. They found the effect of surface slope geometry to be minimal during normal fault rupture but quite significant during reverse fault rupture. At different fault dip angles, they showed that ground surfaces sloping upward over the footwall tend to increase the inclination of the reverse fault rupture surface as it approaches the ground surface, and downward sloping surfaces tend to decrease the inclination of the reverse fault rupture surface. The fault rupture essentially veers towards regions of lower stress nearest a free surface, which serves yet as another example of fault rupture propagating along a path of lowest resistance.

Smart & Ferrill (2018)

Smart & Ferrill (2018) highlight the importance of including inhomogeneities in a discrete element model when modeling naturally observed faulting sequences. They used the parallel bond contact model of Potyondy & Cundall (2004) to create thin, weak layers interbedded between thicker, stronger layers of a 2D particle assemblage containing a total of approximately 25,000 disks. Their model domain represented a 1 km x 0.2 km region of normal faulting within a volcanic region in Iceland. Unlike in other fault rupture studies, they applied a constant downward velocity to the hanging wall at a dip angle of 60° as well as an equal and opposite velocity to the footwall. The bedrock fault itself changed in dip from 80° to 60°, which opened up a gap beneath the overlying particle assemblage during fault displacement. Their simulation results were consistent with previous studies of layered sequences (e.g., Schöpfer et al. 2007a,b) in that rupture through the strong layers produced large rotating blocks of bonded particles. Smart & Ferrill (2018) made the important comparison of their layered model with homogeneously strong and weak particle assemblages. In their layered model, Smart & Ferrill (2018) captured faulting and folding features that were qualitatively consistent with those observed in the natural extensional regime on which they based their model. Their homogeneous particle assemblages did not capture the same features,

and thus Smart & Ferrill (2018) emphasize that such layering or other inhomogeneities is important for accurately modeling regional scale faulting with DEM.

2.6.2 Review of Discrete Element Studies of Soil-Foundation-Structure Interaction

Brennan et al. (2007)

The only known attempt to model FR-SFI using DEM was made by Brennan et al. (2007). The purpose of their study was to evaluate the effectiveness of a block protection mechanism for shallow foundations affected by normal fault rupture. The block protection mechanism involves the installation of circular or rectangular blocks arranged in the soil beneath the foundation. Brennan et al. (2007) arranged 2D disks of uniform diameter in a hexagonal arrangement. They modeled the foundation as a rigid, rectangular mass with an interface friction angle equal to that of the particles. They analyzed "treated" and "untreated" FR-SFI cases, with the treated cases containing the blocks of the protection mechanism beneath the foundation. This mitigation strategy is still preliminary and requires further assessments of its effectiveness. Brennan et al. (2007) recognized that their DEM results were overconstrained by the hexagonal packing arrangement of their disks, which tends to have a geometric preference for the path of shear rupture propagation.

El Shamy & Zamani (2012)

El Shamy & Zamani (2012) present the only known DEM study of *dynamic* soil-foundation-structure interaction (SFSI). Using PFC3D with over 450,000 non-uniform spheres, they successfully captured many non-linear soil responses such as shear modulus reduction followed by an increase in shear modulus as continued shaking densified the soil and ground motion amplification from the bedrock to the ground surface. El Shamy & Zamani (2012) employed some novel ideas that are also applicable to FR-SFI and FR-SFSI. By applying a gravitational acceleration of 50*g*, they were able to perform prototype-scale analyses as in centrifuge experimentation. They also demonstrated the effectiveness of periodic boundary conditions, which essentially repeated their model infinitely many times in both horizontal directions. Thus, the footing is not considered isolated in their study. The foundation itself was one large sphere-cluster composed of many constituent spheres arranged in the shape of a square footing placed at the center of the ground surface. El Shamy & Zamani (2012) showed that a structure can be modeled as rigid atop the footing by clumping spheres together or be made flexible by bonding the spheres together using the parallel bond contact model of Potyondy & Cundall (2004). Thus, the entire foundation-structure system moves freely with 6 degrees of freedom and may decouple from the soil during ground acceleration without changing the basic numerical solution scheme. Their study shows that DEM is capable of capturing effectively the dynamics of SFSI with the basic input properties for a linear elastic contact model. The main drawback to this study is its practicality. El Shamy & Zamani (2012) report that their simulations took 30 days on average with 4 computing cores, which is too long for most practical engineering applications.

Guo & Zhao (2016a)

Guo & Zhao (2014) developed a multiscale modeling approach that couples FEM and DEM. Their developed scheme applies to each gauss point of an FEM mesh a representative

volume element (RVE) containing DEM particles. A simple stress homogenization scheme is used in place of a constitutive law at each RVE. The deformations of the mesh are used as boundary displacements for the RVE, and the resultant forces based on the DEM calculation are used to update the stresses at the Gauss point. As shown in Guo & Zhao (2014), this approach effectively captures strain localization in large-strain problems, and the scheme can be extended to include disk-clusters (Zhao & Guo 2015) and extended to three dimensions (Guo & Zhao 2016b). Guo & Zhao (2016a) applied this method to different boundary-displacement problems including retaining wall translation and rotation and foundation bearing capacity. They solved the bearing capacity problem symmetrically with a half-footing width on the edge of the domain, and they analyzed the failure mechanisms by incrementally displacing the rigid-wall footing downward until a triangular failure wedge developed beneath the footing and a log-spiral shaped failure surface propagated from beneath the footing out to the ground surface. In this specific application of their study, Guo & Zhao (2016a) did not find a significant influence from the frictional properties of the footing. With their solution scheme, the authors could macroscopically analyze the failure surfaces through shear strains and changes in void ratio, and the RVEs at the Gauss points allowed the authors to view different contact force orientations in different failure zones. They also note that particle rotations effectively delineate zones of strain localization and that the direction of rotation indicates the mode of failure and sense of shear.

2.7 Additional Research Needs in Discrete Element Modeling of Surface Fault Rupture

The review of the literature on surface fault rupture highlights a plethora of advances made towards understanding this hazard, yet there are still gaps in the existing knowledge base. Scientific understanding of surface fault rupture will always benefit from additional case studies through reconnaissance activities with organizations such as GEER that extract valuable knowledge and scientific lessons from natural hazards. Physical experiments using sandbox models of surface fault rupture can always provide additional data with which to calibrate numerical models. Some of the research needs for continuum modeling of surface fault rupture are discussed in the dissertation of Oettle (2013). With an understanding that discrete element methods are valuable in supplementing the findings of physical experiments, continuum models, and reconnaissance activities, the following points discuss the progress made with respect to discrete numerical studies of surface fault rupture and highlight gaps in the literature where further research is needed:

- Early DEM studies of surface fault rupture are overwhelmingly two-dimensional, and few recent studies have performed three-dimensional analyses of this hazard (e.g., Taniyama 2011, 2017, and Schöpfer et al. 2016, 2017). While 2D studies can advance understanding of this hazard and show general trends, 3D simulations of shear deformation (e.g., Hazzard & Mair 2003, Cui & O'Sullivan 2006) show that even plane-strain shear cases produce significant out-of-plane particle movement. Thus, additional surface fault rupture research with DEM should be three-dimensional to capture more accurate particle motion.
- Of all the DEM studies of surface fault rupture discussed, none have directly captured the non-spherical nature of real sand grains, although some studies included rheological rolling resistance at the inter-particle contacts to indirectly account for non-spherical grain shape (e.g., Hazeghian & Soroush 2015, 2016, 2017, 2018, and Taniyama 2011, 2017). This rheological rolling resistance can capture more accurate peak strengths for the particle assemblage

(Iwashita & Oda 1998, 2000), but the rate of dilation produced is not significantly affected by this type of rolling resistance (e.g., Salazar et al. 2015). Furthermore, signatures of strain localization appear earlier when rolling resistance is incorporated at the inter-particle contacts instead of directly through non-spherical particle shapes (Zhou et al. 2013). This suggests a different shearing or strain softening mechanism between non-spherical particles and spherical particles with rheological rolling resistance. Non-spherical and non-elliptical particles can also interact through multiple points of contact (e.g., Yan 2009), which will alter the distribution of contact forces in a particulate assemblage. Since most DEM codes are capable of simulating some form of non-spherical particle such as with sphere-clusters, further DEM research on surface fault rupture should capture directly the non-spherical nature of real sand grains.

- The number of particles in DEM simulations of surface fault rupture has steadily increased since the early studies of Saltzer & Pollard (1992), who used approximately 900 disks. Simulations with numbers of particles on the order of 100,000 are becoming more routine, and advanced computing has facilitated simulations of over 1 million particles (Taniyama 2011, 2017). Particle sizes should be made as close as possible to the physical material of interest, since characteristics such as shear band thickness are directly related to particle size (Wood 2002). Furthermore, more refined details of shear rupture may be observed when finer particles are used (e.g., Botter et al. 2014).
- Simulation of greater numbers of particles requires more advanced computing. Most of the studies discussed, with some exceptions, used serial computing or at most performed simulations on a single computing node. A direct shear laboratory test on sands may include over 1 million particles alone, and field-scale shear rupture will involve possibly trillions of grains. Serial computation of surface fault rupture simulations would require months to complete a single simulation with over half a million particles (Hazeghian & Soroush 2015), and the simulation time is even longer for 3D simulations than for 2D simulations. High-performance computing and GPU computing are much more practical for large-scale simulations involving over 1 million particles, so parallel DEM codes such as LIGGGHTS (Kloss et al. 2012) should be used to capture finer details of surface fault rupture by simulating greater numbers of smaller particles.
- The shear rupture surface itself is of most interest in DEM simulations, and little attention is usually paid to the particle interactions and motions away from the rupture surface near the model boundaries. Thomas (1997) and Schöpfer et al. (2017) both used larger particles away from the region where rupture occurs to reduce the computational costs of their simulations. The influence of such boundary particles should be explored to verify that they do not significantly affect the simulation results around the shear zone. In addition, the use of periodic boundaries to approximate an infinitely long strike-length, as was done by Taniyama (2011, 2017), should also be explored for dip-slip fault rupture. These latter two methods can significantly reduce the number of particles in regions of lesser interest and in turn minimize the computational costs of surface fault rupture simulations.
- More DEM studies of surface fault rupture should be validated against physical experiments, as is very often done amongst continuum modelers (e.g., Anastasopoulos et al. 2007, 2008, 2009, and Lin et al. 2006). Hazeghian & Soroush (2015, 2016) validated the capability of their model to closely replicate the results of Bransby et al. (2008a,b) and showed that their rupture surfaces are consistent with those predicted via closed-form solution by Cole & Lade (1984). Other researchers captured the development of a graben structure during shallow normal fault rupture (e.g., Egholm et al. 2007) and lack thereof during steep normal fault rupture (e.g.,

Hardy 2011) as predicted by Cole & Lade (1984). Chang et al. (2013) also showed consistency between their DEM model and physical experiments but with a relatively low number of total particles, and Hardy et al. (2009) validated their basal extension simulations against physical experiments. Schöpfer et al. (2007a,b), Abe et al. (2011), and Hardy (2013) all captured the friction-dominated strength of bonded particle assemblages under high stresses and cohesion-dominated strengths of bonded particle assemblages under low stresses. Their results are consistent with findings of friction-dominated behavior of clays under high stresses observed by Roth et al. (1981). Chevalier et al. (2012) validated their 3D DEM simulations of trapdoor displacement with physical experiments. As of yet, no 3D studies of surface fault rupture have been validated against experimental results.

- Validation against continuum-based simulations as was done by Zhang et al. (2013) is also necessary to ensure that DEM results truly complement FEM and FDM results. Hazeghian & Soroush (2017) also verified their findings through comparisons with FEM studies, and the influences of soil ductility observed in their study were similarly observed through the FEM simulations of Anastasopoulos et al. (2007). Moving forward, the results of 3D models of surface fault rupture should be assessed against analogous physical experiments and continuum models for accuracy and realism before relying on their insights.
- The boundary conditions of the centrifuge experiments of Bransby et al. (2008a,b) are adequate for DEM simulations of surface fault rupture. This model setup requires no initiation or "seeding" of the rupture surface. It is essentially a blind fault underneath the particulate assemblage as modeled by Finch et al. (2003, 2004). The rigid wall boundaries of the simulation must be made frictional, though. If the underlying horizontal wall representing the hanging wall of the bedrock has a lower coefficient of friction than the overlying particulate medium, multiple rupture surfaces may initiate away from the distinct bedrock offset (e.g., Egholm et al. 2007 and Hardy et al. 2009). The hanging wall also needs to move uniformly with its associated vertical boundary to initiate rupture only from the distinct bedrock offset. Rupture initiates at velocity gradients in horizontal extension (e.g., Saltzer 1992), so the only velocity gradient should be located at the distinct offset between the basal hanging wall and footwall to avoid producing additional rupture surfaces along the length of the hanging wall.
- The macroscopic properties determined through laboratory-scale simulation help inform the processes observed in field-scale simulations of surface fault rupture. Many studies (e.g., Schöpfer et al. 2007a, and Hazeghian & Soroush 2015, 2016) calibrated or characterized their material using laboratory-scale simulations. Bransby et al. (2008a,b) used direct shear testing to determine the frictional strength and dilational characteristics of Fontainebleau sand, and Anastasopoulos et al. (2007) calibrated their constitutive model using direct shear test simulations. Given that the shear rupture process in the direct shear test has parallels to regional-scale surface fault rupture (Tchalenko 1970), this test is recommended for such a calibration or characterization using DEM.
- The literature review includes many different methods of simulating materials of different ductilities and hence shear characteristics. Saltzer & Pollard (1992) observed ductile and brittle shear responses in well-graded and poorly graded assemblages, respectively. Finch et al. (2003, 2004) used different inter-particle bond strengths to simulate fault rupture through materials of different shear strengths and showed that the inter-particle bond strength affects the amount of fault displacement that produces ground surface outcropping. The differentiation of inter-particle bond strengths in alternating horizontal layers allowed Cardozo et al. (2005), Hardy & Finch (2005, 2006, 2007), and Schöpfer et al. (2007a,b) to study fault rupture through

inhomogeneous, layered media. None of these aforementioned studies utilize the capability of DEM to directly capture the effect of void ratio on ductility. The peak strength and dilation of a granular material are directly related to void ratio, or relative density, which is conceptually equivalent in both real sands and DEM assemblages. Further research in DEM should take advantage of the real void space between DEM particles to study the effects of void ratio on surface fault rupture propagation. This is one of the principal advantages of discrete methods over continuum methods.

- Only free-field cases of surface fault rupture have been analyzed in-depth using DEM. The fault rupture-soil-foundation interaction (FR-SFI) studied by Bransby et al. (2008a,b) and simulated by Anastasopoulos et al. (2008a, 2009, 2010) has not been studied extensively using DEM.

Fig. 2.1. Surface fault rupture trace showing left-stepping en echelon fractures from the 2014 South Napa, California, earthquake. Image courtesy of NSF-Sponsored GEER Report #GEER-037 (Bray et al. 2014).

Fig. 2.2. Example of a surface fault rupture trace in asphalt resulting from the 2014 South Napa, California, earthquake. The center lane divider indicates right-lateral offset. Image courtesy of NSF-Sponsored GEER Report #GEER-037 (Bray et al. 2014).

Fig. 2.3. Example of a sidewalk buckling in response to compressional ground movement during the 2014 South Napa, California, earthquake. Image courtesy of NSF-Sponsored GEER Report #GEER-037 (Bray et al. 2014).

Fig. 2.4. View of a strand of the Futagawa Fault crossing through the Oh-Kirihata Dam after the 2016 Kumamoto, Japan, earthquake. Image courtesy of NSF-Sponsored GEER Report #GEER-048 (Kayen et al. 2016).

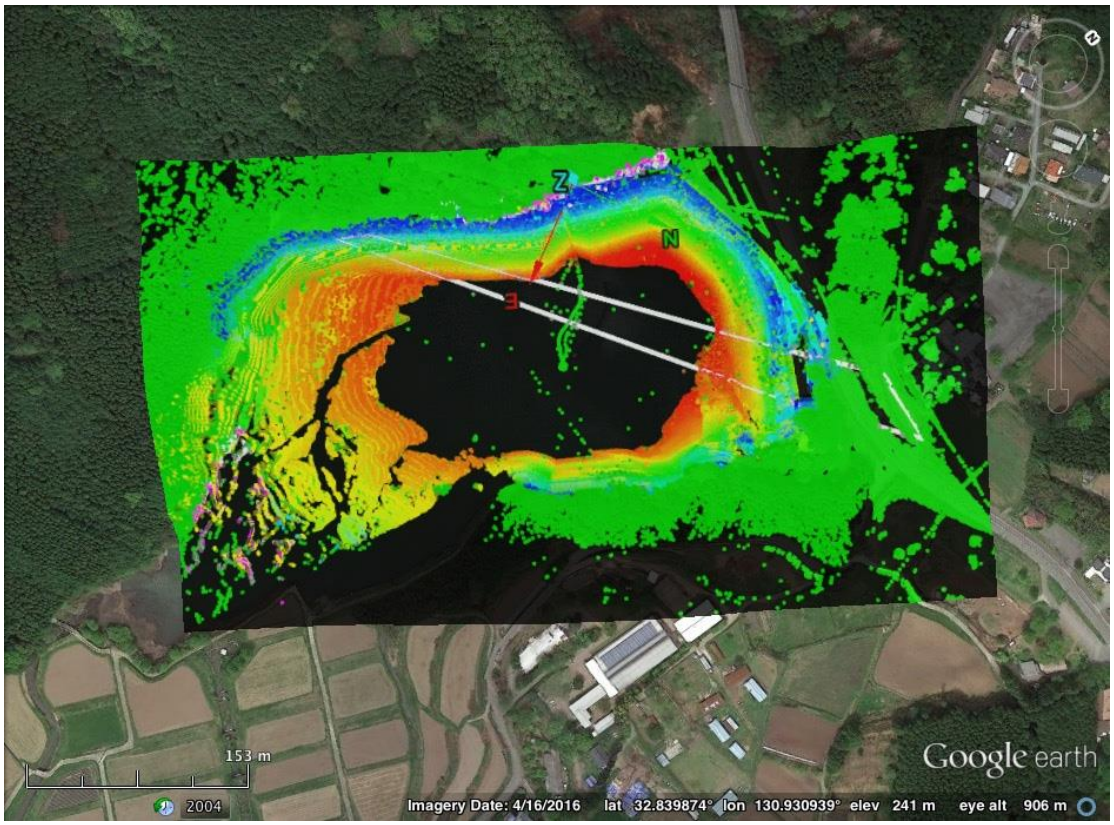

Fig. 2.5. LIDAR scan of surface fault rupture through the Oh-Kirihata Dam. The width of the rupture zone is indicated by the white polygon. Image courtesy of NSF-Sponsored GEER Report #GEER-048 (Kayen et al. 2016).

Fig. 2.6. Soil intrusion into the spillway due to fault movement that opened up a gap in a retaining wall of the Oh-Kirihata Dam. Image courtesy of NSF-Sponsored GEER Report #GEER-048 (Kayen et al. 2016).

Fig. 2.7. Along-strike view of the Aso Caldera Depression Zone traversing a rice field following the 2016 Kumamoto, Japan, earthquake. Image courtesy of NSF-Sponsored GEER Report #GEER-048 (Kayen et al. 2016).

(a)

(b)

Fig. 2.8. Buildings located in close proximity to a normal fault trace on the footwall side of the trace. These buildings exhibited negligible damage from surface fault rupture during the (a) 2016 Kumamoto, Japan, earthquake (Kayen et al. 2016) and (b) the 1999 Kocaeli, Turkey, earthquake (from Lettis et al. 2000 and Bray 2001, reproduced with permission of the Earthquake Engineering Research Institute). Image in (a) courtesy of NSF-Sponsored GEER Report #GEER-048.

Fig. 2.9. Bridge located across the Aso Caldera Depression Zone that underwent negligible settlement in comparison to the surrounding soil. Image courtesy of NSF-Sponsored GEER Report #GEER-048 (Kayen et al. 2016).

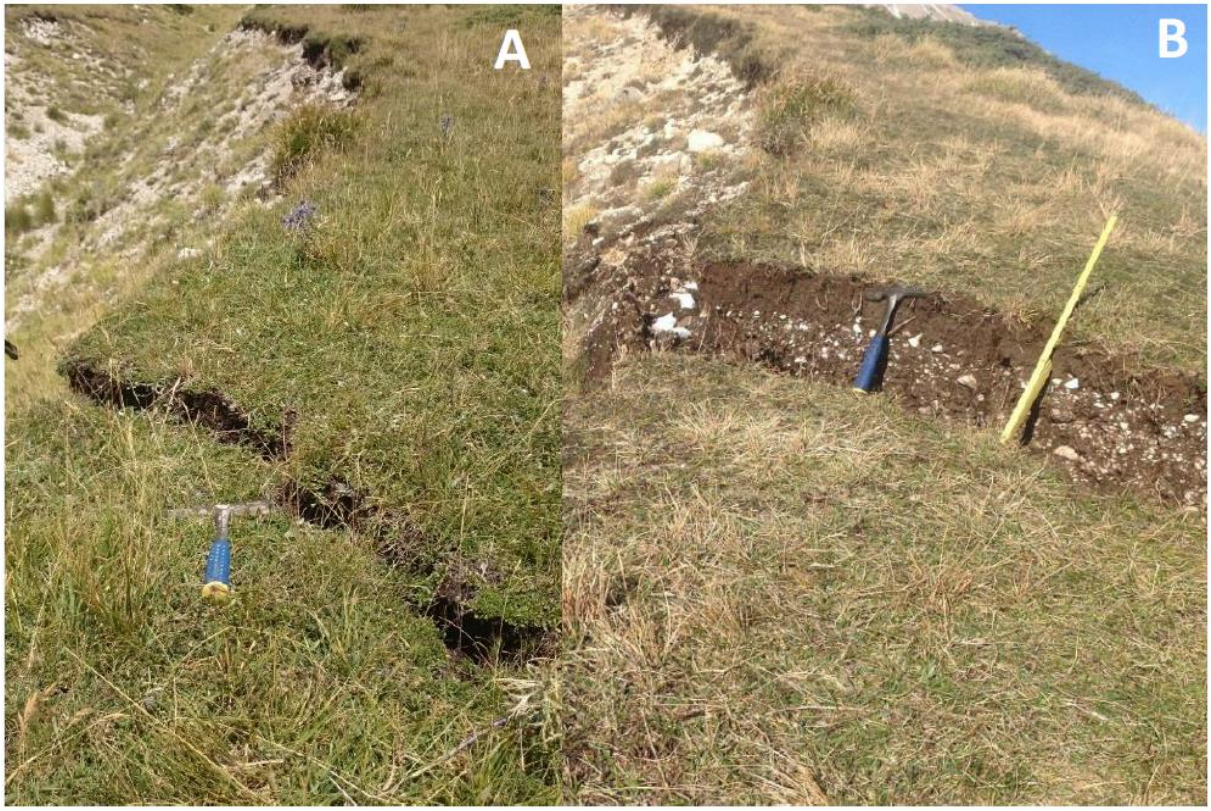

Fig. 2.10. Comparison of ground surface displacements due to surface fault rupture at the same location of the Mt. Vettore Fault. (a) 10 cm vertical displacement from the August 24, 2016, Central Italy earthquake and (b) 30 cm vertical displacement from the October 30, 2016, Central Italy earthquake. Image courtesy of NSF-Sponsored GEER Report #GEER-050d (Zimmaro & Stewart 2017b).

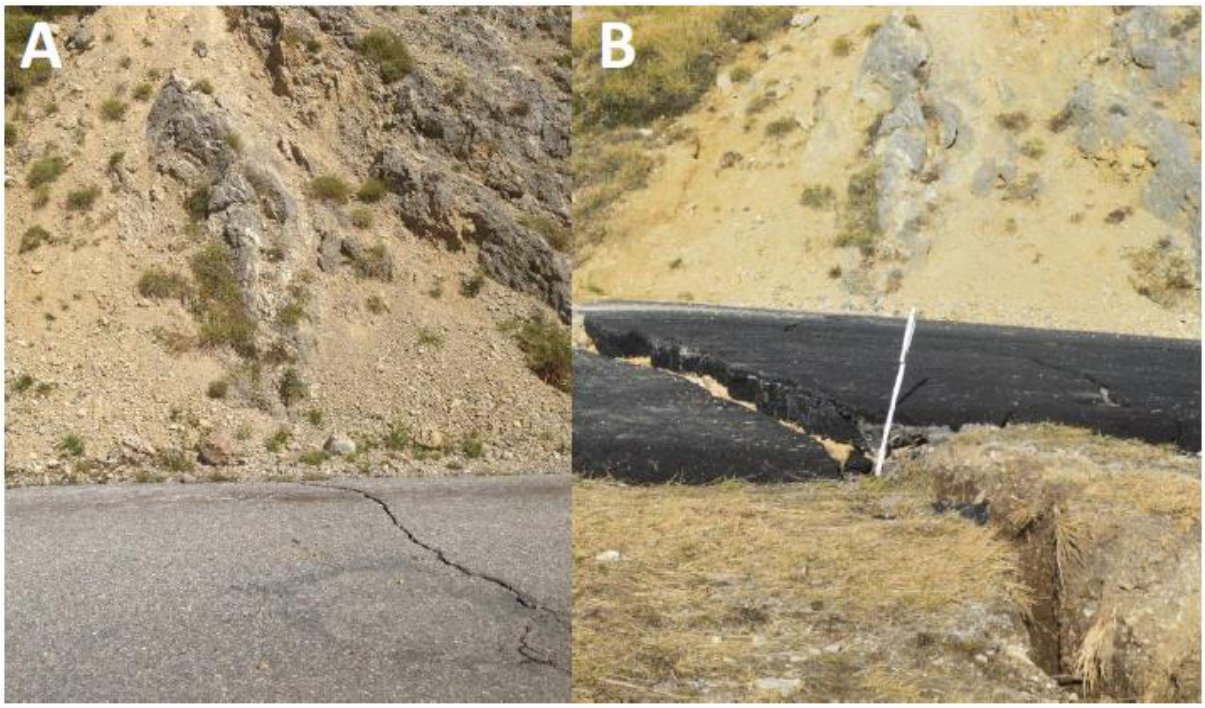

Fig. 2.11. Re-ruptured segment of the Mt. Vettore fault showing (a) 2 cm of vertical offset after the August 24, 2016, Central Italy earthquake and (b) 18-20 cm of vertical offset after the October 30, 2016, Central Italy earthquake. Image courtesy of NSF-Sponsored GEER Report #GEER-050d (Zimmaro & Stewart 2017b).

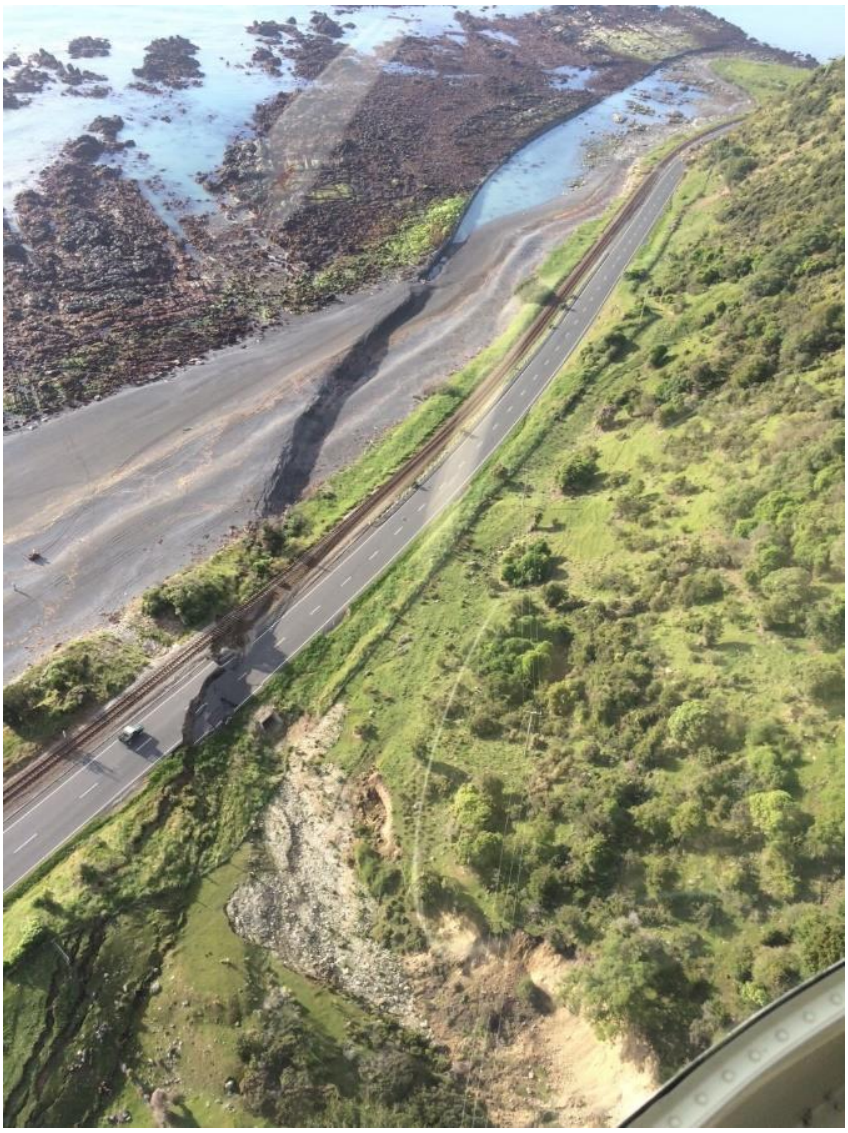

Fig. 2.12. Fault rupture through State Highway 1 in Kaikoura, New Zealand after the 2016 Kaikoura, New Zealand, earthquake (from Stirling et al. 2017, reproduced with permission of the New Zealand Society for Earthquake Engineering Inc.). The exposed seabed is seen at the top of the figure.

Fig. 2.13. Single-story home next to the Kaikoura coast damaged by reverse fault surface rupture from the 2016 Kaikoura, New Zealand, earthquake (from Stirling et al. 2017, reproduced with permission of the New Zealand Society for Earthquake Engineering Inc.; photo by Tim Little).

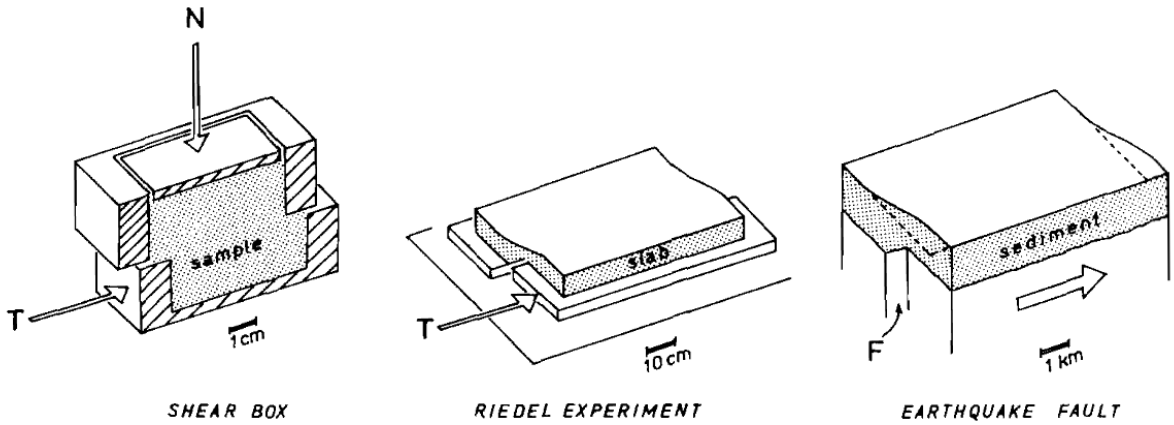

Fig. 2.14. Modes of deformation at different scales with similar boundary conditions. Republished with permission of Geological Society of America, from Tchalenko (1970); permission conveyed through Copyright Clearance Center, Inc.

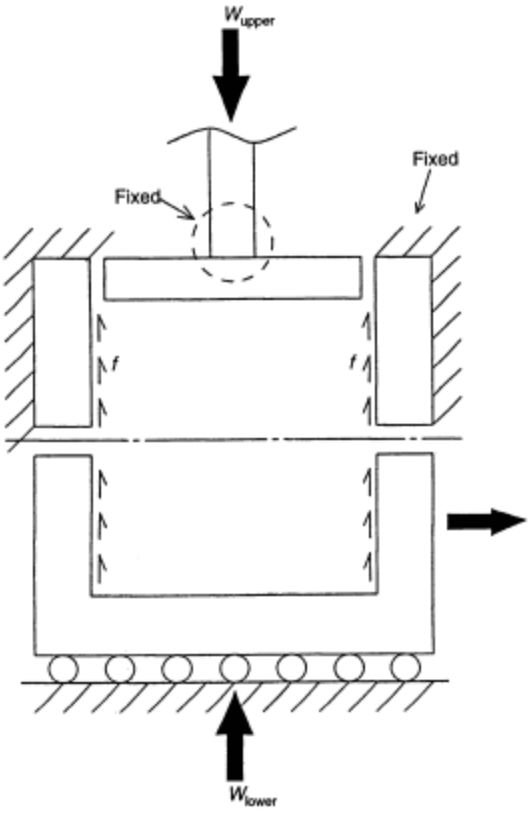

(a)

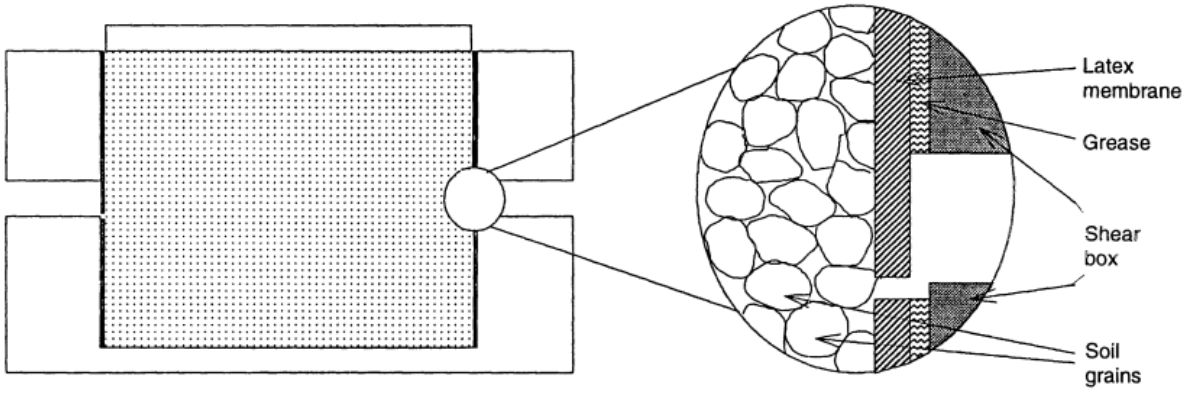

(b)

Fig. 2.15. (a) Shear box and loading platen kinematic conditions for quasi-simple shear interpretation of the direct shear test. (b) Scheme for minimizing friction on lateral walls of the direct shear box. Republished with permission of ICE Publishing, from Shibuya et al. (1997); permission conveyed through Copyright Clearance Center, Inc.

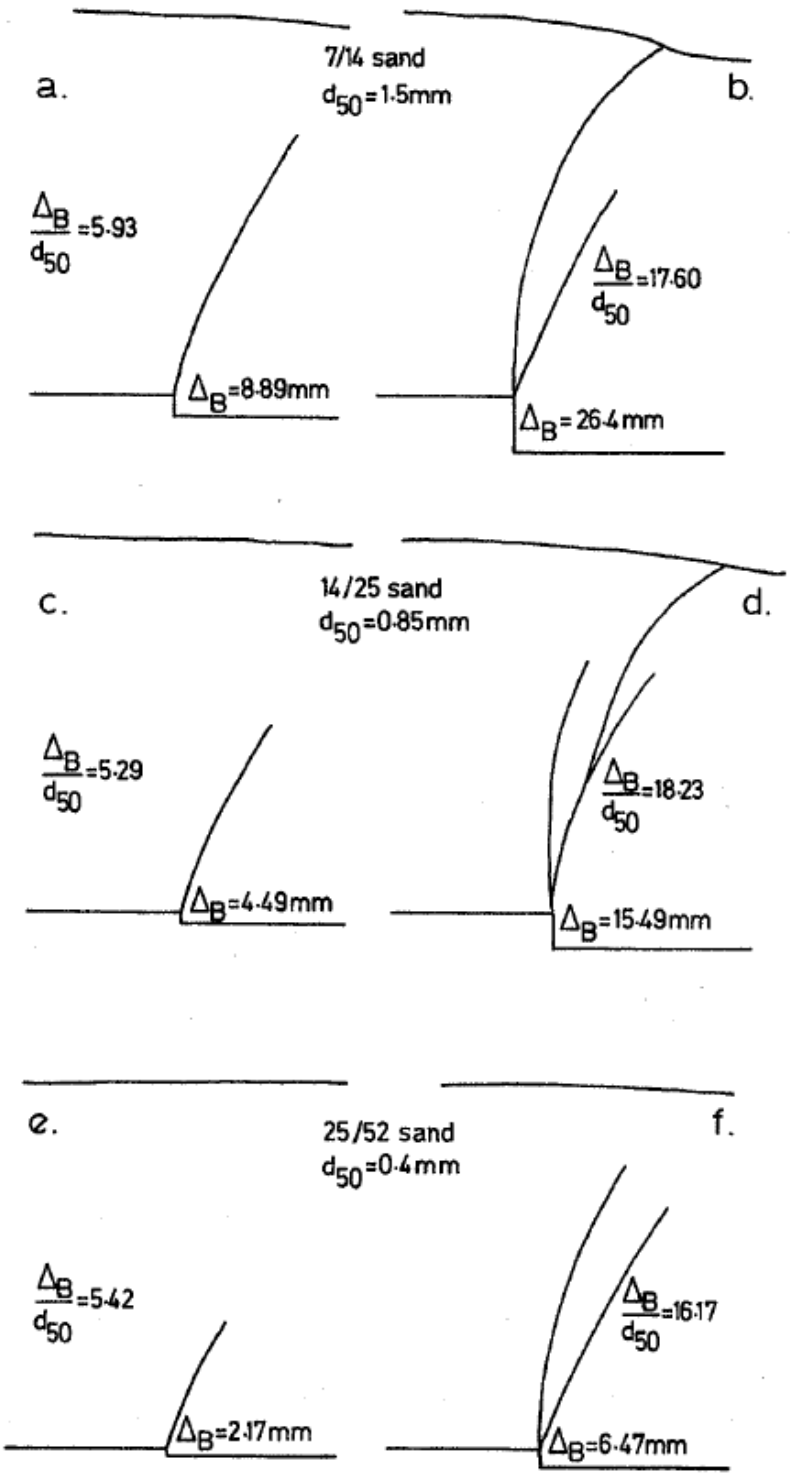

Fig. 2.16. Patterns of shear rupture development in Leighton Buzzard sands with different grain size distributions at similar stages of single-gravity trapdoor displacement normalized by the median grain diameter (from Stone & Wood 1992).

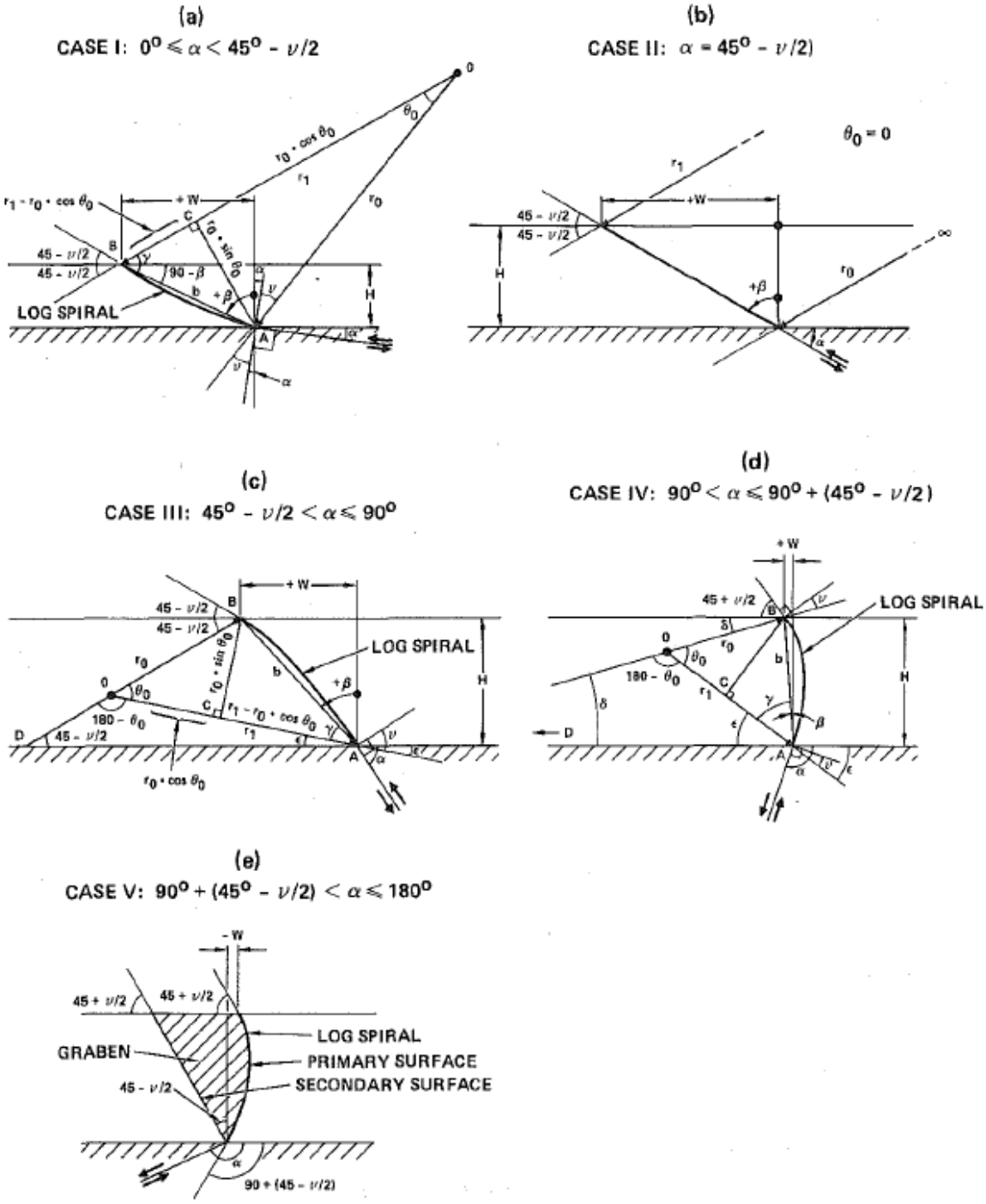

Fig. 2.17. Different cases for the closed-form solution for the shape and location of the fault rupture surface developed and shown by Cole & Lade (1984, reprinted with permission from ASCE).

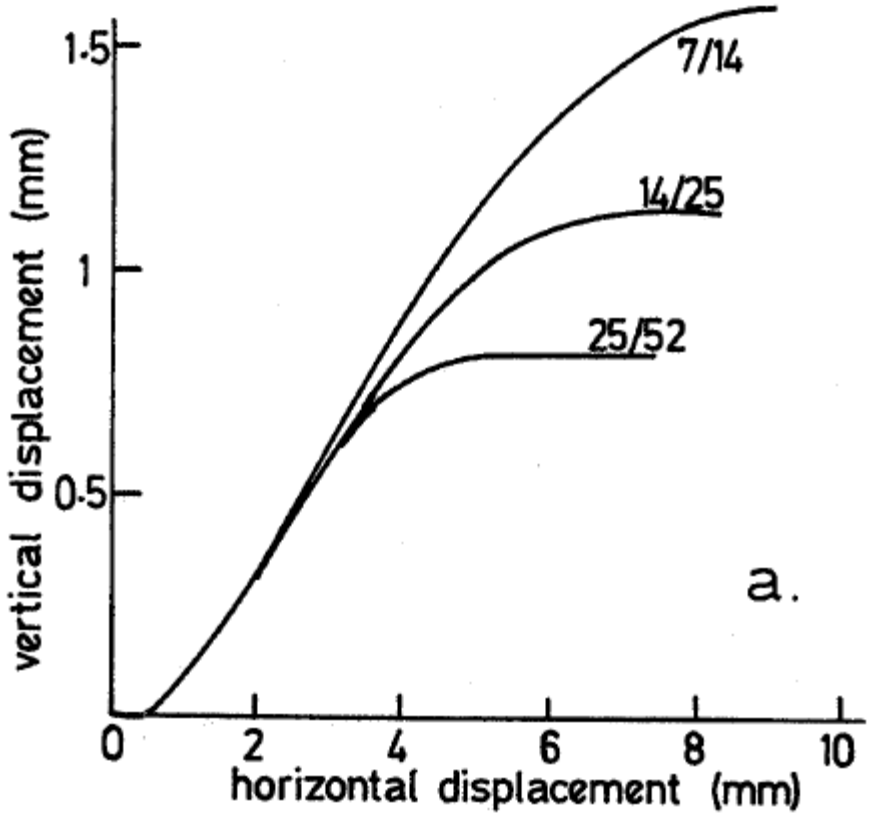

Fig. 2.18. Vertical displacement direct shear test results on three different samples of Leighton Buzzard sand under a normal stress of 325.3 kPa with median grain sizes of 0.4 mm, 0.8 mm, and 1.5 mm (from Stone & Wood 1992).

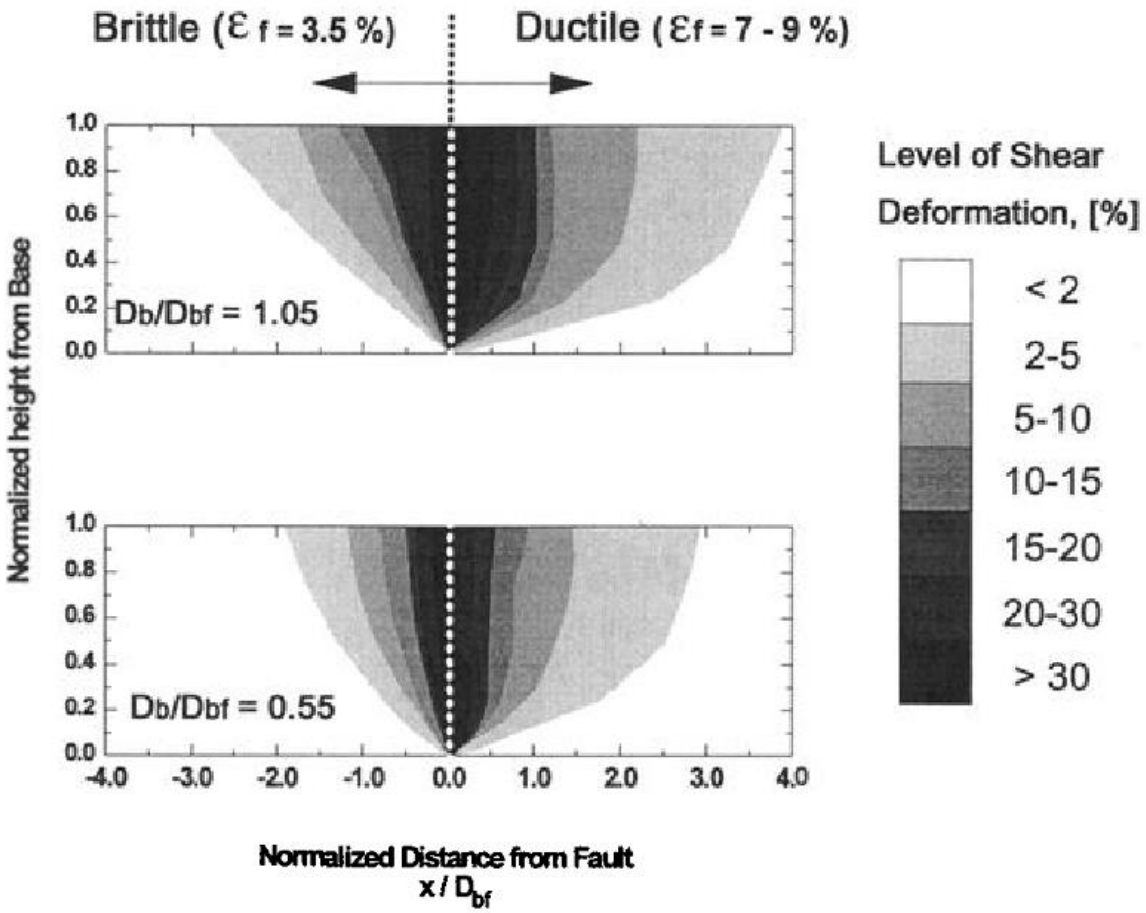

Fig. 2.19. The effect of soil ductility on the width of the shear zone in strike-slip fault rupture. Reproduced, with permission from Lazarte & Bray (1996), copyright ASTM International, 100 Barr Harbor Drive, West Conshohocken, PA 19428.

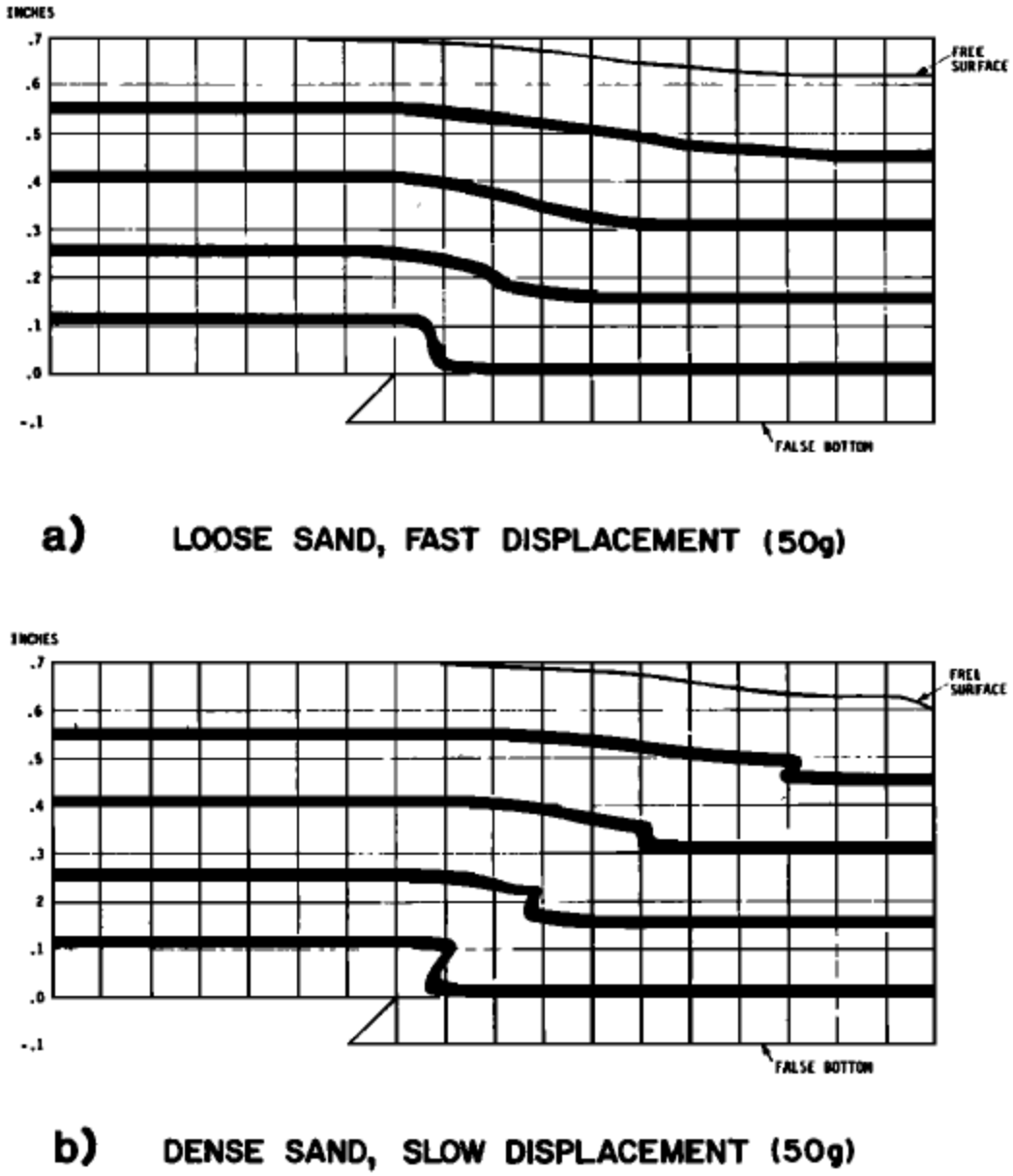

Fig. 2.20. Effect of rate of rupture on the characteristics of the rupture surface in centrifuge experiments of reverse fault rupture (reprinted from Roth et al. 1981, copyright 1981 by the American Geophysical Union, published by John Wiley and Sons).

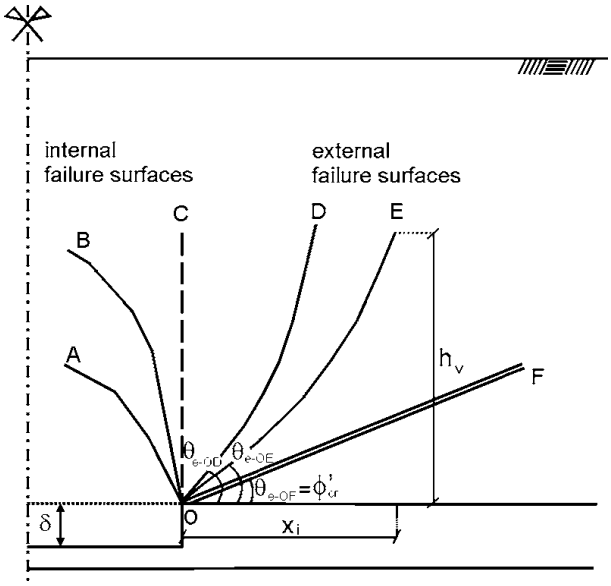

Fig. 2.21. Internal and external failure surfaces described and shown in Costa et al. (2009, reprinted with permission from ASCE).

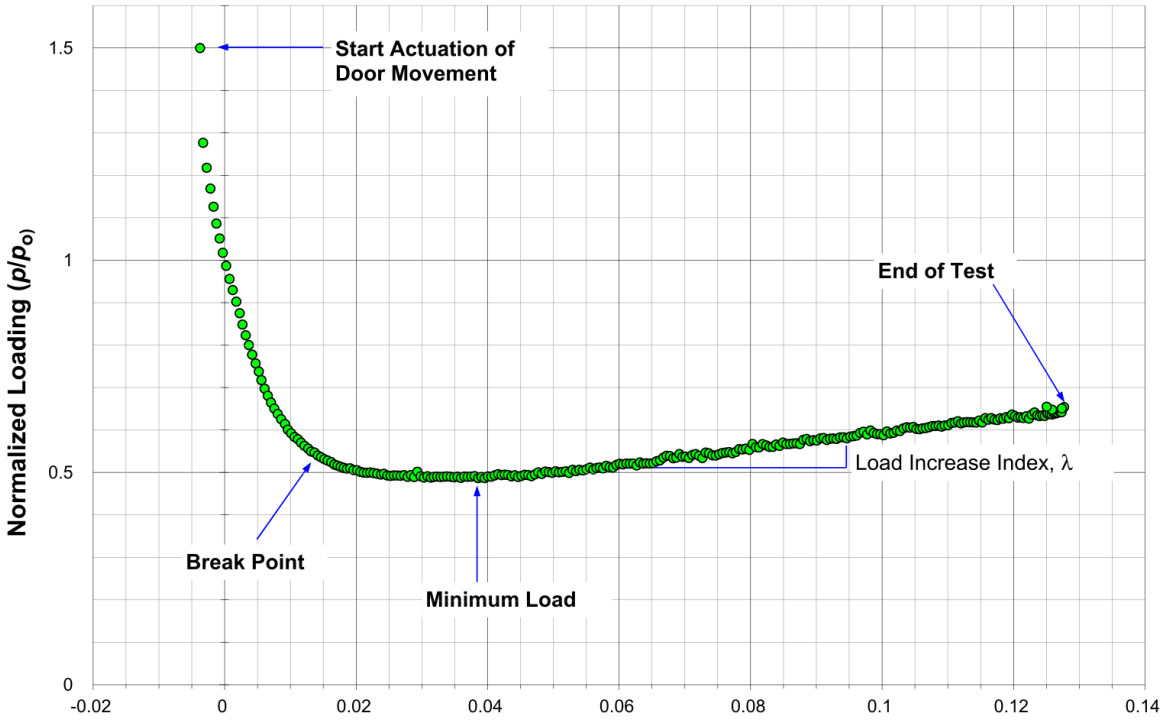

Fig. 2.22. Development of trapdoor load with increasing trapdoor displacement (from Iglesia et al. 2013, with permission from ASCE).

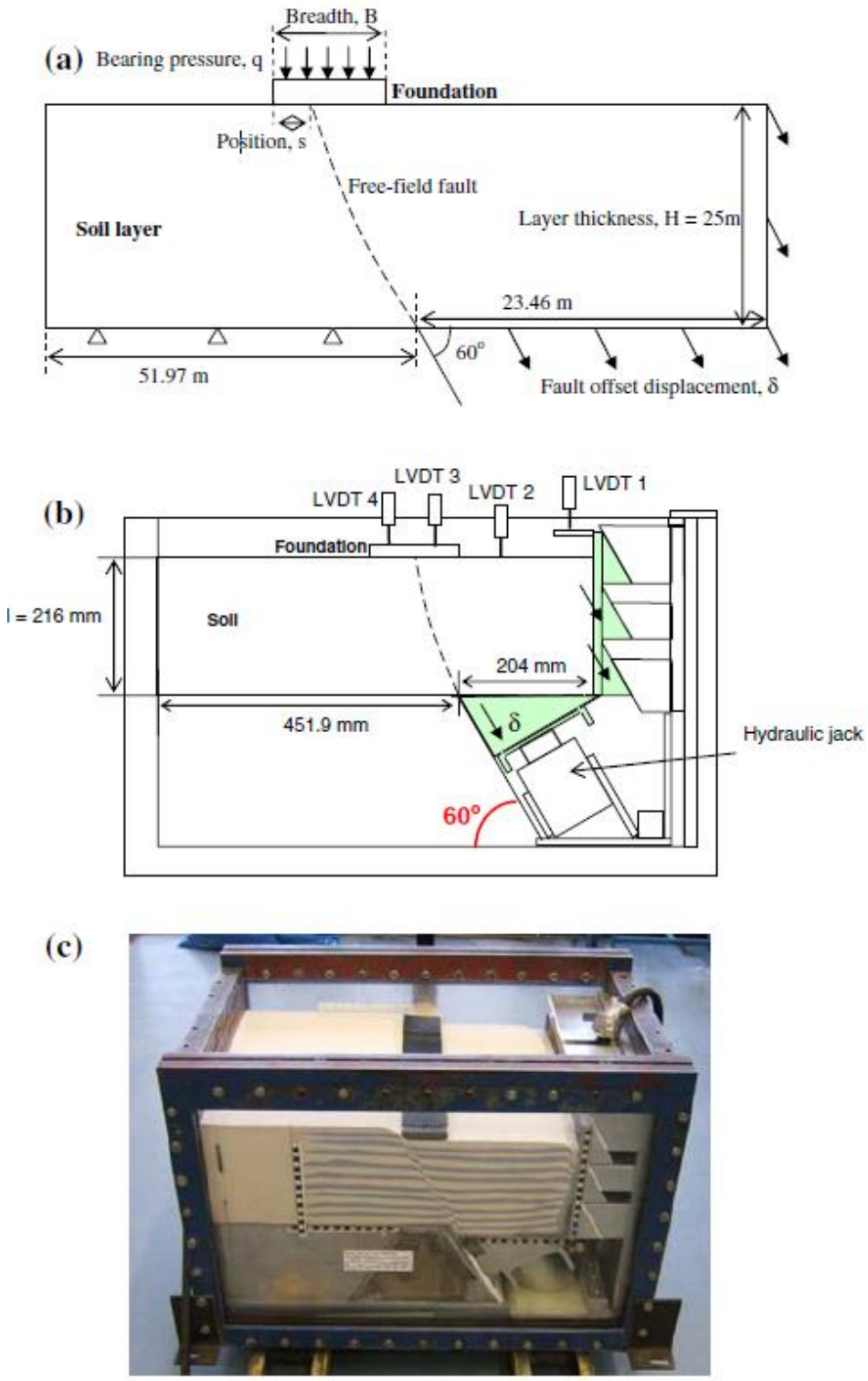

Fig. 2.23. Experimental layout for QUAKER centrifuge experiments of normal fault rupture at (a) prototype-scale and (b) model scale. (c) Photo showing the sandbox used in the centrifuge experiments. Reprinted by permission from Springer Nature Customer Service Centre GmbH: Springer Nature, Bulletin of Earthquake Engineering, Bransby et al. (2008a).

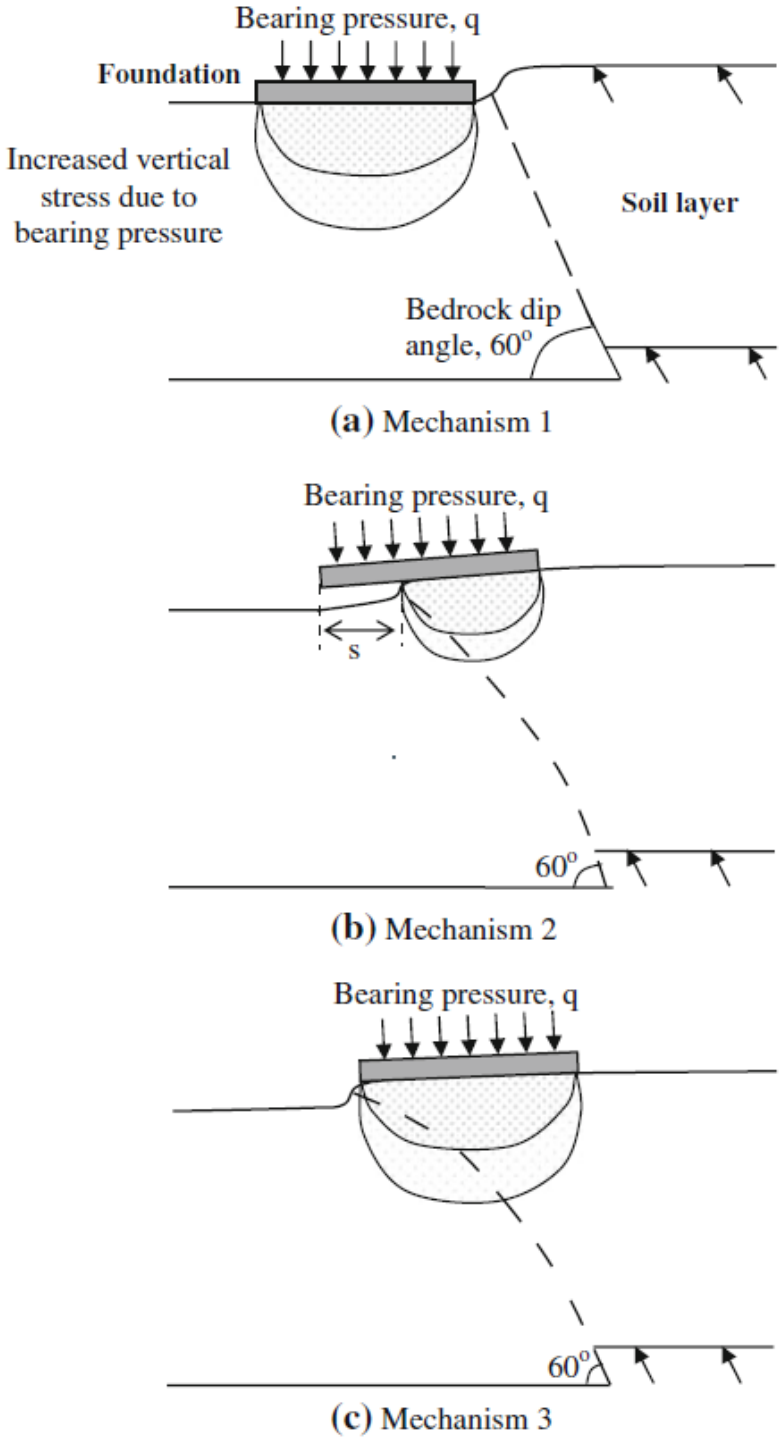

Fig. 2.24. Mechanisms of fault-foundation interaction for reverse fault rupture. Reprinted by permission from Springer Nature Customer Service Centre GmbH: Springer Nature, Bulletin of Earthquake Engineering, Bransby et al. (2008b).

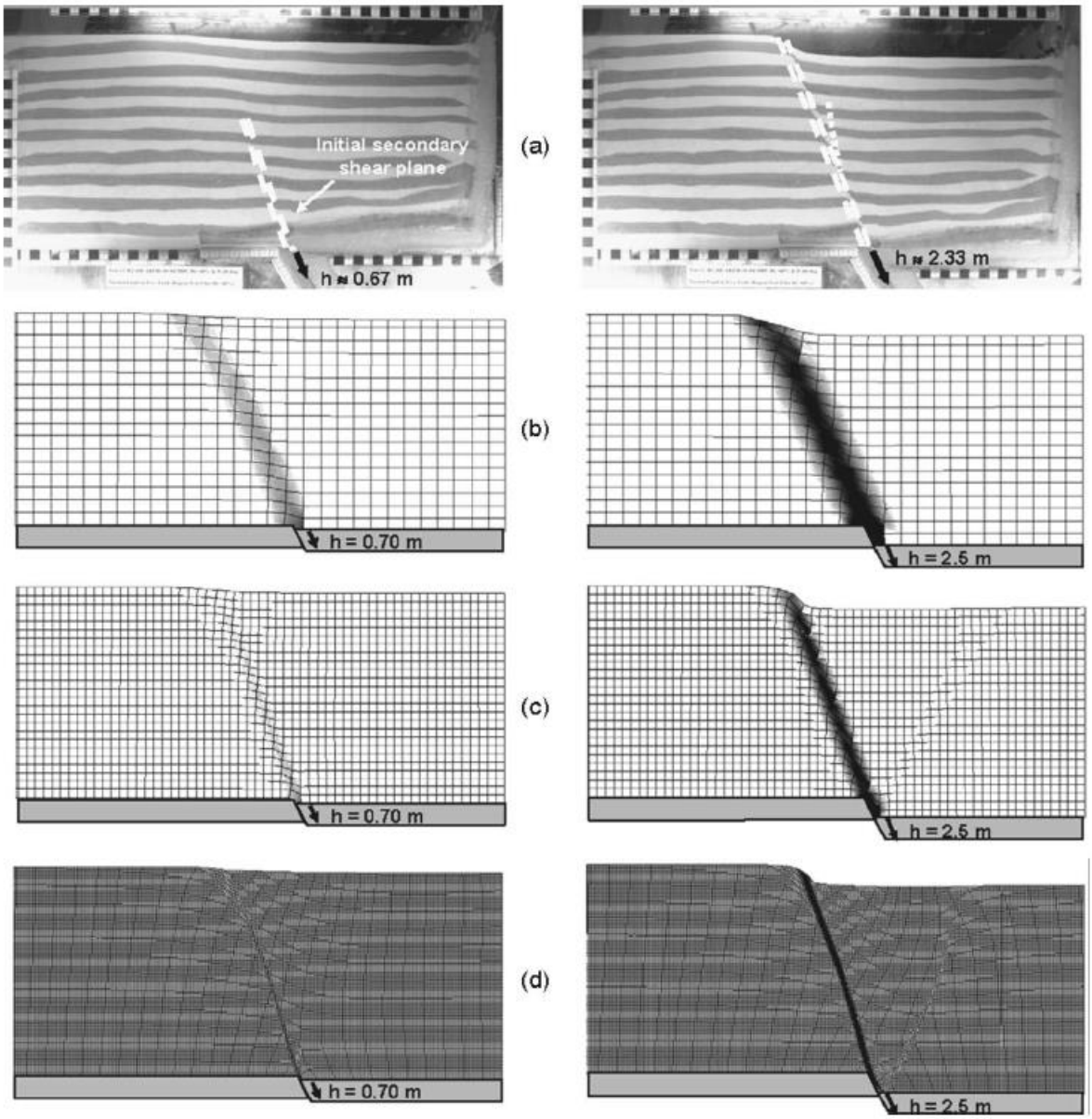

Fig. 2.25. Effect of mesh size on shear band width as shown in Anastasopoulos et al. (2007, reprinted with permission from ASCE). (a) Photographs of centrifuge experiments. (b) Mesh size of 2 m. (c) Mesh size of 1 m. (d) Mesh size of 0.25 m.

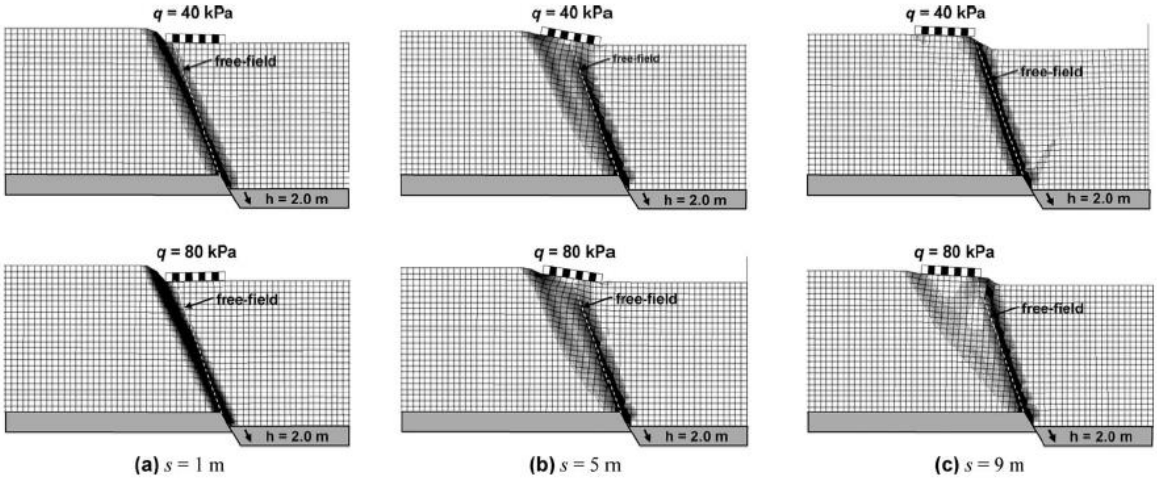

Fig. 2.26. Parametric analysis showing the influences of foundation contact pressure (*q*) and foundation position on fault rupture propagation (from Anastasopoulos et al. 2009, with permission from ASCE). The parameter *s* is the distance from the free-field outcrop location to the footwall edge of the foundation.

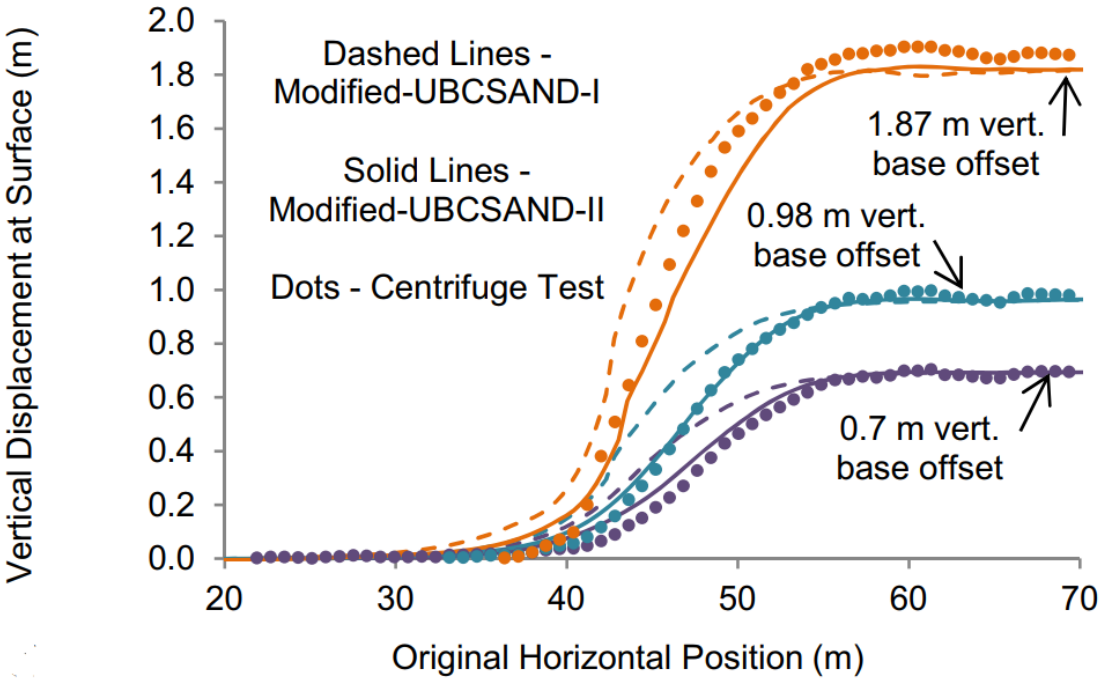

(a)

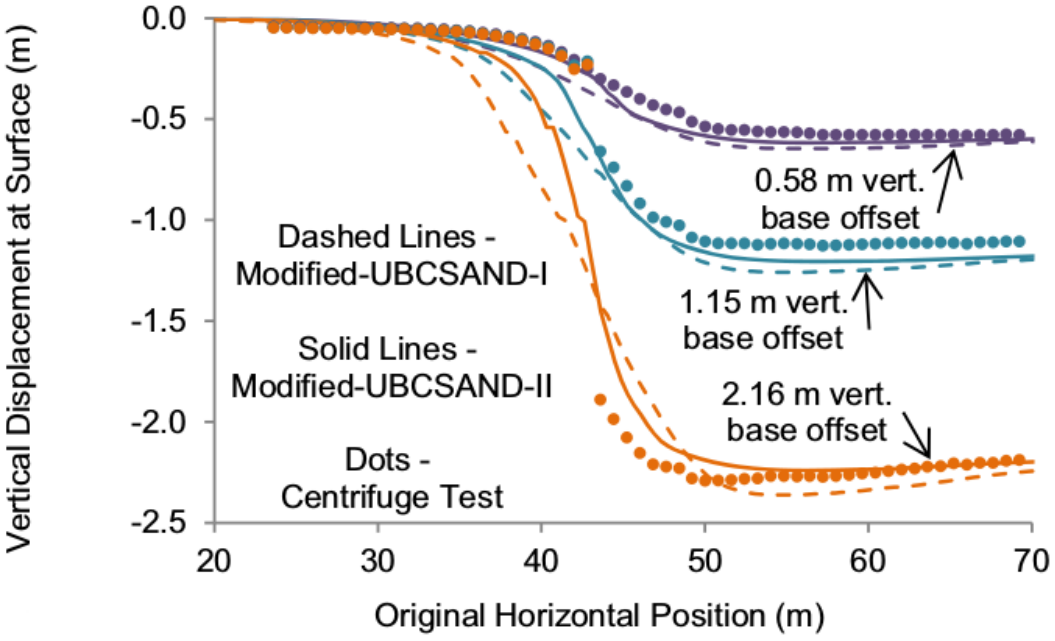

(b)

Fig. 2.27. Comparison of (a) 60°-dip normal fault rupture and (b) 60°-dip reverse fault rupture simulations using the Modified-UBCSAND-I and Modified-UBCSAND-II models with free-field centrifuge test results from Bransby et al. (2008). Figures from Oettle & Bray (2016, with permission from ASCE).

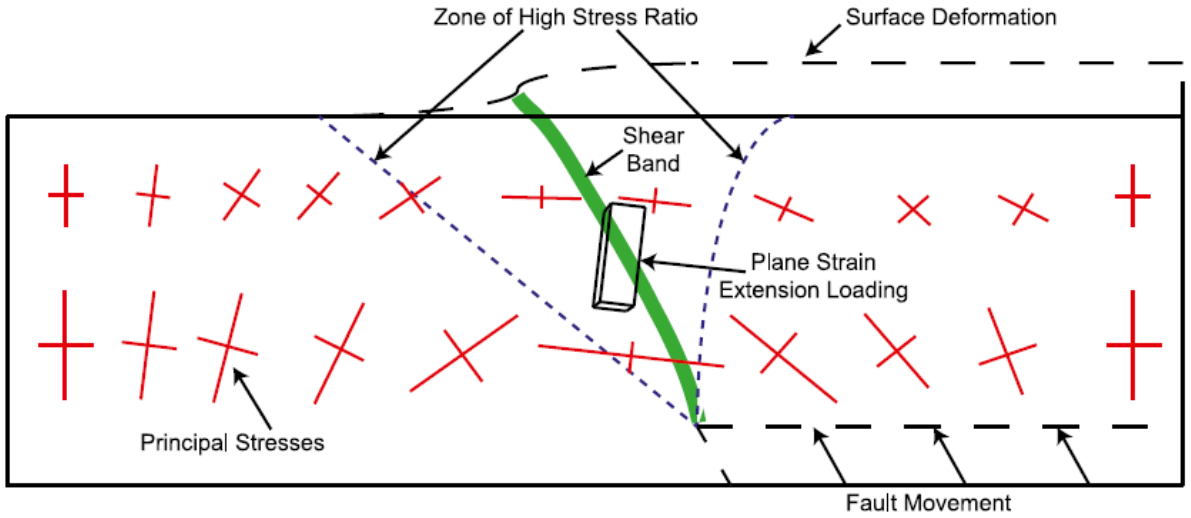

(a)

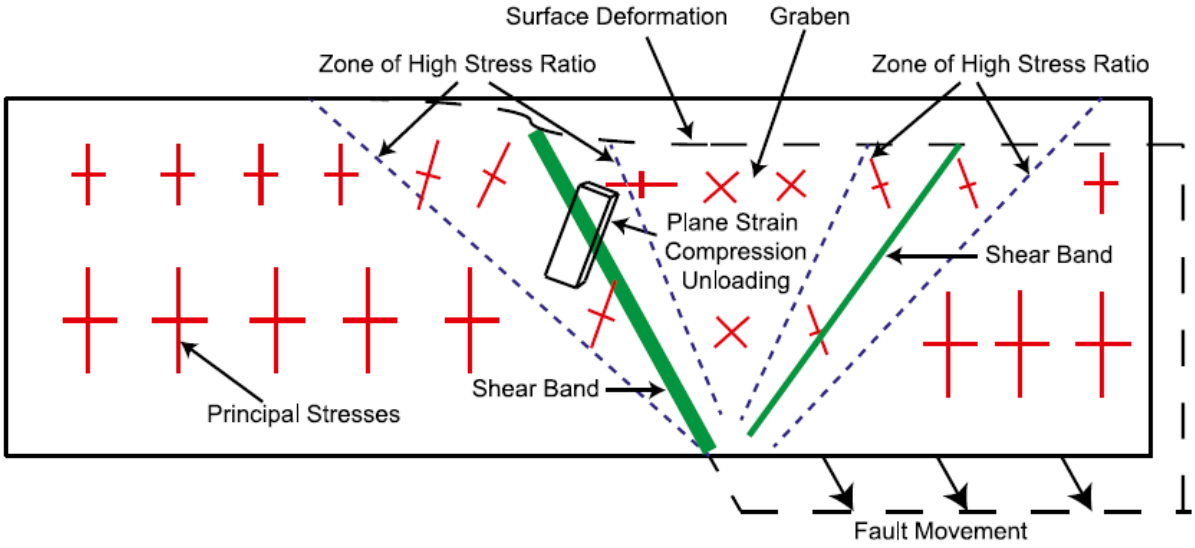

(b)

Fig. 2.28. Distributions of principal stress orientations showing loading conditions in (a) reverse fault rupture and (b) normal fault rupture. Figures from Oettle & Bray (2013a, with permission from ASCE).

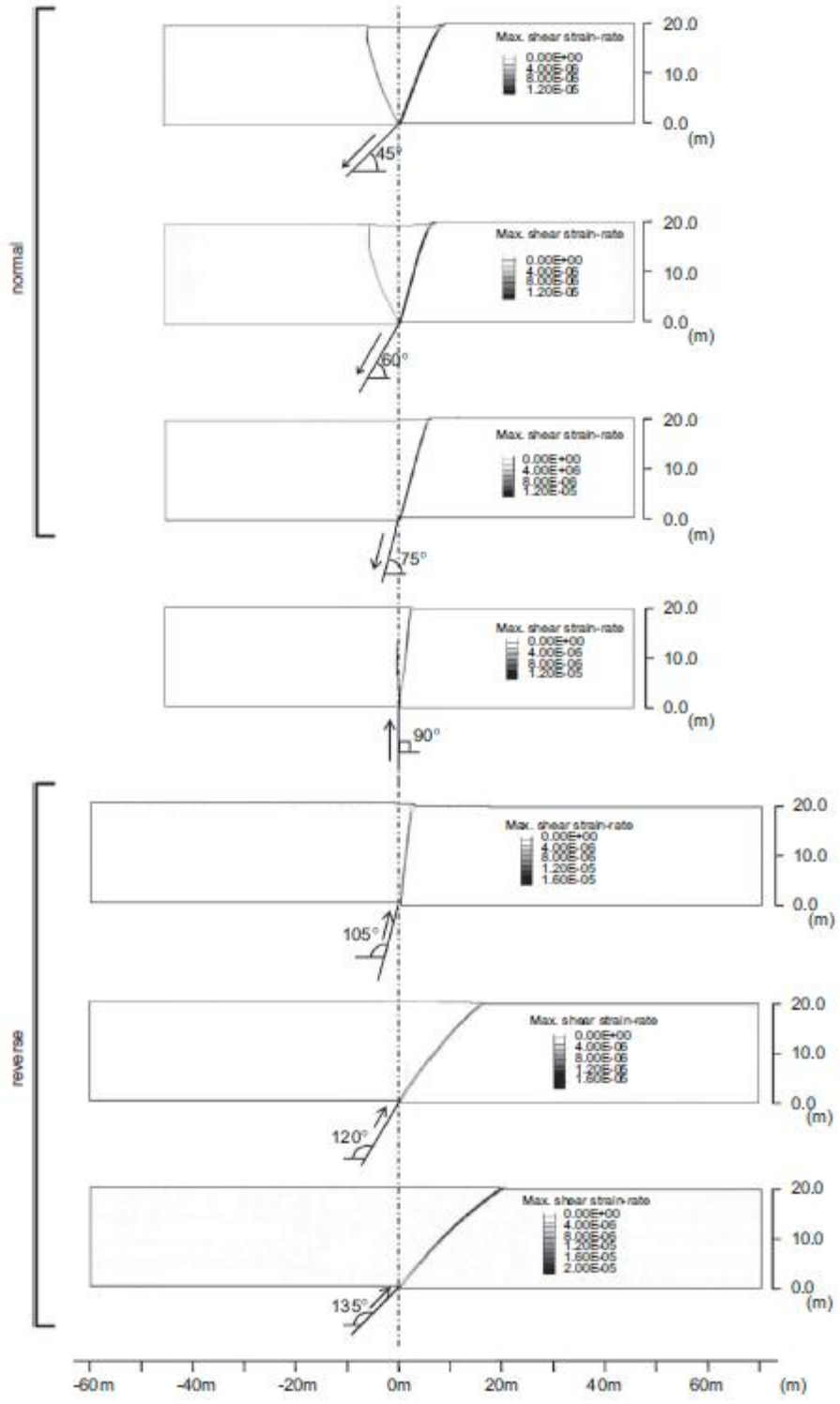

Fig. 2.29. Surface fault rupture results through dense sand as shown in Loukidis et al. (2009). Republished with permission of Elsevier Science and Technology Journals, from Loukidis et al. (2009); permission conveyed through Copyright Clearance Center, Inc.

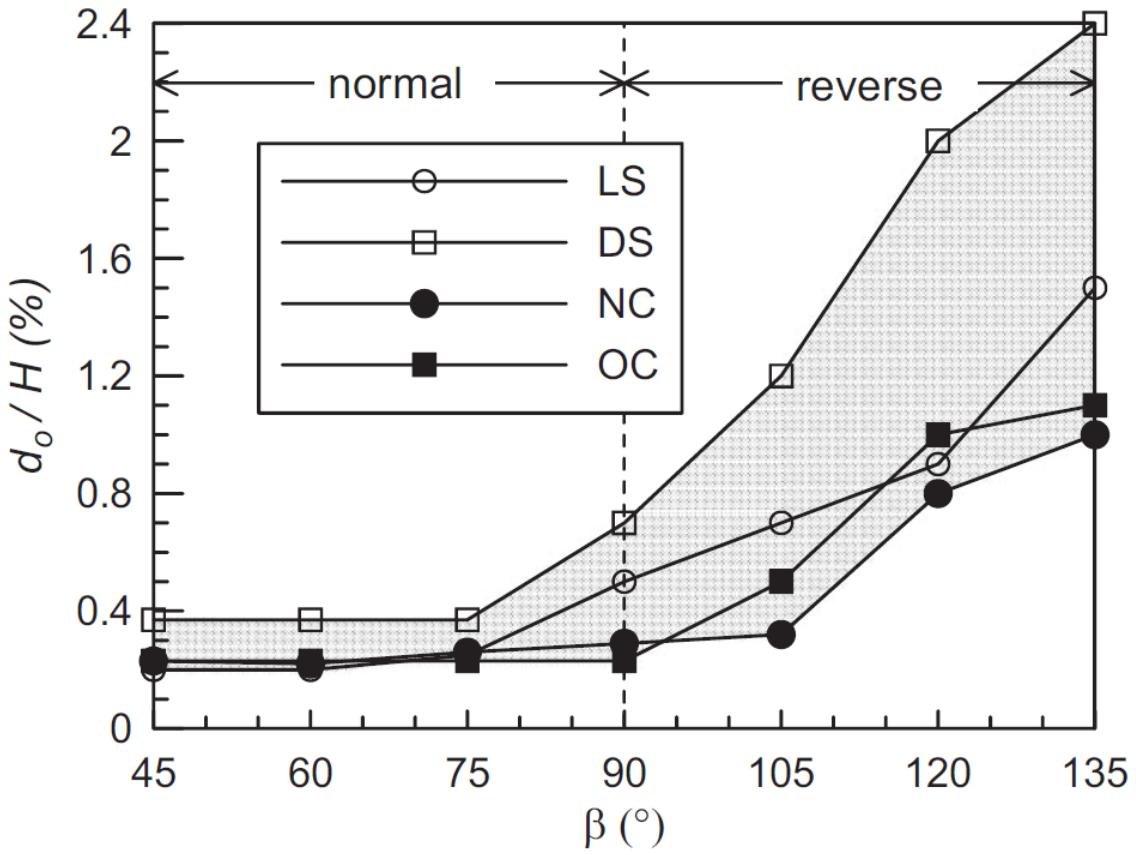

Fig. 2.30. Relation between fault dip angle (β) and the amount of vertical bedrock displacement required for the fault rupture surface to outcrop at the ground surface (d_0) as shown in Loukidis et al. (2009). Data are shown for loose sand (LS), dense sand (DS), normally consolidated clay (NC), and overconsolidated clay (OC). Republished with permission of Elsevier Science and Technology Journals, from Loukidis et al. (2009); permission conveyed through Copyright Clearance Center, Inc.

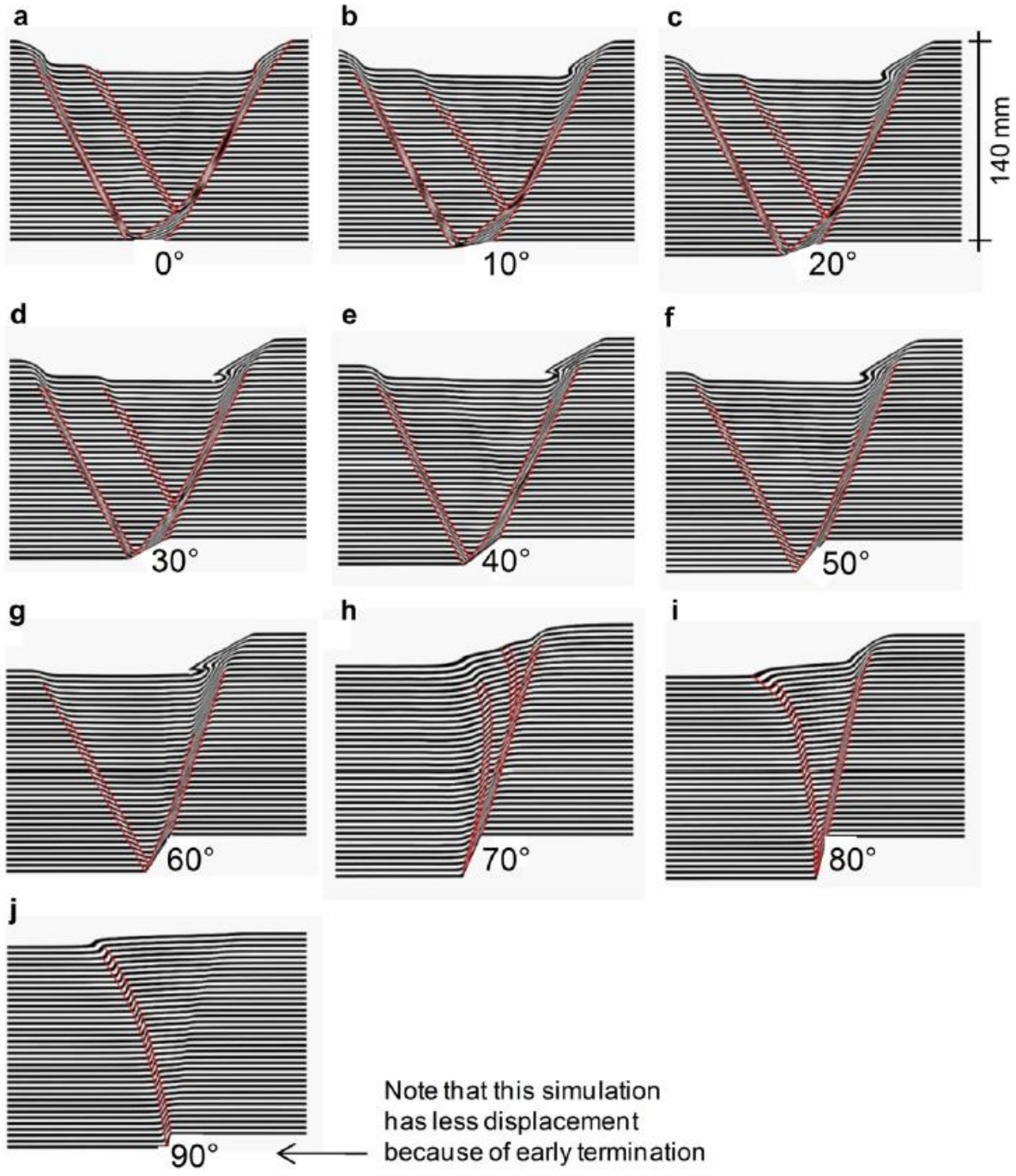

Fig. 2.31. Fault rupture surfaces in uniformly dense soil during normal fault rupture with dip angles between 0° and 90°. Republished with permission of Elsevier Science and Technology Journals, from Nollet et al. (2012); permission conveyed through Copyright Clearance Center, Inc.

(a)

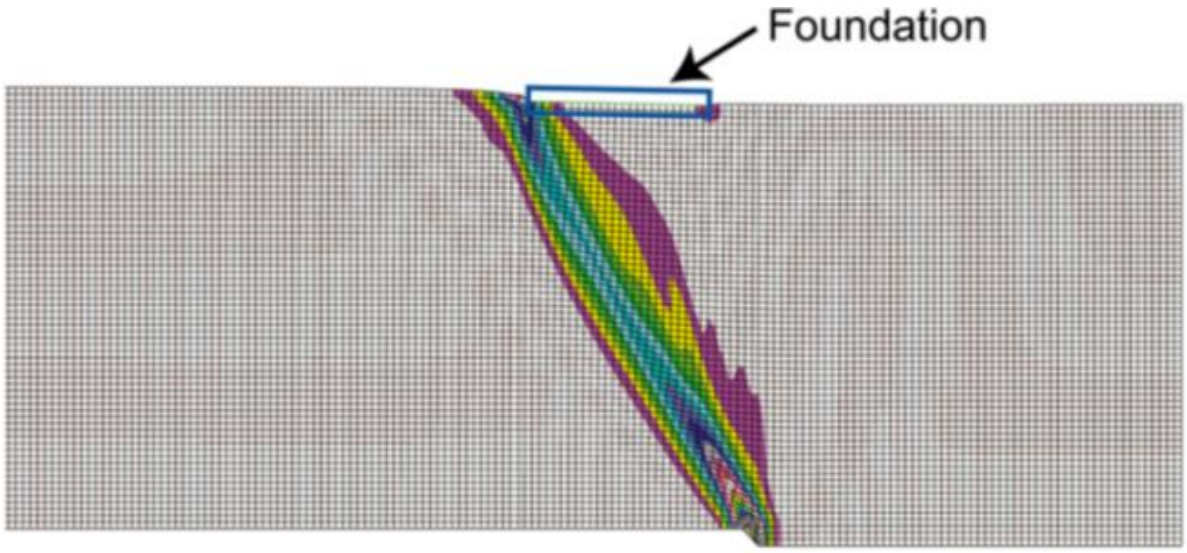

(b)

Fig. 2.32. (a) Results of centrifuge test 12 of Bransby et al. (2008a). Reprinted by permission from Springer Nature Customer Service Centre GmbH: Springer Nature, Bulletin of Earthquake Engineering, Bransby et al. (2008a). (b) Finite difference model of Oettle & Bray (2013b, reprinted with permission from ASCE) calibrated to match results of centrifuge test 12.

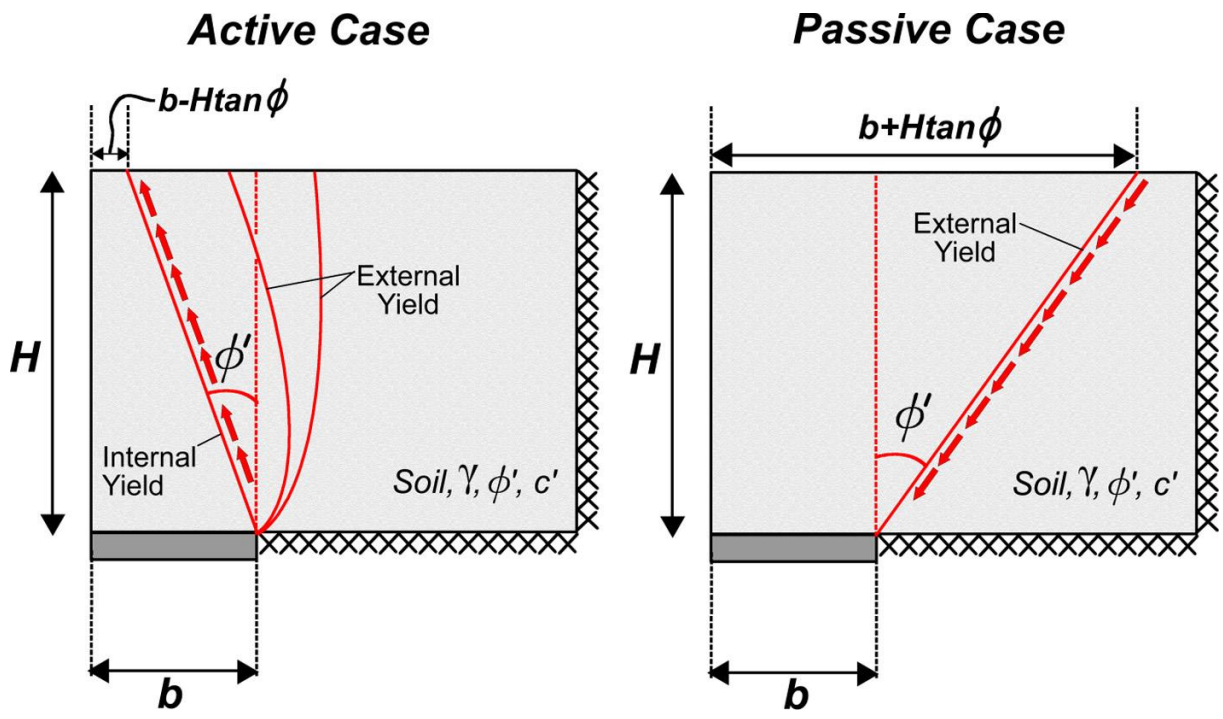

Fig. 2.33. Typical failure surface shapes in active and passive trapdoor displacement, as described and shown in Wang et al. (2017). Republished with permission of Elsevier Science and Technology Journals, from Wang et al. (2017); permission conveyed through Copyright Clearance Center, Inc.

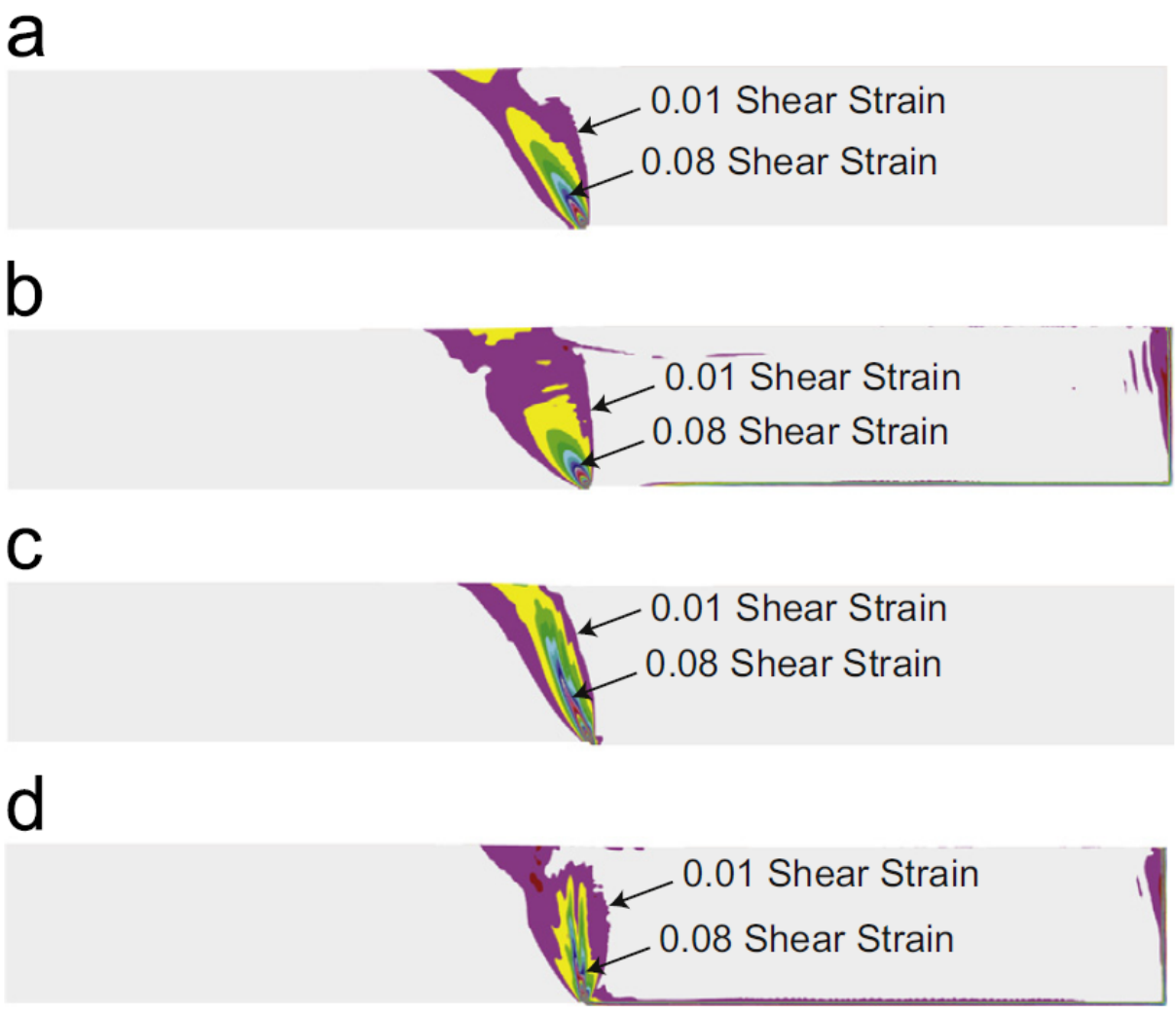

Fig. 2.34. Effects of dynamic rates of bedrock displacement in surface fault rupture simulations performed with the finite difference method. (a) Quasi-static reverse fault rupture. (b) Dynamic reverse fault rupture. (c) Quasi-static normal fault rupture. (d) Dynamic normal fault rupture. Republished with permission of Elsevier Science and Technology Journals, from Oettle et al. (2015); permission conveyed through Copyright Clearance Center, Inc.

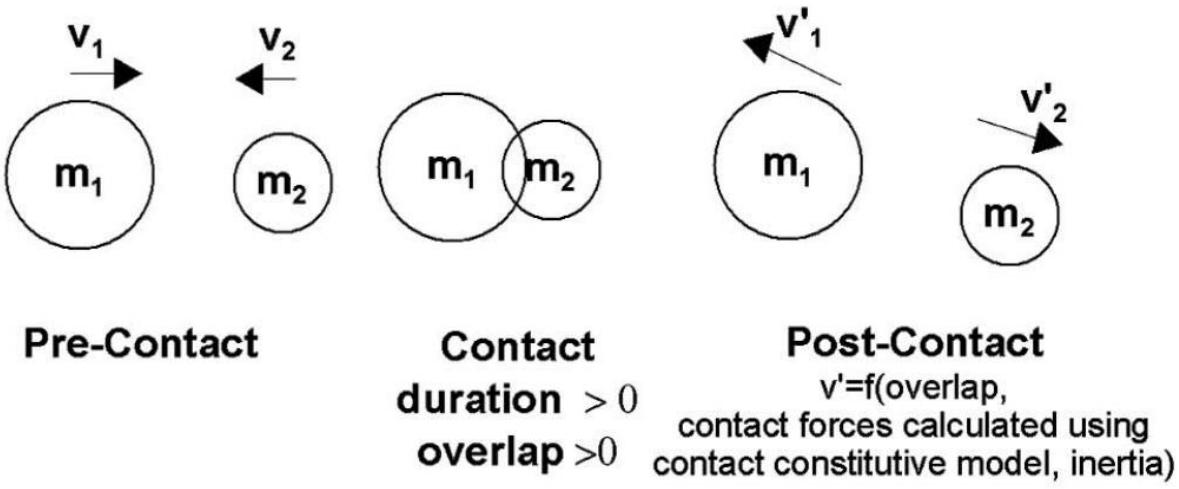

Fig. 2.35. Soft-sphere approach for inter-particle interactions (from O'Sullivan 2011a, with permission from ASCE).

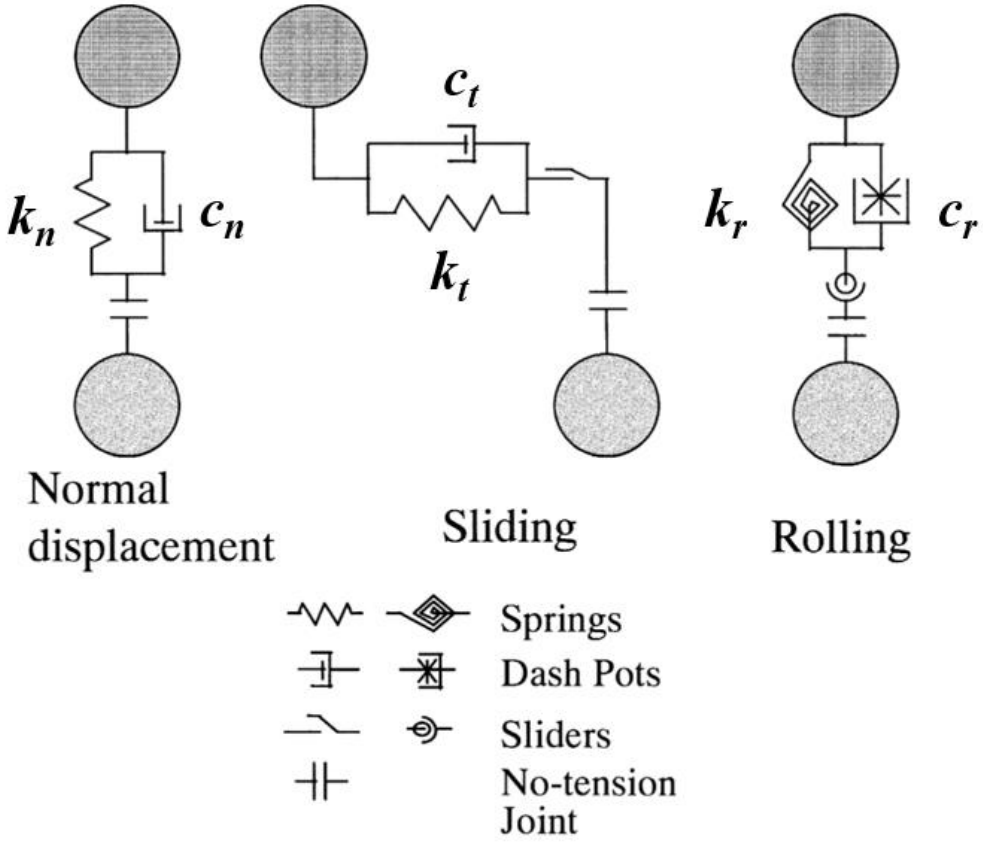

Fig. 2.36. Rheological model for a contact law governing the forces between particles via penalty springs, dashpots, sliders, and no-tension joints. Republished with permission of Elsevier Science and Technology Journals, from Iwashita & Oda (2000); permission conveyed through Copyright Clearance Center, Inc.

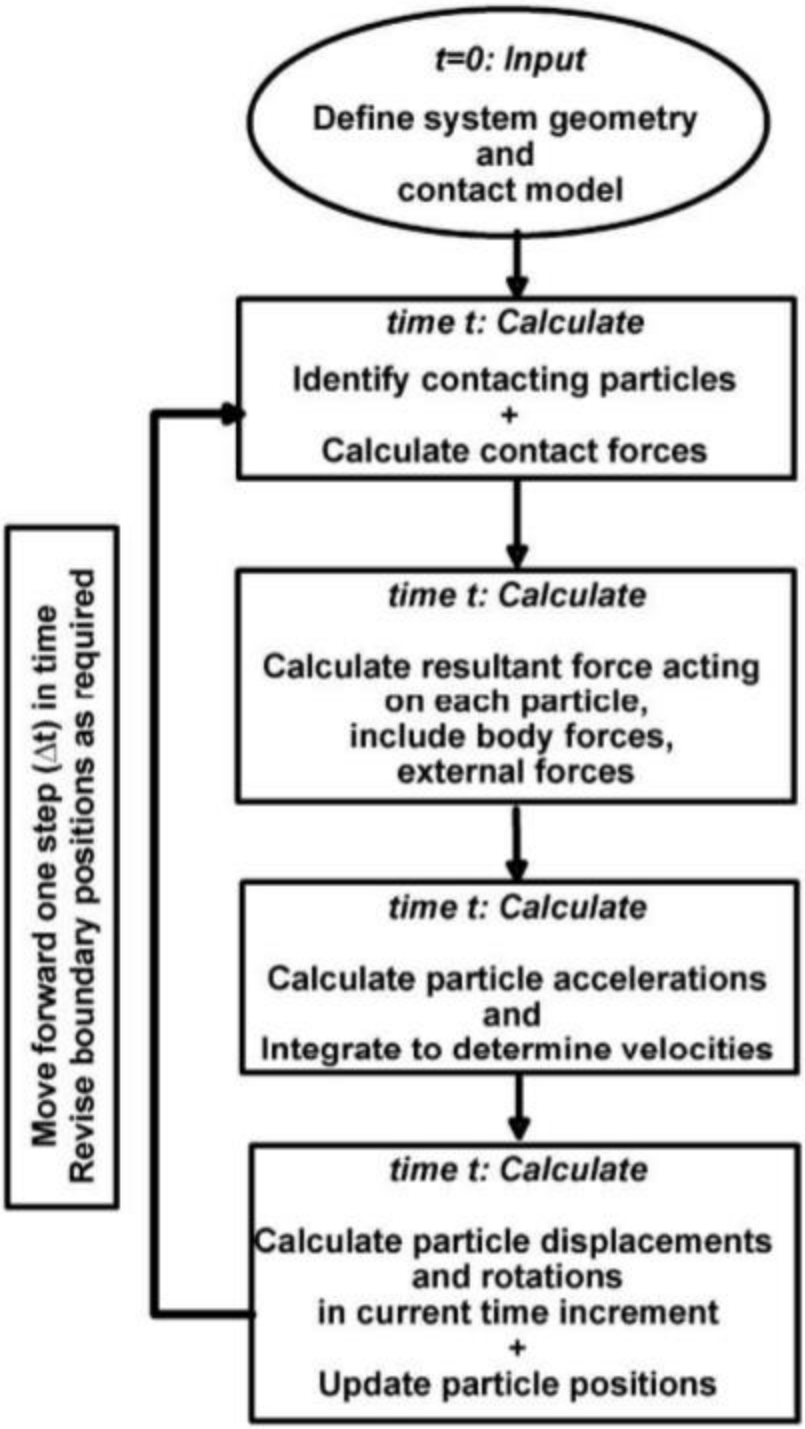

Fig. 2.37. DEM calculation sequence as shown and explained in O'Sullivan (2011a, reprinted with permission from ASCE).

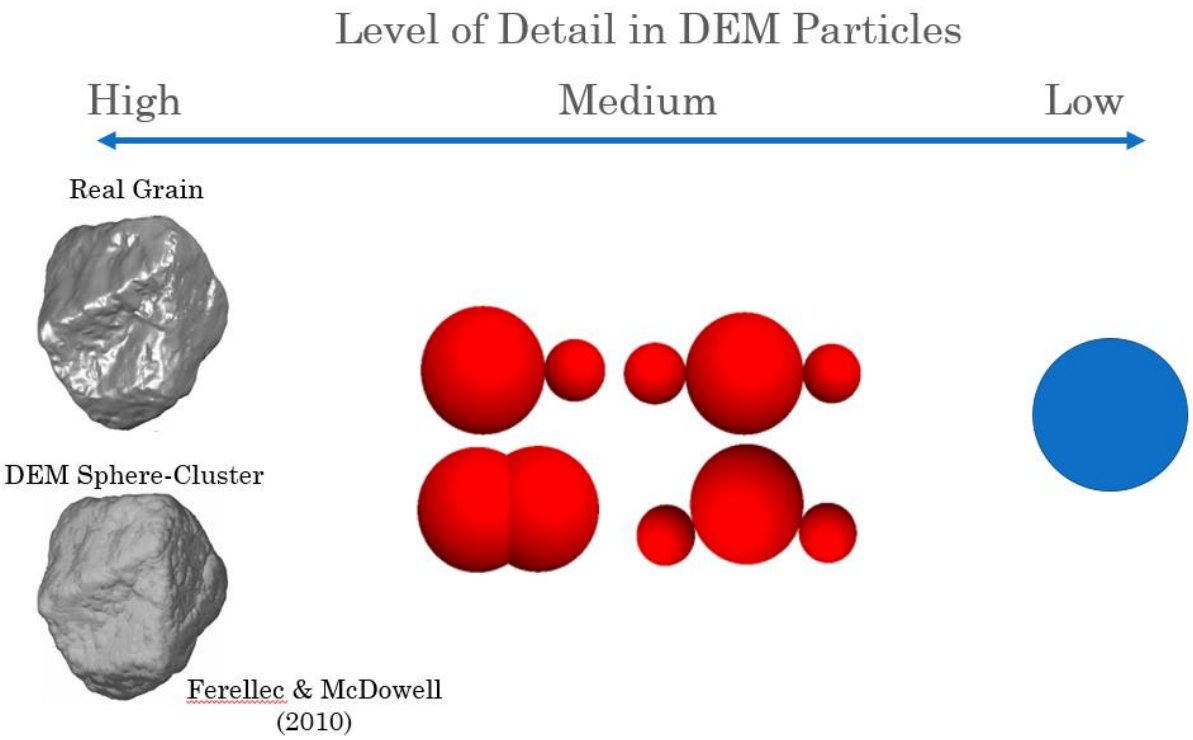

Fig. 2.38. Examples of sphere-clusters with varying degrees of complexity and detail. 2D disks represent the lowest degree of complexity. Real Grain and DEM Sphere-Cluster adapted by permission from Springer Nature Customer Service Centre GmbH: Springer Nature, Granular Matter, Ferellec & McDowell (2010).

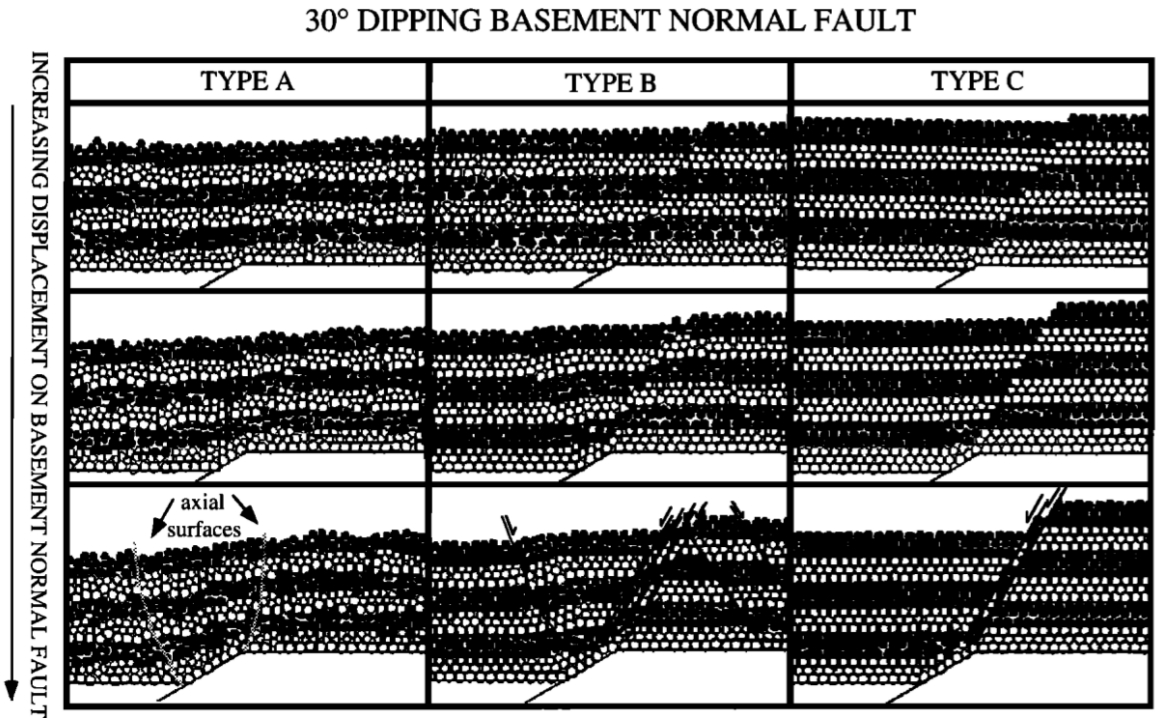

Fig. 2.39. Simulation results for 30°-dip normal fault rupture shown in Saltzer & Pollard (1992, copyright 1992 by the American Geophysical Union, published by John Wiley and Sons).

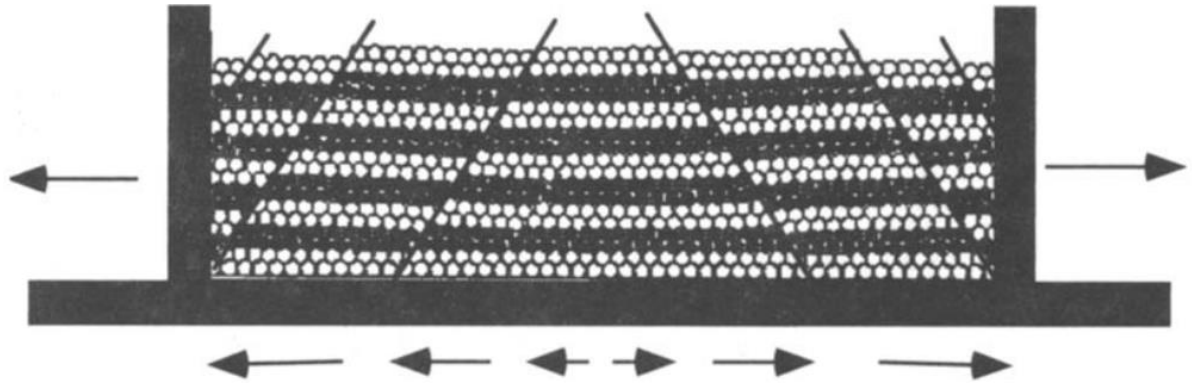

Fig. 2.40. Observations of graben formation through a gradient of basal extension, as shown in Saltzer (1992). Republished with permission of Elsevier Science and Technology Journals, from Saltzer (1992); permission conveyed through Copyright Clearance Center, Inc.

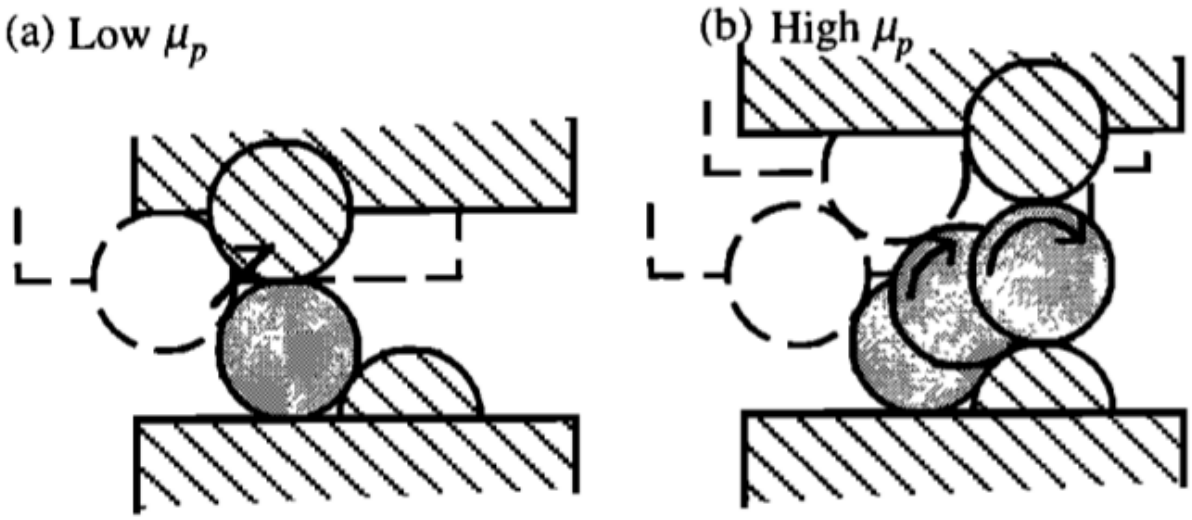

Fig. 2.41. Different mechanisms of inter-particle interaction as shown in Morgan (1999). (a) Relative sliding due to low inter-particle friction. (b) Rolling due to high inter-particle friction. Copyright 1999 by the American Geophysical Union. Published by John Wiley and Sons.

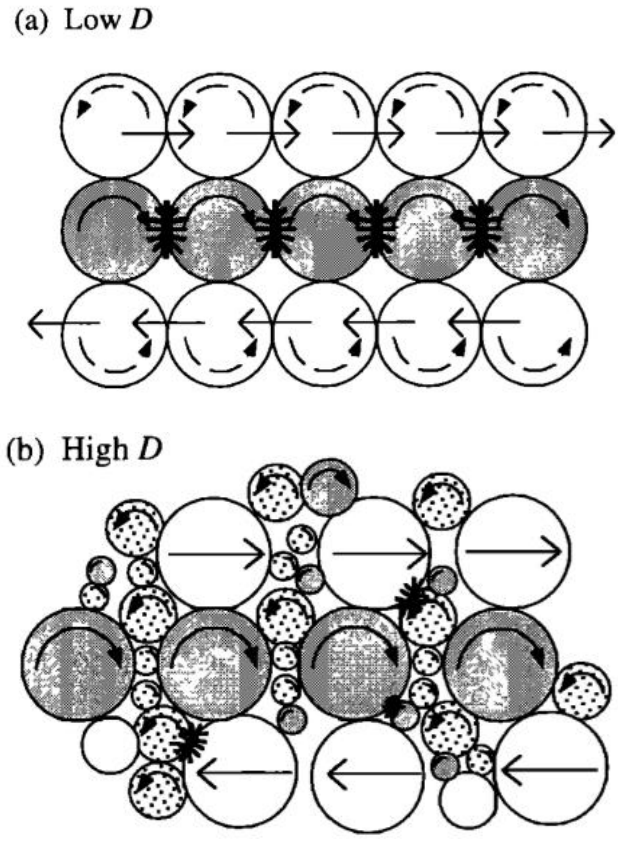

Fig. 2.42. Mechanisms of shear with (a) uniformly coarse particle assemblages and (b) coarse particles in a matrix of fine particles (from Morgan & Boettcher 1999, copyright 1999 by the American Geophysical Union, published by John Wiley and Sons).

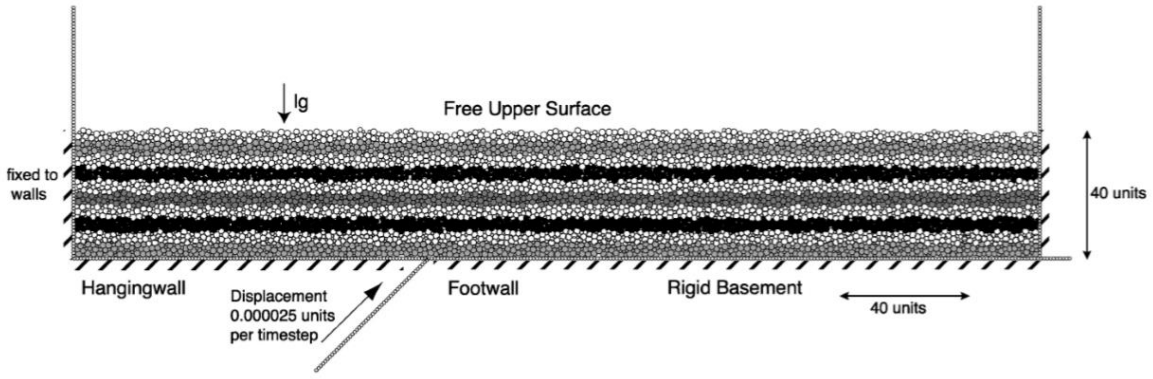

Fig. 2.43. Simulation set-up for contractional basement faulting. Republished with permission of Elsevier Science and Technology Journals, from Finch et al. (2003); permission conveyed through Copyright Clearance Center, Inc.

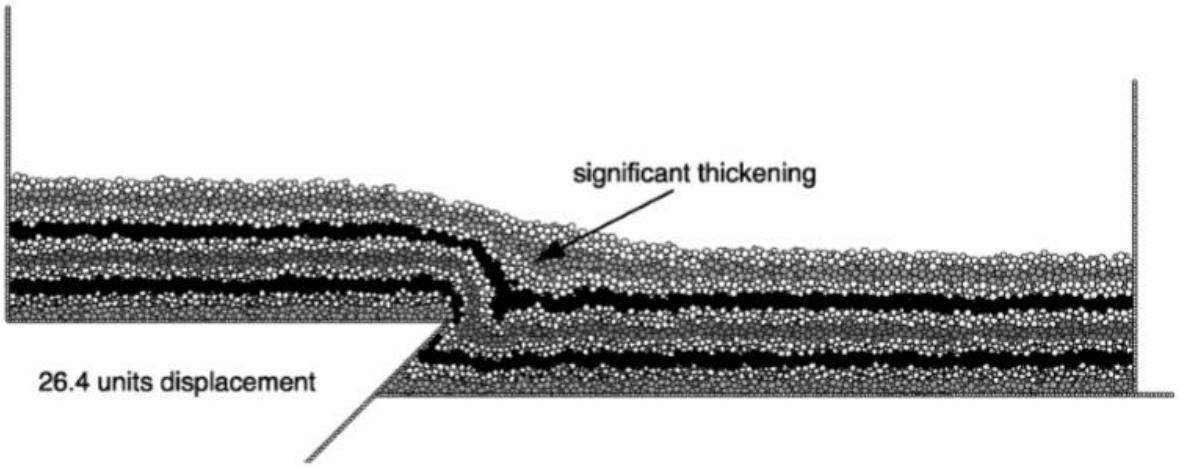

Fig. 2.44. Weak cover strength simulation results with 45°-dip contractional fault movement. Republished with permission of Elsevier Science and Technology Journals, from Finch et al. (2003); permission conveyed through Copyright Clearance Center, Inc.

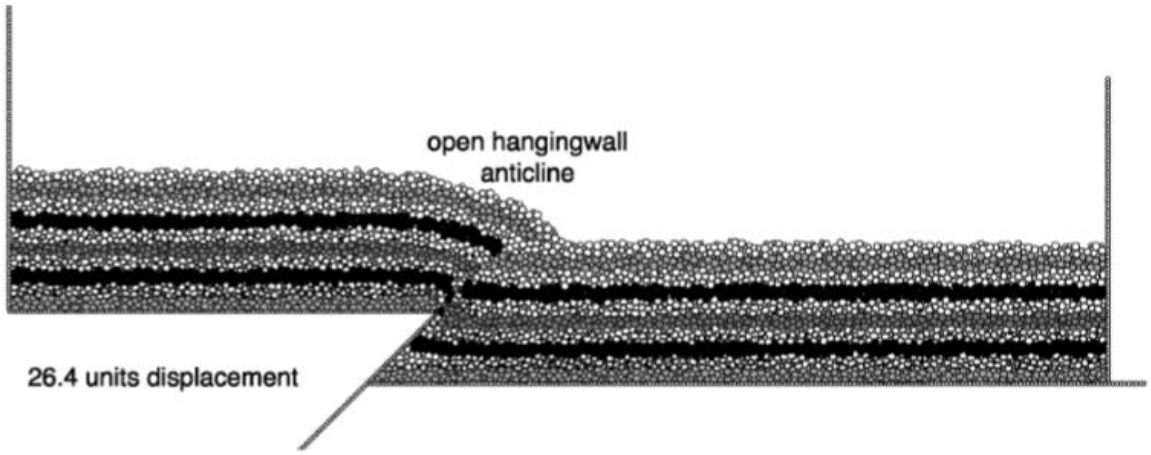

Fig. 2.45. Strong cover strength simulation results with 45°-dip contractional fault movement. Republished with permission of Elsevier Science and Technology Journals, from Finch et al. (2003); permission conveyed through Copyright Clearance Center, Inc.

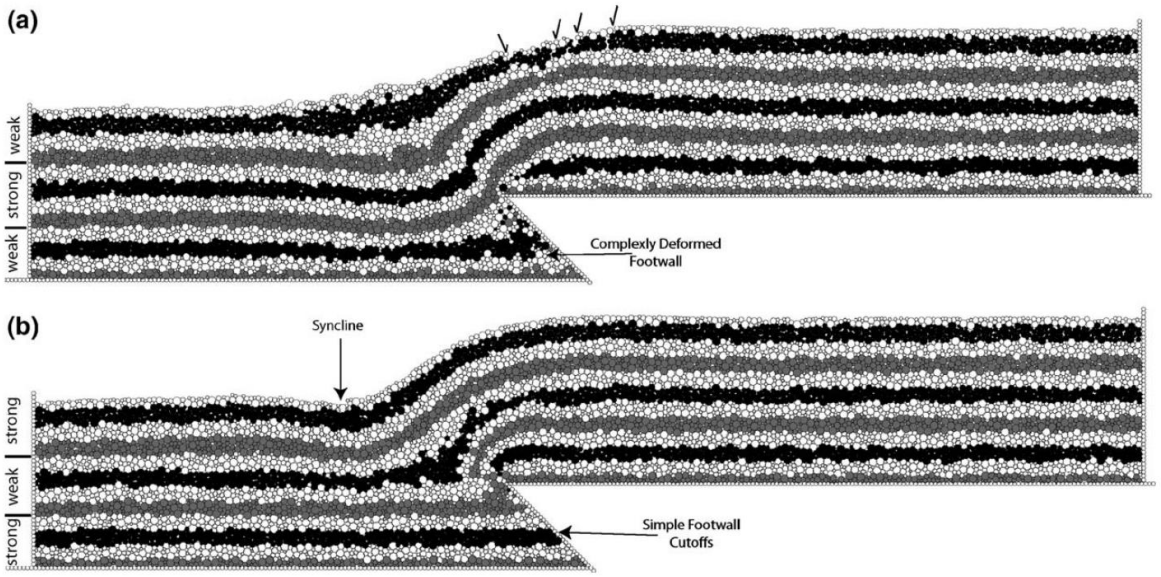

Fig. 2.46. Contractional basement faulting results with 3-layer sequence of alternating strong and weak layers. Republished with permission of Elsevier Science and Technology Journals, from Hardy & Finch (2006); permission conveyed through Copyright Clearance Center, Inc.

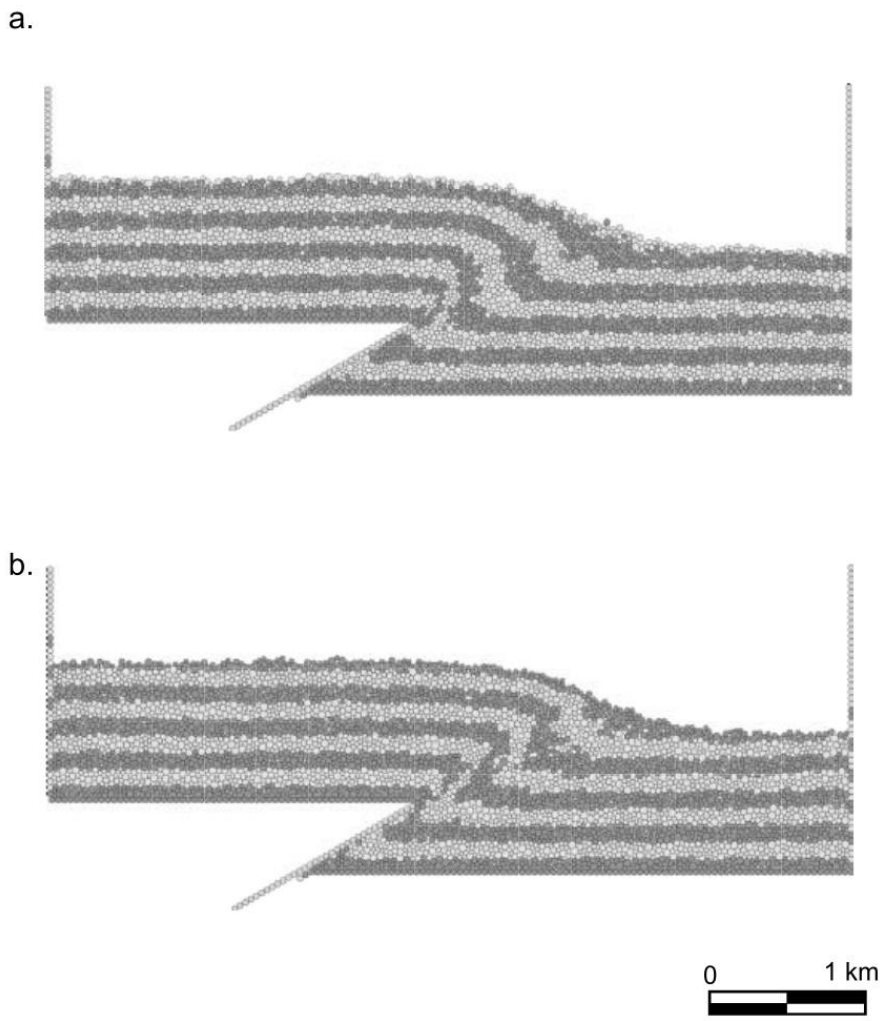

Fig. 2.47. Results of fault rupture through (a) normally consolidated and (b) over-consolidated particulate material. Republished with permission of Elsevier Science and Technology Journals, from Cardozo et al. (2005); permission conveyed through Copyright Clearance Center, Inc.

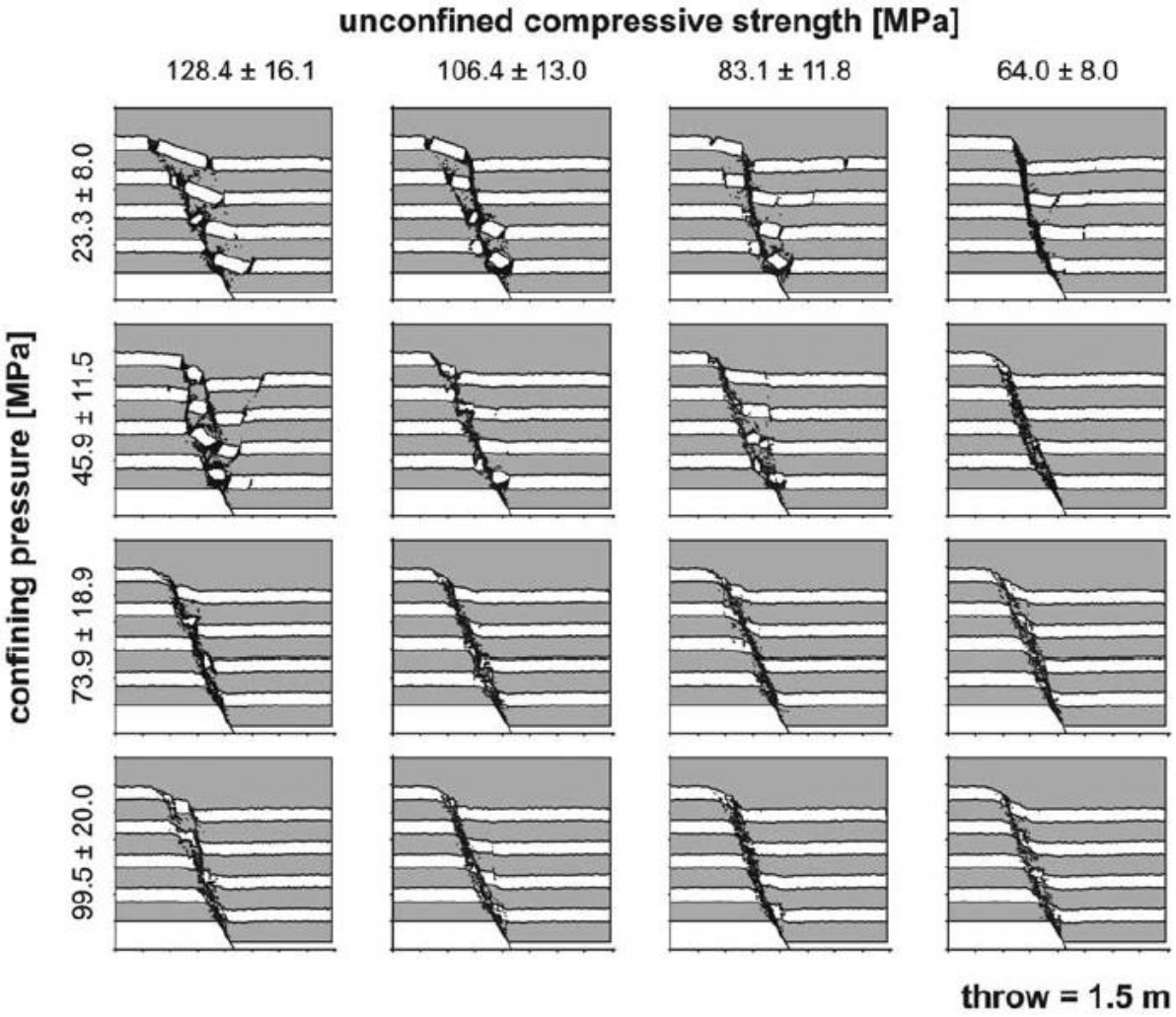

Fig. 2.48. Influence of unconfined compressive strength for bonded particle layers and confining pressure on the mechanisms of shear rupture as shown in Schöpfer et al. (2007b). Copyright 2007 by the American Geophysical Union. Published by John Wiley and Sons.

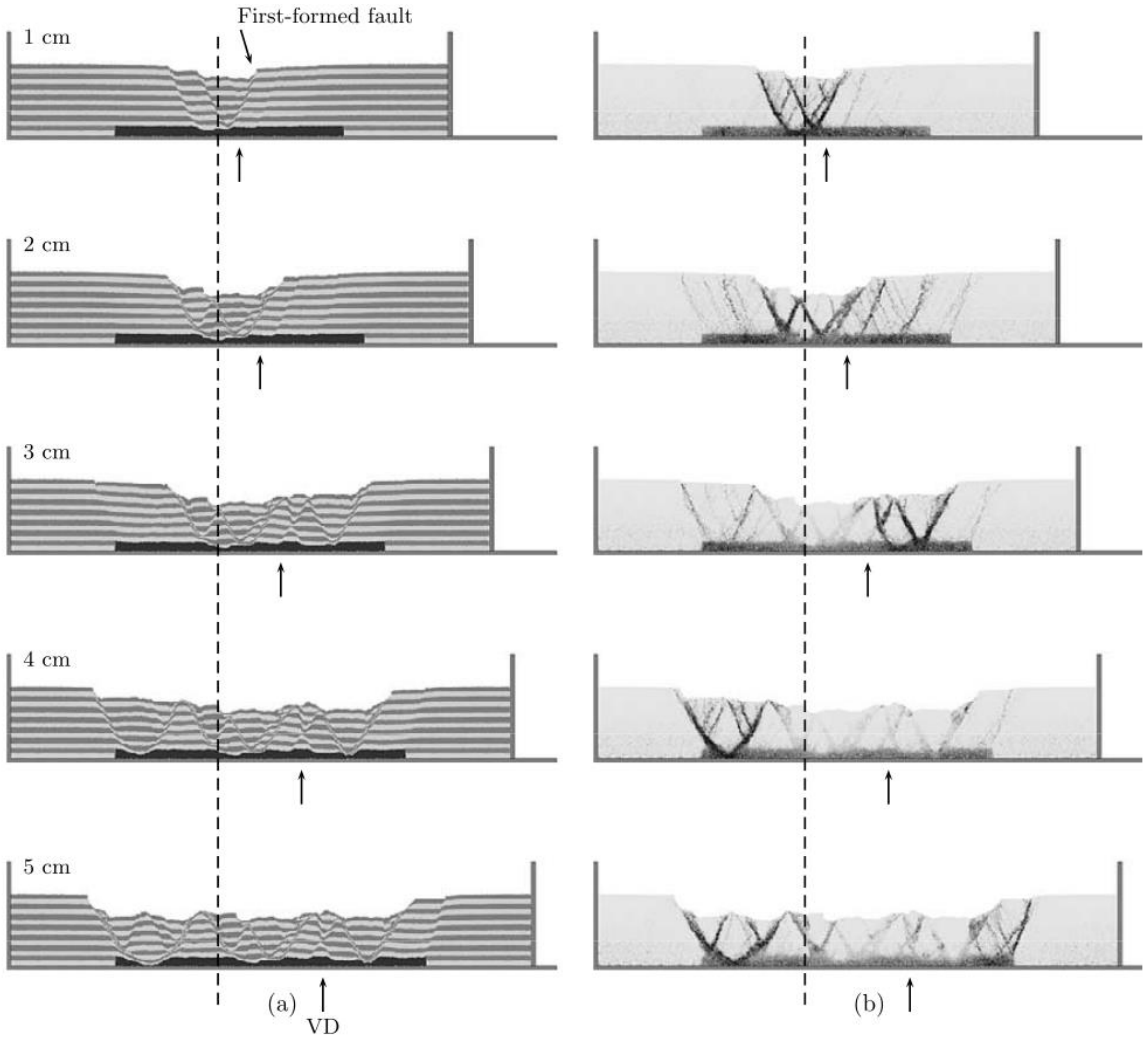

Fig. 2.49. SDEM simulations of lateral extension shown through (a) colored layers and (b) strain-rate contours. Extension is achieved with a velocity discontinuity (VD, indicated by arrows) underneath a layer of weak particles (darker colored particles). The dashed lines indicate the original center of the model. From Egholm et al. (2007). Copyright 2007 by the American Geophysical Union. Published by John Wiley and Sons.

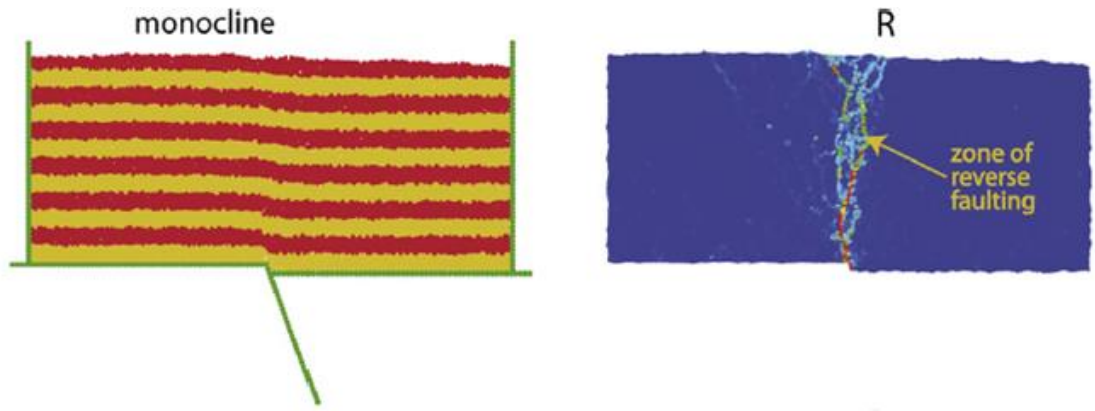

(a) 250 m hanging wall displacement.

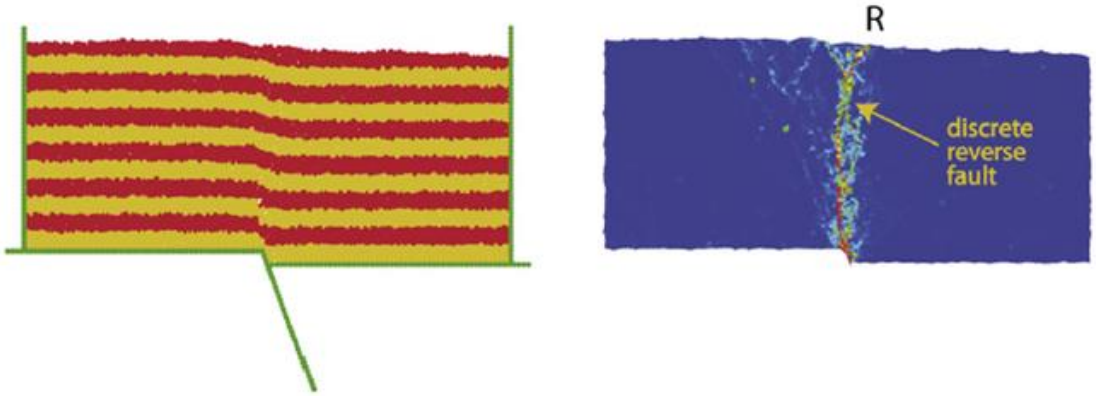

(b) 375 m hanging wall displacement.

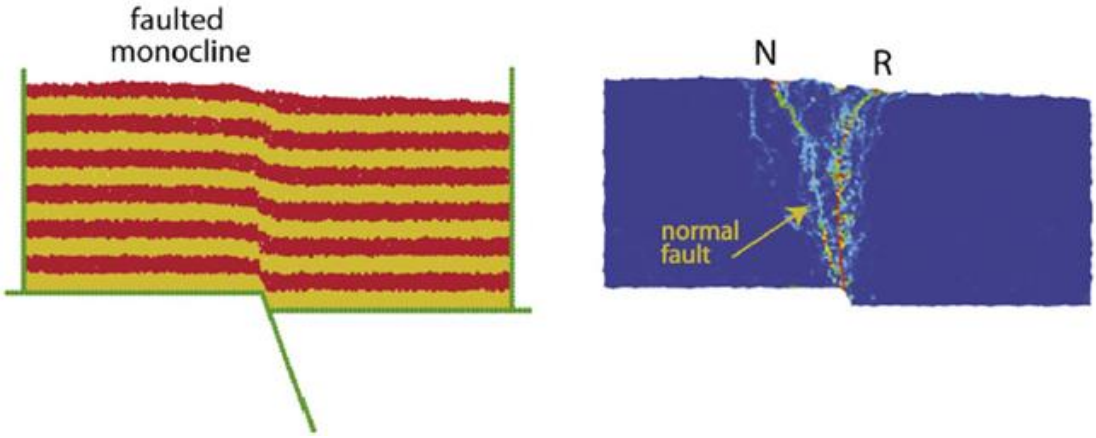

(c) 500 m hanging wall displacement.

Fig. 2.50. Select stages of fault rupture through a frictional assemblage of disks with a depth of 5.5 km overlying a 70°-dip normal fault. Republished with permission of Elsevier Science and Technology Journals, from Hardy (2011); permission conveyed through Copyright Clearance Center, Inc.

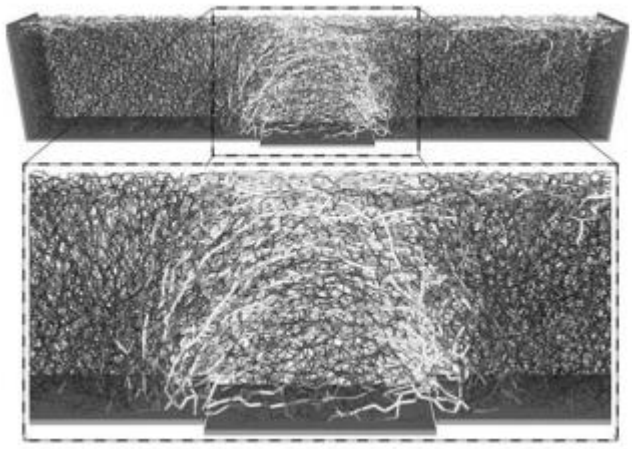

Fig. 2.51. Contact force distribution in the discrete element trapdoor simulations performed by Chevalier et al. (2012). The whitest lines indicate the largest normal forces and the darkest lines indicate the smallest normal forces. Reprinted by permission from Springer Nature Customer Service Centre GmbH: Springer Nature, Acta Geotechnica, Chevalier et al. (2012).

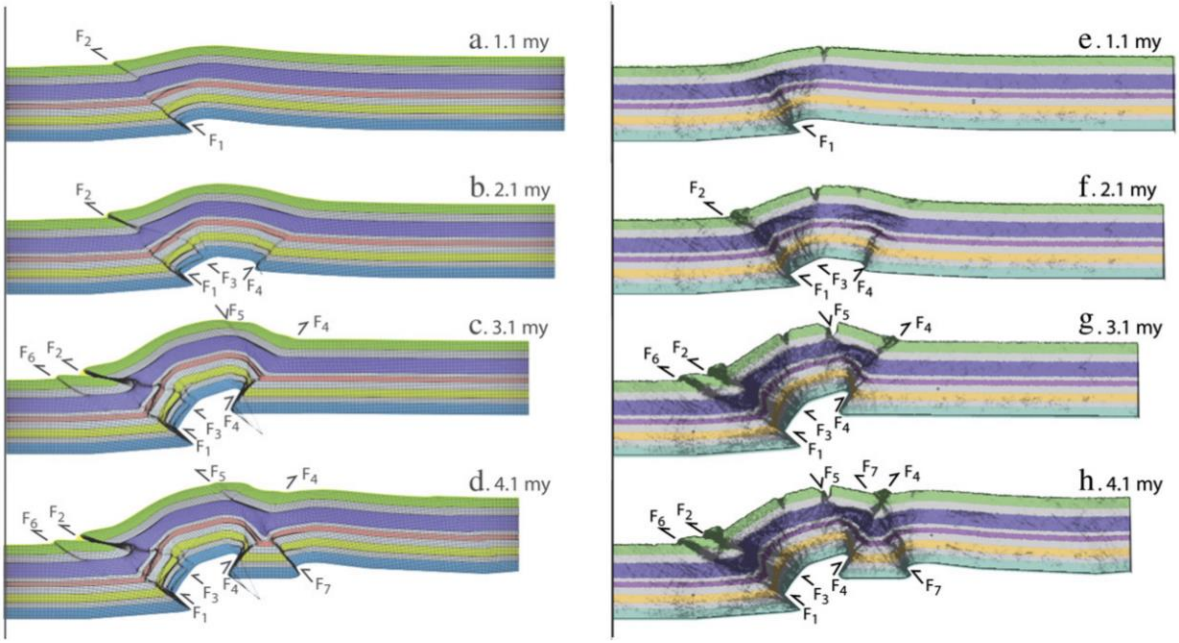

Fig. 2.52. Sequence of faulting and development of folding features in FEM (left) and DEM (right) simulations. Republished with permission of Elsevier Science and Technology Journals, from Zhang et al. (2013); permission conveyed through Copyright Clearance Center, Inc.

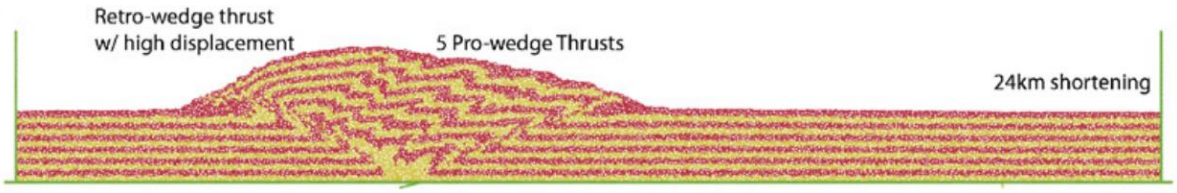

(a)

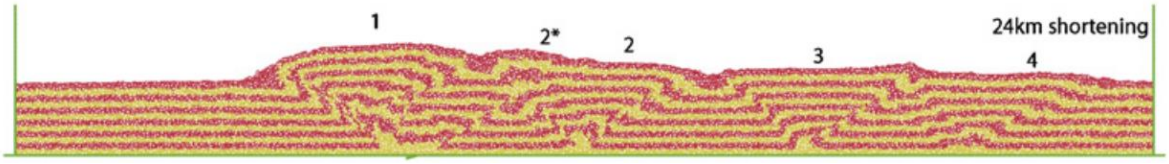

(b)

Fig. 2.53. Detachment folding simulation results with (a) base friction equal to the inter-particle friction in the overburden and (b) base friction lower than the inter-particle friction in the overburden. Republished with permission of Elsevier Science and Technology Journals, from Hardy et al. (2009); permission conveyed through Copyright Clearance Center, Inc.

CHAPTER 3: DISTINCT ELEMENT SIMULATIONS OF SHEAR RUPTURE IN DILATANT GRANULAR MEDIA

The majority of this chapter is taken directly from a manuscript published by the International Journal of Geomechanics *titled "Distinct Element Simulations of Shear Rupture in Dilatant Granular Media" (Garcia & Bray 2018a). Jonathan Bray is the only co-author of this manuscript.*

3.1 Introduction

Drained failures of dilatant granular soils often involve the localization of shear strains in a thin shear band. The formation of shear bands in granular materials has important implications for geologic hazards including earthquake surface fault rupture, landslides, and ground subsidence. Shear band development can be captured in experiments, but it is more challenging to capture numerically. Continuum models are used predominantly to analyze boundary-displacement problems involving shear rupture propagation through soil (e.g., Bray et al. 1994, Anastasopoulos et al. 2007, and Oettle & Bray 2013), but continuum modeling does not capture the true granular nature of the shear rupture process in sandy or gravelly soils. The distinct element method (DEM; Cundall & Strack 1979) is an alternative numerical tool that is particularly well-suited for analyses of large-strain shear rupture problems that are governed inherently by particle interactions. However, DEM requires a critical evaluation of its capability of capturing accurately the shear rupture processes in three-dimensional (3D) problems beyond the laboratory scale. This paper investigates its capability by utilizing 3D DEM simulations of several boundary deformation problems including earthquake surface fault rupture. All simulations are performed using the Particle Flow Code (PFC; Itasca 2014).

After this introduction, previous relevant research is reviewed. Direct shear test simulations are used to characterize the strength and dilatancy parameters for an assemblage of sphere clusters. A granular media preparation technique that produces realistic profiles of void ratio and the desired depth-dependent linear stress distribution for a level soil deposit is presented. Classic problems such as anchor pullout and trapdoor displacement are used to demonstrate the capability of DEM of capturing the stress-arching phenomenon in boundary-displacement problems. Simulations of earthquake fault rupture propagation through soil are presented and discussed. The implications of the DEM results for engineering research and practice are discussed, and concluding remarks are made.

3.2 Previous Research

DEM's applicability to evaluating earthquake fault rupture propagation through soil should be investigated thoroughly before it is relied upon in engineering practice. Finch et al. (2003, 2004) demonstrated that 2D assemblies of up to 8906 disks can capture large-scale sedimentary deformation features in contractional and extensional basement faulting. Schöpfer et al. (2007a, 2007b) showed that smaller-scale features of normal fault growth in layered sequences can be captured using alternating layers of bonded and nonbonded disks. Hazeghian & Soroush (2015, 2016, 2017) simulated surface fault rupture using over 500,000-700,000 disks with added rotational resistance and captured well-documented trends of reverse and normal fault rupture with key insight into the particulate nature of shear rupture. Other boundary deformation problems

analogous to surface fault rupture were analyzed previously using DEM. Chevalier et al. (2012) used 3D DEM simulations to study stress arching during trapdoor displacement.

Often boundary deformation problems are modeled in 2D assuming plane strain conditions. However, even plane strain problems modeled in 3D involve significant out-of-plane particle movements (e.g., Cui & O'Sullivan 2006). 2D assemblies almost always exhibit dilatant shearing response because particle movement is restricted due to the reduced degrees of freedom (Deluzarche & Cambou 2006). Furthermore, real soil grains are non-spherical and naturally resist rotation. Realistic macroscopic granular media behavior is achievable with relatively simple particle shapes if the key attributes of the problem are captured (Thomas & Bray 1999, Ni et al. 2000, and O'Sullivan & Bray 2002). DEM should employ 3D, non-spherical soil particles.

3.3 Direct Shear Test Simulation Results

The shear rupture mechanisms in direct shear (DS) tests are analogous to the mechanisms of surface fault rupture (Tchalenko 1970). Anastasopoulos et al. (2007) used numerical direct shear test models to calibrate their constitutive model for finite element simulations of the centrifuge fault rupture experiments performed by Bransby et al. (2008a, 2008b). They interpreted their simulations as "quasi-simple shear" by allowing the simple shear mode of deformation to develop at the mid-height of the specimen (Shibuya et al. 1997). The conditions necessary for a quasi-simple shear interpretation are incorporated into the following DS test simulations by making all vertical boundaries frictionless and by allowing the upper loading platen to translate horizontally without rotating. This arrangement produces a more uniform distribution of normal stresses from the applied load and allows a more distinctive peak strength to develop in strain-softening materials. The length and width of the DS test box are both 60 mm, and the initial height of the box is 20.5 mm. The lateral walls of the upper box remain stationary during shearing while the servo-controlled upper loading platen maintains a constant normal load. Strain-controlled shearing was induced by translating the walls of the lower box horizontally at a constant velocity. A non-viscous local damping factor of 0.7 is applied to all particles as recommended by Itasca (2014) for quasi-static simulations.

The sphere clusters shown in Fig. 3.1 incorporate an irregular-shaped 3D particle's inherent resistance to rolling, and they are used throughout this paper. The roundness of the particles, defined as the ratio of the average radius of curvature of surface features to the radius of the maximum sphere that can be inscribed within a particle, ranges from 0.83 to 1.0 (Krumbein & Sloss 1963). The sphericity of the particles, defined as the ratio of the diameter of a sphere of equal volume to the diameter of the circumscribing sphere around a particle, ranges from 0.54 to 0.79 (Santamarina et al. 2001). All four sphere cluster shapes are used in equal proportions. The equivalent sieve size of the particles is based on the diameter of the largest constituent sphere in each sphere cluster. The particle sizes are selected to approximate the shape of the grain size distribution of Fontainebleau sand with a coefficient of uniformity (C_u) of 1.57, as shown in Fig. 3.1 (Delfosse-Ribay et al. 2004), because this sand has been used in physical boundary-displacement experiments (e.g., Anastasopoulos et al. 2007, and Bransby et al. 2008a, 2008b). However, exact replication of Fontainebleau sand and the experiments is not the goal of this research.

The DS test simulation specimens are prepared using a radius expansion method in which the particle sizes are gradually scaled up until the assemblage achieves a desired isotropic stress state. The specimen is brought to different void ratios by varying the initial interparticle friction

coefficient (μ_0) between 0.0 and 0.5 during the particle radius expansion procedure. In the DS simulations, 100,986 particles consisting of 253,207 constituent spheres were generated initially without overlap within the DS box boundaries. Ni et al. (2000) showed that at least 30,000 sphere-clusters are required in DS test simulations for further increases in total number of particles to have negligible effect on the material's peak friction angle and angle of dilation. The number of particles used in the DS test simulations of this study is sufficiently large for the measured strengths and rates of dilation to be unaffected by further increases in the number of particles.

The shearing velocity of each simulation was sufficiently slow such that slower shear velocities still produced insignificant differences in the measured results (i.e. the simulations were run quasi-statically). Initial simulations were performed under different shear velocities to determine the conditions for quasi-static shearing, and the influence of shear velocity on the measured strengths and dilations was found to be insignificant if the measured stresses on the upper and lower parts of the DS device were within 2.5% of each other during most of the simulation. At these quasi-static shear velocities, the ratio of the average unbalanced force on all particles to the average force acting on all particles (i.e. R_{avg}, Itasca 2014) was maintained below 0.0005.

A linear contact model is used in which the normal spring stiffness (K_n) at each contact is a function of the elastic modulus (E) and radii of the contacting spheres (R_i) (Itasca 2014):

$$K_n = \frac{\pi \min(R_1^2, R_2^2) E}{R_1 + R_2} \tag{3.1}$$

The elastic modulus is 200 MPa in all simulations. The ratio of normal to shear spring stiffness (K_n/K_t) is 4 for inter-particle contacts and 1 for particle-wall contacts. The microscopic roughness of the surfaces of real sand grains is approximated with a coefficient of friction (μ) of 0.5 to be consistent with friction measurements of natural quartz surfaces (Mitchell & Soga 2005). The coefficient of friction for the horizontal walls of the DS box is made the same as that of the particles.

Representative results of the DS test simulations of specimens with different initial void ratios (e_o) under an applied normal stress (σ_n) of 106.7 kPa are shown in Fig. 3.2. A distinct shear band does not develop in the loosest assemblage shown in Fig. 3.2a; deformation is distributed throughout the specimen. The horizontal displacement of particles within the specimen varies linearly with their vertical position. The densest assemblage in Fig. 3.2c shows a more distinct offset of the colored columns with a shear band forming at the mid-height of the specimen where differential deformations localize. The soil columns retain their vertical orientation near the top and bottom boundaries but are angled through the shear zone at the mid-height. The deformation of the medium density specimen in Fig. 3.2b is intermediate to the deformations shown in Figs. 3.2a and 3.2c.

The mobilized friction angle and vertical displacement of the DS top cap are shown in Fig. 3.3 for some of the DEM simulations. The mobilized friction angle is calculated as:

$$tan\ \phi = \frac{\tau}{\sigma_n} \tag{3.2}$$

where τ is the sum of all forces acting in the direct of box movement on the lower shear box divided by its horizontal area and σ_n is the applied normal stress. The results in Fig. 3.3 are consistent with the principles of critical state soil mechanics (Schofield & Wroth 1968). As seen

in Figs. 3.3a and 3.3b, the peak friction angle and the rate of dilatancy increase with decreasing void ratio, and the two loosest specimens exhibit contractive responses. The residual friction angle at large shear displacements is approximately 31° for all values of e_0. At large horizontal displacements, the rate of dilation tends toward zero in all assemblages. A distinct shear band only forms through the dilatant assemblies that undergo significant strain softening.

A limitation of these simulations is the dense specimens exhibit negligible contraction prior to the onset of dilation. As shown in Fig. 3.3c and 3.3d, higher applied normal stresses tended to decrease the peak friction angle, to reduce the initial stiffness, and to suppress the maximum rate of dilation in assemblages of particles having similar void ratios, but the reductions in strength and dilation were less than what is observed in laboratory tests on real sands. The effects of grain-crushing and breakage of grain surface asperities were not included in the simulations; they would significantly affect results at high normal stresses. Despite the simplifications inherent in these DEM simulations, 3D, non-spherical particle assemblages with realistic contact properties capture key aspects of critical state soil mechanics in the DS test, which provides confidence that other boundary deformation problems can be captured adequately.

3.4 Trapdoor and Anchor Pull-Out Problems

The anchor pull-out and trapdoor problems are good analogies to other boundary deformation problems, such as earthquake fault rupture, mining subsidence, sinkhole formation, and tunneling. 136,784 sphere clusters with 344,604 constituent spheres are assembled to model these problems. The assemblage has a median void ratio of 0.67 with a slightly higher value of 0.69 near the surface. The DS test results in Fig. 3.3 show that this material will dilate during shear. The anchor width is 3 times shorter than the depth of material above the anchor, and the trapdoor width is 2 times shorter than its depth. Periodic boundaries are used in the out-of-plane direction to approximate an infinitely long simulation space. The length of the periodic dimension is at least $10D_{50}$ in all simulations. Trial simulations with longer periodic dimensions yielded similar results. The particle geometries described previously are also used in the boundary deformation simulations, but they are larger. In trapdoor and anchor pull-out simulations, the particles are uniformly scaled by a factor of 20 times larger than Fontainebleau sand (i.e. D_{50} = 4.4 mm) while still maintaining C_u = 1.57. The trapdoor/anchor is represented by a horizontal wall at the center of the base that displaces vertically with frictionless lateral walls preventing particles from displacing underneath it. The trapdoor/anchor displaces vertically at a rate of 1% of the depth of soil per second.

The particles are initially generated without overlap in a rectangular box having a height of 300 mm. Centrifuge-scale stress conditions are applied by gradually incrementing the gravitational acceleration by a prototype scaling factor (n) over 100 iterations. Each iteration involves several calculation cycles and checks for attainment of a predetermined equilibrium criterion. An index of unbalanced forces is recommended as an indicator of equilibrium (Ng 2006). After each iteration, the bulk density of the particle assemblage is set to 1650 kg/m^3. The particles are initially allowed to settle with μ = 0.05 until the gravitational acceleration reaches approximately 50-75% of its final value depending on when the assemblage reaches the predetermined equilibrium criterion; μ is then increased to 0.5, and the iterations continue to completion. When the final gravitational acceleration is achieved, the centrifuge scaling factor is applied to the bulk density of the material, and the gravitational acceleration is reduced to 1 g. This maintains a stress distribution equivalent to that felt in an $n \times g$ centrifuge test with a material having

a bulk density of 1650 kg/m^3. This also allows a longer time-step to be used, because the longest stable time-step is directly proportional to the square root of the particle mass (Thornton 2000, and O'Sullivan & Bray 2004). In trapdoor and anchor pull-out simulations, the final bulk density is 22,770 kg/m^3 (n = 13.8) so that the stress distribution within the assemblage is equivalent to that of a 3-m depth of soil, and the width of the simulation is 13.1 m.

Fig. 3.4 shows the network of strong contact forces in each simulation. The contact forces are normalized by their depth below the ground surface, because contact forces increase as particle depth increases and the intent is to examine relative increases in contact forces due to base deformation. The strong contact forces are defined as those that when normalized by their depth below the surface exceed one standard deviation above the median contact force normalized by depth on a lognormal scale in the initial configuration.

The mechanism of the stress arching phenomenon depicted in Fig. 3.4a is consistent with Chevalier et al. (2012). The downward displacing trapdoor relieves the stress between the particles directly above the trapdoor. Material weight of shallow particles, which was initially supported by the trapdoor, transfers to the surrounding stationary material, which increases the contact forces of the particles on both sides of the trapdoor. Particles immediately atop the trapdoor are supported fully by the trapdoor; whereas particles near the surface are partially supported by surrounding stationary material. The transition from partial lateral support to zero lateral support with increasing depth creates an arched structure of strong contact forces and high stresses along the shear bands developed in the soil overlying the trapdoor. Two half-arches of strong contact forces emanate in outward directions from both sides of the anchor in Fig. 3.4b with zones of stress relief below each half-arch. The kinematics of the uplifted anchor pull-out problem are opposite to that of the trapdoor displacement.

3.5 Earthquake Fault Rupture Simulations

3.5.1 Model Analyzed

Bransby et al. (2008a,b) performed a series of controlled geotechnical centrifuge experiments of earthquake fault rupture propagation through granular media. These experiments provide an exceptional basis for evaluating the capabilities of the proposed DEM simulations to capture this boundary deformation problem. The dimensions of the centrifuge box utilized by Bransby et al. (2008a) are used to create the boundaries of the DEM model shown in Fig. 3.5. The DEM particle assemblage with Height (H) of 215 mm is underlain by rigid walls representing the bedrock of width (W) of 950 mm with hanging wall (HW) and footwall (FW) on the right and left sides, respectively, of a fault having a dip angle δ. As discussed previously, non-overlapping particles are initially generated within a rectangular box having a height of 300 mm. A low critical damping ratio of 0.1 was applied at the particle contacts only during the assemblage preparation stage to help bring the system to equilibrium (Itasca 2014). The simulations contain a total of 175,660 sphere clusters with 442,509 total constituent spheres. Centrifuge-scale stress conditions are applied by gradually incrementing the gravitational acceleration by n. The final bulk density is 189,750 kg/m^3 (n = 115, which is identical to the scaling factor used by Bransby et al. 2008a,b) so the stress distribution is equivalent to that in 25 m of soil at prototype scale.

The void ratio and stress distributions of the final particle assemblage are compared in Fig. 3.6 for two granular deposits generated with particles scaled in size by a factor of 15 and particles scaled in size by a factor of 20. The latter assemblage does not include larger boundary particles.

The nearly identical void ratio and stress distributions justify that it is acceptable to use larger particles away from the area of interest so that more, smaller sized particles can be employed in the zone of expected shear rupture. This approach is similar to mesh refinement in finite element methods without affecting the overall void ratio or stress distribution. The periodic dimension length of at least $10D_{50}$ and the ratio W/H are sufficiently long for the two horizontal stresses, σ_x and σ_y, to be equal in both directions. The assemblage of particles is normally consolidated with a realistic range of K_o of 0.40-0.45 throughout its depth (Holtz & Kovacs 1981). This suggests that the procedure for modeling the soil deposit is an adequate approximation to natural depositional processes.

The simulations are run quasi-statically to minimize the differences in the scaling of velocity depending on if n is applied to gravity or density (Wood 2004), although surface fault rupture is consistently found to be only minimally sensitive to the rate of rupture (Oettle et al. 2015). As done previously, quasi-static rupture is monitored using R_{avg}, which is maintained below 0.0005. A rupture rate, defined by the rate of hanging wall displacement in the dip direction normalized by H, of 0.01-0.02 s^{-1} is used in all surface fault rupture simulations. The hanging wall and right vertical boundary move together as a unit to induce rupture while the footwall remains stationary. Several trial simulations showed that rupture strain rates of 0.04 s^{-1} still resulted in negligible differences in observed results, and measured results differed insignificantly at even slower rates of rupture.

Ten simulations of reverse and normal faults were performed with bedrock faults dipping at 30°, 45°, 60°, 75°, and 90° for each fault type. The shear rupture surface is identified through particle rotations, frictional dissipation, shear strains, and volumetric strains. The particle rotations are calculated as the magnitude of counterclockwise rotation about the principal axis of rotation for each particle. The frictional dissipation is shown as contours of energy dissipated through frictional slip at active interparticle contacts. All volumetric and shear strains are calculated using the meshfree strain homogenization procedure of O'Sullivan et al. (2003). Results were recorded for different values of h/H, where h is the vertical component of hanging wall displacement.

3.5.2 Results

The shear rupture zone developed in the 60°-dip reverse fault at h/H=0.1 is shown in Fig. 3.7. The zone of shear deformation increases slightly in thickness as it approaches the ground surface. Additionally, the granular media's void ratio is higher near the surface (see Fig. 3.6a), which produces less brittle offset. The fully developed shear band is approximately 7-10 particle diameters thick. This width is consistent with other researchers who found that shear bands through sands are typically 8 to 16 times D_{50} (e.g., Oda & Kazama 1998, and Wood 2002), albeit the DEM width is at the lower end of those reported in the literature. The width of the entire shear zone in Fig. 3.7 is 23-33 mm. This width scales to approximately 2.6-3.8 m with n=115. The particles themselves, however, are not treated as if they are scaled to the size of cobbles and boulders. Kutter (1995) states that the interparticle contact forces depend on stress level and coordination number and not on gravity or scaled particle sizes. Therefore, the shear band widths measured in the DEM simulations are considered representative of the prototype material under the same stress state.

Absolute particle size does affect shear rupture development if the boundary conditions and stress state are held constant. Anastasopoulos et al. (2007) observed that the width of the shear band was directly related to the mesh size. This is analogous to the width of the shear band being related to particle size in a DEM simulation, assuming that the shear band will consistently be on

the order of 10 particle diameters irrespective of particle size. Stone & Wood (1992) found different patterns of shear rupture development in trapdoor experiments with sands of different particle sizes. They observed that multiple rupture surfaces tended to develop in finer sands, and movement along existing rupture surfaces ceased when the rate of dilation fell to zero and continued movement along the shear band became kinematically inadmissible. When movement stopped along one rupture surface, a second rupture surface would develop at an even steeper angle, and this process would continue until one rupture surface finally reached the soil surface. While these additional rupture surfaces tended to develop at different absolute base displacements in sands having different grain sizes, they developed at approximately the same relative base displacement normalized by grain size. This normalization of shear rupture development with grain size can be explored with DEM by repeating the simulations with even smaller particles. However, such an effort would require orders of magnitude more particles, which is outside the scope of this study in which simulations were performed on a computer with an Intel Xeon processor having 8 computing cores.

Fig. 3.8 portrays different stages of the shear rupture process for the 60°-dip reverse fault simulation. At h/H=0.05, only a small amount of surface deformation is visible in Fig. 3.8a. Distinctive offsets of the particle layers are only noticeable in the lower 60% of the assemblage height, and the shallower layers initially accommodate the impending fault displacement through distributed deformation. Particle rotations and frictional dissipation provide excellent signatures of propagating shear rupture because they delineate effectively the final form of the rupture surfaces in Fig. 3.8b and 3.8c well before the rupture develops fully. The shear rupture surface develops progressively and is not yet developed fully as seen through the shear and volumetric strain plots in Figs. 3.8d and 3.8e. At h/H=0.1, the rupture surface is developed fully with distinct offsets through most of the assemblage of particles as shown in Fig. 3.8f. The warping of the ground surface above the hanging wall is consistent with field case studies by Bray et al. (1994). The shear rupture is clearly discernable in Fig. 3.8g, 3.8h, 3.8i, and 3.8j. However, the shear rupture surface is less distinct near the ground surface when viewed in terms of the shear strains in Fig. 3.8i, because the mode of deformation is less brittle offset at shallow depths as discussed previously. The positive volumetric strains in Fig. 3.8j indicate dilation occurring within the shear band. Nearly zero volumetric or shear strains are observed outside of the shear rupture zone, especially on the footwall side of the fault movement.

Fig. 3.9 shows the fault rupture propagation process for the 30°-dip normal fault simulation. At h/H = -0.02, a primary shear rupture surface that refracts at the base and increases in dip slightly as it propagates upward is visible in Fig. 3.9a, which is consistent with field observations by Bray et al. (1994). The ground surface begins to deform broadly but no distinct surface fault offset is yet visible. Fig. 3.9b-e clearly show the primary shear rupture (to the left in the plots), but only Figs. 3.9b-c show the initial development of a secondary, antithetic rupture surface that forms over the hanging wall. At h/H = -0.08, both primary and secondary shear rupture surfaces are developed fully, separated by a gravity graben, and are clearly visible in Figs. 3.9f-j. The shear rupture develops at a lower amount of base displacement for the case of the 30°-dip normal fault case than the 60°-dip reverse fault case. Mostly positive shear strains develop within the primary rupture surface in Fig. 3.9i; whereas, more negative shear strains develop in the secondary rupture surface due to the opposite senses of shearing between the two rupture surfaces. Outside of the rupture surface, only minor shear and volumetric strains develop.

3.5.3 Comparison with Experiments of Earthquake Fault Rupture

Cole & Lade (1984) developed an expression that captures the shape and outcrop location of the shear rupture surface observed in their sandbox experiments composed of a dry, granular material. The only material property required for their expression is the angle of dilation. Previous researchers showed that the fault rupture trends of Cole & Lade (1984) are captured well using 2D DEM (Hazeghian & Soroush 2016). Such a comparison has not yet been completed using 3D DEM simulations. An angle of dilation of 20° is used in the Cole & Lade (1984) expression based on the direct shear test simulation results presented previously. Particle rotations are used to delineate the shear rupture surface because they are judged to provide the most detail for its shape and location.

Fig. 3.10 shows the predicted rupture surface compared with the rupture surface developed in select reverse and normal fault simulations. The 30° reverse fault in Fig. 3.10a extends linearly from the bedrock fault all the way to the ground surface with insignificant curvature. Cole & Lade (1984) present a logarithmic spiral rupture surface solution in which the center of the spiral is located infinitely far away, essentially giving a linear rupture surface. This occurs when the dip angle is 45°-ψ/2, and it represents a transition from upwards to downwards curvature. The 30°-dip reverse fault simulation is close to this transition, which is predicted to occur at a dip angle of 35°. The reverse fault results in Figs. 3.10b-c show the rupture surfaces bending over the downthrown block as do the predicted rupture surfaces. The predicted rupture surface for the 60°-dip reverse fault in Fig. 3.10b is located at the center of the zone of large-magnitude particle rotations that curves over the downthrown block, indicating a good match between simulated result and empirical solution. Some particle rotations are also seen on the surface of the upthrown block immediately adjacent to the outcrop locations for the 90°-dip reverse fault in Fig. 3.10c. Relative surface displacement reduces lateral support at the top of the upthrown block adjacent to the fault outcrop, and the material near the outcrop location tends to slump over the downthrown block.

The propagation of a secondary, antithetic rupture surface and formation of a graben occur for the same normal fault rupture cases in which the closed-form solution predicts a secondary rupture surface to form. As was seen in the 30°-dip normal fault simulation, the secondary rupture surface for the 45°-dip normal fault simulation propagates linearly at approximately the same angle as the predicted secondary rupture surface as shown in Fig. 3.10d. The large horizontal component of hanging wall displacement for shallow normal faults contributes to the shearing of the soil deposit through lateral extension. The horizontal component of hanging wall displacement is less significant in the case of 60°-dip normal fault rupture in Fig. 3.10e, and a graben does not form. The primary rupture surfaces for the 30°, 45°, and 60°-dip normal faults all appear approximately linear, but the location at which the ground surface transitions from sloped to level is close to the predicted fault outcrop location in Figs. 3.10d-e. This suggests that the curvature in the empirical solution from Cole & Lade (1984) is a product of the finite width of the fault scarp in a granular material rather than due to a complete reversal in the path of the rupture surface. The normal fault rupture surface outcrops at the lower end of the fault scarp. As the fault dip angle transitions from 60° to 90° in normal fault rupture, the primary rupture surface transitions from extending almost linearly over the footwall to curving over the hanging wall.

The 90°-dip normal fault rupture surface in Fig. 3.10f mirrors the 90°-dip reverse fault rupture surface at the same amount of relative hanging wall displacement. As discussed previously, the kinematics of these two simulations are similar given the quasi-static nature of the simulations. The rupture surfaces for the 90°-dip scenarios initially propagate at an approximately linear angle. Stone & Wood (1992) observed that initial regions of strain localization in trapdoor experiments

were linear and inclined 15°-20° to the vertical. When coarse sand was used, this initial rupture surface fully propagated to the ground surface. Hence, the DEM results, which use coarse particles with D_{50} = 3.3 mm, are consistent with experimental observations.

3.5.4 Particle Rotations

Discrete element methods provide complete information on particle rotations. Iwashita & Oda (1998, 2000) showed that 2D assemblies of disks with rheological rotational resistance tend to rotate in the same direction within the same shear band. 3D assemblages of non-spherical particles are expected to exhibit a similar bias towards rotating about a particular axis. Fig. 3.11 shows the percentages of dominant Cartesian components of rotation for select simulations. The dominant Cartesian component of rotation is the vector component of the principal axis of rotation with the largest magnitude. The statistics shown in Fig. 3.11 can also be interpreted as the percentages of Cartesian axes that form the largest positive dot product with the particle principal axes of rotation. Particle rotations are calculated from the onset of fault rupture, and only particles that rotate at least 30° about their principal axis are shown so that the data consists mostly of particles within the shear bands. The proportion of the total particles that rotate by at least 30° are shown at the left side of the plot.

The +X axis makes up the largest proportion of dominant Cartesian components in the reverse fault simulations. The +/-Y directions have slightly higher percentages than the +/-Z directions because the elongated sphere clusters tend to orient in the horizontal direction during deposition. The significantly greater percentage of particles rotating about the +X axis compared to other axes reflects a tendency for particles to rotate with the sense of shear, or in the direction of relative movement of two blocks of soil above the footwall and hanging wall of the fault. This tendency is further exemplified by the normal fault rupture data. In 60°-dip and 90°-dip normal fault simulations, the sense of shear along a single rupture surface is opposite to that of reverse fault rupture. Hence, the -X axis makes up the largest proportion of dominant Cartesian components. The proportion of dominant Cartesian components about the +X axis during 90°-dip reverse fault rupture is close to the proportion about the -X axis during 90°-dip normal fault rupture due to the opposite directions of the base displacements of these two simulations. In the case of the 30°-dip normal fault simulation, the development of two rupture surfaces with opposing senses of shear results in both the +X and -X axes making up significantly large proportions of the dominant Cartesian components.

The tendency for particles to rotate in the sense of shear as well as the dilative volumetric strains within the shear bands seen in Figs. 3.8 and 3.9 are consistent with observations of bending and buckling of column-like structures in 2D simulations (Iwashita & Oda 2000). However, 2D explanations are only partially applicable to the present simulations. In all simulations, the +X or -X axes made up the largest proportion of dominant Cartesian components but not always the majority proportion. More than 50% of dominant Cartesian components are in directions other than the direction associated with the sense of shear, and approximately half of dominant Cartesian components are about the +/-Y or +/-Z directions. Even those particles having the +/-X axes as their dominant Cartesian component will still have smaller magnitude components of rotation about the +/-Y and +/-Z axes. While the tendency for particles to rotate in the sense of shear is evident, significant out-of-plane rotations are associated with the particle kinematics during earthquake fault rupture propagation through soil.

3.5.5 Contact Forces

The capability to calculate interparticle contact forces is a unique advantage of DEM relative to physical tests and continuum analytical methods. The forces present in the earthquake fault rupture simulations are used to gain insight into its underlying mechanisms. Fig. 3.12 shows the final strong contact force network in select simulations performed with particles scaled by a factor of 20. As stated previously, the strong contacts are normalized by their depth below the surface and exceed one standard deviation above the median value of contact force normalized by depth in the assemblage just before the onset of fault rupture. The stress distribution and void ratio distribution for this particle assemblage are shown in Fig. 3.6 without the use of larger boundary particles.

The reverse fault force networks in Fig. 3.12a-c show a thinning of the strong force network with increasing fault dip. The half-arch structure of strong contact forces observed in the anchor pull-out simulation also develops in the 90°-dip reverse fault case in Fig. 3.12c. Fig. 3.12a shows strong contact forces percolating from the hanging wall lateral boundary to the rupture surface through regional horizontal compression (Prucha et al. 1965). This lateral compression during shallow reverse fault rupture can produce linear or upward curving rupture surfaces. The reverse fault simulation results indicate that stress relief occurs near the ground surface when the shear fault rupture surface shallows in dip as it approaches the ground surface over the downthrown block. As the reverse fault dip angle increases, the stress relief reduces the magnitude of regional horizontal compression and produces more localized arches of strong contact forces around the shear rupture zone.

Arches of strong contact forces reflective of that seen during trapdoor displacement in Fig. 3.4a develop in the 45°-dip and 60°-dip normal fault cases in Figs. 3.12d-e. Unlike in trapdoor displacement, only one discontinuity in the base exists in the normal fault rupture simulations. The horizontal component of hanging wall displacement during shallow normal fault rupture relieves horizontal stresses on both sides of the bedrock fault and causes the particles on the hanging wall side to displace towards the footwall to maintain horizontal equilibrium. The strong forces in the arch structure appear much lower in magnitude than those that develop for the reverse fault simulations, which indicates that the arch develops largely from a reduction in the magnitudes of the forces below the arch instead of solely from increased shear stresses along the rupture surface. Although the force arches for the 45°-dip and 60°-dip normal faults appear similar, a graben is associated with the 45°-dip normal fault of Fig. 3.12d but not with the 60°-dip normal fault of Fig. 3.12e. The mechanism behind graben formation is discussed in more detail later. The strong force network in Fig. 3.12f is a mirror image of that in Fig. 3.12c due to the kinematic similarity of both simulations. The forces are predominantly transferred through the arched network of strong contact forces and not through the material located further away from the rupture surface.

Fig. 3.13 compares the orientations of the strong contacts normalized by depth for two different cases. The vertical orientations of the strong contacts in the initial state in Fig. 3.13a suggest that the deposit is largely supported through column-like structures of strong contacts (Iwashita & Oda 2000). Reverse fault rupture induces widespread reorganization of the contact force structure as shown in Fig. 3.13b. The passive loading conditions increase the number and magnitudes of the contact forces oriented closer to the horizontal direction. The normal fault scenario shown in Fig. 3.13c shows little change to the orientation of the strong contact forces, because the active loading conditions of normal fault rupture tend to reduce the magnitudes of existing contacts rather than create new contacts.

3.5.6 Mechanism of Graben Formation

The stress arching phenomenon does not always persist during shallow-dipping normal fault rupture. Fig. 3.14 shows the evolution of the depth-normalized strong force network for the 30°-dip normal fault simulation. As shown in Fig. 3.14a, stress arching does appear at earlier stages of the 30°-dip normal fault displacement. The downward displacing graben material is analogous to the downward displacing material above a trapdoor. The weight of material that will eventually form the graben is temporarily supported by the surrounding material at h/H = -0.04, which creates the arched structure of strong contact forces.

A bridge of strong contact forces is evident at the top of the arched structure that transfers load between the lateral sides of the graben. The horizontal component of hanging wall displacement reduces the magnitudes of these forces along the top of the arch as shown in Fig. 3.14b at h/H = -0.06. The graben gradually loses its lateral support during continued lateral extension of the particle assemblage. Eventually the bridge of strong contact forces collapses, which allows the graben block of particles to displace downward relatively uniformly under the pull of gravity. Fig. 3.14c shows the strong force bridge completely collapsed at h/H = -0.08. The gap in the strong contact forces that is visible in Fig. 3.14a-b below the arch is filled in Fig. 3.14c because the weight of the graben transfers from the surrounding particles to the bedrock below it.

3.6 Discussion

Key mechanisms of shear rupture development in particulate media are better elucidated through the DEM analyses than with conventional continuum-based analyses. For instance, the particle rotations shown in Figs. 3.8 and 3.9 are judged to be better indicators of the shear rupture location than the homogenized strains. Particle rotations have the advantage of showing the pending location of a rupture surface well before it is clearly defined through strains or visually. The link between soil deformations resulting from trapdoor displacement or normal fault rupture is clearly shown through similar arched patterns of strong contact forces, and the distribution of strong contact forces proved useful in revealing the collapse mechanism involved in graben formation. While DEM cannot currently replace continuum-based methods in engineering practice due to its high computational costs, its capability of showing the micro-mechanical mechanisms in boundary deformation problems is desirable.

The trapdoor, anchor pull-out, and surface fault rupture simulations presented in this paper all involved dense particle assemblages to emphasize the important role of dilation. Analyses of these problems with materials of various relative densities is examined in another paper as this is an important consideration. Bray et al. (1994) observed dramatically different surface fault rupture characteristics in dense and loose materials. While dense materials exhibited sharp localizations and often distinct fault scarps at the ground surface, loose materials tended to locally absorb distinct bedrock offsets and distribute this offset over a broad zone, thus producing little to no perceived surface deformation. DEM is well-suited to analyze these different scenarios. As shown in the DS test simulations, DEM can capture a wide range of shearing responses in dense and loose materials. The distributed deformation of the loose particle assemblage along the specimen height shown previously in Fig. 3.2a is analogous to the local absorption observed in surface fault rupture through loose soil. Surface fault rupture simulations with materials having a loose relative density would also exhibit broad deformation instead of the sharp localizations seen in this study. Study

of the distinct shear localizations and shear rupture propagation in this study requires the material to be sufficiently dilative for a shear band to develop.

3.7 Conclusion

DEM is capable of capturing important characteristics of the shear rupture process. Simulations of direct shear tests at different void ratios showed that DEM can capture both contractive and dilatant behavior. The results show higher peak friction angles and higher maximum rates of dilatation in materials having lower void ratios, and the residual strengths are approximately the same regardless of initial void ratio. Simulations performed under various normal stresses revealed a reduction in strength, dilatancy, and stiffness with increased applied load, but the effect of stress was not as strong as the effect of void ratio in the DEM simulations due primarily to the lack of modeling particle crushing.

A procedure that constructs a model for level ground at-rest earth conditions is developed for generating a particle assemblage with linearly increasing stress distribution and a K_0 between 0.4-0.45. The procedure also produces a void ratio distribution that decreases slightly with depth. Assemblages of particles can be generated with uniformly scaled particle sizes or with zones of smaller diameter particles across the zone of interest. The size of the particles and the use of larger boundary particles does not significantly affect the void ratio or stress distribution.

Anchor pull-out and trapdoor simulations are performed to analyze the stress-arching phenomenon. An arched structure of strong contact forces develops in the trapdoor simulation as the weight of the downward displacing material partially transfers to the surrounding stationary material. Half-arched structures emanating away from each other develop in the anchor pull-out simulation. The mechanisms of stress arching are present in normal fault displacement cases, and 90°-dip reverse and normal fault rupture produce half-arched structures similar to those developed in the anchor pull-out simulation.

The progressive development of the rupture surface is shown through 60°-dip reverse fault and 30°-dip normal fault simulations. Particle rotations, frictional dissipation, volumetric strains, and shear strains depict the response of granular media. The shear rupture surfaces developing from reverse and normal faults with dips between 30° and 90° are shown to be consistent with those estimated using the empirically supported expression of Cole & Lade (1984). Particle rotations and frictional dissipation provide excellent signatures of propagating shear rupture because they delineate effectively the final form of the rupture surface before the rupture surface develops fully. Assemblage deformations are concentrated in thin shear rupture surfaces. The statistics on particle rotations show particles tend to rotate in the same sense of shearing as viewed from within a single shear band. Although there is a bias towards rotation in the sense of shear, significant out-of-plane components of rotation emphasize the importance of performing 3D simulations with DEM.

The evolution of contact forces is discussed for several cases of normal and reverse fault displacements. Widespread regional horizontal compression is shown to reduce with increasing fault dip angle during reverse fault rupture. Normal faults are shown to be associated with the reduction of horizontal forces, causing little disturbance to the strong contact force structure. However, reverse fault rupture produces widespread reorientation of strong contact forces and an increase in the magnitude of horizontally oriented contacts. The mechanism of graben formation is shown to be a loss of lateral support and a reduction in horizontally oriented contact force

magnitudes due to a large horizontal component of hanging wall displacement in shallow normal fault rupture.

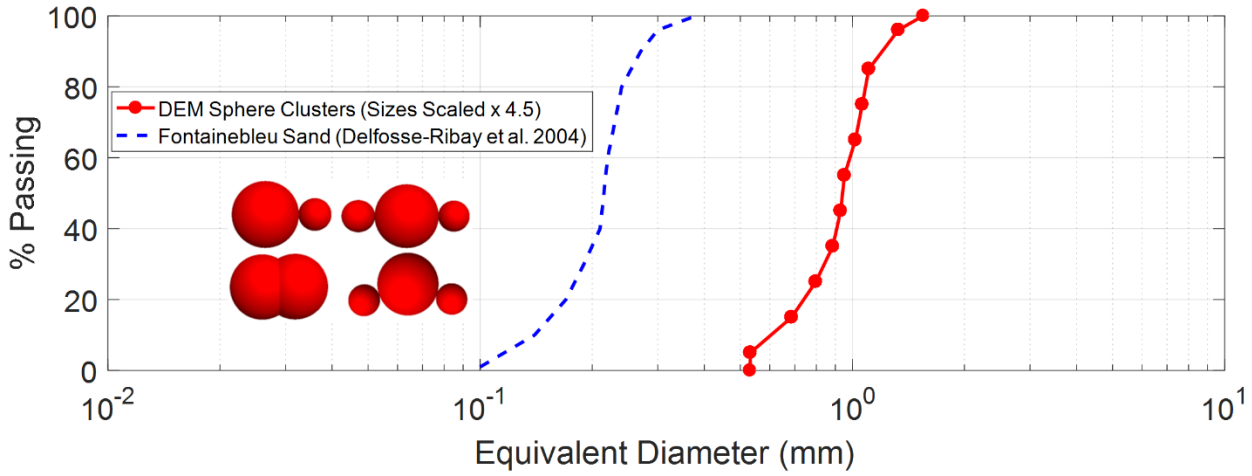

Fig. 3.1. Particle shapes used in DEM simulations and grain size distribution of a particle assemblage scaled relative to that of Fontainebleau sand (Delfosse-Ribay et al. 2004).

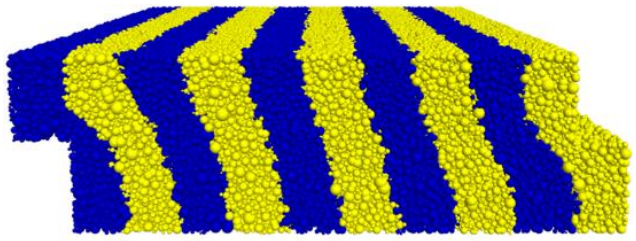

(a) $e_0 = 0.891$

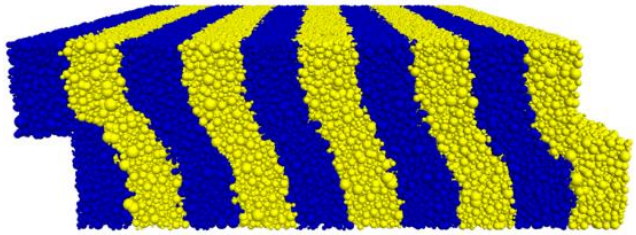

(b) $e_0 = 0.794$

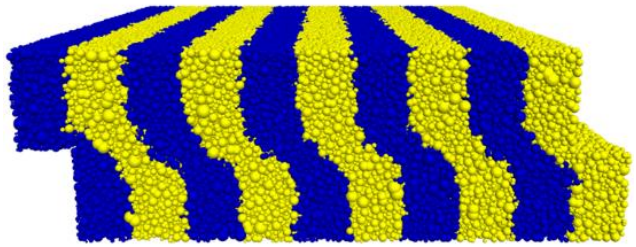

(c) $e_0 = 0.653$

Fig. 3.2. Representative results from DS test simulations (σ_n = 106.7 kPa).

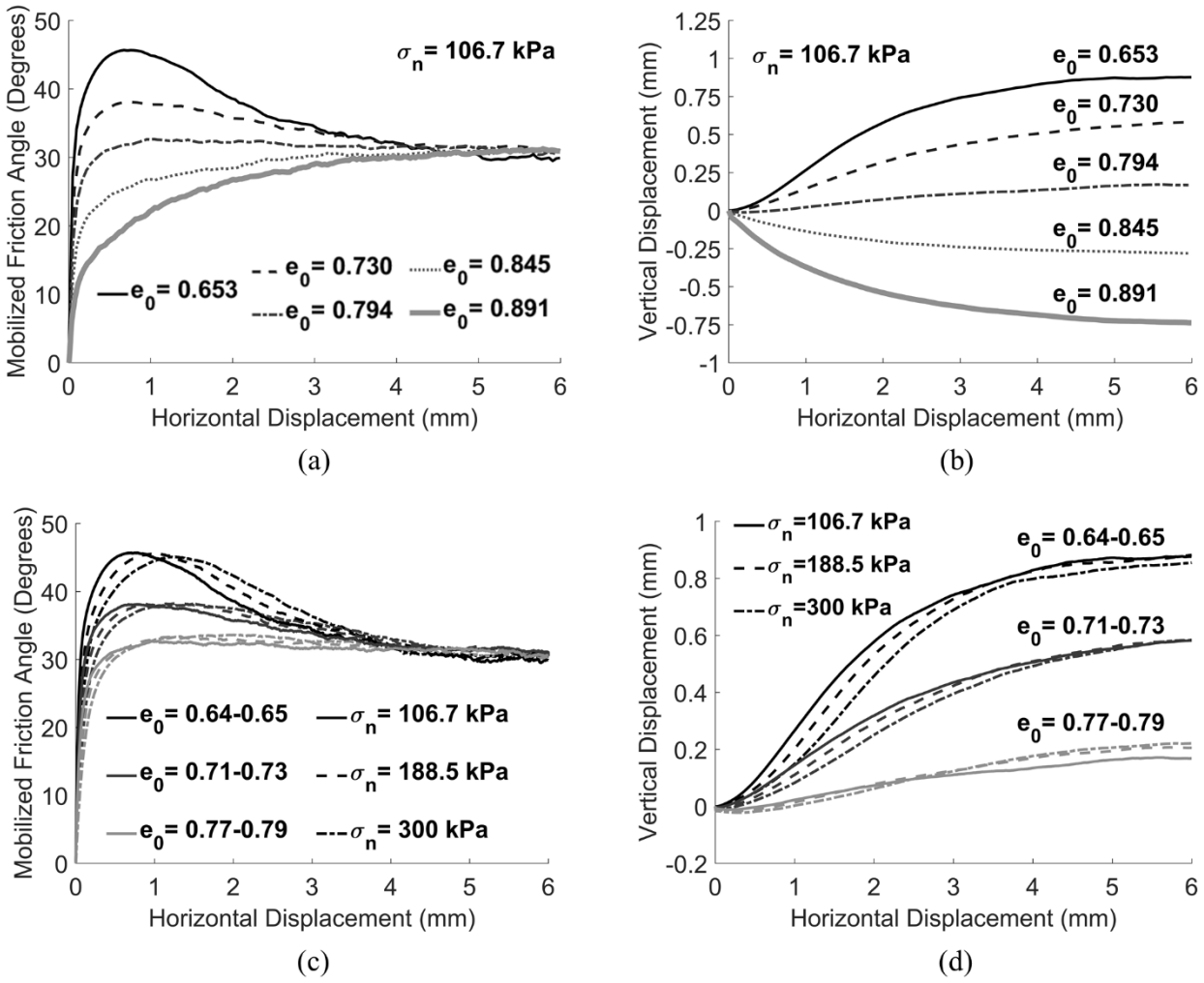

Fig. 3.3. DEM DS test simulation results: (a) mobilized friction angle under an applied normal stress of 106.7 kPa, (b) vertical displacement of the upper loading platen under an applied normal stress of 106.7 kPa, (c) mobilized friction angle for dilatant specimens under different applied normal stresses, and (d) vertical displacement of the upper loading for dilatant specimens under different applied normal stresses.

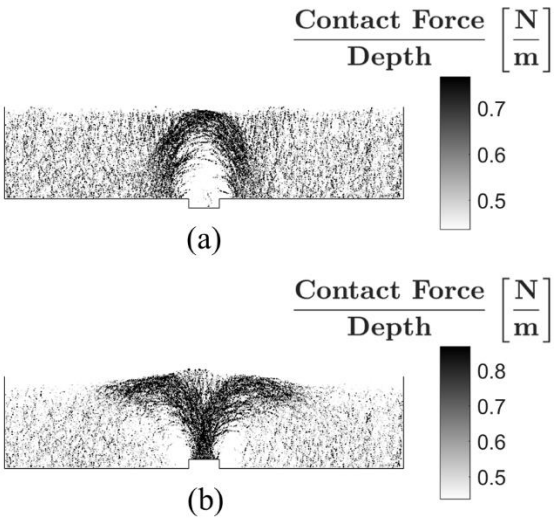

Fig. 3.4. Normalized strong contact force network for: (a) trapdoor simulation and (b) anchor pull-out simulation.

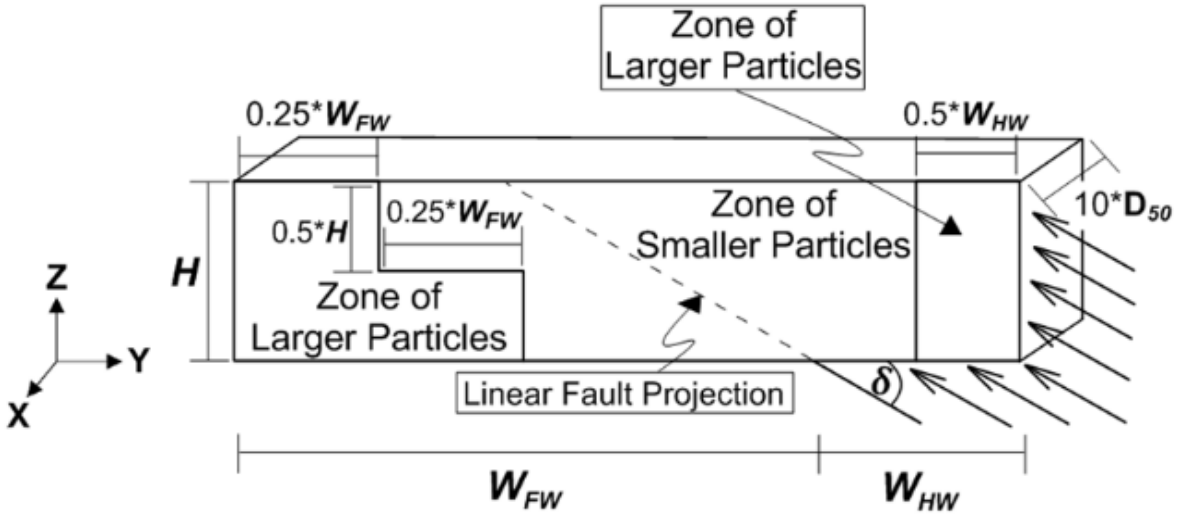

Fig. 3.5. Arrangement of particles into zones of smaller particles where shear rupture occurs and zones of larger particles at the boundaries.

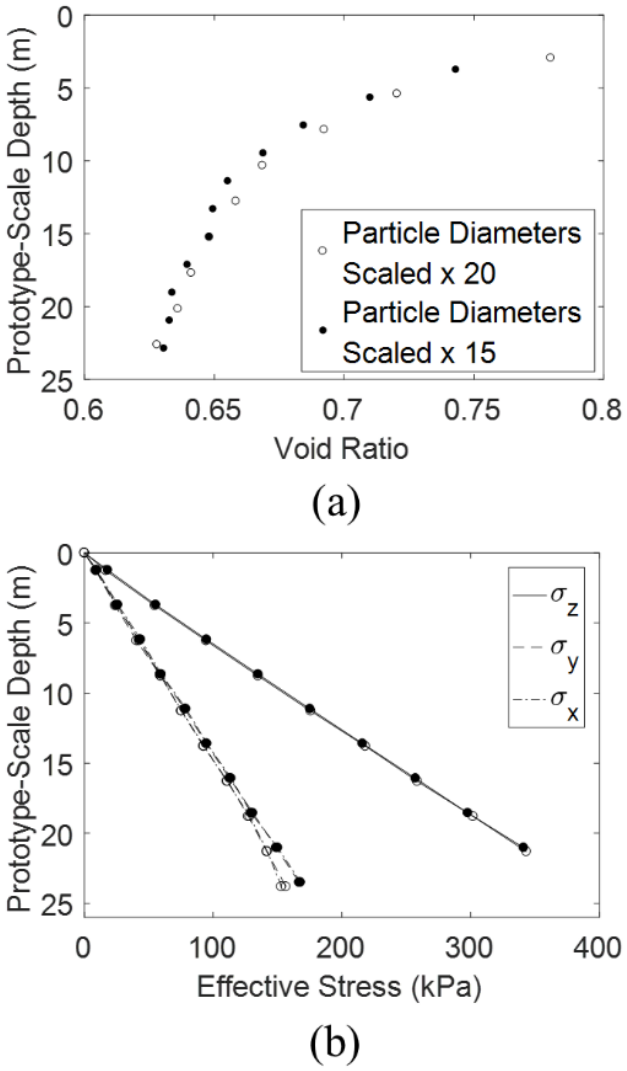

Fig. 3.6. (a) Void ratio profile and (b) stress profile for a particle assemblage scaled by a factor of 15 with larger boundary particles and a particle assemblage scaled by a factor of 20 without larger boundary particles.

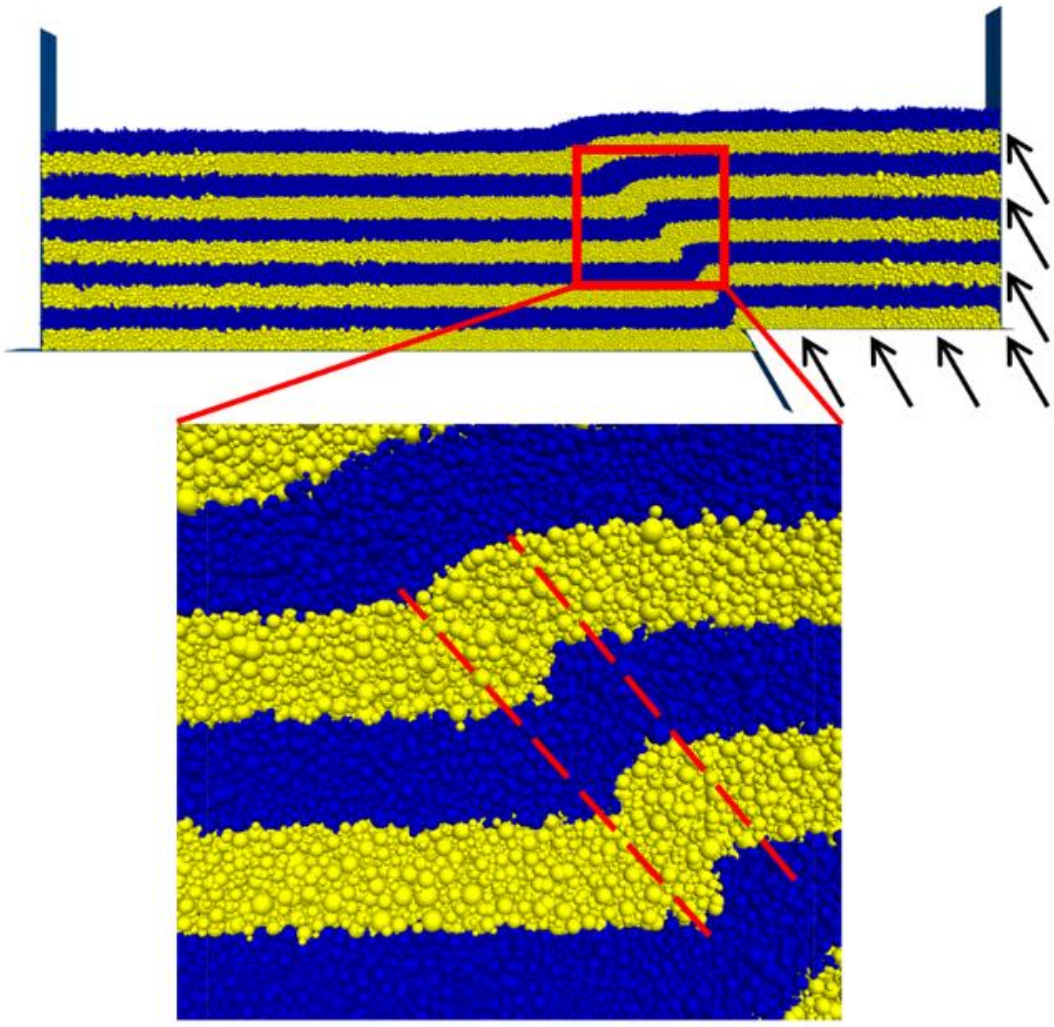

Fig. 3.7. Shear band developed in a 60°-dip reverse fault simulation at h/H = 0.1. The dashed red lines delineate the width of the shear band.

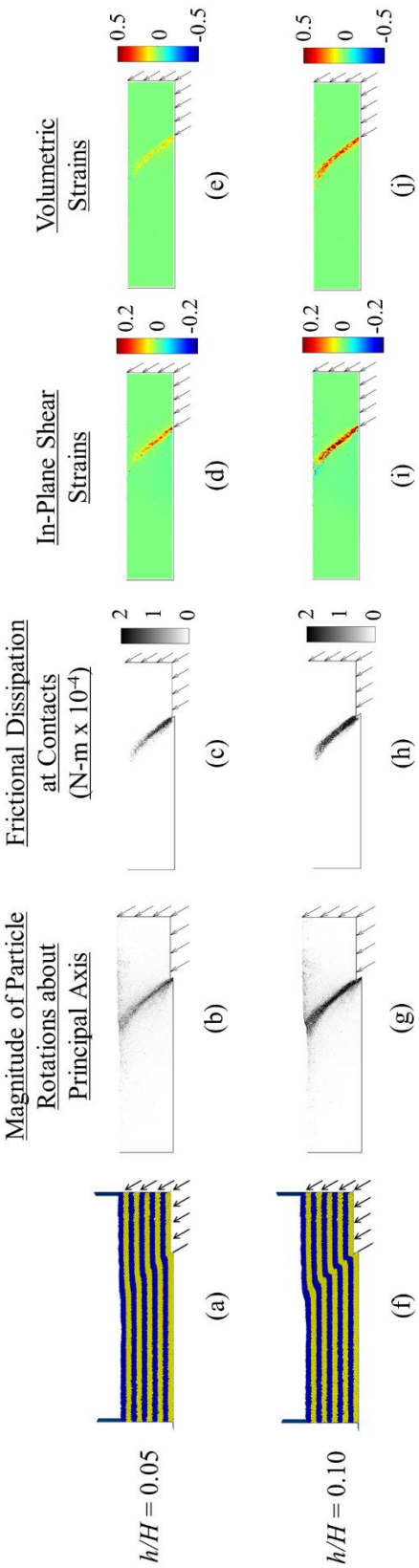

Fig. 3.8. Evolution of surface fault rupture at various stages for a 60°-dip reverse fault.

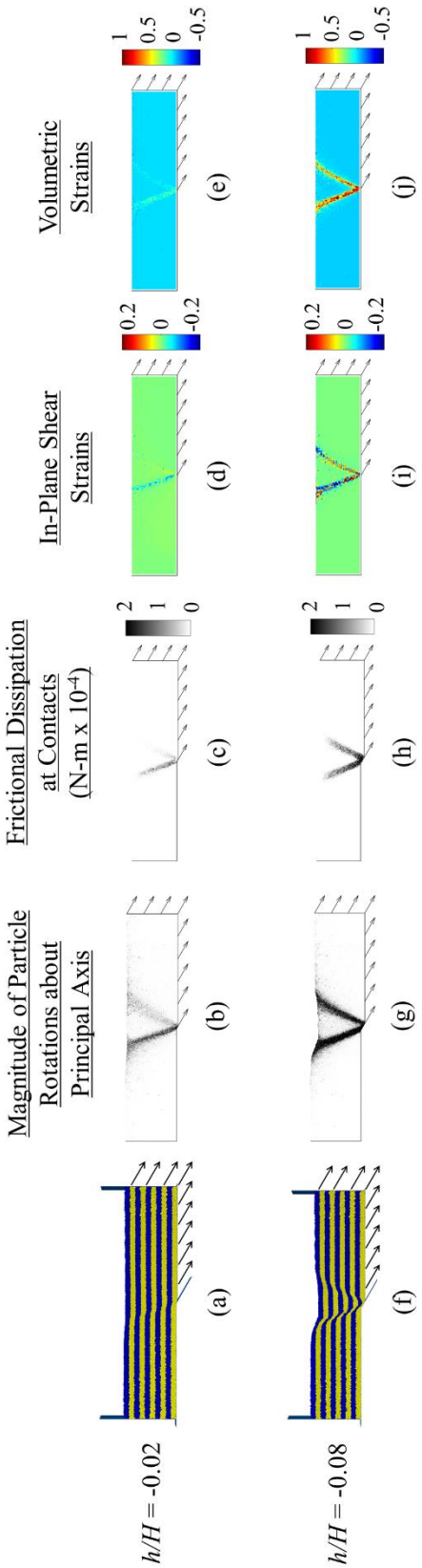

Fig. 3.9. Evolution of surface fault rupture at various stages for a 30°-dip normal fault.

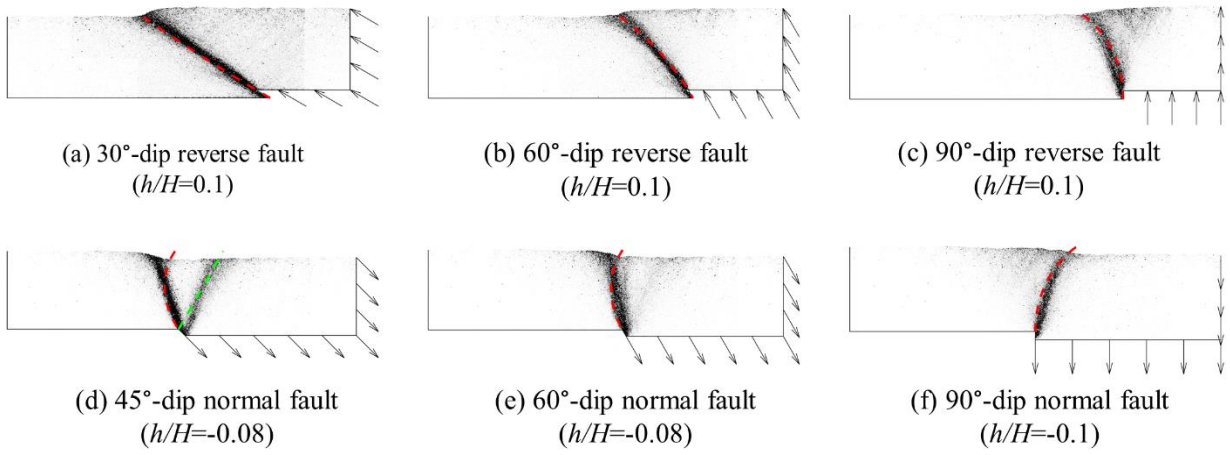

Fig 3.10. Comparison of DEM-simulated and Cole & Lade (1984) model shear rupture surfaces. The DEM-simulated shear rupture surfaces are delineated using zones of maximum particle rotation. The Cole & Lade (1984) model shear rupture surfaces are shown as red or green dashed lines.

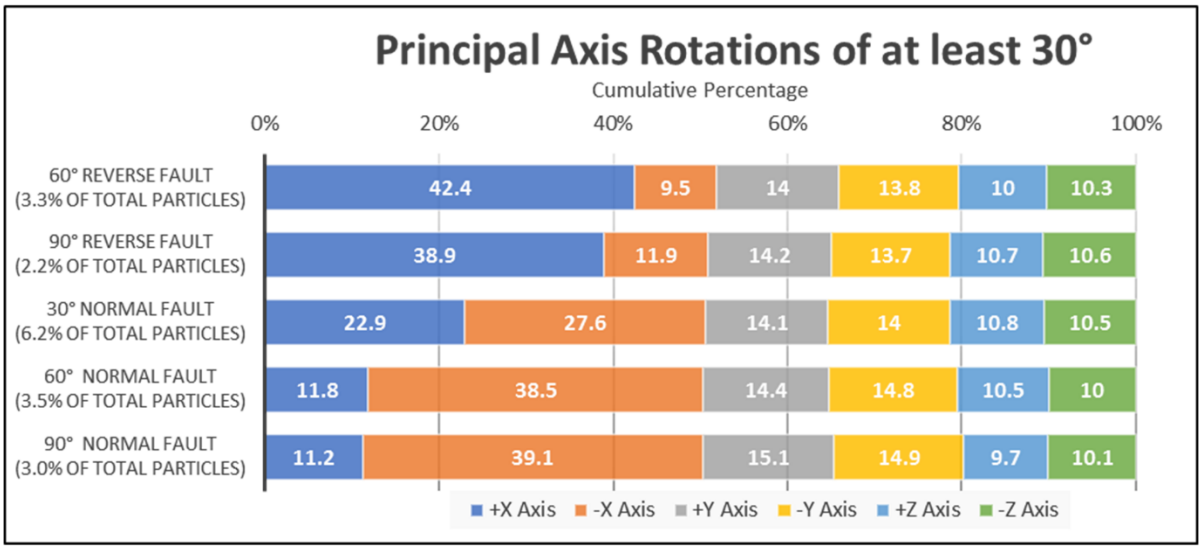

Fig. 3.11. Statistics for the dominant Cartesian components of rotation for particles rotating by 30° or more about their principal axis. The percentage of particles exceeding a rotation of 30° is shown on the right-hand side for each simulation.

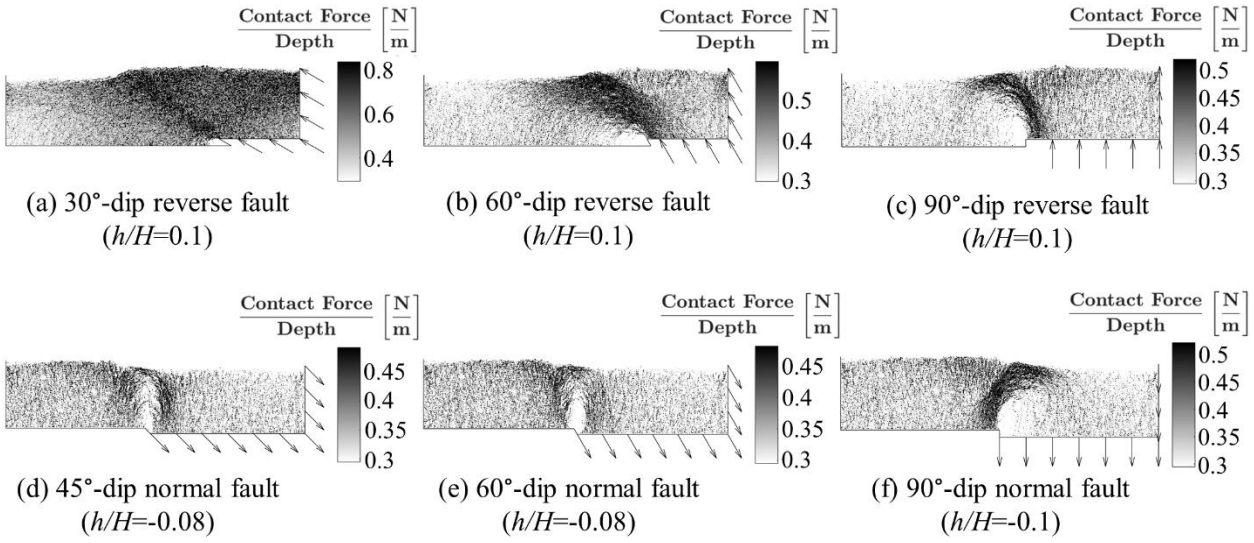

Fig. 3.12. Distribution of strong contact forces normalized by their depth below the surface for reverse and normal fault simulations with varying dip angles.

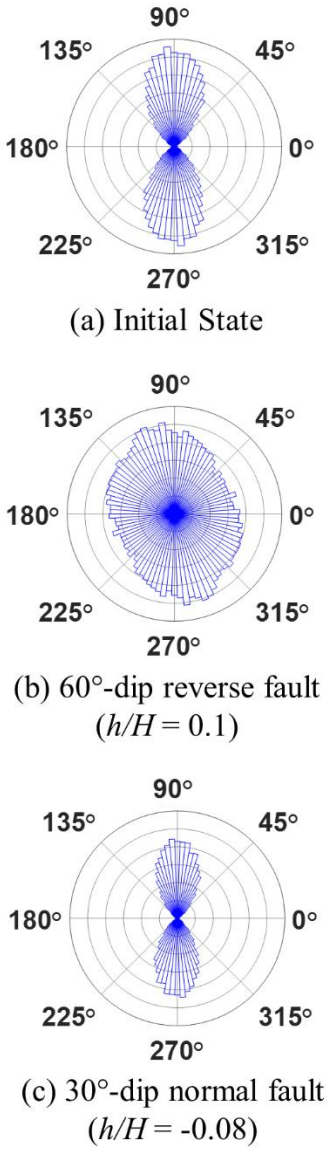

Fig. 3.13. Polar histograms of the orientations of strong contact forces normalized by depth in *Y*-Z plane: (a) Initial state, (b) *h/H* = 0.1 for a 60°-dip reverse fault, and (c) *h/H* = -0.08 for a 30°-dip normal fault. Radial contours are in increments of 200 contacts.

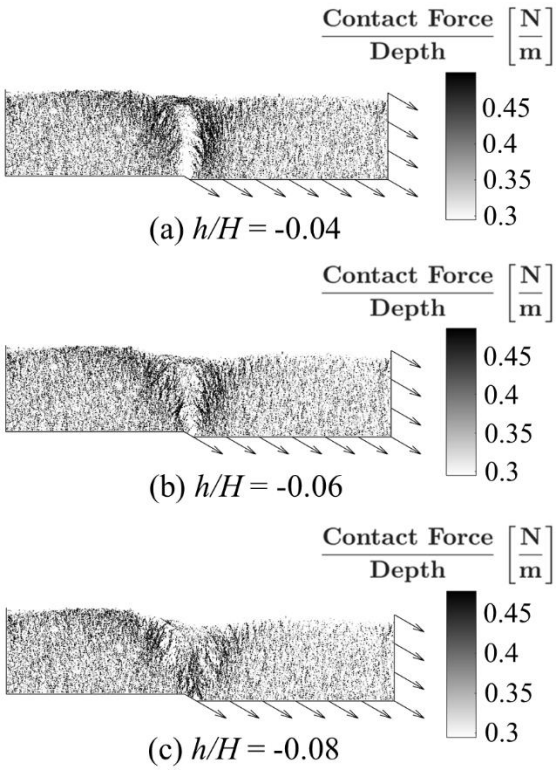

Fig. 3.14. Stages of graben formation for a 30º-dip normal fault shown through networks of strong contact forces normalized by their depth below the surface.

CHAPTER 4: DISTINCT ELEMENT SIMULATIONS OF EARTHQUAKE FAULT RUPTURE THROUGH MATERIALS OF VARYING DENSITY

The majority of this chapter is taken directly from a manuscript published by Soils and Foundations *titled "Distinct Element Simulations of Earthquake Fault Rupture through Materials of Varying Density" (Garcia & Bray 2018b). Jonathan Bray is the only co-author of this manuscript.*

4.1 Introduction

The permanent ground displacements produced by earthquake surface faulting pose a significant hazard to the built environment in near-fault regions. Linear infrastructure such as pipelines, roads, and high-speed rails often cannot avoid traversing an active fault trace, and life-threatening damage can result if large fault offsets occur beneath a structure. The ductility of the soil affects the earthquake fault rupture propagation process and its surface manifestations (e.g., Bray et al. 1994a,b, Bray 2001, Anastasopoulos et al. 2007, and Oettle & Bray 2013a,b). The ductility of granular soil is strongly affected by its dilatancy, which is in turn determined by its void ratio and effective confining stress. Void ratio and its effects can be modeled directly by the distinct element method (DEM; Cundall & Strack 1979). DEM provides quantitative insight into the development of shear rupture within soil while also capturing the inherent granular nature of soil. This study uses DEM to analyze earthquake surface fault rupture through particle assemblages having different void ratio distributions and shows how void ratio affects the resulting ground surface deformation. All simulations are performed using the Particle Flow Code (PFC3D) (Itasca 2014) with 3D sphere-cluster particles (O'Sullivan & Bray 2002).

The paper is organized into seven sections including this introduction. Section 2 briefly reviews relevant case studies, physical experiments, and numerical models of surface fault rupture. Section 3 presents the results of direct shear test simulations used to characterize particle assemblage properties. Section 4 describes the preparation of the fault rupture granular media DEM model. Section 5 explores the influence of void ratio on earthquake fault rupture propagation through soil. Section 6 analyzes the micro-scale characteristics of surface fault rupture through particle assemblages with different void ratio distributions. The paper ends with concluding remarks.

4.2 Previous Work

The effects of soil ductility on ground surface deformations resulting from earthquake fault rupture are documented in several field case histories (e.g., Bray et al. 1994a, Bray 2001). Ruptures through brittle materials tend to localize within relatively thin zones, but ductile soils distribute distinct base rock fault offsets over a wider area. For example, surface fault rupture along the Homestead Valley fault during the 1992 Landers earthquake was confined to a zone only 0.5 m wide when in outcropping weathered bedrock but spread out over a 5-m wide zone of distributed deformation when crossing through alluvial material overlying the bedrock (Lazarte et al. 1994). Bray et al. (1994a) describe a case from the 1964 Alaska earthquake in which 2.3 m of vertical displacement on the Patton Bay fault produced no visible offset in its continuation at the top of a 150-m high fractured rock cliff. Rupture is more difficult to discern when it is widely spread through ductile soils, and the rupture seems to disappear entirely in some cases (Bray 2001).

Therefore, ductile soil deposits overlying bedrock faults are capable of locally absorbing bedrock offsets, yielding smaller distinct displacements at the ground surface.

The characteristics of ground surface deformation affect the type of surface fault rupture hazards that can cause structural damage. Surface fault rupture hazards include distinct shear rupture, differential settlement, compressive or tensile strains, and tensile cracks (Bray 2001). Distinct shear rupture is the most severe surface fault rupture hazard and typically governs design of infrastructure built near active faults. The height of a distinct fault scarp is usually lower than the amount of bedrock displacement, but once a rupture surface outcrops at the surface, the ratio between incremental surface displacement and incremental bedrock displacement is closer to one (Lade et al. 1984).

Several physical model studies explored the effects of soil ductility on surface fault rupture. Bray et al. (1993) found that the height of the shear zone in laboratory models of rupture through saturated clay was related to the soil's failure strain, which is a direct indicator of soil ductility. Lazarte & Bray (1996) showed that ductile clay mixtures displayed broadly distributed surficial offsets in laboratory strike-slip models, and brittle clay mixtures exhibited more distinct surface offsets. Numerical simulations have also captured the important role of soil ductility in the development of surface fault rupture, typically through the use of nonlinear constitutive models in continuum analyses (e.g., Bray et al. 1994b, Anastasopoulos et al. 2007, and Oettle & Bray 2013a). For example, the finite element simulations of Anastasopoulos et al. (2007) showed greater fault scarp heights in medium-dense soils than in medium-loose soils. The fault scarps also developed at the surface at lower base rock displacements in the medium-dense models. Limited DEM analyses of surface fault rupture have been performed. Hazeghian & Soroush (2016) performed DEM simulations of surface fault rupture using 2D disks with added rotational resistance and showed that the fault rupture trends in their dense DEM assemblages are consistent with well-established localization phenomena observed in real granular soils during fault rupture. Other 2D DEM simulations performed by Hazeghian & Soroush (2015, 2017) showed that the ground surface slopes less and requires greater hanging wall displacements for the fault rupture surface to reach the ground surface in looser soils. Hazeghian & Soroush (2017) point out that 2D assemblages exhibit excessive dilatancy, because out-of-plane movement is restricted. Hence, 3D DEM simulations are required to capture more accurately the true response of soil grains, as discussed in Chapter 3. The work of Hazeghian & Soroush (2015, 2016, 2017) was done using a graphics processing unit to reduce the length of time to run a single simulation. This study takes advantage of the parallel processing capabilities of PFC3D and uses an Intel Xeon central processing unit with 8 computing cores and a clock speed of 3.40 GHz to reduce the runtimes of the simulations.

4.3 Direct Shear Test Simulations

Direct shear test DEM simulations of 3D spheres have been performed by several investigators (e.g., Cui & O'Sullivan 2006). Fewer DEM simulations of this problem have used 3D sphere-cluster assemblages (O'Sullivan & Bray 2002), which due to their non-spherical shape resist excessive rolling. This study builds on the work of Chapter 3 through simulating the response of sphere-cluster assemblages of varying void ratio using PFC3D (Itasca 2014). The length and width of the direct shear test box are 60 mm, and its initial height is 20.5 mm. Shearing is induced by quasi-statically moving the upper box while keeping the lower box stationary. As discussed in detail in Chapter 3, the ratio of the average unbalanced force on all particles to the average total

force acting on all particles (R_{avg}, Itasca 2014) was maintained below 0.0005 as a condition for quasi-static shearing. An index of unbalanced forces is commonly used in DEM studies to monitor quasi-static conditions during shearing (e.g., Ng 2006).

In keeping with the suggestions of Shibuya et al. (1997) to interpret direct shear tests as quasi-simple shear, the lateral walls are frictionless and the upper loading platen independently moves vertically without rotating to maintain a constant normal stress. 3D sphere-clusters are used to capture the inherent rotational resistance of real non-spherical sand and gravel grains. 100,986 sphere-clusters are generated within the direct shear box using a radius expansion procedure. Four sphere-cluster shapes are used in equal proportions to develop the particle size distribution shown in Fig. 4.1, which has a coefficient of uniformity (C_u) of 1.57 (Delfosse-Ribay et al. 2004). The number of particles used is sufficiently large to minimize particle size effects in the direct shear test simulations, because Ni et al. (2000) showed that particle size has little effect on the results of direct shear test simulations with sphere-clusters if the total number of particles exceeds 30,000. Normal stresses of 107, 188, and 300 kPa were applied to the top of the direct shear box in the DEM simulations. The linear contact model governing particle interactions has an elastic Young's modulus of 200 MPa, and the normal spring stiffness at each contact is 4 times higher than the shear spring stiffness. The interparticle friction coefficient (μ) is varied between 0.0 and 0.5 during radius expansion to obtain lower or higher initial void ratio values (e_0); μ=0.5 during shearing.

The results of direct shear tests performed with an applied normal stress of 107 kPa are shown in Fig. 4.2. These results are representative of the typical effect of void ratio on shearing response. The normal stress of 107 kPa matches that used for the direct shear test calibrations by Anastasopoulos et al. (2007). The mobilized friction angle (ϕ) is calculated using the Coulomb definition of frictional strength in a cohesionless material:

$$tan\phi = \frac{\tau}{\sigma_n} \tag{4.1}$$

where τ is the sum of all forces acting on the lower shear box in the direction of box movement, and σ_n is the normal stress applied on the upper loading platen of the upper shear box. Strain softening in Fig. 4.2a and dilatancy in Fig. 4.2b are observed in simulations of sphere-cluster assemblages with $e_0 < 0.8$, and the assemblages with the lowest void ratios exhibit the most brittle offset. The monotonically rising mobilized friction angle for the two loosest particle assemblages is characteristic of ductile materials with contractive soil responses. The densest particle assemblages with e_0=0.64-0.65 have angles of dilation (ψ) between 18° and 20°. Particle assemblages with e_0=0.71-0.73 and e_0=0.77-0.79 produce ψ=10°-11° and ψ=3°-4°, respectively. Despite the simplifications inherent in DEM simulations, sphere-cluster assemblages with realistic contact properties capture key aspects of critical state soil mechanics in the direct shear test, which provides confidence that DEM can capture the development of shear rupture due to earthquake fault rupture.

4.4 Earthquake Fault Rupture DEM Model

4.4.1 Sandbox Experiment Model

Bransby et al. (2008a,b) performed a comprehensive series of geotechnical centrifuge experiments of earthquake fault rupture through dry, clean sand. Importantly, their experiments captured the stress-dependent stress-strain and volumetric strain response of soil. Their

experimental results are compared with the results of the PFC3D sphere-cluster analyses to evaluate the reasonableness of the DEM simulations. The dimensions of their centrifuge box are used to create the boundaries of the DEM model. A centrifuge scaling factor (n) of 115 is used to match the factor used by Bransby et al. (2008a, 2008b). This scaling factor is gradually applied by scaling the particle masses instead of gravity so that a longer stable time-step can be used. Scaling mass instead of gravity changes the scaling of time, but the difference in time scaling is negligible for quasi-static rates of boundary displacements (Wood 2004). The hanging wall is displaced quasi-statically in the dip direction a distance equal to 2% of the soil height every model second. This is equivalent to a rupture velocity of 4.2-4.5 mm/s in model scale in the dip direction. The time step is adjusted throughout the simulation and varies between 10^{-6} sec/step and $1.5x10^{-5}$ sec/step. As with the direct shear test simulations, R_{avg} is monitored throughout the simulation and maintained below 0.0005 to ensure that the conditions for quasi-static shear are met. In addition to monitoring R_{avg}, trial simulations were performed at slower rates of rupture to ensure that the rupture speed used is sufficiently slow for rate of rupture to not significantly affect the results of fault rupture propagation. All boundary lengths are reported in prototype scale.

The out-of-plane boundaries are periodic so that particles adjacent to the front and rear boundaries can interact, which appropriately models an infinitely long plane strain model undergoing dip-slip fault displacements. The periodic length is 4 m in prototype scale, which is approximately 10 times the median equivalent grain diameter. All simulations use zones of larger boundary particles located far enough away from the rupture surface to not influence its path as shown in Fig. 4.3. The sizes of the particles at the center of the model are scaled by a factor of 15 relative to the grain size distribution of the experimental Fontainebleau sand (Delfosse-Ribay et al. 2004), giving D_{50} = 3.3 mm. The larger boundary particles are 4 times larger in volume. Dense, medium-dense, medium-loose, and loose assemblages with the void ratio distributions shown in Fig. 4.4 are prepared by setting μ = 0.05, 0.15, 0.3, and 0.5, respectively, during preparation of the particle assemblages. At the end of the preparation, μ is reset to 0.5 for all cases. The respective heights (H) of the simulations in the prototype scale are 24.7 m, 24.6 m, 24.8 m, and 25.0 m for the dense, medium-dense, medium-loose, and loose assemblages, respectively. The model width (W) is 109 m, and W_{HW} ranges from 29-35 m in reverse fault simulations and 46-55 m in normal fault simulations. The number of particles increases with decreasing void ratio, so the dense, medium-dense, medium-loose, and loose assemblages contain 175,660, 164,225, 158,959, and 154,402 sphere-clusters, respectively.

The gradual increase in the particle masses to achieve centrifuge stress conditions produces a consistent vertical stress distribution in all models, which reflects level-ground conditions as shown in Chapter 3. The resulting lateral earth pressure coefficient (K_0) is 0.40-0.45, which is consistent with that of naturally deposited, normally consolidated granular soils (Holtz & Kovacs 1981). The dense, medium-dense, medium-loose, and loose assemblies have median void ratios of 0.65, 0.73, 0.83, and 0.90, respectively. Some void ratio reduction with increasing depth is reasonable because cohesionless, angular soils tend to decrease in void ratio with increasing vertical effective stress during 1D compression (Pestana & Whittle 1995). Furthermore, deeper granular soil deposits are usually older, and older soils in seismically active regions have a longer history of densification through seismic shaking than younger soils. Thus, the void ratio and stress profiles within the DEM model are reasonable.

4.4.2 Sandbox Experiments and DEM Simulations Comparison

Chapter 3 showed that DEM simulations with sphere-clusters captured the response of dense particle assemblages to base deformation from reverse and normal fault offsets at a variety of dip angles. Additional DEM simulations are performed in this study to explore comparisons between the results of sandbox experiments and corresponding DEM simulations of granular media of a variety of void ratio profiles. One simulation was prepared to match the conditions of Test 28 by Bransby et al. (2008b) as closely as possible. This centrifuge test modeled the response of a medium-loose sand deposit undergoing a 60°-dip reverse fault offset. This simulation contains 148,414 sphere-clusters and a D_{50} of 2.2 mm as opposed to the D_{50} of 3.3 mm in the other simulations. The periodic length is $10D_{50}$, and the prototype height is 15.2 m, which closely matches the 15.1 m depth of soil in centrifuge Test 28.

Test 28 of Bransby et al. (2008b) was performed on Fontainebleau sand in a state that produced a relatively low angle of dilation (ψ) of about 6°. The DEM simulation was prepared at a void ratio profile to produce a similar ψ of about 5° throughout most of its depth. The void ratio ranged from 0.78 just above the bedrock to 0.86 at the surface. The critical state friction angle of the sand in Test 28 was 30.2°, and the DEM model value was 31.0°. The sand's peak friction angle was 35°; whereas the DEM model produced a peak friction angle of 32.5°. Capturing the angle of dilation and critical state friction angle are of greater importance in these analyses.

Fig. 4.5a and 4.5b show the results of Test 28 and the corresponding DEM simulation at a normalized base offset of about h/H=0.145 (h≈2.2 m), where h refers to the vertical displacement of the hanging wall, also called the fault throw. The coloring of the layers enables visualization of the rupture surface; it has no effect on the material's mechanical response. The shape of the shear rupture surface in Fig. 4.5b is similar to that in Fig. 4.5a in that it bends over the downthrown block as it nears the surface. In both Test 28 and its DEM simulation, the offsets of the layers are more distinct near the bottom of the particle assemblage and spread more widely up towards the surface. The shear rupture surface that develops in the physical model shown in Fig. 4.5a is seen more easily than in the DEM simulation shown in Fig. 4.5b because of the larger particle sizes used in the DEM simulation. Smaller-sized sphere-clusters would better define the shear rupture surface in a manner similar to mesh refinement in the finite element method, but doing so would increase computational time extensively. The most noticeable difference between the simulation and experiment is the sharper offset in the upper layers in Test 28. Additionally, the DEM particle preparation procedure produces higher void ratios near the top of the model, which makes the shallowest layer in the simulation more contractive than in Test 28.

Fig. 4.5c compares the vertical displacement profiles near the surface in Test 28 and the DEM simulation at a fault throw of 2 m. The vertical surface displacement profile is slightly different than a surface profile because its horizontal positions are based on the initial locations instead of their offset locations at a given stage of fault rupture. The vertical displacements of the DEM simulation are modeled 0.9 m below the actual ground surface to reduce the erratic deformations that can occur at the top of a clean sand. The shapes of the vertical displacement profiles nearly overlay one another. The maximum surface gradients in Test 28 and the DEM simulation are approximately 0.27 and 0.25, respectively, and occur 9 m away from the bedrock fault. The locations of the displacements in the simulation are offset from Test 28 by less than 1 m towards the footwall side along most of the fault scarp, and this offset increases to approximately 2 m at the bottom of the scarp. The greater offset at the bottom of the scarp reflects the more distinct surface offset in the physical experiment relative to that from the DEM simulation. The

FEM simulation results of Anastasopoulos et al. (2008a) also capture the vertical displacement profile in Test 28. Quantitative differences are expected given the simplifications inherent to DEM simulations. The sphere-clusters in Fig. 4.1 are simplified idealizations of the complex shapes of real sand grains, and the true distribution of void ratio can only be inferred in physical experiments. Overall, the quantitative differences between the vertical displacement profiles of the two numerical methods and the centrifuge experiment in Fig. 4.5c are minor, and the choice of method used to study surface fault rupture should be based on the type of insight a researcher seeks to gain.

Fig. 4.6 compares the vertical surface displacement profile of centrifuge Test 12 of Bransby et al. (2008a) at h=-1.6 m with the medium-dense assemblage having the void ratio distribution shown in Fig. 4.4 and a D_{50} of 3.3 mm. The density of Test 12 was considered to be "medium-loose", and the angle of dilation in Test 12 is approximately 6°. The angle of dilation for the medium-dense DEM assemblage is approximately 10°, and this angle will decrease to approximately 3° near the surface where the void ratio increases. The DEM fault scarp develops in the same vicinity of that of Test 12, although the DEM fault scarp is considerably wider. The increased width is primarily a result of the low void ratio near the surface that distributes the shear localization over a broader area. Moving to the right along the hanging wall side of the surface, the total vertical displacement of the DEM simulation approaches that of the fault throw. Between -2 m and 20 m, the vertical displacement magnitude of the simulation is actually greater than the base offset, which indicates the initial development of a graben structure and a secondary rupture surface dipping antithetically to the primary rupture surface. This graben development is not apparent in the centrifuge experiment. Cole & Lade (1984) predict that a graben will develop during normal fault rupture if the fault dip angle is less than 45°-ψ/2. The DEM simulation with ψ=10° is closer to this condition than the experiment with ψ=6° but does not exceed the threshold for a graben to develop fully. There are also differences between the imposed fault throw and the measured vertical displacement in the experiment, which is likely an artifact of the technique used to measure the displacements. Thus, the interpretation of the physical model test also has uncertainty that contributes to the differences observed between the test and the DEM simulations.

At such low levels of dilatancy, the DEM simulations are unable to develop the nearly vertical shear face that develops at the surface in Test 12. In Fig. 4.5c, the main difference between the DEM simulation and Test 28 occurred near the bottom of the fault scarp where the experimental surface gradient was highest. The reduction in void ratio near the surface distributes the shear band over a wider length and decreases the sharpness of the fault scarp. However, the similar values of ψ between the DEM simulations and centrifuge experiments at greater depths cause the fault scarps in Fig. 4.5c and Fig. 4.6 to emerge at approximately the same locations as those of the experiments. The depth where the void ratio begins to reduce is relatively shallow in Fig. 4.4, but if the void ratio reduction extended to greater depths then it would likely have greater potential to significantly change the path of fault rupture in the DEM simulations.

The scaling of particle size accounts for some of the difference between the DEM simulation and the experimental results shown in Figs. 4.5 and 4.6. The width of the shear band is wider in the DEM simulations, because the DEM particle sizes are scaled by factors of 10 and 15 relative to Fontainebleau sand and the shear band is typically about 8-16 grain diameters wide (Oda & Kazama 1998, and Wood 2002). The greater shear band width will make the fault scarp wider in the horizontal direction, because it increases the width of relative soil offset as seen in the layers of Fig. 4.5b. This dependence of shear band width on particle size is equivalent to the dependence of shear band width on mesh size in the finite element simulations of fault rupture performed by Anastasopoulos et al. (2007).

Particle size also effects the total volumetric dilation, but it does not affect the rate of dilation. Stone & Wood (1992) performed direct shear tests on 3 different samples of Leighton Buzzard sand with different grain size distributions and showed that total dilation was directly related to particle size, but the rate of dilation was equivalent between all 3 samples. Thus, particle size should not affect the fault rupture outcrop location because it is a function of rate of dilation and not total dilation (Cole & Lade 1984).

The experiments of Stone & Wood (1992) showed that finer sands tend to develop multiple rupture surfaces, with new surfaces developing when movements along previous surfaces become kinematically inadmissible. Once a rupture surface reaches the ground surface, all further bedrock fault displacement concentrates along that final rupture surface. In coarser sands, Stone & Wood (1992) showed that the first rupture surface is often the one that ultimately reaches the ground surface, and no other rupture surfaces develop. The strains that develop in the soil are a function of base offset, and similar rupture patterns develop in soils of different grain size distributions when compared at similar values of base offset normalized by median grain size. The ratio between base offset and grain size does not change when converting from the model scale to the prototype scale, so the strains that develop in the simulations are not affected by the conversion of model scale to prototype scale. However, the DEM particles are relatively coarse compared to Fontainebleau sand. As in the coarse sand experiments of Stone & Wood (2002), the first rupture surface that develops in the fault rupture simulations will most often be the rupture surface that eventually reaches the ground surface.

4.5 Influence of Void Ratio on Development of Fault Rupture Shear Surface

Analytical results of two fault rupture scenarios (i.e., 60°-dip reverse fault and 30°-dip normal fault) using the dense, medium-dense, medium-loose, and loose sphere-cluster assemblages shown in Fig. 4.4 are examined. Fig. 4.7 shows the 60°-dip reverse fault simulation results at h/H=0.15. The influence of void ratio on the mechanism of surface fault rupture is visible through distributions of particle rotations and frictional dissipation, as these are excellent signatures of shear rupture. Macroscopic signatures are visible in terms of volumetric strains obtained using the strain homogenization procedure of O'Sullivan et al. (2003). Shear bands develop in the dense and medium-dense assemblages as shown in Fig. 4.7a and 4.7b, respectively. The shear band in the medium-dense assemblage widens out more as it approaches the surface, showing broader deformation than in the dense assemblage. The shear band shape in the loose assemblage in Fig. 4.7c is difficult to visualize because the bedrock displacement is almost completely absorbed in the overlying ductile material. The dense and medium-dense assemblages show brittle thrusting features in which the layers in the upthrown block rise up and over the layers in the downthrown block, although these features die out towards the surface of the medium-dense assemblage. Such features are not observable in the loose assemblage.

The distributions of volumetric strains differ amongst the assemblages in Fig. 4.7. Positive volumetric strains are localized along the shear rupture surface in Fig. 4.7d, indicating high dilation within the shear band. The volumetric strains for the medium-dense assemblage in Fig. 4.7e are less localized and spread out toward the surface. The magnitudes of the volumetric strains decrease in the medium-dense assemblage when they spread over a wider zone yet remain positive, indicating that the material still dilates during shearing. Negative, contractive strains develop over a broad zone that flowers outward from bedrock to surface during rupture through the loose assemblage in Fig. 4.7f.

The particle rotations about their principal axis of rotation and the energy dissipated through friction provide further insight. The localized strains in the dense assemblage are associated with large particle rotations and large amounts of frictional dissipation confined within a thin zone along the rupture surface as shown in Fig. 4.7g and 4.7j. Within the shear band in Fig. 4.7g, the particles rotate by more than 60°. The particle rotations that exceed 60° for the medium-dense assemblage in Fig. 4.7h are initially confined to a narrow zone just above the bedrock fault. The rotations of the particles tend to reduce near the surface. A sharp transition from particles rotating by upwards of 60° to not rotating at all is visible on the hanging wall side of the shear zone in Fig. 4.7h; whereas a smoother transition from large rotations to no rotations is evident on the footwall side of the shear zone. The wider blue zone on the footwall side of the shear band in Fig. 4.7h indicates a zone of dragging that expands in width toward the surface on the downthrown block as it approaches the ground surface. The particles in this zone of dragging rotate by approximately 10°-20°, and the material exhibits little dilation as seen in Fig. 4.7e. Fig. 4.7k shows a similar drag-related gradient of frictional dissipation decreasing from the hanging wall side to the footwall side of the shear zone, but this gradient is less visible through frictional dissipation than through particle rotations. This zone of dragging is seen as a zone of relatively uniform overall rotation with little relative displacement between the particles within it. The existence of drag features also shows that the medium-dense assemblage is more ductile than the dense assemblage, due to its lower angle of dilation resulting from its higher void ratio profile. In the loose assemblage, the large particle rotations in Fig. 4.7i and frictional dissipation in Fig. 4.7m are highest near the base of the particle assemblage and spread out toward the surface over a much broader zone than in the dense and medium-dense assemblages. No signs of strain localization are visible through particle rotations or frictional dissipation in the loose assemblage.

The 30°-dip normal fault simulation results at h/H=-0.08 are shown in Fig. 4.8. A graben develops during shallow-dipping normal fault rupture with a primary rupture surface extending over the footwall and a secondary rupture surface extending over the hanging wall. Fig. 4.8a and 4.8b show distinct localizations in both the dense and the medium-dense assemblages on both sides of the graben. Distinct localizations do not develop in the loose assemblage in Fig. 4.8c, and the surface deformation at the outcrop location of the secondary rupture surface is insignificant. In Fig. 4.8a and 4.8b, the thicknesses of the colored layers significantly reduce due to lateral extension and downward movement of the graben in the dense and medium-dense assemblages. Such reduction of layer thicknesses is less prominent in the loose assemblage.

The bedrock fault offset-induced volumetric strains are positive and localized in each shear band for the dense and medium-dense assemblages in Fig. 4.8d and 4.8e, and limited volumetric strains develop within the body of the graben. The primary and secondary rupture surfaces in the dense assemblage are oriented approximately 20° and 32° to the vertical direction, respectively. In the medium-dense assemblage, the primary and secondary rupture surfaces are oriented approximately 30° and 40° to the vertical direction, respectively. The angles of the secondary rupture surfaces are consistent with the Cole & Lade (1984) model that predicts the secondary rupture surface to be oriented $45^o - \psi/2$ to the vertical, where ψ is 20° for the dense assemblage and 10° for the medium-dense assemblage. Only small differences (< 3°) between the results of the DEM simulation and the Cole & Lade prediction are observed. However, Cole & Lade (1984) predict more curvature of the primary shear rupture surface.

The volumetric strains for the loose assemblage undergoing normal fault offset are mostly positive due to lateral extension of the particle assemblage from the horizontal component of the hanging wall displacements. Although the distribution of volumetric strains is more widespread in

the loose assemblage than in the dense and medium-dense assemblages, the largest volumetric strains still tend to concentrate around two zones emanating linearly in opposite directions from the bedrock fault. Low magnitude contractive strains develop within the body of the graben, particularly at its edges closest to the shear bands. This apparent contraction at the graben boundaries shows that the material within the graben in the loose assemblage does not move as uniformly as in the case with dense sand.

Fig. 4.9 shows displacement contours for each assemblage at h/H=0.15 during 60°-dip reverse fault rupture. The contours are evenly spaced between zero and the prototype-scale magnitude of hanging wall displacement. Relative deformation is concentrated over the shear rupture surface with little strain development in the relatively intact assemblages of particles over the upthrown and downthrown blocks. The shear zone widens as ductility increases due to increasing void ratio. The more brittle, denser materials show the thinnest shear zones whereas the looser, more ductile soils have wider shear zones. In all simulations, the shear zones are thinnest at the bedrock level because of the boundary condition of distinct bedrock offset.

The rupture surfaces estimated using the Cole & Lade (1984) model are also shown for each assemblage in Fig. 4.9. The only material property required for the model is the angle of dilation, and the positions of the rupture surfaces are estimated assuming ψ = 20°, 10°, 0°, and 0° for the dense, medium-dense, medium-loose, and loose assemblages, respectively. Chapter 3 also showed that the shear rupture surfaces in dense, dilatant material are consistent with those estimated with the Cole & Lade (1984) model with bedrock fault offsets for reverse and normal fault dip angles between 30° and 90°. Comparisons of rupture zones in looser materials with the Cole & Lade (1984) model are less meaningful because a distinct rupture surface does not form. Thus, displacement contours are better suited for comparisons. Fig. 4.9a shows that the predicted rupture surface passes through the center of the displacement contours in the dense assemblage. The predicted rupture surfaces in Fig. 4.9b-d do not pass through the center of the displacement contours and instead closely coincide with the 1.0-1.5 m displacement contours.

Fig. 4.10a shows the ground surface deformations for each assemblage. Unlike in Fig. 4.5c and Fig. 4.6, the horizontal axis represents the offset positions at a given fault throw. The bedrock fault is located at the zero position of the horizontal axis. The surface deformations in Fig. 4.10a are shown as the surface heave, which is the vertical surface displacement, normalized by the fault throw, h. The predicted outcrop locations for the dense and medium-dense assemblages are 22.4 m and 21.1 m away from the bedrock fault and 19.7 m away for the medium-loose and loose assemblages using the Cole & Lade (1984) model. At these locations in Fig. 4.10a, the surface just begins to heave upward, which is consistent with where Cole & Lade (1984) predict the top of the rupture surface to be located. The first point of surface heave is located 30-32 m towards the footwall side of the bedrock fault for each assemblage at h/H=0.15, but the locations of the maximum surface slope ($\theta_{s,max}$) widely vary. Fig. 4.10b shows the profile of the slope angle of each ground surface. The point of maximum surface slope occurs 21 m away from the bedrock fault in the dense assemblage but only about 9 m away from the bedrock fault in the loose assemblage. The medium-dense and medium-loose assemblages show intermediate surface deformations to the dense and loose assemblages. Each ground surface levels out 10-20 m towards the hanging wall side of the bedrock fault. $\theta_{s,max}$ differs for each assemblage ranging from 12.3° in the loose assemblage to 28.3° in the dense assemblage. This demonstrates that more brittle materials will tend to exhibit greater amounts of differential surface heave, leading to greater amounts of distinct offset and potentially more significant structural damage.

Moving from the footwall side to the hanging wall side of the surface in Fig. 4.10a, the surface slope goes through a point of maximum curvature, a point of maximum surface slope, and a second point of maximum curvature before leveling out again. The locations of the points of maximum surface curvature vary with hanging wall displacement, and as void ratio increases these points of maximum curvature are spaced farther apart. At h/H=0.15, these points are approximately 8 m apart in the dense assemblage, 14 m apart in the medium-dense assemblage, 15 m apart in the medium-loose assemblage, and 19 m apart in the loose assemblage. Less significant structural damage can be expected atop the most ductile soils because the width of differential displacement is spread over a wider zone. Both points of maximum curvature are located furthest on the footwall side of the bedrock fault in the dense assemblage. Greater ground surface slope inclination occurs over a shorter range closer to where the surface begins to heave upward in denser assemblages.

The far-field surface displacements are equal to the hanging wall displacement because the upthrown block remains relatively intact away from the shear zone under quasi-static conditions. Vertical surface displacements far away from the rupture surface and above the hanging wall were generally equal to the fault throw in the centrifuge models of normal and reverse fault rupture performed by Bransby et al. (2008a, 2008b). The normalized values of surface heave in Fig. 4.10a increase from zero at the far end of the footwall to 1.0 at the far end of the hanging wall. Even the surface of the loose assemblage moves upward by the amount of the hanging wall displacement far away from the rupture zone. Fig. 4.10c shows that the surface movement above the hanging wall in the dense and loose assemblages consistently approaches the fault throw at different values of h/H, and the slope of the surface increases with fault throw in both assemblages. The observed movement of the location of maximum slope toward the footwall side with increasing fault throw in Fig. 4.10c is consistent with reverse fault observations from Bransby et al. (2008b).

4.6 Discussion of Micro-Scale Shear Rupture Mechanisms

4.6.1 Changes in Coordination Number

The effects of granular media having different densities (i.e., void ratios) on the development of the earthquake fault rupture-induced shearing response of the media are visible through the coordination number, which is the number of contacts acting on a single particle. The average coordination number tends to decrease during shear-induced material dilation as its void ratio increases (Thornton 2000). Conversely, contractive soils tend to increase or change little in their average coordination number during shearing. Fig. 4.11 shows the percentages of particles that increase or decrease in coordination number by at least 2. The results show a systematic trend of contractive particle assemblages showing greater increases in coordination number and dilatant particle assemblages showing greater decreases in coordination number. The rate of increase or decrease in coordination number levels off as h/H increases, and the particles in the shear band approach critical state. Until h/H=0.015, the four different densities of particulate media have about the same increases in coordination number, indicating that even the dilatant assemblages exhibit some contraction initially.

The medium-loose and loose assemblages have about the same percentages of particles decrease in coordination number during all stages of the simulations (Fig. 4.11b). The decreases in coordination number in the contractive assemblages result from random particle rearrangement rather than systematic dilation. The loose assemblage has a noticeably higher percentage of particles with an increase in coordination number than the medium-loose assemblage (Fig. 4.11a),

and more particles within the loose assemblage exhibit an increase in coordination number than a decrease. The change in coordination number in Fig. 4.11 are approximately the same for the medium-loose assemblage, which suggests that the medium-loose assemblage has a void ratio distribution that is initially close to the critical state void ratio. The medium-dense and dense assemblages, which are dilatant, show higher decreases in coordination number than increases. Fig. 4.7d and 4.7e show that the dilative volume changes occur in a narrow zone around the rupture surface, and the decreases in coordination number also occur mostly within this narrow zone.

4.6.2 Frictional Energy Dissipation

Energy is dissipated through friction when contacting particles slide relative to each other during shearing. Fig. 4.7j-m and Fig. 4.8j-m showed that the energy dissipated through this frictional slip is confined to the shear zones, and the shear zone broadens with increasing void ratio. To examine this issue at the micro-scale, the accumulated energy dissipated through frictional slip for the reverse and normal fault simulations is shown in Fig. 4.12.

The dense and medium-dense assemblages display approximately the same amount of frictional dissipation during the reverse fault simulations until they diverge at h/H=0.04. The rate of frictional dissipation in the dense assemblage increases between h/H=0.04 and h/H=0.06. The noticeable rise and fall in the rate of frictional dissipation (referred to as stick-slip herein) in the dense assemblage is indicative of an increased rate of energy dissipation through slippage following sufficient build-up of strain energy. The short-lived reversal in the rate at which particles change in coordination number in Fig. 4.11 suggests that the dense material contracts slightly when slip first occurs. Given the progressive nature of shear band propagation, this contraction most likely occurs at the tip of the rupture surface. More energy is required to shear through the dense material when it is at its peak strength. The rate of frictional dissipation increases as the shear band develops in the dense material but decreases when the material approaches critical state. Because the rupture surface develops progressively, the lower half of the shear band reaches critical state before the upper half. The rate of frictional dissipation is higher when most of the developing shear band has yet to reach its peak strength but then starts to decrease as more of the strength in the shear band drops to the critical state. Eventually, the entire shear band reaches critical state, at which point the rate of frictional dissipation becomes constant.

Stick-slip behavior is not immediately evident in the medium-dense assemblage because the rate of frictional dissipation does not appear to decrease in Fig. 4.12a. The medium-dense assemblage is less dilatant than the dense assemblage and undergoes a smaller drop in strength after reaching the peak state. The shear band bifurcates near the surface as seen in the wider volumetric strains near the surface in Fig. 4.7e. This results in the energy continuing to dissipate at a steady rate as opposed to a higher rate.

A distinct shear band does not develop in the medium-loose or loose assemblages. The medium-loose assemblage dissipates friction at a constant and low rate after h/H=0.07 as shown in Fig. 4.12a. This low rate of frictional dissipation is expected, because contraction and dilation appear to occur in equal proportions as seen through the similar increases and decreases in coordination number in Fig. 4.11. However, the loose assemblage exhibits significantly more frictional dissipation than the other assemblages during the early stages of fault rupture. The average coordination number is smallest in the loose assemblage, and higher coordination numbers give particle assemblages greater stability, because each contact provides an additional supporting force. The loose fabric is considered metastable, because the average coordination number is at or

near a minimum value. This metastable fabric is more easily disrupted by small perturbations from the bedrock fault rupture. The disruption of the loose fabric is seen through the widespread particle rotations and contractive strains in Fig. 4.7f and 4.7i, and a large amount of energy is dissipated through friction at the contacts in a broad zone as seen in Fig. 4.7m.

The energy dissipated through friction during 30°-dip normal fault rupture shows a consistent trend of increased frictional dissipation with higher void ratios. The total energy dissipated increases with void ratio because the zone of shearing is wider in looser particle assemblages. Fewer particles are involved in the distinct localizations that develop in denser assemblages, so there are fewer contacts at which energy is dissipated through friction. None of the assemblages in Fig. 4.12b exhibit the aforementioned stick-slip behavior, because the shear band develops through lateral extension from the horizontal component of hanging wall displacement. The medium-dense and dense assemblages show an increased rate of frictional dissipation just after h/H=-0.02, and the rate of frictional dissipation remains nearly constant in the medium-loose assemblage. In the loose assemblage, the rate decreases with increasing hanging wall displacement. The decrease in the rate of frictional dissipation most likely begins when the void ratios in the contracting sections of the assemblage decrease to a constant and stable value.

Initial void ratio has a more significant effect on total energy dissipated through friction in normal fault rupture than in reverse fault rupture. The active mechanism of normal fault rupture reduces the normal forces acting on the particles, which reduces the frictional resistance at the contacts and facilitates more inter-particle sliding. As will be discussed later, the individual contacts are higher on average in looser assemblages than in denser assemblages with the same stress distribution. More energy is dissipated through friction in looser assemblages, because the particles slide against higher normal forces during shearing. The passive mechanism of reverse fault rupture tends to increase the normal force acting on each particle, which inhibits sliding by increasing the frictional resistance at each inter-particle contact. The dependence of frictional energy dissipation on initial void ratio appears greater in Fig. 4.12b, because two rupture surfaces develop, thus dissipating twice as much energy through friction than with one rupture surface.

4.6.3 Contact Forces

The strong normalized contact force network at h/H=0.15 in the dense and loose assemblages during reverse fault rupture is shown in Fig. 4.13. The normalized contact forces are calculated by dividing the contact forces by their depth below the ground surface in the prototype-scale. The threshold for a normalized contact to be considered a strong contact is based on the distribution of normalized contact forces during at-rest conditions prior to the onset of fault rupture. The normalized contact forces follow an approximately lognormal distribution in the initial state, so the threshold for a contact to be considered a strong contact at later stages of fault rupture is calculated as one standard deviation above the median value on a lognormal basis in the initial state. The threshold contact force normalized by depth for a normalized contact to be considered a strong contact is 0.197 N/m in the dense assemblage, 0.267 N/m in the medium-dense assemblage, 0.404 N/m in the medium-loose assemblage, and 0.472 N/m in the loose assemblage.

The threshold value for a strong normalized contact force increases with increasing void ratio, because the stress distribution is approximately the same in each assemblage. The dense and loose assemblages both show a half-arch of strong contacts bending over the downthrown block, but the strong contacts are much more densely distributed in the dense assemblage than in the loose assemblage. The total number of particles decreases with increasing void ratio, so looser

assemblages have fewer particles to carry the same force that is present in denser assemblages. The particles in the looser assemblages must each support a greater force to compensate for their lower number of particles. Hence, while more total contacts are present in denser assemblages, the individual contact forces are higher on average in looser assemblages. In a real soil, the greater force per particle contact increases the likelihood of grain crushing in loose assemblages. The higher average normalized contact force in the loose assemblage helps explain its greater amount of frictional dissipation in Fig. 4.12. When sliding occurs at the inter-particle contacts in the loose assemblage, the sliding occurs on average against a larger normal force than in a dense assemblage. Hence, more work is done in sliding against a higher normal force, which dissipates more energy through friction.

The strong normalized contact forces are strongly oriented in the vertical direction in the initial state. Normal fault rupture does not change the vertical orientation of the strong contacts but does reduce the total number of strong contacts. Widespread contact reorientation occurs during reverse fault rupture, which reduces the bias of the contact orientations in the vertical direction and greatly increases the number of contacts oriented closer to the horizontal direction. Fig. 4.14 shows that these trends are evident in the dense and loose assemblages. The distributions are symmetric to account for equal and opposite contact forces. The contacts are strongly oriented in the vertical direction in the initial state. The contacts are well distributed in every direction during 60°-dip reverse fault rupture at h/H= 0.15. The contacts in the dense assemblage show a small bias towards the 120°/300° directions, and the contacts in the loose assemblage are biased more towards the 145°/325° directions. The loose assemblage exhibits widespread contact reorientation during reverse fault rupture as in the dense assemblage. The contacts are still strongly oriented in the vertical direction at h/H= -0.08 during 30°-dip normal fault rupture in both the dense and loose assemblages. This indicates that whether the particle assemblage is dense or loose, normal fault rupture reduces the number of strong contacts through lateral extension above the bedrock fault but does not significantly disrupt the distribution of strong contacts oriented in the vertical direction.

4.7 Conclusion

DEM simulations with 3D sphere-clusters can capture the important role the density of particulate media has on its dilatancy and ductility and hence its response to earthquake fault rupture. Direct shear test simulations show that 3D particle assemblages with low void ratios exhibit strong dilation and strain softening during shear, and assemblages with higher void ratios respond contractively. The assemblage preparation procedure for surface fault rupture simulations is capable of consistently producing materials with reasonable void ratio and vertical and horizontal stress profiles. Lower void ratios result from preparing assemblages with lower coefficients of friction. The DEM simulations are able to capture qualitatively earthquake fault rupture characteristics observed in a physical model test with medium-loose sand performed by Bransby et al. (2008b). Thus, 3D DEM can be employed to examine an array of macro-scale and micro-scale aspects of earthquake fault rupture mechanisms.

Thin shear bands develop during reverse and normal fault rupture in the dense particle assemblage, and the distributions of volumetric strains, large particle rotations, and frictional dissipation are confined to the shear bands. Brittle thrusting features are observed during reverse fault rupture through the dense and medium-dense particle assemblages. A wider shear band that bifurcates near the surface develops during reverse fault rupture in the medium-dense particle

assemblage. The magnitudes of frictional dissipation and particle rotations decrease from the footwall edge of the shear band toward the hanging wall edge of the shear band due to the upthrown block dragging on the downthrown block. The loose particle assemblage exhibits widespread contractive strains, particle rotations, and frictional dissipation during reverse fault rupture. No brittle features of dislocation are observable in the loose particle assemblage.

The DEM simulations capture the formation of a graben during the normal fault rupture case. Relative deformation localizes in the two shear bands that form, and there is little internal deformation of the material within the graben. The surface deformations show shallower slope inclinations as the void ratio increases, and the location of the steepest slope inclination moves closer to the hanging wall side as the void ratio increases. Because the hanging wall shows little internal strain away from the shear zone during bedrock fault rupture, the maximum ground surface displacement on the hanging wall surface is nearly equal to the vertical bedrock displacement. Displacement contours show the increasing width of the zone of shearing with increasing void ratio and material ductility. DEM results are consistent with those of the Cole & Lade (1984) model, which emphasizes the important role of the soil's angle of dilation.

Micro-scale analyses of earthquake fault rupture, which are possible with DEM, depict several mechanisms not observable using continuum models or physical models. The tendency of a particulate assemblage to dilate or contract is intimately related to changes in the average coordination number of the particle assemblage. Dilatant materials exhibit a reduction in coordination number as void ratio increases within a distinct shear band; whereas contractive materials tend to increase in coordination number. The loose particle assemblage has a metastable fabric, because its initial coordination number is at or near the minimum value, and the widespread contraction in the loose assemblage dissipates more energy through frictional slip than denser particle assemblages during both reverse and normal fault rupture. The dense particle assemblage exhibits stick-slip behavior during reverse fault rupture as seen by the rise and fall in its rate of frictional dissipation. This stick-slip behavior is not observed during normal fault rupture. The strong contact forces exhibit a half-arch structure in both the dense and loose particle assemblages, but a greater number of closely-spaced strong contact forces develop within the dense assemblage. The magnitudes of individual forces within the loose particle assemblage are higher typically than within the dense assemblage because the forces in the loose assemblage carry a greater load to compensate for their lower number of contacts.

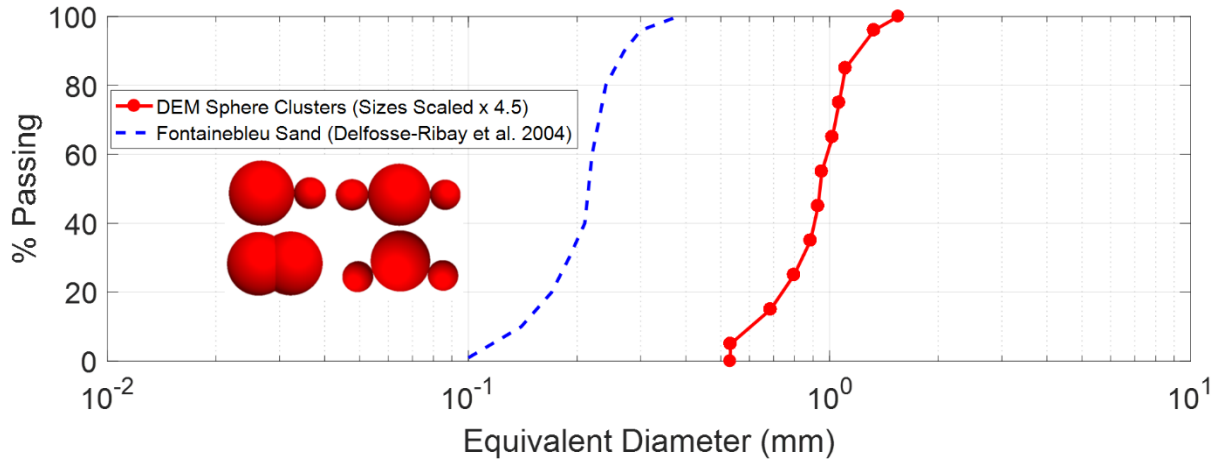

Fig. 4.1. Particle shapes used in DEM simulations and grain size distribution of a particle assemblage scaled relative to that of Fontainebleau sand (data from Delfosse-Ribay et al. 2004).

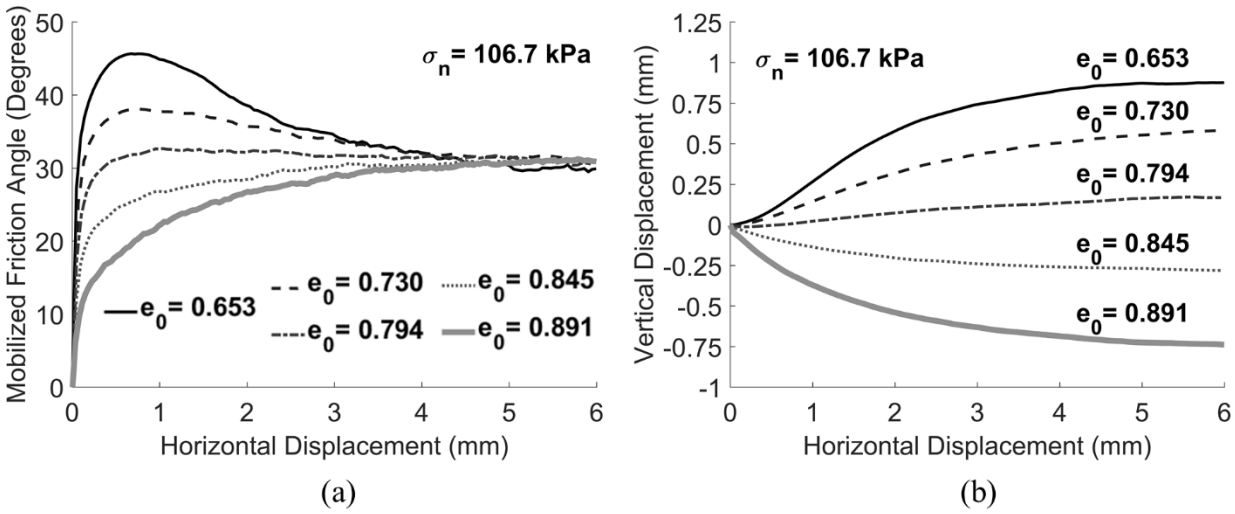

Fig. 4.2. (a) Friction angle and (b) vertical displacement results from numerical direct shear test simulations with normal stress of 107 kPa (from Chapter 3).

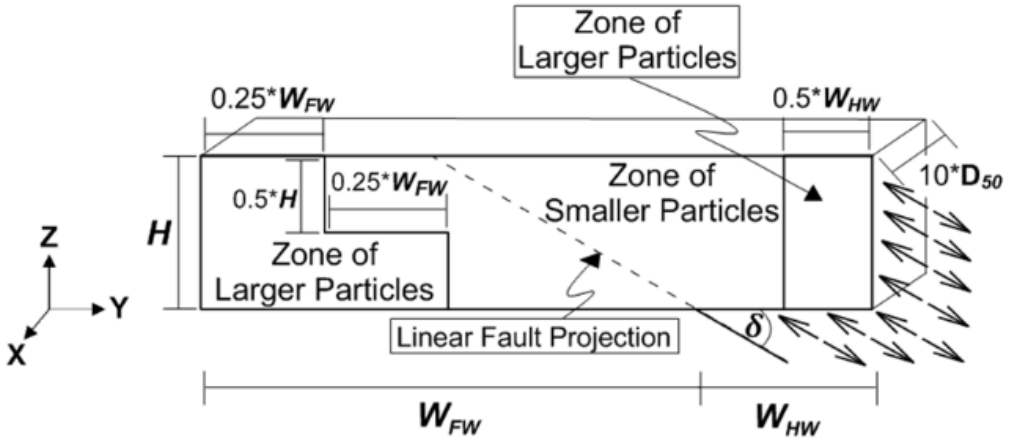

Fig. 4.3. Earthquake fault rupture propagation DEM model.

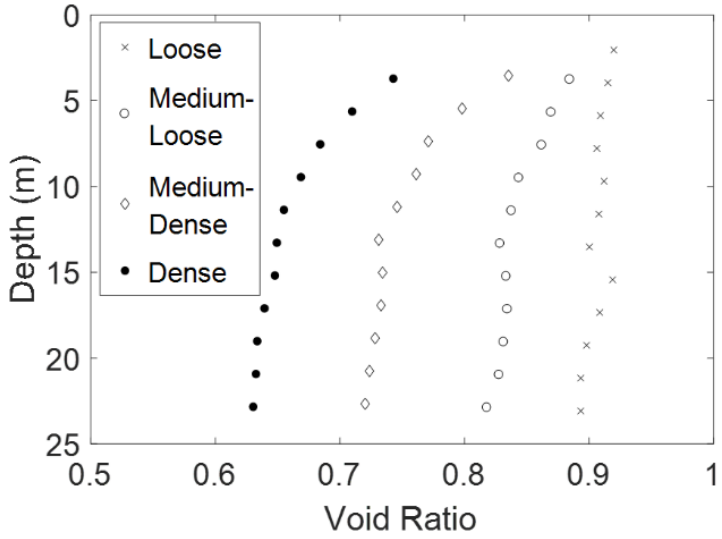

Fig. 4.4. Void ratio profiles of the assemblages of particles studied.

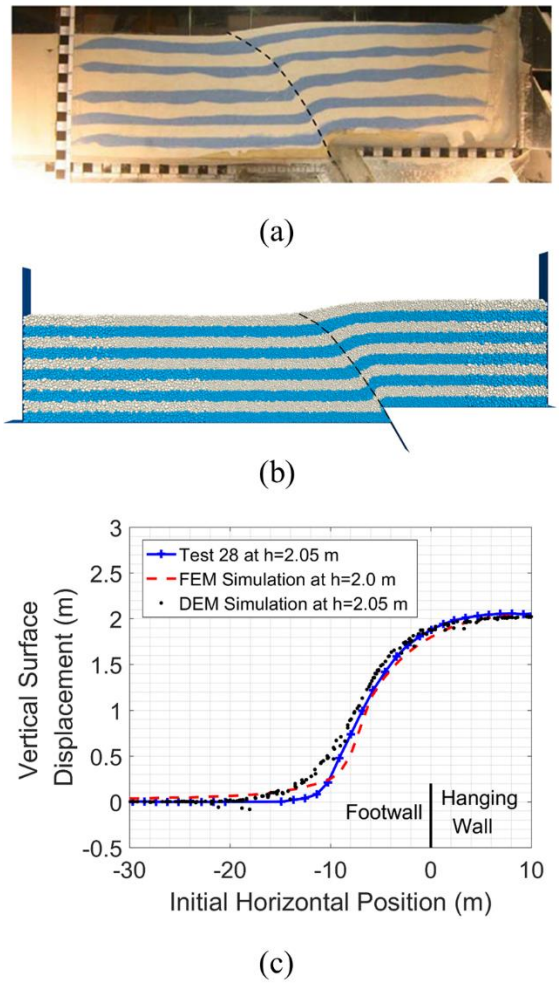

Fig. 4.5. (a) Photograph of Test 28 from Bransby et al. (2008b) at h/H=0.147. (b) DEM simulation result for a comparable DEM assemblage at h/H=0.145 during 60°-dip reverse fault rupture. (c) Comparison of vertical surface displacements from Test 28 and the results from a comparable DEM simulation and the finite element analyses of Anastasopoulos et al. (2008a).

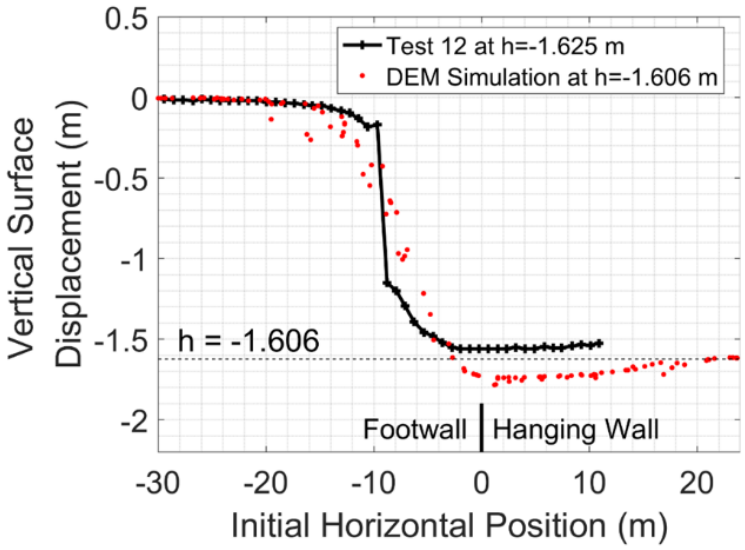

Fig. 4.6. Comparison of vertical surface displacements between Test 12 of Bransby et al. (2008a) and the medium-dense DEM assemblage at similar fault throws during 60°-dip normal fault rupture.

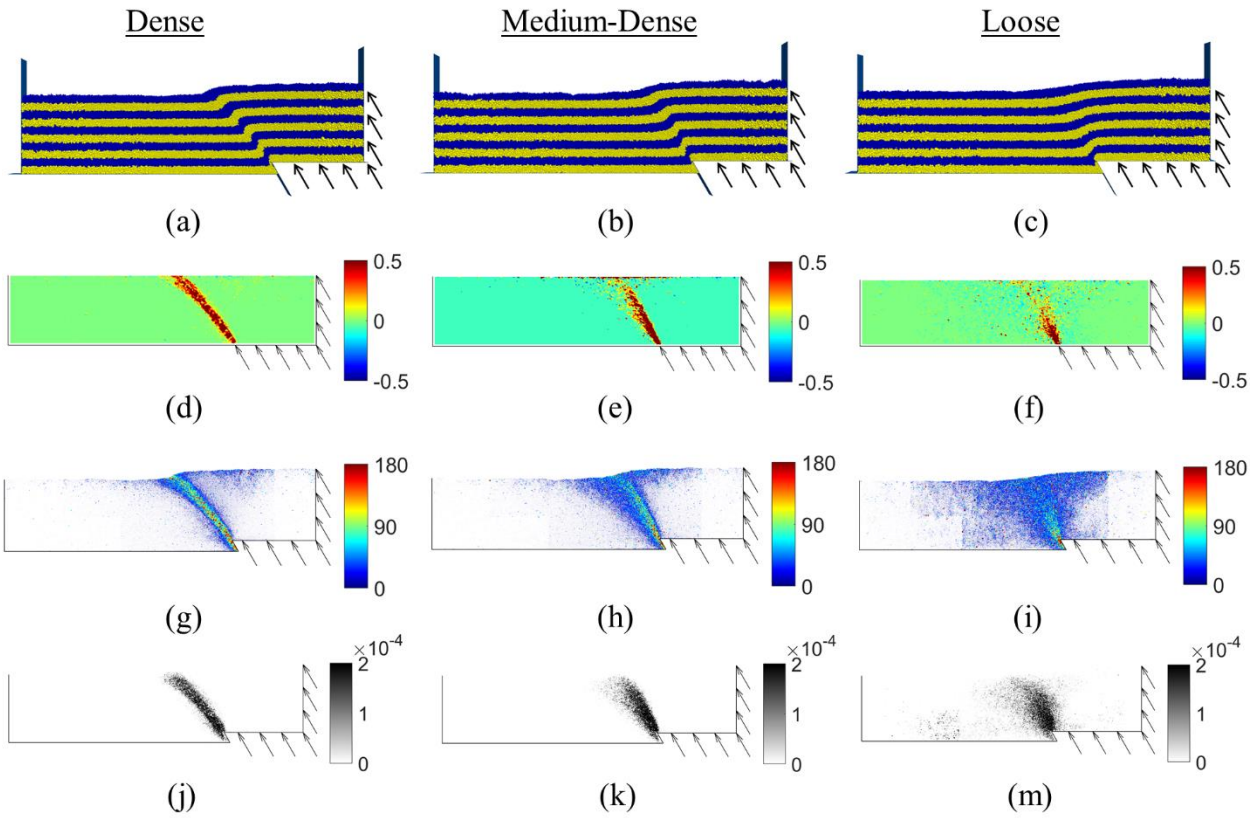

Fig. 4.7. Results of 60°-dip reverse fault simulations at h/H = 0.15. (a-c) Offset layers of particles. (d-f) Contours of volumetric strains. (g-i) Distribution of particle rotations in degrees about the principle axis of each particle. (j-m) Contours of frictional dissipation in N-m at each contact.

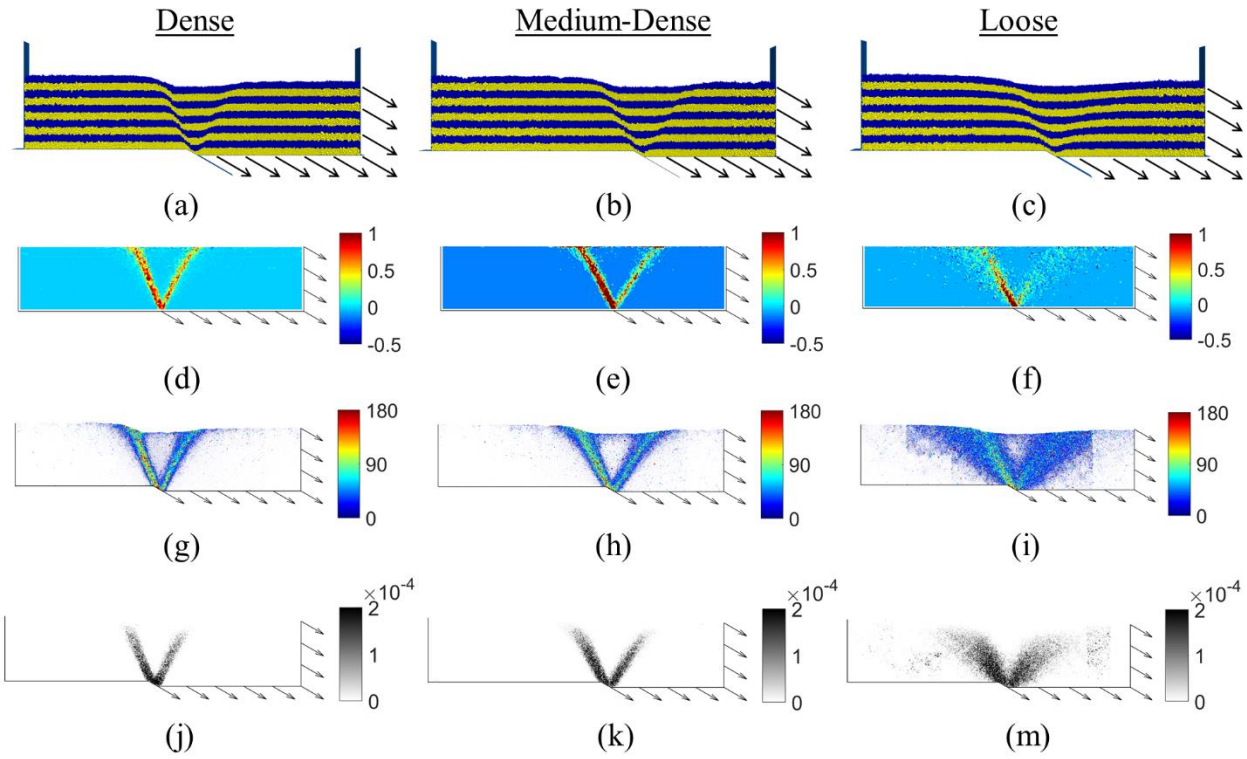

Fig. 4.8. Results of 30°-dip normal fault simulations at *h/H*=-0.08. (a-c) Offset layers of particles. (d-f) Contours of volumetric strains. (g-i) Distribution of particle rotations in degrees about the principle axis of each particle. (j-m) Contours of frictional dissipation in N-m at each contact.

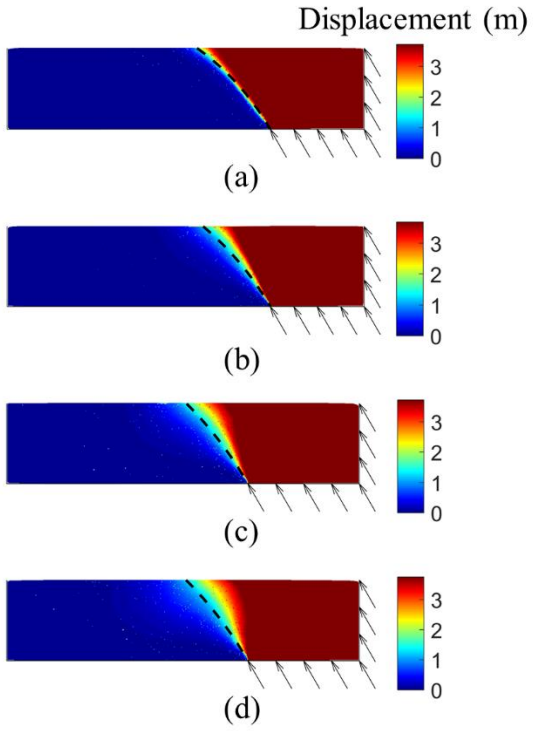

Fig. 4.9. Contours of particle displacement magnitudes (in meters) in 60°-dip reverse fault simulations at *h/H*=0.15. The predicted rupture surface from Cole & Lade (1984) is shown with a black dashed line.

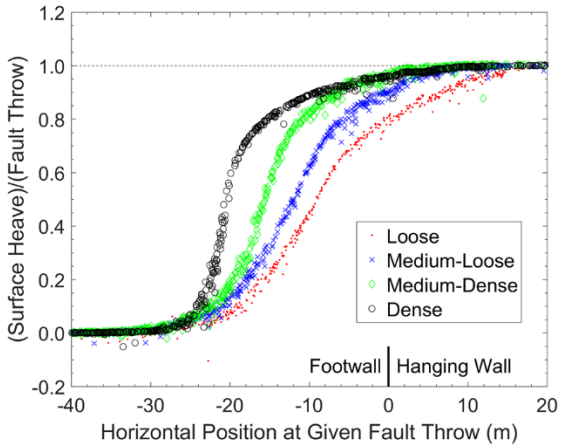

(a)

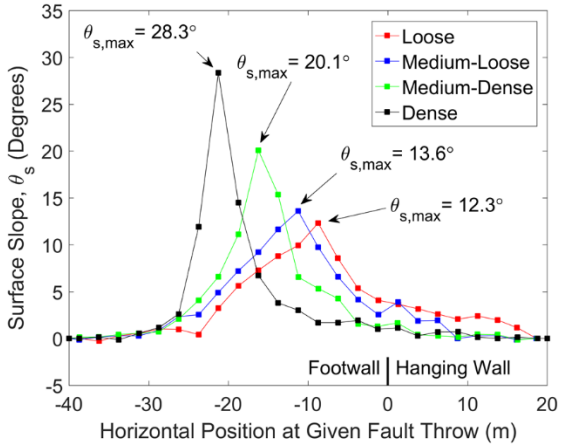

(b)

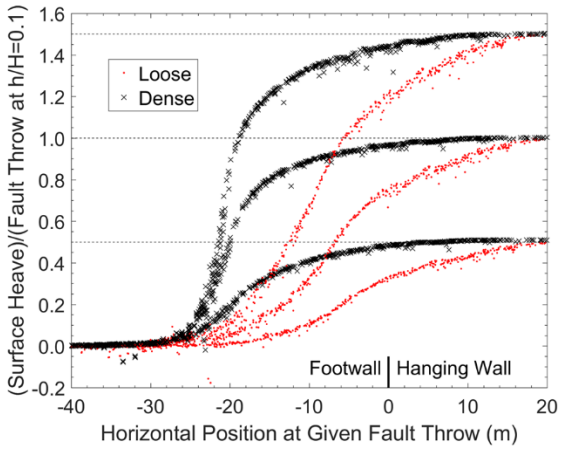

(c)

Fig. 4.10. (a) Ground surface deformations at h/H = 0.15 for each assemblage. (b) Ground surface slopes for each assemblage. (c) Ground surface deformations for h/H = 0.05, 0.1, and 0.15 for a 60°-dip reverse fault in the dense and loose assemblages.

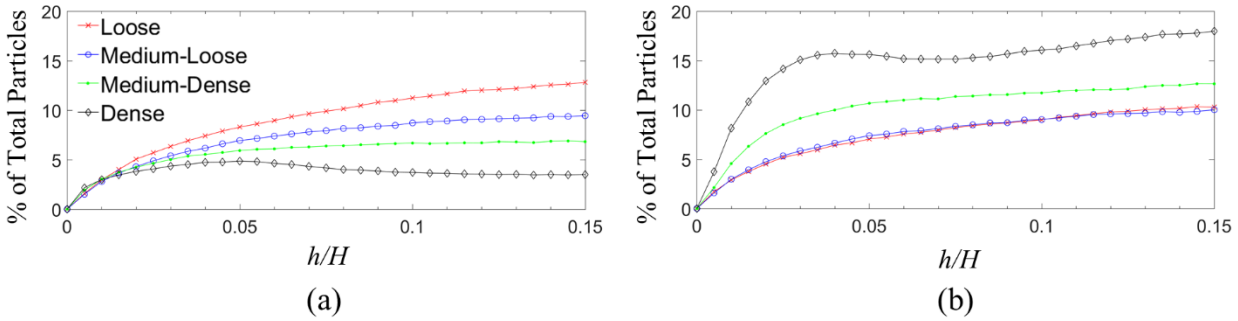

Fig. 4.11. Percentages of particles exhibiting changes in coordination number by 2 or more at different stages of surface fault rupture for a 60°-dip reverse fault. (a) Increases in average coordination number. (b) Decreases in average coordination number.

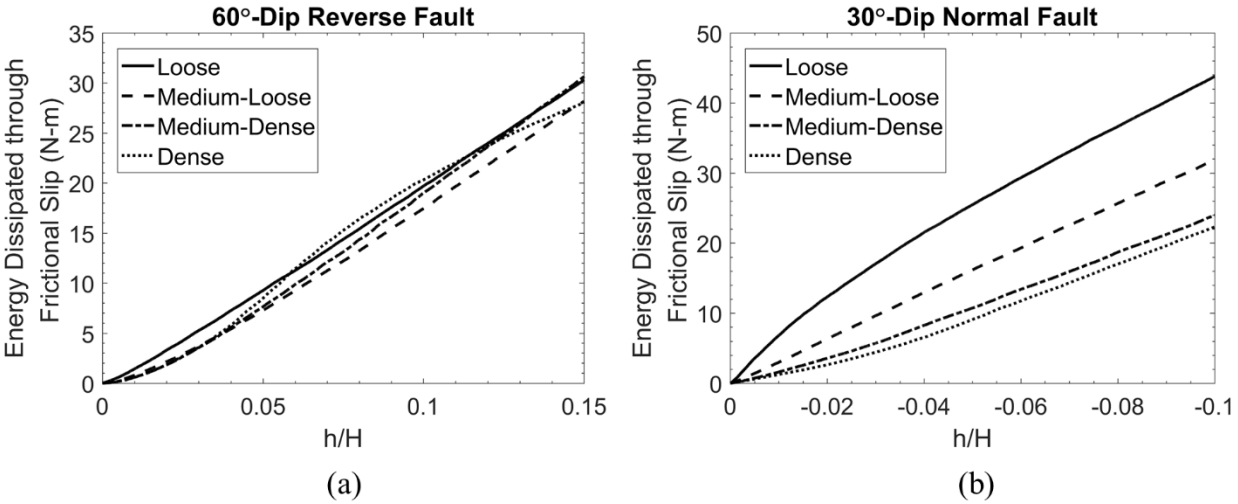

Fig. 4.12. Total energy dissipated through friction in (a) 60°-dip reverse fault simulations and (b) 30°-dip normal fault simulations.

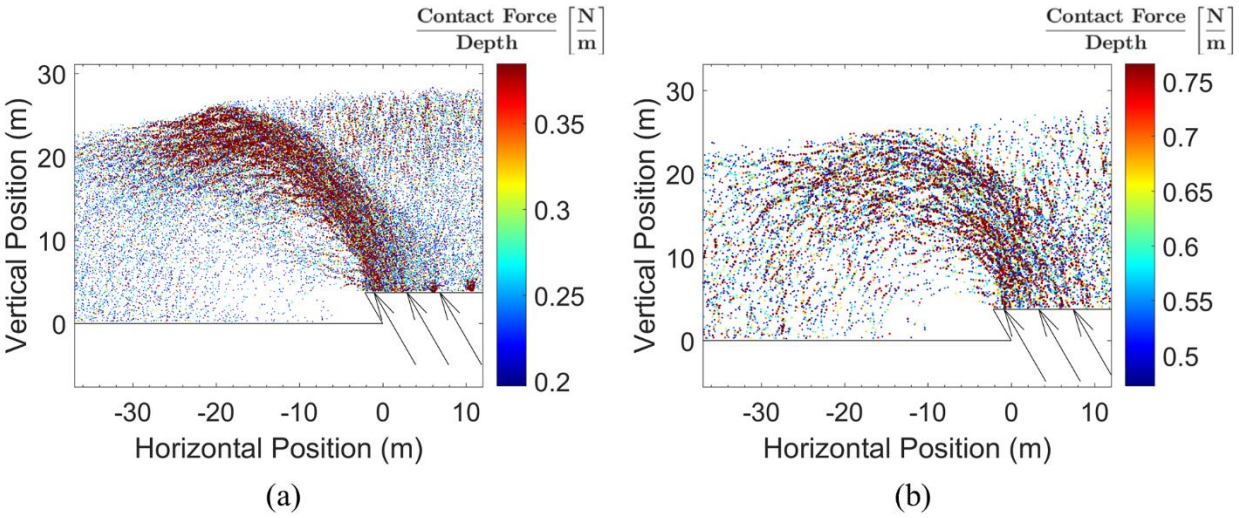

Fig. 4.13. Strong normalized contact force distribution for a 60°-dip reverse fault at h/H = 0.15 for the (a) dense and (b) loose assemblage.

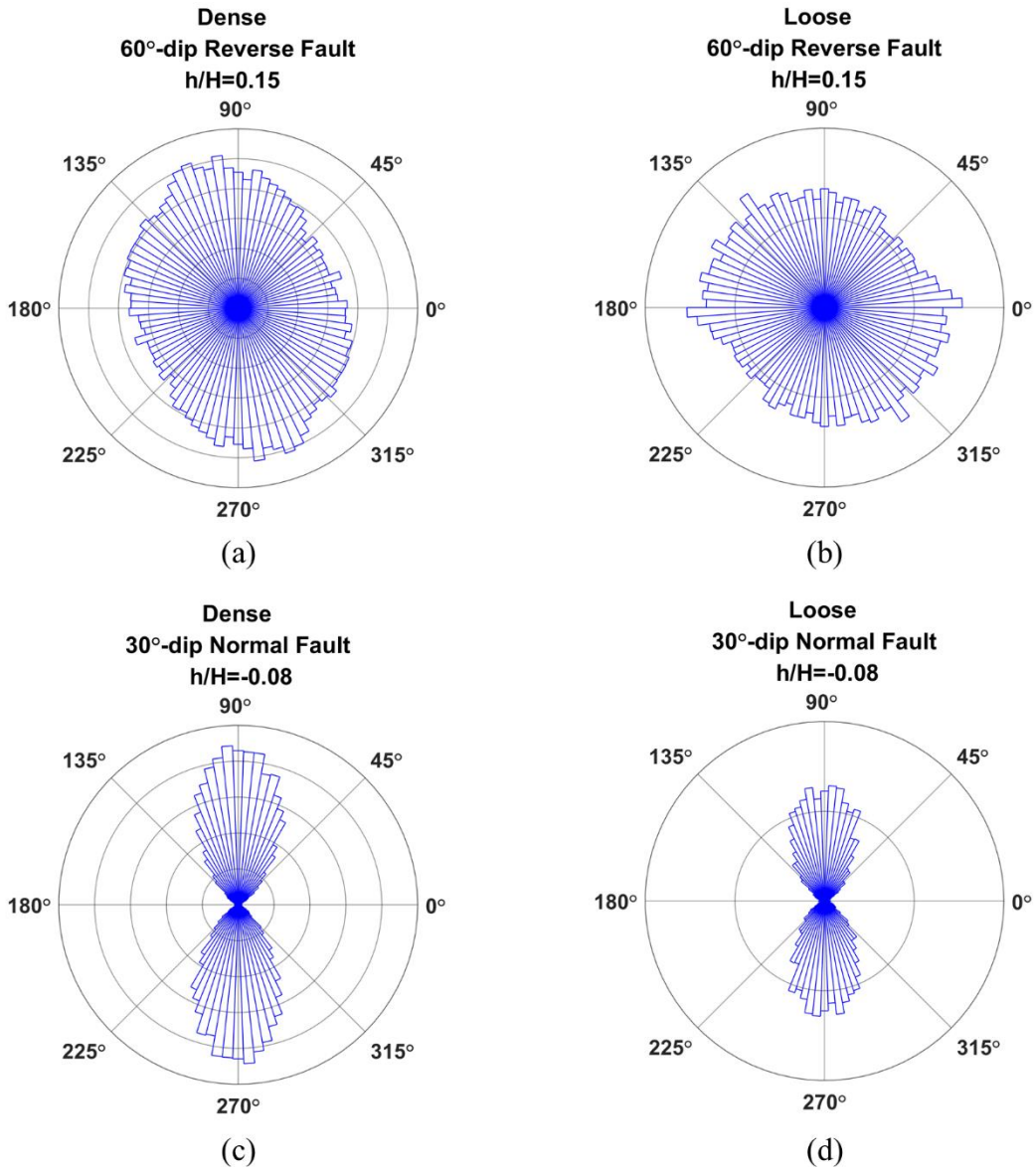

Fig. 4.14. Polar histograms of contact normal orientations for strong contacts in the Y-Z plane. The radial contours indicate the number of strong contacts at a given angle between 0° and 360° to the horizontal direction. All radial contours are spaced in increments of 200 contacts.

CHAPTER 5: MODELING THE SHEAR RESPONSE OF GRANULAR MATERIALS WITH DISCRETE ELEMENT ASSEMBLAGES OF SPHERE-CLUSTERS

The majority of this chapter is taken directly from a manuscript accepted for publication by Computers and Geotechnics *titled "Modeling the Shear Response of Granular Materials with Discrete Element Assemblages of Sphere-Clusters" (Garcia & Bray 2019). Jonathan Bray is the only co-author of this manuscript.*

5.1 Introduction

The direct shear (DS) test provides important insights into the shear response of granular media in boundary-displacement problems. The shear patterns that develop in large-scale boundary-displacement problems, such as earthquake surface fault rupture, are reproducible in direct shear tests (Tchalenko 1970). Thus, the DS test is an appropriate tool for characterizing the strength and dilatancy of a soil that is to be used in experiments or simulations of earthquake fault rupture, trapdoor displacement, and other similar boundary-displacement problems (e.g., Anastasopoulos et al. 2007, Bransby et al. 2008a,b, Hazeghian & Soroush 2015, and Stone & Wood 1992). The interpretation of the DS test requires that the material properties inferred from measurements made at the specimen boundaries reflect the mechanical response of the soil in the shear band developing along the mid-plane of the test specimen.

This chapter explores the relation between material characterization from within the shear band and at the boundaries of DS test simulations using the discrete element method (DEM) on high-performance computing (HPC) clusters with the highly-efficient, parallel DEM code LIGGGHTS (Kloss et al. 2012) with enhancements developed through this study and described in Appendix A. The significant computational speed-ups gained using parallel processing facilitate a broad parametric study on the influences of particle shape, relative density, and applied stress on shear band formation in a suite of three-dimensional (3D) DS test simulations with assemblages of irregularly-shaped sphere-clusters. Quasi-static simulations using 96 cores were able to reach a horizontal displacement of 15% of the horizontal width in under 24 hours. Homogenization techniques are used to characterize the material strength and dilatancy from within the developing shear zone and compare them with measurements made from the rigid-wall boundaries. The evolution of shear stresses is compared with real sands, and the results are evaluated in the context of critical state soil mechanics. Micro-mechanical analyses are performed to gain insight into shear zone development in dense and loose particle assemblages.

5.2 Characteristics of Particle Assemblages

5.2.1 Grain-Scale Characteristics

Sphere-clusters are advantageous for modeling large quantities of particles, because they use the efficient sphere contact detection scheme of the original distinct element method (Cundall & Strack 1979). The idealized shapes in Fig. 5.1 capture the inherent rotational resistance of real soil particles, as discussed in Chapter 3. Inter-particle contact models with rheological rolling resistance can also account indirectly for some effects of grain non-sphericity, but these do not capture accurately the particle shape-dependent large-strain volumetric changes of real sands (Salazar et al. 2015) or fabric effects related to depositional direction (Yan 2009). The spheres

shown in Fig. 5.1a are used as a control group, and the sub-rounded sphere-clusters in Fig. 5.1b are less concave than the sub-angular sphere-clusters in Fig. 5.1c. Within the sphere-cluster assemblages, all 4 shapes occur in equal proportions. The largest constituent sphere diameter of each particle is used to represent the effective diameter of each particle.

The nonlinear Hertz contact model available in LIGGGHTS is used to calculate normal and tangential spring forces. Inter-particle slip occurs when the tangential spring force exceeds the frictional resistance of the particle surface. The measured mechanical properties of quartz minerals are: Young's modulus (E) = 76 GPa, Poisson's ratio (ν) = 0.31 (Santamarina et al. 2001), and friction coefficient (μ) = 0.5 (Mitchell & Soga 2005). In the DEM simulations, E is set to 7.6 GPa to increase the stable time-step while still maintaining small inter-particle overlaps throughout the simulations, and the measured properties of ν and μ are used. The particle density is 2650 kg/m^3 based on the specific gravity of quartz (Santamarina et al. 2001). A coefficient of restitution of 0.9 is estimated for the particle impacts based on experiments performed by Imre et al. (2008). Additionally, a local non-viscous damping factor of 0.3 is included to damp the motion of accelerating particles (Itasca 2014).

5.2.2 Macroscopic Characteristics

Fontainebleau sand is used for physical comparison because it is well-characterized with DS tests and used in boundary-displacement experiments (Bransby et al. 2008a,b). The shape of the grain size distribution of the DEM particle assemblage is matched to that of Fontainebleau sand, which has a coefficient of uniformity (C_u) of 1.6, as shown in Fig. 5.2 (Delfosse-Ribay et al. 2004). The DEM particles, either sphere-cluster or individual sphere, are generated with sizes scaled up such that approximately 100,000 particles fill a shear box with horizontal dimensions 60 mm x 60 mm and a height of 20-21 mm under a desired normal stress applied through the upper loading platen as shown in Fig. 5.3. This number of sphere-clusters is sufficient for the assemblage's friction angle and angle of dilation to be captured well in DS test simulations because it is greater than the minimum required number of 30,000-50,000 particles (Ni et al. 2000). The use of 100,000 particles results in them being approximately 5 times larger in effective diameter than real Fontainebleau sand grains but with the same particle-size distribution shape.

Fontainebleau sand has minimum and maximum void ratios (e_{min} and e_{max}) of 0.523 and 0.863, respectively (Gaudin et al. 2005). Standardized procedures do not exist for determining e_{min} and e_{max} in DEM simulations. In this study, e_{max} is obtained through an air pluviation simulation. e_{min} is obtained by uniaxially compressing the particle assemblages to 1 MPa with μ = 0.0. Inter-particle overlaps are monitored when determining e_{min} to ensure that the void ratio changes result from particle rearrangement rather than excessive overlaps. The calculated e_{min} and e_{max} values for the particle assemblages examined in this study are shown in Fig. 5.1. The range e_{max} - e_{min} of the sphere-cluster assemblages is nearly twice as high as that of the spheres. Because peak strength and dilatancy depend significantly on void ratio as discussed in Chapter 4, sphere-cluster assemblages will have a wider range of contractive and dilatant behaviors than spheres.

5.3 Direct Shear Test Simulation Procedures

5.3.1 Specimen Preparation and Test Procedures

The DS test specimens are prepared by quasi-statically compressing the particles via the upper and lower horizontal platen walls until a desired normal stress (σ_n) is achieved on both walls. Dense specimens are prepared with initial inter-particle friction coefficient (μ_0) = 0.0, and loose specimens are prepared with μ_0 = 0.5. After reaching the desired normal stress, the contact properties are reset to those stated in Section 2.1, and compression via the lower platen wall ceases. Quasi-static shearing is then induced by moving the entire lower shear box, as shown in Fig. 5.3, at a constant velocity of 0.02-0.05 m/s while maintaining constant σ_n on the upper loading platen using a servo-controlled wall. The lateral walls are frictionless and the upper wall is restricted from rotating so that the simple shear mode of deformation develops within the shear band (Shibuya et al. 1997). The frictionless lateral walls allow the forces measured on the upper and lower shear boxes to be equal when the system is in equilibrium. When the forces on the upper and lower walls are within 5% of each other, the system is considered in quasi-equilibrium and the shear rate is considered sufficiently quasi-static, as discussed in Chapter 3.

5.3.2 Measured Quantities

In the DS test, material strength is characterized using the mobilized Coulomb friction angle (ϕ) measured at the specimen boundaries as:

$$tan\phi = \frac{\tau}{\sigma_n} \tag{5.1}$$

In the simulations, the shear stress (τ) is the sum of all forces in the *Y*-direction acting on the walls of the lower shear box divided by the specimen horizontal area. Although the specimen horizontal area actually reduces slightly during shearing, the ratio of stresses in Eqn. (5.1) is unaffected, because the same area is used to calculate σ_n and τ. The internal stresses are homogenized within the center 2 mm of the particle assemblage within an unchanging volume that is never intruded upon by the lower shear box, as shown in Fig. 5.3. The stresses are homogenized using (Christoffersen et al. 1981):

$$\bar{\sigma}_{ij} = \frac{1}{V}\sum_{k=1}^{N_C} f_i^k l_j^k \tag{5.2}$$

where V is the volume of the measurement region, N_c is the number of inter-particle contacts within the measurement region, f_i^k is the i-component of the k^{th} contact force, and l_j^k is the j-component of the k^{th} branch vector connecting the centroids of the contacting sphere-clusters. The homogenized stress tensor ($\bar{\sigma}_{ij}$) is used to calculate the homogenized Coulomb friction angle within the measurement region as:

$$tan\,\bar{\phi}_{zy} = \frac{\bar{\sigma}_{zy}}{\bar{\sigma}_{zz}} \tag{5.3a}$$

$$tan\,\bar{\phi}_{yz} = \frac{\bar{\sigma}_{yz}}{\bar{\sigma}_{zz}} \tag{5.3b}$$

If moment equilibrium is satisfied perfectly, $\bar{\sigma}_{ij}$ is symmetric and $\bar{\phi}_{yz} = \bar{\phi}_{zy}$. However, small unbalanced forces in DEM simulations inevitably prevent $\bar{\sigma}_{ij}$ from being perfectly symmetric.

The angle of dilation (ψ) in physical DS tests is inferred from the vertical displacement (ΔZ) of the upper loading platen during shearing relative to the horizontal displacement (ΔY) of the non-stationary shear box:

$$\tan\psi = \frac{\Delta Z}{\Delta Y} \tag{5.4}$$

The strain increment tensor ($\Delta\bar{\epsilon}_{ij}$) is homogenized using the particle velocities within the measurement region as described in the manual for the Particle Flow Code (Itasca 2014). The homogenized angle of dilation ($\bar{\psi}$) is calculated within the measurement region using (Thornton & Zhang 2006):

$$\tan\bar{\psi} = \frac{\Delta\bar{\epsilon}_{yy} - \Delta\bar{\epsilon}_{zz}}{\Delta\bar{\epsilon}_{zy}} \tag{5.5}$$

5.4 DEM Simulation Results

5.4.1 Overview

At the peak and critical states, the intermediate stress ratio ($b = \frac{\bar{\sigma}_2 - \bar{\sigma}_3}{\bar{\sigma}_1 - \bar{\sigma}_3}$, where the subscripts 1, 2, and 3 represent the major, intermediate, and minor principal stresses) was typically 0.25-0.35 in all simulations, which is consistent with the *b*-value of 0.3-0.4 for plane strain tests on sands (Kulhawy & Mayne 1990). Eigenvalue analyses of the stress tensor showed that the assumption of plane-strain shearing is justified, because the median orientation of $\bar{\sigma}_2$ at the peak state was 1° from the *X*-axis and the maximum orientation was only 3.8°. Homogenization of the strain increment tensor further showed the horizontal strain increments are small in comparison to the vertical and shear strain increments, which is consistent with zero horizontal extension in the simple shear mode of deformation.

5.4.2 Relative Density Effects and Homogenized Mechanical Response

As demonstrated in Figs. 5.4a and 5.4b, the DEM simulations capture localized shearing along the mid-plane of very dense specimens and uniformly distributed shearing across the specimen height in very loose specimens. Fig. 5.5 shows the evolution of mobilized friction angle, vertical platen displacement, and mobilized dilation angle for representative simulations of each particle assemblage with different relative densities ($D_R = \frac{e_{max} - e}{e_{max} - e_{min}}$) with σ_n = 100 kPa. Homogenized values are also shown for friction and dilation angles. The results show an appropriately strong dependence on initial relative density. Denser particle assemblages show a distinctive peak strength and rate of dilation followed by strain-softening down to a consistent critical state strength and zero rate of dilation. Looser particle assemblages tend to show a monotonically increasing friction angle as well as a dilation angle becoming less negative, indicating a decreasing rate of contraction. The vertical platen displacement attains a constant value at the critical state that increases with D_R. Each particle assemblage that exhibits dilation

achieves its peak friction angle (ϕ_{pk}) at approximately the same horizontal displacement at which it also achieves its maximum angle of dilation (ψ_{max}), and each particle assemblage approaches a consistent critical state friction angle (ϕ_{crit}) by the end of shearing regardless of initial D_R, which is consistent with the principals of critical state soil mechanics (Schofield & Wroth 1968).

$\bar{\phi}_{yz}$ is approximately equal to $\bar{\phi}_{zy}$ throughout shearing in each simulation, indicating that the stress tensor is approximately symmetric within the shear band and the simulations are in quasi-equilibrium. The trends in $\bar{\phi}_{yz}$ and $\bar{\phi}_{zy}$ in Fig. 5.5 are equivalent to those of ϕ, and ϕ is only 1°-2° higher than $\bar{\phi}_{yz}$ and $\bar{\phi}_{zy}$ due to the finite thickness of the measurement region (Cui & O'Sullivan 2006). The quantitative similarity between ϕ, $\bar{\phi}_{yz}$, and $\bar{\phi}_{zy}$ shows the stresses measured at the boundaries of the shear box represent accurately the stresses within the shear band when the lateral walls are frictionless.

The peak value of $\bar{\psi}$ occurs at the same horizontal displacement as ψ, and the overall trend of $\bar{\psi}$ is consistent with ψ despite the greater scatter in the data for $\bar{\psi}$. However, ψ can underestimate $\bar{\psi}$ by as much as 4° with $\bar{\psi}$ being homogenized within the 2 mm thick measurement region of Fig. 5.3. Homogenization of $\bar{\psi}$ within an 18 mm thick measurement region produced lower peak values of $\bar{\psi}$ that were closer to the values of ψ. This suggests that the vertical strain in the particle assemblage tends to be partially absorbed by the less sheared material outside of the shear band in dilatant particle assemblages. Thus, external measurements of material dilation underestimate the true dilation of the sheared material within the shear band.

A summary of results for ϕ_{pk} and ψ_{max} for all simulations with $\sigma_n \leq 1$ MPa is provided in Fig. 5.6 with best-fit relations shown with associated R^2 values to indicate goodness of fit. ϕ_{pk} of each particle assemblage decreases systematically with decreasing D_R at a constant rate down to ϕ_{crit}, and ψ_{max} decreases at a constant rate down to zero. At similar values of D_R in Fig. 5.6, the sphere assemblages exhibit significantly lower values of $\phi_{pk} - \phi_{crit}$ and ψ_{max}, because spheres do not interlock during shearing. Particle interlocking is a key contributing factor to shear strength, especially at higher relative densities (Lee & Seed 1967). The interlocking of the sphere-clusters also results in ϕ_{crit} = 29°-31° as opposed to ϕ_{crit} = 23° for the sphere assemblage.

Fig. 5.7 compares the mobilized friction angle for dense sphere-cluster assemblages at different applied loads with ϕ measured in a series of DS tests on Fontainebleau sand with $D_R \approx$ 80% (Gaudin 2002). The shape of the DEM-calculated curves with σ_n = 30-200 kPa in Fig. 5.7 are consistent with the experimental data, though the DEM peak friction angles are slightly higher with $D_R \approx$ 73%. When $D_R \approx$ 73% and σ_n = 30-200 kPa, ψ_{max} for the DEM assemblage is 20°, which is higher than the measured ψ_{max} of 11° for Fontainebleau sand under σ_n = 188.5 kPa (Anastasopoulos et al. 2007). Thus, a DEM assemblage with idealized particle shapes may need to be prepared to a slightly lower value of D_R than its physical analogue if the DEM assemblage is to capture a similar peak strength and angle of dilation.

5.4.3 Stress Dependency

The linear relations of ϕ_{pk} and ψ_{max} with D_R shown in Fig. 5.6, which occur until reaching ϕ_{crit} and 0, respectively, take a similar form as the relation of Bolton (1986) for plane-strain (*ps*) conditions:

$$\phi_{ps} - \phi_{ps,crit} = 0.8\psi_{\max} = 5\,[D_R(Q - \ln p) - R] \tag{5.6}$$

where R = 1 and Q = 10 for quartz-based sands and p is the mean stress, i.e., $p = \frac{1}{3}(\sigma_1 + \sigma_2 + \sigma_3)$. Bolton (1986) includes dependence of ϕ_{pk} and ψ_{max} on p, whereas the data in Fig. 5.6 do not show significant dependence on σ_n below 1 MPa. If the mean stress term is removed from Eqn. (5.6), then the form of Eqn. (5.6) is exactly the same as the form of the relations in Fig. 5.6.

The issue of stress dependency is best illuminated in *e-log(p)* space. Void ratio is calculated within the shear band at critical state using a series of closely-spaced measurement spheres with diameters of 8 mm by re-generating all constituent sphere positions at the critical state into the PFC3D software (Itasca 2014). The mean stress at critical state is calculated as $p = \frac{1}{3}(\bar{\sigma}_1 + \bar{\sigma}_2 + \bar{\sigma}_3)$. Fig. 5.8 shows that the critical state void ratio (e_{crit}) depends on the shapes of the particles, and it consistently corresponds to $D_R \approx 7\%$ for the sub-angular sphere-clusters, $D_R \approx 9\%$ in the sub-rounded sphere-clusters, and $D_R \approx 10\%$ in the spheres when $p \leq 1$ MPa. At critical state when $p > 1$ MPa, e_{crit} tends to decrease as p increases, but this decrease is largely due to increased inter-particle overlaps under high stresses. Hanley et al. (2015) observed a similar lack of stress-dependence at relatively low stresses in simulations of triaxial compression with non-crushable spheres, and significant decreases in void ratio at high stresses also resulted from increased inter-particle overlaps (Hanley et al. 2015). Incorporation of particle crushing produced more realistic critical state lines in their simulations.

These DEM simulations capture the dependence of strength on relative density, but it underestimates the effects of confining stress on peak strength. At high confining stresses (i.e. σ_n = 10 MPa), particle crushing would occur to offset dilation, and no distinct peak should occur (Lee & Seed 1967). When the DEM particles do not crush, they must inevitably rise over one another even at high stresses. As σ_n increases from 200 kPa to 1 MPa in Fig. 5.7, ϕ_{pk} remains nearly constant. When σ_n = 5-10 MPa, ϕ_{pk} only decreases slightly due to increased inter-particle overlaps surpassing 5% of the smaller contacting sphere diameter in a small percentage of the contacts. The initial stiffness of the DEM assemblages systematically decreases with increasing σ_n, so the failure strain of the DEM assemblage is stress-dependent even though the strength is nearly independent of stress. More stress-dependency could be achieved by reducing the spring stiffness at the inter-particle contacts or using a lower value of μ. However, reducing inter-particle stiffness treats inter-particle overlap as a proxy for particle crushing, which may violate the small-overlap assumption of DEM (Huang et al. 2014b). Using too low a value of μ may produce unrealistically low peak strengths. Therefore, only explicit methods of particle crushing (e.g., Hanley et al. 2015) are recommended to achieve greater stress dependency over a larger stress range. However, over a smaller stress range, wherein e_{crit} does not vary significantly, particle crushing is not required to capture key aspects of critical state soil mechanics (e.g., effects of relative density), and the effects of particle crushing can be ignored if a simulation remains in a relatively low-stress regime.

The DEM results do exhibit stress dependency in coordination number (*CN*), which is the average number of contacts per particle. Under the same σ_n, the sub-angular sphere-clusters tend towards a consistent *CN* within the measurement region at the critical state, as shown in Fig. 5.9a. The densest particle assemblage exhibits a slightly lower *CN*, because it dilates much more than the other particle assemblages and therefore loses a greater number of contacts. Fig. 5.9b shows the critical state coordination number (CN_{crit}) from all simulations at all relative densities and stresses. The data for each curve follow a trend of the form:

$$CN_{crit} = a + b\left(\frac{p}{p_a}\right)^n \tag{5.7}$$

p_a is the atmospheric pressure. This is the same functional form suggested by (Li & Wang 1998) for e_{crit} and used by (Hanley et al. 2015) to fit their DEM data. In the assemblages of spheres and sub-angular sphere-clusters, the parameters of Eqn. (5.7) are fit with R^2 = 0.99 with values of p up to 10 MPa. The stress-dependence of CN_{crit} shows that the particles rearrange to achieve greater stability with more contacts as the applied stress increases. The curvatures of the functional forms of the two sphere-cluster assemblages are similar, and they have higher coordination numbers than the spheres. The rate of increase in CN_{crit} with increasing p is higher in the sphere-cluster assemblages than in the spheres.

5.4.4 Shear Zone Development and Thickness

DEM can capture key aspects of shear rupture formation in granular media. The evolution of the shear zones in representative simulations in the DS tests are shown through principal axis particle rotations of every individual particle in Fig. 5.10. At the ΔY corresponding to the peak strength in Fig. 5.10b, the start of a shear zone developing along the mid-plane of the specimen appears. This zone is not perfectly horizontal, and two other inclined shear zones also emanate from the edges of the shear box in Fig. 5.10b. The centers of these inclined shear zones are indicated in Fig. 5.10b by dashed red lines. Conversely, the loosest particle assemblage in Fig. 5.10a does not exhibit a distinct shear localization at this amount of ΔY. The loose particle assemblage in Fig. 5.10c,e shows more distributed shearing with no distinct linear shear zone at the same values of ΔY shown in Fig. 5.10d,f for the dense particle assemblage.

Fig. 5.11 shows the displacements of each individual particle in select simulations at different values of ΔY. At the top of the loose assemblage of sphere-clusters in Fig. 5.11a, the range of particle displacements is centered around the zero position and about 10 times wider by the critical state than at ΔY = 0.6 mm. At the bottom of the particle assemblage, the range of displacements is about 3.5 times wider by the critical state than at ΔY = 0.6 mm. Although there is a significant increase in the amount of particle displacement in the range Z = 0-2 mm, the increases in the range of particle displacements near the upper and lower boundaries during shearing in Fig. 5.11a reflect the broad shear zone in Fig. 5.10a,c,e. In the dense assemblages of sphere-clusters and spheres in Fig. 5.11b-c, the ranges of particle displacements at the tops of the assemblages remain relatively constant, and at the bottoms of these assemblages the range is only about 40-60% wider at the critical state than at the peak state. This small amount of relative displacement at the upper and lower bounds of the particle assemblages in Fig. 5.11b-c allows the limits of the shear bands along the mid-plane to be determined quantitatively as the Z-positions at which the ranges of particle displacements just begin to expand more than at the upper and lower bounds. These limits are delineated in the dense assemblages of sphere-clusters and spheres in Fig. 5.10f-g. The indicated shear band limits are consistent with the edges of the zones of high-magnitude particle rotations, which effectively delineates the distinct shear band that is kinematically forced by the direct shear box constraints to develop along the mid-plane. The shear band develops fully by the end of strain softening in the densest particle assemblage, as shown by the higher-magnitude particle rotations in Fig. 5.10d, and further shearing to the critical state increases the magnitude of particle rotations within the shear band in Fig. 5.10f.

The interlocking of the sphere-clusters inhibits rotations away from the shear band relative to that of the assemblage of spheres. The shear zone in Fig. 5.10f for the sub-angular sphere clusters is significantly thinner than the shear zone in the assemblage of spheres shown in Fig. 5.10g. The

disturbance of the fabric of spheres propagates further away from the mid-plane, because the spheres adjust to the changing stress state more easily through rotation. The shear band thickness for the sphere-clusters shown in Fig.10f is 7.5 times the median grain diameter of D_{50} = 1.0 mm, and the shear band thickness for the spheres shown in Fig. 5.10g is approximately 10 times the median grain diameter of D_{50} = 1.1 mm. These shear band thicknesses are consistent with the radiographic measurements of shear band thicknesses 5-10 times the average grain size in direct shear tests on Leighton Buzzard sand by Scarpelli & Wood (1982). The shear zones in slightly looser strain-softening particle assemblages are thicker than in the densest particle assemblages, because the shear zone tends to increase in thickness as D_R decreases until a distinct shear zone does not develop.

The velocities of the particles highlight the fluid-like nature of granular materials in shear. Fig. 5.12 shows colored contours of the magnitude of particle velocity normalized by the horizontal velocity of the lower shear box. Flowlines in Fig. 5.12 indicate the directions of the particle velocities. At early stages of shearing in Fig. 5.12a-c, the flowlines follow a relatively uniform pattern analogous to laminar flow, especially in the dense particle assemblages. The dense assemblages of sphere-clusters and spheres in Fig. 5.12b-c dilate, so at the peak state the flowlines transition from horizontal to vertical moving up the particle assemblage. The contractive nature of the loose assemblage of sphere-clusters in Fig. 5.12a produces significant particle movement downward and towards the right boundaries.

The velocity contours show a zone of high velocities immediately adjacent to the displacement discontinuity above the mid-plane in Fig. 5.12a-f. This displacement discontinuity produces circular, counterclockwise velocity patterns near it at the critical state, and it leaves a wake of flow paths with a turbulent, chaotic appearance near the leftmost edge of the upper shear box. The influence of this displacement discontinuity does not extend across the entire length of the direct shear box. As shown in Fig. 5.12d and e, the loosely packed sphere-cluster velocities in the right half of the upper shear box, although of relatively low magnitude, are predominantly horizontal, while the densely packed sphere-cluster velocities are predominantly vertical within the same region.

The flow paths at the critical state of the dense assemblage of spheres in Fig. 5.12f are more random than in Fig. 5.12e. The inability of the spheres to resist rotation causes contacting spheres to roll antithetically to each other (Iwashita & Oda 2000), and these opposing particle rotations contribute to a more random velocity field in the upper shear box of Fig. 5.12f as opposed to Fig. 5.12e. The inherent rotational resistance of sphere-clusters causes contacting sphere-clusters to rotate more uniformly in the manner of a bending column of particles (Iwashita & Oda 2000). The more uniform rotations in the dense assemblage of sphere-clusters produce strongly localized vortex patterns in the flowlines within the shear zone in Fig. 5.12e. Similar vortex patterns in the particle velocities within shear bands were observed in 2D biaxial simulations by Thornton & Zhang (2006). These velocity vortexes are a result of the instability associated with the drop in mobilized shear stress in strain-softening materials.

5.5 Conclusion

The large number of direct shear test simulations facilitated by the use of HPC verify that measurements of friction angle and angle of dilation made at the test boundaries of a specimen enclosed by frictionless lateral walls reflect accurately the mechanical response within the shear zone. The overall mobilization trend, including the horizontal displacement at which the peak state

occurs, was consistent between boundary-measured and homogenized values of friction and dilation angle. The angle of dilation is slightly underestimated at the boundaries due to partial absorption of the vertical strain throughout the specimen height, but the friction angles only differed by 1°-2°. The sphere-cluster assemblages exhibited significantly higher peak strengths and dilations than the sphere assemblages at similar relative densities due to their inherent resistance to rotation.

The trends in mobilization of friction angle in the dilatant assemblages of sphere-clusters are consistent with those of Fontainebleau sand, but the sphere-cluster assemblages exhibit slightly higher peak strength and dilatancy. The results suggest that when a DEM sphere-cluster assemblage is treated as an analogue material for a physical sand, the sphere-cluster assemblage should be prepared at a slightly lower relative density to capture the macroscopic strength and dilation of the physical sand of interest. The DEM assemblages exhibit behaviors that are consistent with critical state soil mechanics, such as constant-volume shearing at large strains, a consistent critical-state friction angle that is independent of the initial relative density of granular media, and simultaneous peaks in the angle of dilation and friction angle in dilatant materials.

The simulation results showed stress-dependency in the critical state coordination number, which follows a trend with increasing mean stress consistent with the critical state line of sands and in the initial stiffness of the particle assemblages. Due to the lack of particle crushing in the DEM particles, however, the void ratios at critical state were not stress-dependent. Methods of incorporating stress-dependency in the critical state void ratio other than explicitly incorporating particle crushing are not recommended.

The large number of particles simulated with the use of HPC facilitated highly detailed analysis of the shear zone development. In dense particle assemblages, the shear band begins to develop at the peak state and forms fully by the end of strain softening, as shown through particle rotations. Continued shearing distinguishes the shear band even further but does not significantly change its thickness. Loose particle assemblages show a more widespread distribution of shearing with no distinct localization at any stage of shearing. Analysis of particle velocities revealed fluid-like characteristics of the particle assemblages in shear, in particular the appearance of vortex patterns in the velocity fields of strain-softening materials. The inability of the spheres to interlock and resist rotation produced thicker shear bands than in the sphere-clusters and a more random velocity field within the upper shear box, and the shear band thicknesses in denser assemblages of spheres and sphere-clusters were consistent with measurements made in physical direct shear tests.

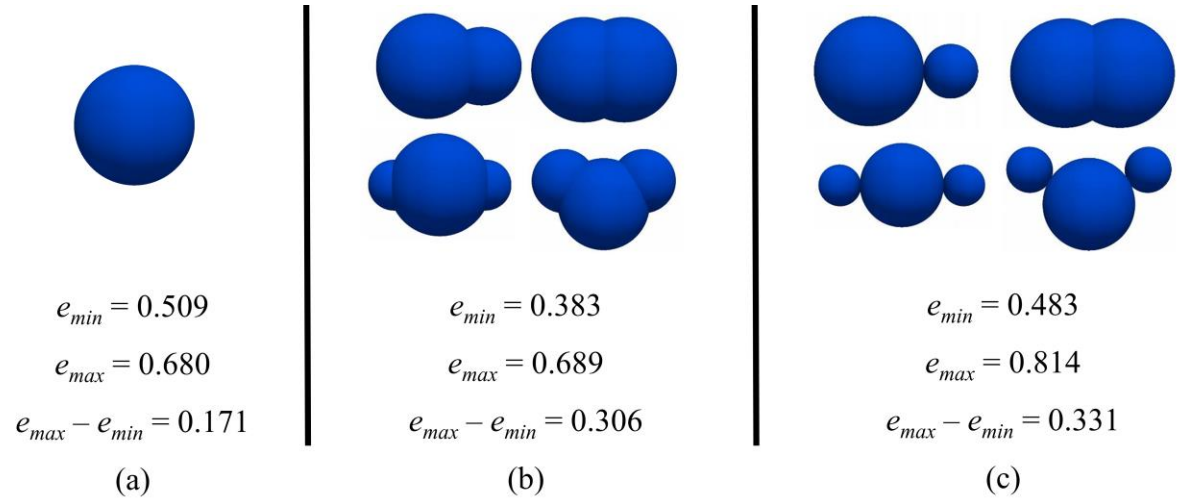

Fig 5.1. Particle shapes: (a) spheres, (b) sub-rounded sphere-clusters, (c) and sub-angular sphere-clusters.

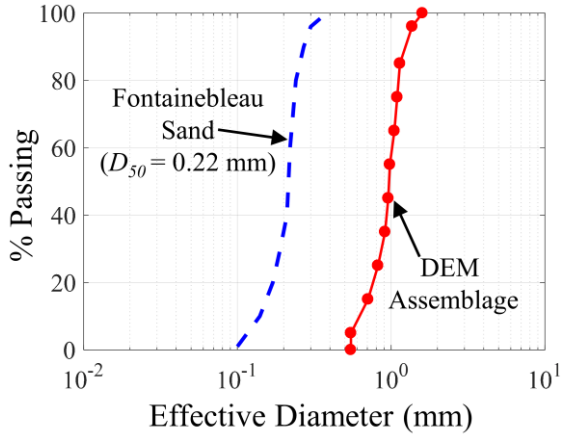

Fig. 5.2. Grain size distributions for Fontainebleau sand (Delfosse-Ribay et al. 2004) and a sample DEM assemblage of sub-angular sphere-clusters.

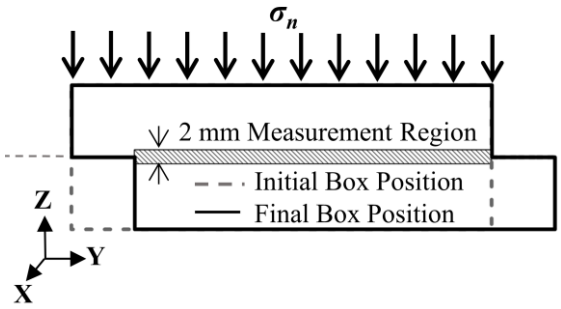

Fig. 5.3. Schematic of direct shear test simulation boundary conditions.

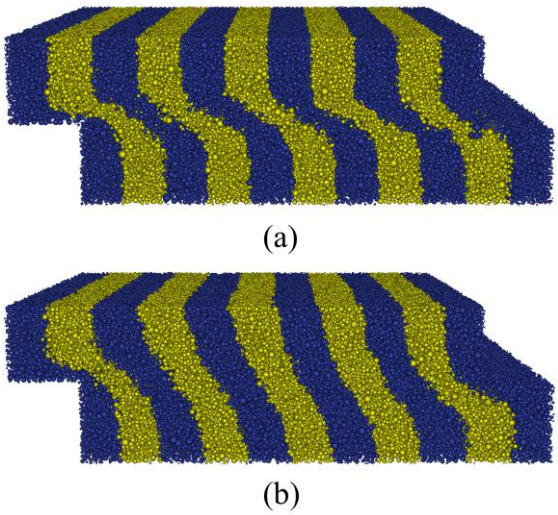

Fig. 5.4. Representative results of a sub-angular sphere-cluster assemblage with σ_n = 100 kPa for (a) D_R = 98% and (b) D_R = 9%.

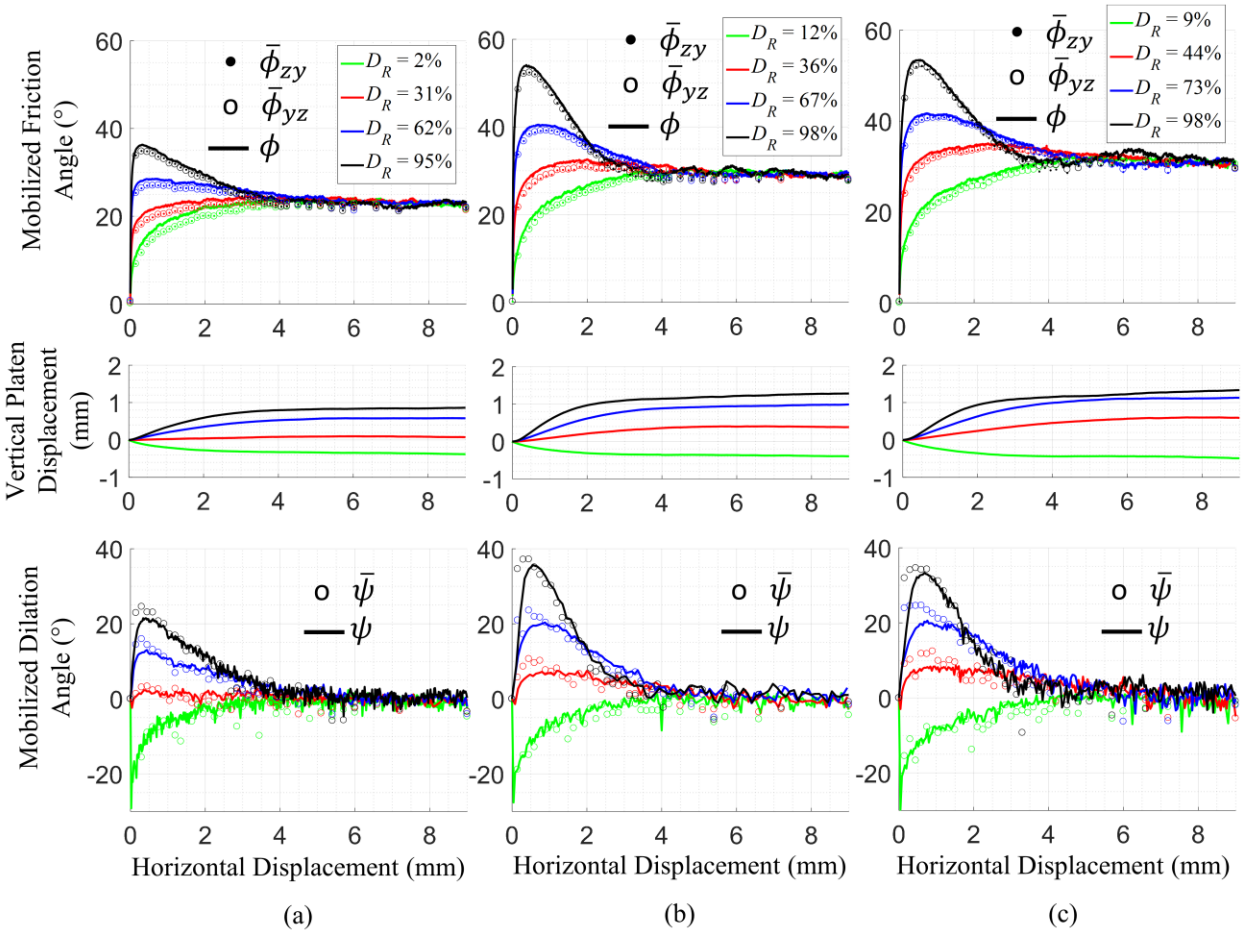

Fig. 5.5. Representative results of mobilized friction angle, vertical platen displacement, and mobilized dilation angle under σ_n = 100 kPa for assemblages of (a) spheres, (b) sub-rounded sphere-clusters, and (c) sub-angular sphere-clusters.

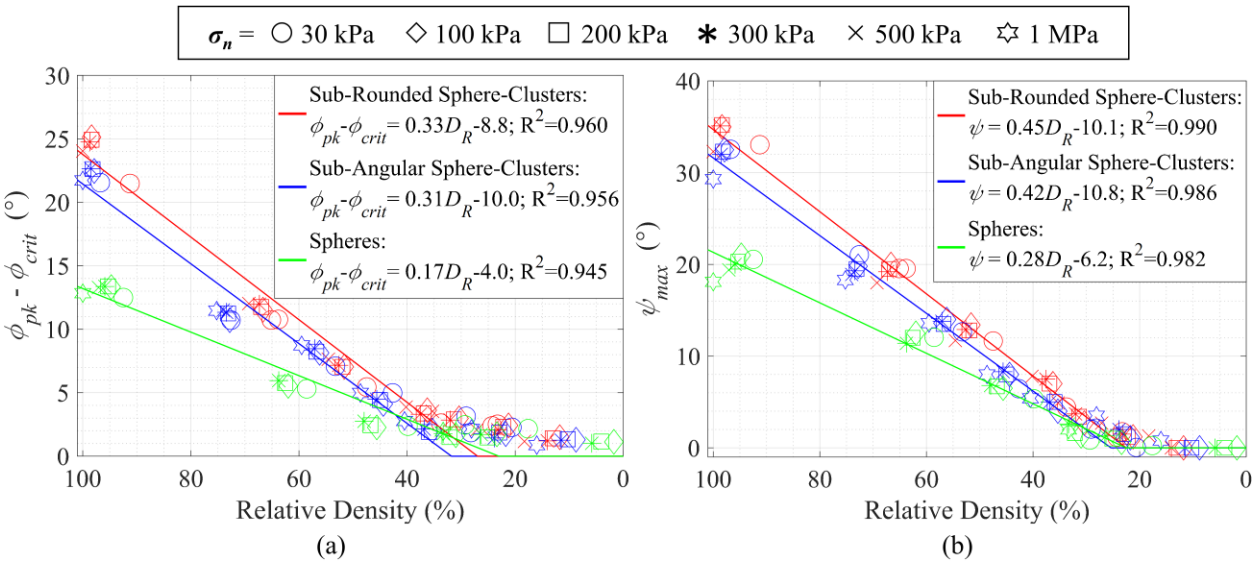

Fig. 5.6. Summary of (a) peak friction angles and (b) maximum angles of dilation from direct shear test simulations with normal loads up to 1 MPa.

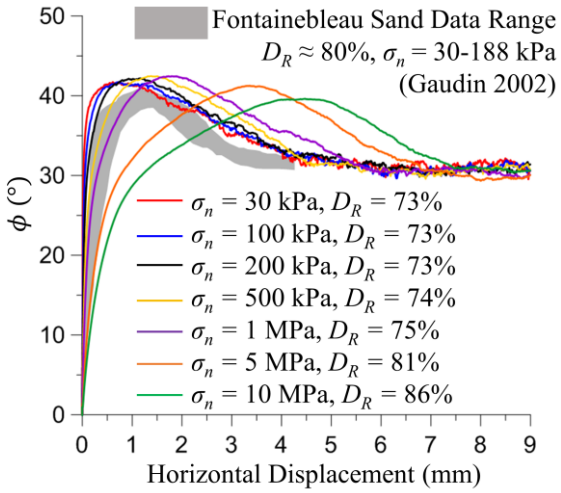

Fig. 5.7. Mobilized friction angles measured at the wall boundaries of some DEM assemblages of sub-angular sphere-clusters and measured in DS test results on Fontainebleau sand. Experimental data from (Gaudin 2002).

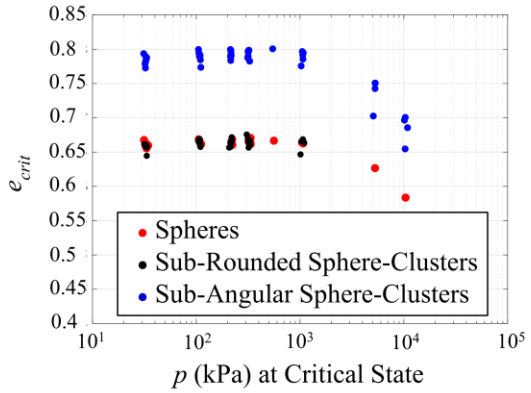

Fig. 5.8. Variation of critical state void ratio with mean stress within the measurement region.

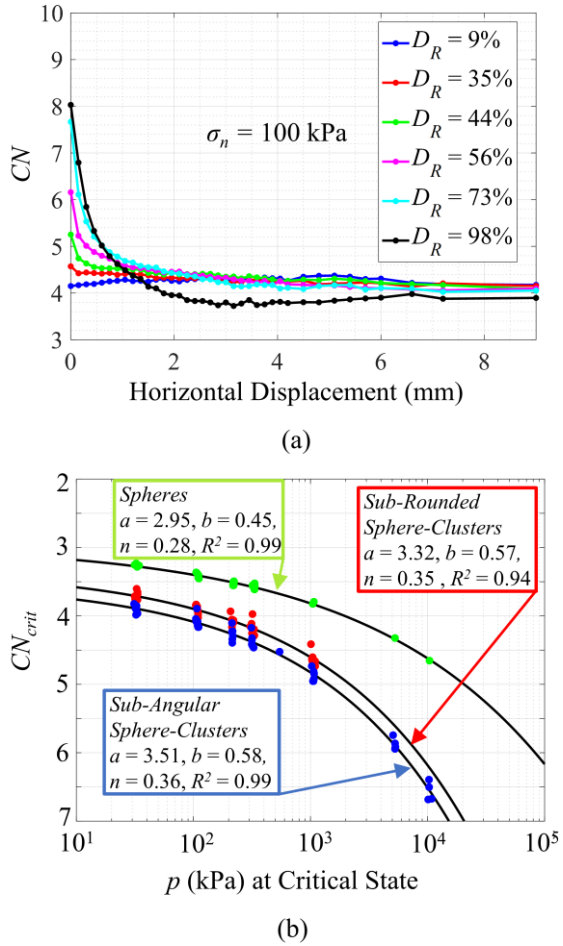

Fig. 5.9. (a) Evolution of coordination number within the measurement region in assemblages of sub-angular sphere-clusters. (b) Variation in critical state coordination number within the measurement region for each particle assemblage.

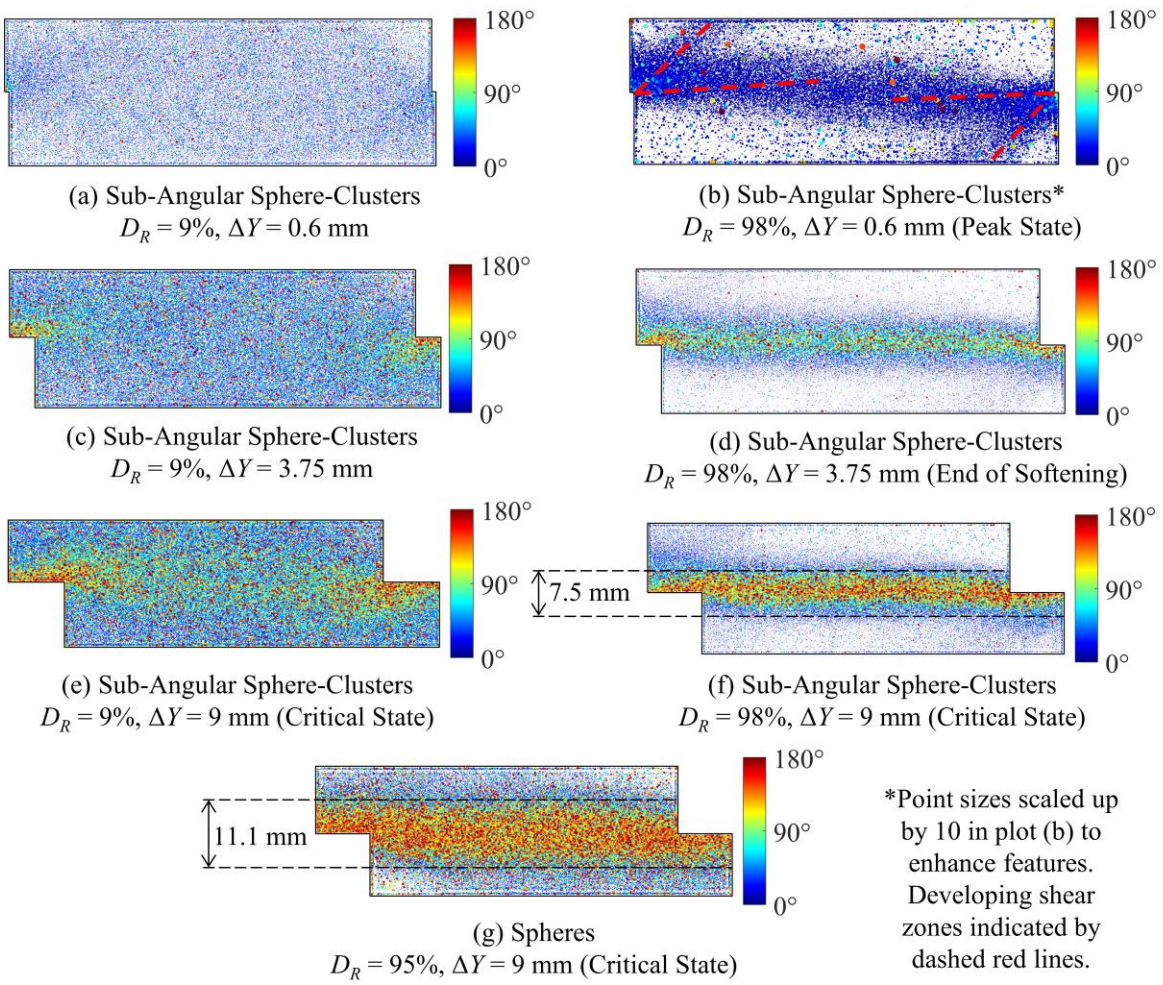

Fig. 5.10. Evolution of shear zone shown through distributions of individual particle rotations for sub-angular sphere-clusters and spheres under σ_n = 100 kPa.

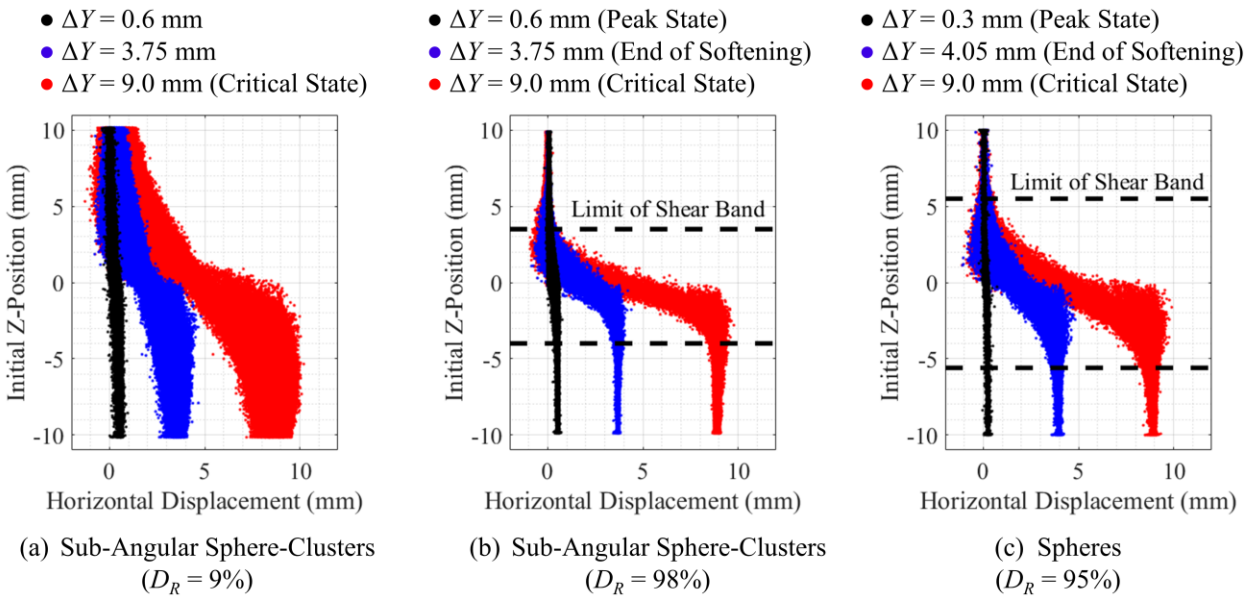

(a) Sub-Angular Sphere-Clusters (D_R = 9%)

(b) Sub-Angular Sphere-Clusters (D_R = 98%)

(c) Spheres (D_R = 95%)

Fig. 5.11. Summary of individual particle displacements within entire model domain for select simulations with σ_n = 100 kPa.

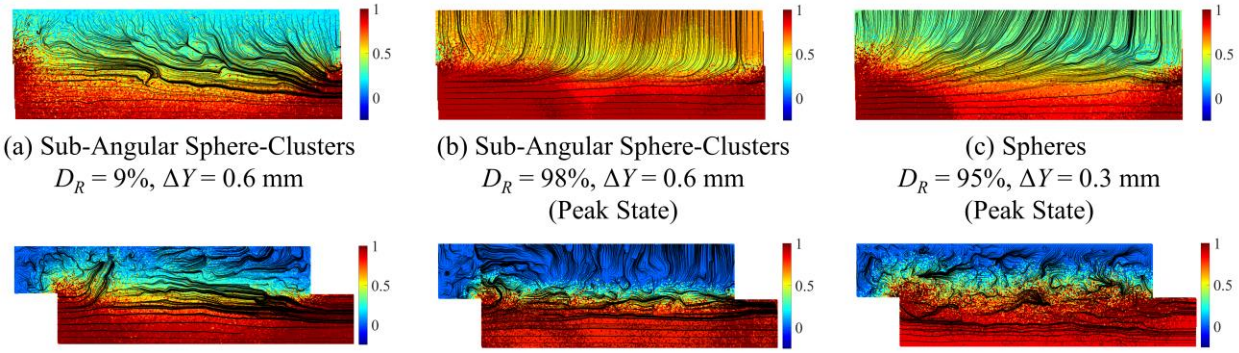

(a) Sub-Angular Sphere-Clusters D_R = 9%, ΔY = 0.6 mm

(b) Sub-Angular Sphere-Clusters D_R = 98%, ΔY = 0.6 mm (Peak State)

(c) Spheres D_R = 95%, ΔY = 0.3 mm (Peak State)

(d) Sub-Angular Sphere-Clusters D_R = 9%, ΔY = 9 mm (Critical State)

(e) Sub-Angular Sphere-Clusters D_R = 98%, ΔY = 9 mm (Critical State)

(f) Spheres D_R = 95%, ΔY = 9 mm (Critical State)

Fig. 5.12. Contours of particle velocities normalized by the horizontal velocity of the lower shear box. Velocity flowlines are represented by black lines.

CHAPTER 6: DISCRETE ELEMENT ANALYSIS OF EARTHQUAKE FAULT RUPTURE-SOIL-FOUNDATION INTERACTION

6.1 Introduction

Earthquake surface fault rupture can cause significant structural damage (e.g., Lettis et al. 2000, Bray 2001, Kelson et al. 2001, and Stirling et al. 2017). Avoidance of this hazard in seismic regions is increasingly difficult in urbanized areas crossing active faults and when lifelines must cross active faults to connect communities. The development of advanced numerical methods to evaluate and provide insight into the effects of earthquake surface fault rupture on the built environment has merit.

This study utilizes the discrete element method (DEM) to analyze the development of shear ruptures within a soil deposit overlying a displaced bedrock fault as they interact with a stiff building foundation. DEM is an invaluable tool for capturing the inherent particulate nature of a soil deposit as it responds to a bedrock fault displacement. The parallel-computing code LIGGGHTS (Kloss et al. 2012), with enhancements developed through this study (see Appendix A), enables performing DEM simulations incorporating hundreds of thousands of three-dimensional (3D) sphere-clusters using high-performance computing. Following this introduction, previous experimental and numerical studies of earthquake fault rupture-soil-foundation interaction (FR-SFI) are summarized. The numerical procedure for preparing particle assemblages and inducing fault rupture in simulations analogous to the geotechnical centrifuge experiments of Bransby et al. (2008a,b) is provided. Free-field surface fault rupture results are first compared with the experimental results for reverse and normal faulting. The response of the foundation in reverse and normal FR-SFI simulations is then compared with experimental results involving rigid mat foundations. Lastly, micromechanical aspects of FR-SFI are investigated using results available from DEM analyses, and concluding remarks are made.

6.2 Previous Research

Earthquake fault rupture propagation through soil has been modeled successfully in several studies. Bransby et al. (2008a,b) used a geotechnical centrifuge to investigate surface fault rupture and its interaction with rigid mat foundations in 15-m deep and 25-m deep (prototype scale) sandbox model experiments under an acceleration of 115 g. These carefully-controlled experiments are useful to back-analyze for evaluating the strengths and limitations of various numerical methods. They were used to validate the finite element method (FEM) analyses of Anastasopoulos et al. (2007, 2008, 2009), who achieved satisfactory numerical results with a constitutive model that incorporates strain softening. After validating their model, Anastasopoulos & Gazetas (2007b) were able to replicate qualitatively the interaction of outcropping faults with different buildings observed in the 1999 Kocaeli earthquake (Anastasopoulos & Gazetas 2007a). Similarly, Oettle & Bray (2013a) used the Bransby et al. (2008a,b) results to calibrate their finite difference method (FDM) simulations of FR-SFI with previously ruptured soil. Their constitutive model captured the nonlinear, stress-dependent response and post-peak strain softening of soil. Oettle & Bray (2013b) then used their validated simulations to develop fault diversion methods and to establish appropriate setback distances from active fault traces.

Continuum-based methods (i.e. FEM and FDM) are able to capture macroscopic characteristics of surface fault rupture and its interaction with the built environment. However,

they cannot capture the true granular nature of the soil undergoing deformation resulting from this phenomenon. Chapters 3 and 4 showed that 3D simulations of free-field fault rupture through dilatant particle assemblages with the Particle Flow Code (PFC; Itasca 2014) produce rupture surface shapes that are consistent with the sandbox experiments of Cole & Lade (1984) and centrifuge experiments of Bransby et al. (2008a,b). The types of grain-scale analyses in these studies are valuable for studying the interaction between the soil deposit responding to a bedrock fault and a structural foundation atop of it. The particulate mechanics insights provided by DEM simulations make it an invaluable tool for investigating FR-SFI problems.

6.3 Model Preparation and Simulation Procedure

Assemblages of the 3D sphere-clusters shown in Fig. 6.1 (with D_{50} = 1.61 mm) are used to model the Fontainebleau sand used by Bransby et al. (2008a,b) in their centrifuge experiments with a gradation curve parallel to that of Fontainebleau sand (Delfosse-Ribay et al. 2004). Particle shapes are selected such that the effective diameter (D_{eff}) of a sphere-cluster that may reorient to pass through a sieve is represented by the diameter of its largest constituent sphere. Grain size distribution and median grain diameter (D_{50}) are based on the particles in the center of the sandbox where the fault rupture surface propagates (Fig. 6.2a). Zones of particles 4 times larger in volume are located at the left and right sides of the sandbox where they will not influence the path of fault rupture propagation to reduce the computational costs of the simulation in a manner analogous to FEM mesh refinement. Periodic boundaries are spaced $10D_{max}$ apart, where D_{max} is the maximum effective grain size, in the direction of the strike of the bedrock fault to approximate an infinitely long domain in which particles across one periodic boundary interact with particles across the other periodic boundary. The periodic length is based on the ASTM standard for direct shear test height (ASTM D3080).

Young's modulus (E), Poisson's ratio (ν), friction coefficient (μ), and coefficient of restitution values of 7.6 GPa, 0.31, 0.50, and 0.9, respectively, are used for all inter-particle contacts with the Hertz contact model in LIGGGHTS, and the particle density is 2650 kg/m^3 based on the specific gravity of quartz (Santamarina et al. 2001). Additionally, a local non-viscous damping factor of 0.3 is included to damp the motion of accelerating particles (Itasca 2014). Assemblages of these sub-angular sphere-clusters were characterized with direct shear test simulations in Chapter 5 to obtain the peak angle of dilation (ψ_{pk}), peak friction angle (ϕ_{pk}), and critical state friction angle (ϕ_{cs}), as well as realistic mobilization of shear stress and volumetric strain in addition to strain-softening with horizontal.

Particle assemblages are prepared by first generating a random group of particles within a virtual sandbox. The particles settle with a reduced value of μ as the gravitational acceleration quasi-statically increases incrementally to ng (where g = 9.81 m/s^2 and n = 115) to match the scaling factor used in the centrifuge experiments of Bransby et al. (2008a,b). When the maximum particle height stops decreasing with increasing gravity (typically around 0.5-0.6 ng), the ground surface is smoothed by removing particles positioned above the desired assemblage height, and μ is increased to 0.5. The increments of gravity then continue for another 40-50 increments until the final gravitational acceleration of ng is reached. This procedure produces an earth pressure coefficient (K_o) of 0.45±0.05.

The vertical and horizontal boundaries of the hanging wall displace up or down for reverse or normal fault displacements, respectively, while the footwall boundaries at the left remain stationary. The widths of the footwall and hanging wall (W_{FW} and W_{HW}) are 51.75 m and 23 m

(prototype scale), respectively. Bedrock fault displacement is induced by quasi-statically moving the hanging wall boundaries in the dip direction, which is 60° in all simulations, at 0.05 m/s. Simulations with rates of rupture of 0.025 m/s to 0.1 m/s showed negligible differences.

The foundation is one rectangular sphere-cluster 10 mm in height (model scale) with an out-of-plane width equal to the periodic length of the simulation domain. Figure 2b shows the foundation sphere-cluster atop a ruptured assemblage of irregularly-shaped sphere-clusters. The foundation is composed of hundreds of constituent spheres arranged in the shape of a mat foundation. It is placed at the ground surface after the particle assemblage reaches equilibrium under *ng*. As in the centrifuge experiments, the foundation is modeled as a rigid body in the DEM simulations. The foundation is restricted from rotating about the *Y*- and *Z*-axes and from displacing along the *X*-axis (i.e. plane-strain movement). The contact properties of the foundation are the same as those for the soil particles.

6.4 Free-Field Fault Rupture

The DEM models are prepared with heights (*H*) matching those of the centrifuge experiments of Bransby et al. (2008a,b). The macroscopic properties of the particle assemblage (i.e. ψ and φ) are not direct inputs to the DEM simulation but instead emerge mechanistically from the void ratio of the particle assemblage, the particle shapes, and the properties of the inter-particle contacts. The particle assemblages are generated to estimate the fault outcrop location and patterns of shear rupture based on the known properties of Fontainebleau sand used in the centrifuge experiments and are not calibrated directly to match the experimental results. Bransby et al. (2008a,b) report that Fontainebleau sand with $D_R \approx 60\%$ has $\psi_{pk} = 6°$, $\phi_{pk} = 35°$ and $\phi_{cs} = 30.2°$ in direct shear with 200 kPa of applied pressure. The DEM particle assemblages in this study have $\phi_{cs} \approx 31°$. Because fault rupture through granular soil is governed by dilatancy (Cole & Lade 1984), DEM particle assemblages are generated to have an angle of dilation close to that of the Fontainebleau sand used in the centrifuge experiments. For normal fault rupture validation, the DEM model contains 703,091 sphere-clusters of D_{50} = 1.61 mm with 1,770,625 constituent spheres, has a prototype depth of 25 m, and has an average void ratio ranging from 0.670 at the bottom to 0.688 at the ground surface. Chapter 5 showed that the DEM particle assemblages have minimum and maximum void ratios of 0.483 and 0.814, respectively, so the void ratio range of the 25-m particle assemblage corresponds to $D_R \approx 42\%$. Based on direct shear test characterizations in Chapter 5, $\psi_{pk} \approx 7°$ and $\phi_{pk} \approx 35°$ in this particle assemblage. Two 15-m deep particle assemblages are generated for reverse fault rupture validation. The first particle assemblage contains 422,988 sphere-clusters of D_{50} = 1.61 mm with 1,055,884 constituent spheres. The second particle assemblage contains 1,704,669 sphere-clusters of D_{50} = 0.81 mm with 4,292,644 constituent spheres. The void ratios in these assemblages range from 0.673 to 0.687, which corresponds to $D_R \approx 40\%$ and gives $\psi_{pk} \approx 6°$ and $\phi_{pk} \approx 34°$-$35°$.

The comparisons between the normal fault rupture results of experimental Test 12 by Bransby et al. (2008a) and its analogous DEM simulation are shown in Fig. 6.3 for different bedrock fault vertical displacements (*h*) normalized by *H*. The rupture surfaces in the simulation and in the experiment in Fig. 6.3a-b extend almost linearly from the bedrock fault with little curvature of the rupture surface towards the hanging wall during propagation. The inset of Fig. 6.3b shows that the shear band thickness is approximately $10D_{50}$, which is close to the thickness of $11.7D_{50}$ observed by Bransby et al. (2008a) for the experiment shown in Fig. 6.3a. The ground surface displacements are calculated 1 m below the ground surface to reduce the erratic

displacements of the free surface. The vertical ground surface displacement, or surface heave, profiles in Fig. 6.3c nearly overlie each other with the experimental profile showing a slightly steeper fault scarp at $h \approx 2.1$ m than the DEM-calculated profile. The total surface heave at the far edge of the hanging wall side is equivalent between experiment and simulation at all values of h, which indicates relatively uniform particle displacement above the hanging wall away from the shear zone. Both experiment and simulation show a lowest point in the surface heave profile near $Y = 0$ m at $h \approx 2.1$ m, and the surface heave becomes less negative moving to the right. The dip in the surface heave profile in Fig. 6.3c results from incomplete graben formation, but this incomplete graben formation cannot be confirmed in Fig. 6.3a or 6.3b. However, Fig. 6.4 shows additional particle fabric disturbance as small-magnitude particle rotations above the hanging wall that are indicative of a partially-developed secondary rupture surface dipping antithetically to the primary rupture surface, the latter of which is delineated by substantial particle rotations extending over the footwall. Shallower bedrock fault dip angles would produce full graben formation with a fully developed secondary rupture surface, as seen in Chapter 3.

The free-field reverse fault results from Test 28 of Bransby et al. (2008b) and its analogous DEM simulations with $\psi_{pk} \approx 6°$ are compared in Fig. 6.5. The experimental and numerical results, the latter shown for $D_{50} = 0.81$ mm, in Fig. 6.5a-b are qualitatively similar in that both rupture surfaces bend over the downthrown block and appear to widen as they approach the ground surface. The inset of Fig. 6.5b shows that the thickness of the upward-widening numerical shear band is 15-20D_{50}. The equivalent simulation with $D_{50} = 1.61$ mm showed a shear band thickness of approximately 10D_{50}. The smaller particle sizes in Fig. 6.5b allow finer details to develop, but the rupture surface at the macroscopic level is not significantly affected by particle size. The location of the fault scarp in the DEM simulations with $\psi_{pk} \approx 6°$ is relatively independent of particle size as seen in the surface heave profiles at different stages of reverse fault rupture in Fig. 6.5c, but the fault scarp steepens slightly as particle size decreases. Similar results were found in simulations with denser and looser soils where a single rupture surface developed (see Appendix C). The computational costs of the simulation with $D_{50} = 0.81$ mm were much higher, requiring 576 2.3-GHz computing cores to complete 500 calculation cycles in approximately 55 seconds with a timestep of 5×10^{-8} seconds as opposed to 96 2.5-GHz cores for the simulation with $D_{50} = 1.61$ mm to complete 500 calculation cycles in approximately 24 seconds with a timestep of 1×10^{-7} seconds.

The DEM simulations capture important trends such as the increasing surface slope and translation of the mid-point of the fault scarp towards the footwall as h increases, which was observed by Bransby et al. (2008b). The 3-4 m offset between the $\psi_{pk} \approx 6°$ particle assemblage and the experimental results at different values of h in Fig. 6.5c is reasonable given the relatively small influence of stress on ϕ_{pk} and ψ_{pk} and an early onset of dilation shown through numerical direct shear test characterizations of the sphere-cluster assemblages in Chapter 5. Oettle & Bray (2016) showed that reverse fault rupture may outcrop further out on the footwall when dilation begins earlier at a lower stress ratio, and Anastasopoulos et al. (2007) observed a 3 m offset between their experimental and FEM-calculated ground surface deformation profiles when simulating reverse fault rupture through dense sand with a uniform value of ψ_{pk} in a strain-softening Mohr-Coulomb constitutive model. A smaller difference is seen in the DEM comparison with the experimental data in Fig. 4.5c because the relative density, and hence ψ_{pk}, in that simulation is less uniform. The lack of stress-dependent strength reduction in this study and the early onset of dilation are attributed to the inability of the particles to fracture or crush, which can be expected during the passive loading induced by reverse fault rupture. Techniques for including particle crushing

typically work exclusively for spherical particles (e.g., Hanley et al. 2015, Ciantia et al. 2015) or require many more than 3 constituent spheres per sphere-cluster (e.g., Cheng et al. 2003). The simulations in this study were simplified for the sake of computational efficiency by not incorporating particle crushing under high stresses.

The surface heave profile for a non-dilatant ($D_R \approx 7\%$, $\psi_{pk} = 0°$), 15-m deep particle assemblage containing 396,177 sphere-clusters with 977,422 constituent spheres is also shown in Fig. 6.5c to show that calibration of the DEM model based strictly on the experimental fault outcrop location is possible by reducing the relative density of the particle assemblage. Anastasopoulos et al. (2008a) also used $\psi_{pk} = 0°$ in their first described FEM method with an elastic-perfectly plastic Mohr-Coulomb constitutive model to obtain their most satisfactory agreement with experimental normal and reverse fault rupture results. However, Chapter 4 showed that lower density particle assemblages produce less distinctive shear rupture throughout the particle assemblage height, and, as will be shown later via micromechanical analyses, such indistinct shear rupture in very loose particle assemblages is not desirable for the study of shear rupture propagation in dilatant soils. The 3-4 m offset shown in Fig. 6.5c for the dilatant particle assemblage ($\psi_{pk} \approx 6°$) is consistent with other numerical simulations and is more reasonable to use in this study.

6.5 Earthquake Fault Rupture-Soil-Foundation Interaction

FR-SFI simulations analogous to the centrifuge experiments of Bransby et al. (2008a,b) are performed with the simulated foundations placed at the same location relative to the base fault location as in the centrifuge experiments. The FR-SFI simulations are characterized in terms of foundation width (B), foundation contact pressure (q), and foundation position, which is represented by s = distance from the free-field outcrop location at the ground surface to the footwall edge of the foundation as shown in Fig. 6.2a ($s > 0$ when the footwall edge of the foundation is further out on the footwall than the free-field fault outcrop location). The comparisons of DEM results in this section verify the capability of DEM to capture physically realistic trends of FR-SFI so that micromechanical interpretations of FR-SFI mechanisms in the simulations represent reliably the physical phenomena. All FR-SFI simulations and analyses are performed with particle assemblages having D_{50} = 1.61 mm for computational efficiency.

6.5.1 Reverse Fault Rupture

Reverse FR-SFI simulations are performed using 40-48 computing cores with the 15-m deep particle assemblage having $\psi_{pk} \approx 6°$. The simulation cases are defined as: baseline (B = 10 m, q = 91 kPa, s = 4.4 m), light foundation (B = 10 m, q = 37 kPa, s = 4.4 m), shifted foundation (B = 10 m, q = 91 kPa, s = -1.0 m), and wide foundation (B = 15 m, q = 91 kPa, s = 6.9 m). The baseline, light, and wide foundations are each centered at Y_0 = -13.2 m, and the shifted foundation is centered at Y_0 = -7.8 m. The rupture surfaces that develop through the particle assemblages are labeled as *S1* and *S2* in the order of when they first begin to develop. As will be discussed later, determinations of *S1* and *S2* in the simulations were made through analyses of void ratio changes and particle rotations. *S1* and *S2* for the experimental results are labeled as reported by Bransby et al. (2008a,b).

The results of the centrifuge experiments and analogous FR-SFI simulations with $\psi_{pk} \approx 6°$ are shown in Fig. 6.6 at similar values of h. The shear rupture does not follow its free-field path,

because it interacts with and is affected by the presence of the foundation. The FR-SFI DEM simulations produce patterns of fault rupture propagation similar to those in the experiments because the foundations are located at the same position relative to the bedrock fault and the simulated and experimental materials have similar angles of dilation. *S1* and *S2* develop near each other in the experiment and to *S1* in the simulation for the baseline case in Fig. 6.6a. The simulation for the baseline case produces only one rupture surface, because the larger particle sizes in the simulation as compared to the experiment inhibit the formation of a second distinctive rupture surface in the proximity of *S1*. In the light foundation case shown in Fig. 6.6b, two distinct rupture surfaces develop in both simulation and experiment. In the experiment, *S1* propagates to a left-of-center position underneath the foundation, because the reduced pressure of the light foundation does not fully inhibit fault outcropping directly below it. *S2* in the experiment outcrops on the hanging wall edge of the light foundation. In the simulation for the light case, *S1* and *S2* began developing nearly simultaneously with *S1* beginning to form only slightly earlier than *S2*. *S2* does not fully reach the ground surface in the simulation, and shear activity only occurs intermittently along *S2* while most shear activity occurs along *S1*.

The experimental and simulation results for the shifted foundation case shown in Fig. 6.6c are similar except for a different interpretation of what constitutes a rupture surface in the simulation. In the experiment, the colored layers are gently sloped as they move from *S1* towards the hanging wall side of the sandbox. This slope in the colored layers also appears in the simulation, and the upper end of these slopes is interpreted as a second rupture surface *S2*. The deforming soil surface passively pushes the foundation towards the footwall in both simulation and experiment and produces a small mound of soil building up at the footwall edge of the foundation. In the wide foundation case shown in Fig. 6.6d, *S1* initially propagates towards the hanging wall edge of the wide foundation, and *S2* only propagates halfway up the height of the sand in the experiment; whereas, *S1* propagates towards a left-of-center position underneath the foundation in the simulation, because the foundation is too wide to fully deflect *S1* towards its footwall edge. *S2* in the simulation occupies a location close to that of *S1* in the experiment and outcrops on the hanging wall edge of the foundation. In the shifted foundation and wide foundation cases, *S1* and *S2* are both active at $h/H = 0.23$.

The simulated foundation response for the $\psi_{pk} \approx 6°$ particle assemblage is compared with that in the experiment in terms of its rotation and displacement in Fig. 6.7. Except for the wide case, the experimental and simulated foundation rotations shown in Fig. 6.7a are similar. The simulated wide foundation response undergoes greater rotations than in the experiment, because the rupture surface that propagates underneath the foundation in Fig. 6.6d propagates further in the simulation than in the experiment and remains active at the end of the simulation. The greater amount of shearing underneath the foundation in the simulation induces larger foundation displacements than in the experiment. This suggests that shearing through the soil underneath the foundation should be minimized to reduce the adverse effects of the fault rupture on the structure.

The light foundation undergoes the most displacement due to ground surface deformation, and the simulated and experimental displacements for this case are compared in Fig. 6.7b. The simulated horizontal displacements are within 0.5 m (prototype scale) of the experimental displacements. The vertical and horizontal displacements coincide at larger base displacement. The larger discrepancy between the vertical displacements at $h = 0.98$ m results from *S1* and *S2* forming in different sequences in the simulation and experiment.

Fig. 6.7a also shows foundation rotations for the same FR-SFI cases in the 15-m deep, $\psi_{pk} = 0°$ particle assemblage with foundations placed at the same Y_0 locations, and thus with different

values of s than for the $\psi_{pk} \approx 6°$ particle assemblage. The foundation rotations in Fig. 6.7a are lower in the $\psi_{pk} = 0°$ particle assemblage than in the $\psi_{pk} \approx 6°$ particle assemblage. Most shearing developed in the $\psi_{pk} = 0°$ particle assemblage above the hanging wall in the wide foundation case (Fig. 6.8a). This can be seen clearly in the plot of particle rotations about the principal axis of rotation of each individual particle in Fig. 6.8b. As shown in Chapters 3 and 4, substantial particle rotations indicate large shear strains. Fig. 6.8b also indicates that additional deformation occurs underneath the foundation. The wide foundation is able to deflect the shear rupture more easily because the $\psi_{pk} = 0°$ particle assemblage is weaker than the $\psi_{pk} \approx 6°$ particle assemblage. This causes the simulated foundation rotation for the wide case of the $\psi_{pk} = 0°$ particle assemblage to be lower and thus quantitatively closer to that of the experiment than in the simulation with the $\psi_{pk} \approx 6°$ particle assemblage in Fig. 6.7a. The base and shifted cases for the $\psi_{pk} = 0°$ particle assemblage also show foundation rotations similar to the experimental results. However, the light foundation simulation for the $\psi_{pk} = 0°$ particle assemblage shows significantly lower foundation rotations than the experiment due to greater deflection of the shear zone towards the hanging wall side of the foundation. Therefore, the coincident surface deformations between the free-field reverse fault experiment and the free-field simulation with the $\psi_{pk} = 0°$ particle assemblage do not imply the foundation rotations will also be coincident in the FR-SFI simulations. The DEM simulations using the $\psi_{pk} \approx 6°$ particle assemblage and its mechanisms of shear rupture are judged to be more realistic than with the $\psi_{pk} = 0°$ particle assemblage, because the sand dilates in the experiments, which produces more distinct shear rupture than a DEM particle assemblage with zero dilatancy.

6.5.2 Normal FR-SFI

Normal fault rupture simulations are performed using 60 computing cores with the 25-m deep particle assemblage having $\psi_{pk} \approx 7°$. The simulations of normal fault rupture include the baseline (B = 10 m, q = 91 kPa, s = 2.3 m), the light foundation (B = 10 m, q = 37 kPa, s = 2.3 m), and the shifted foundation (B = 10 m, q = 91 kPa, s = 6.1 m). The foundations are centered at the same locations as they are in the experiments of Bransby et al. (2008a), where Y_0 = -7.8 m in the baseline and light foundation cases and Y_0 = -13.3 m in the shifted foundation case. The values of s are equivalent between simulation and experiment, because the free-field outcrop locations are equivalent between simulation and experiment as shown in Fig. 6.3c.

The experimental results for the baseline and light foundation cases shown in Fig. 6.9a-b show an initial rupture surface *S1* terminating partway up the soil height and a second rupture surface *S2* outcropping at the footwall edge of the foundation. One rupture surface develops in the simulations of these cases, but no other significant differences between the simulated and experimental results occur. The comparison of foundation rotations in Fig. 6.10a shows that the baseline foundation undergoes a smaller magnitude of rotation than the light foundation in the simulations and in the experiments. The simulation and experimental results show the rate of foundation rotation leveling off by h = -2.6 m in the baseline and light foundation cases. The simulation rotations for the light foundation case show an initially lower rate of rotation than the experimental rotations but later approach the experimental rotations by h = -2.4 m. In the baseline case, the simulation rotations deviate from the experimental rotations at larger h by up to 1° more rotation, which is minor compared to the ground surface gradient which exceeds 25° by h/H = -0.085. The simulated foundation displacements for the baseline case are similar to those of the experiment. The baseline case horizontal displacements shown in Fig. 6.10b for the simulation

and experiment are within 0.1 m (prototype scale) of each other. The vertical displacements are also within 0.1 m of each other up to h = -0.99 m before they deviate at larger h due to increasing difference in the amount of foundation rotation between baseline simulation and experiment.

The shifted foundation case shown in Fig. 6.9c shows a more complex sequence of rupture propagation than the baseline and light foundation cases. The initial rupture surface *S1* reverses direction and curves away from the hanging wall side of the foundation. A second rupture surface propagates linearly and emerges on the footwall side of the foundation. *S1* and *S2* in the simulation occupy locations consistent with *S1* and *S2* in the experiment. A third rupture surface *S3* forms a triangular shape with *S2* underneath the foundation in the simulation. Although not reported in Bransby et al. (2008a), *S3* may be present in the experiment as indicated by small amounts of deformation in its corresponding location. The foundation rotation in the shifted foundation case eventually exceeds 4° in the experiment and simulation.

6.6 Micromechanical Analysis of FR-SFI

The rigid foundations in the experiments of Bransby et al. (2008b) and in the DEM simulations alter the path of fault rupture propagation. Micromechanical analyses of DEM results through tracking the interactions and kinematics of individual particles provide insights into the mechanisms of FR-SFI which are not seen with the continuum-based or experimental methods. DEM captures directly particle interactions and the evolving void space between particles, which shows local changes in void space due to dilation and contraction. Plots of individual particle rotations about their individual axes of rotation in 3D space delineate the rupture surfaces as zones of substantial particle rotations. Plots of incremental particle rotations over increments of h show which rupture surfaces remain active at different times by showing which shear bands still have actively rotating particles. Analyses of inter-particle contact forces reveal how individual inter-particle interactions affect the macroscopic response of the particle assemblage to induced fault rupture.

6.6.1 Mechanisms of Rupture Surface Deflection in Reverse FR-SFI

Fig. 6.11 shows plots of total rotation for each individual particle in the 15-m deep $\psi_{pk} \approx$ 6° particle assemblage simulations of FR-SFI. Free-field fault rupture is shown in Fig. 6.11a with the ground surface outcrop location indicated and the center of the rupture zone delineated. This free-field rupture surface is also depicted in Fig. 6.11b-f as a reference. Fig. 6.11d shows an additional case with a heavy (200 kPa) foundation. As q increases from 0 to 200 kPa in Fig. 6.11a-d, the rupture surface systematically deflects away from its free-field path towards the hanging wall side of the foundation. The particle rotations associated with *S2* in the light foundation case with q = 37 kPa show that *S2* is similar to the free-field rupture surface but slightly offset towards the footwall. In the baseline case with q = 91 kPa, *S2* is inhibited, yet small magnitude particle rotations underneath the foundation indicate minor fault-induced deformation within the particle assemblage beneath the foundation. When q = 200 kPa, particle rotations are almost completely inhibited, and all shearing occurs along *S1*. The rupture surface induces less rotation, indicated by θ_f, to the foundation when it is deflected by the presence of the heavier foundation.

Fig. 6.12 shows the orientations of the normal components of the normalized strong contact forces in the *Y-Z* plane perpendicular to the along-strike direction. These are the contact forces that, in a log-normal distribution in which the normal components of the contact forces are

normalized by their depth below the ground surface, exceed 1 standard deviation above the median value prior to the onset of fault rupture in the free-field. In the initial state (Fig. 6.12a), the normalized strong contacts are predominantly oriented in the vertical direction. Contacts that support the stable particle fabric transition from the vertical to the horizontal direction as fault rupture progresses from h/H = 0.0 to h/H = 0.15, as indicated by the decrease in vertically oriented contacts and the increase in horizontally oriented contacts in Fig. 6.12b. This transition of the dominant contact orientation from vertical to horizontal reflects rotation of the major principal stress direction from vertical to horizontal as passive earth pressures develop during reverse fault rupture as described in the continuum-based numerical study of Oettle & Bray (2013a).

The inter-particle contacts reveal the micromechanical mechanism of the systematic deflection of the rupture surface with increasing q. Columns of particles connected through the initially vertically-oriented contacts (e.g., Iwashita & Oda 2000) act as a barrier to shear rupture propagation whose effectiveness in restricting shear rupture beneath the foundation enhances with increasing q. Heavier foundations increase the number of normalized strong contacts, as shown in Fig. 6.12a, as well as the magnitudes of the contact normal forces (N). The increase of N at a contact increases the resistance to sliding at the surfaces of contacting particles, because contact sliding occurs when the tangential force ($T \leq \mu N$) reaches its upper limit $T = \mu N$. If q is low, the particles in these columns can slide more easily due to lower N, and rupture can easily propagate through the particle columns. As q increases, greater numbers of strong contact forces gradually build up in the horizontal direction during reverse fault rupture (Fig. 6.12b) due to the increased inhibition of shear rupture propagation and fabric disturbance beneath the foundation, as indicated by the gradual reduction in the magnitudes of particle rotations beneath the foundation as q increases in Fig. 6.11a-d. The shear disturbance gradually decreases beneath the foundation and increases along a path of less shear resistance towards the hanging wall side of the foundation until, under high enough q, all shear activity occurs along this new, single path of rupture.

6.6.2 Softening of Rupture Surfaces in Reverse FR-SFI

The development of shear rupture observed in the DEM simulations through particle rotations can be ambiguous in some cases. In the light foundation and shifted foundation cases shown previously in Fig. 6.11b and 6.11e, it is not clear if *S2* has fully softened, because the particle rotations are greater in *S1* relative to *S2*. However, the distributions of void ratios shown in Fig. 6.13 show distinctive zones of high void ratios indicating soil dilation in the regions corresponding to *S1* and *S2* for the light, shifted, and wide foundation cases. The void ratios for the light foundation case in Fig. 6.13a show that *S1* develops first, because the soil dilates around *S1* by h/H = 0.12 while the region around *S2* still has a relatively low void ratio of about 0.7. By h/H = 0.225, *S1* has fully softened and reached a void ratio above 0.8 while *S2* only reaches a void ratio of about 0.75 near the ground surface. The fact that *S2* is not fully softened in Fig. 6.13d suggests that *S2* does not fully reach the ground surface in the light foundation case. In the shifted foundation case in which *S1* and *S2* developed at nearly the same time, the void ratios in Fig. 6.13b show the regions around both rupture surfaces increasing in void ratio. The void ratios around the *S1* location beneath the foundation underwent more softening at this point as indicated by slightly higher void ratios in this region. By h/H = 0.225 in Fig. 6.13e, *S1* has fully softened and reached void ratios above 0.8 while the void ratios along *S2* have not fully exceeded 0.8 near the ground surface.

The void ratio distributions for the wide foundation case in Fig. 6.13c show the increases in void ratio beginning from the bedrock fault location and veering towards the center of the foundation along the path of *S1* at h/H = 0.12. Some softening of *S2* is also observable at h/H = 0.12, indicating that *S1* and *S2* are both active at this stage. By h/H = 0.225 in Fig. 6.13f, both *S1* and *S2* have fully softened and reached void ratios of 0.8 or higher. These higher void ratios relative to the surrounding less-disturbed material show how fault rupture propagates through dilation of the soil along its propagation path through the $\psi_{pk} \approx 6°$ particle assemblage. In the wide foundation case of the $\psi_{pk} = 0°$ particle assemblage shown previously in Fig. 6.8c, void ratios also exceed 0.8 along the path of *S1*, but this is only slightly higher than the average void ratio of 0.79 prior to fault rupture in this particle assemblage. While the particle rotations in Fig. 6.8b indicate deformations beneath the foundation, this deformation is not due to shearing. The void ratios underneath the foundation are approximately 0.75, which is lower than the void ratios prior to fault rupture because the material contracts during fault rupture. Although the foundation response in terms of its rotations in the simulated wide foundation case for the $\psi_{pk} = 0°$ particle assemblage shown in Fig. 6.7a was quantitatively close to the experimental foundation rotations for the wide foundation, the contraction observed in Fig. 6.8c is inconsistent with the shear rupture mechanisms for dilatant granular soil.

6.6.3 Development of Shear Rupture in Normal Fault FR-SFI

The rupture surfaces *S1* that develop during normal faulting in the baseline and light foundation cases do not deviate significantly from the free-field rupture path, but a complex pattern of rupture surface formation develops in the shifted foundation case. Fig. 6.14 shows through total particle rotations, incremental particle rotations, and void ratio distributions how the rupture surfaces *S1*, *S2*, and *S3* develop in the shifted foundation case. At early stages of fault rupture such as h/H = -0.04 in Fig. 6.14a-c, shearing is concentrated primarily along *S1*, which follows a path close to the free-field rupture surface. The incremental particle rotations in Fig. 6.14b show that *S1* is significantly more active than *S2* and *S3* at this stage, and the void ratios in Fig. 6.14c show that softening is only occurring along *S1* but not at the ground surface. At late stages of fault rupture such as h/H = -0.12 in Fig. 6.14d-f, *S1*, *S2*, and *S3* are visible. However, only *S1* and *S2* are visible through particle rotations in Fig. 6.14d. *S3* is visible as a region with a void ratio of approximately 0.73 in Fig. 6.14e. The low voids ratio along *S3* compared to those along *S1* and *S2* shows that *S3* does not fully soften, and the incremental particle rotations in Fig. 6.14e indicate negligible shearing along *S3* at this stage.

Active shearing transfers from *S1* to *S2* as normal fault rupture proceeds from h/H = -0.04 to h/H = -0.12 in Fig. 6.14. The incremental particle rotations show a high level of shear activity in Fig. 6.14b only along *S1*, but Fig. 6.14e shows much more shear activity along *S2*. The incremental particle rotations along *S1* are of much lower magnitude at h/H = -0.12 than at h/H = -0.04. This shows that shearing along *S1* is ceasing, while shearing is increasing along *S2*. This migration of intense shearing from *S1* to *S2* produces a staircase structure of ground surface displacement, with a majority of displacement occurring over the hanging wall with some additional displacement at the ground surface in the region bounded by *S1* and *S2*. *S1* does not fully soften at the ground surface, because the void ratios at the tip of *S1* in Fig. 6.14f are not as high as in the lower lengths of *S1*. Thus, *S1* does not develop fully; whereas *S2* does fully develop.

6.7 Conclusion

DEM simulations incorporating 3D irregularly shaped sphere-clusters can capture key aspects of earthquake fault rupture propagation through granular material influenced by a mat foundation. Moreover, DEM can show mechanisms of FR-SFI through micromechanical descriptors. This study demonstrated the viability and attractiveness of employing DEM particle simulations to investigate the response of structural foundations and the soil particles underlying it to the localized deformation field imposed by a bedrock fault displacement. Future enhancements such as including smaller particles in greater quantity to allow finer details to emerge, allowing particle crushing, and increasing the complexity of particle shape are forthcoming as high-speed parallelized computing capabilities continue to increase. There are significant advantages to using a particulate media approach to simulate the development of earthquake shear rupture propagation through soil and its interaction with buildings.

The simulated foundation response to reverse faulting in terms of its rotation and displacement matched that of the centrifuge experiments in all cases explored in this study with a similar angle of dilation except the wide foundation case. In the wide foundation case, more shearing occurred beneath the foundation in the simulation than in the experiment, which induced greater rotation to the foundation. The DEM simulation showed clearly that shear rupture beneath the foundation should be inhibited to minimize foundation rotations resulting from ground surface deformations. The simulated and experimental foundation responses for the normal fault rupture case compared favorably in all cases as the differences in foundation rotation were minor relative to the deformed ground surface slope. The shear rupture surfaces that developed in FR-SFI simulations reflected accurately the shear rupture surfaces that developed in the experiments.

The micromechanical analyses of the DEM simulations provide insights regarding the mechanisms of shear rupture propagation through soil and its effects on a foundation through features only observable in DEM simulations, such as individual particle rotations, inter-particle contacts, and void ratio distributions. These analyses highlighted the drawbacks to using an angle of dilation of zero in numerical continuum studies, showed the micromechanical effect of passive earth pressure development in reverse fault rupture, and revealed regions of fabric disturbance in both normal and reverse fault rupture not easily visualized in experiments. Particle rotations delineated the shear ruptures that developed in the reverse fault simulations, but the change in localized void ratios portrayed the sequence of shear rupture development and indicated clearly which rupture surfaces fully softened and reached the ground surface. Increasing the foundation contact pressure systematically deflected the shear rupture surface away from its free-field propagation path and towards the hanging wall side of the rigid mat foundation. Heavier foundations tended to increase the number and magnitude of contact forces, and these higher contact forces produced greater frictional resistance, making sliding at these contacts more difficult, which essentially created a barrier to shear rupturing beneath the foundation. Analysis of total and incremental rotations and void ratios showed that in the shifted foundation normal fault case, shear rupture begins along one rupture surface close to the free-field rupture path but ceases along this initial rupture path and migrates towards a second rupture surface that emerges on the footwall side of the foundation.

The use of DEM to investigate this class of problems is relatively novel and additional work is warranted before it is used in engineering practice. Additional cases of earthquake fault rupture-soil-foundation interaction should be analyzed and the simulated results compared with those of experiments and field case histories. Enhancements to the DEM simulations of this study

should occur as computing power increases. However, the results of this study are promising and already provide important insights not possible with conventional continuum-based or experimental approaches.

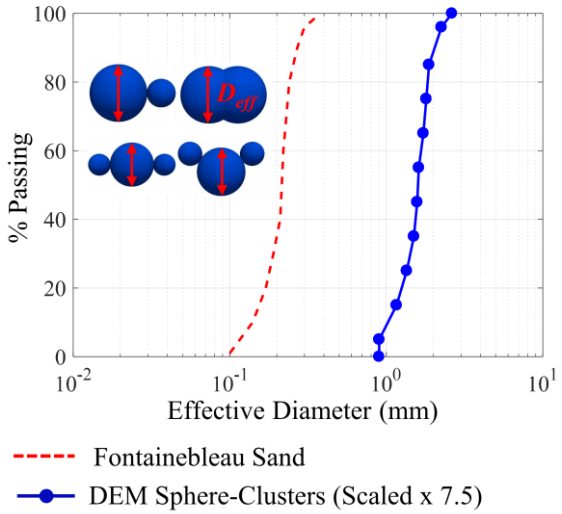

Fig. 6.1. Grain size distribution for sphere-cluster assemblage and for Fontainebleau sand (data from Delfosse-Ribay et al. 2004).

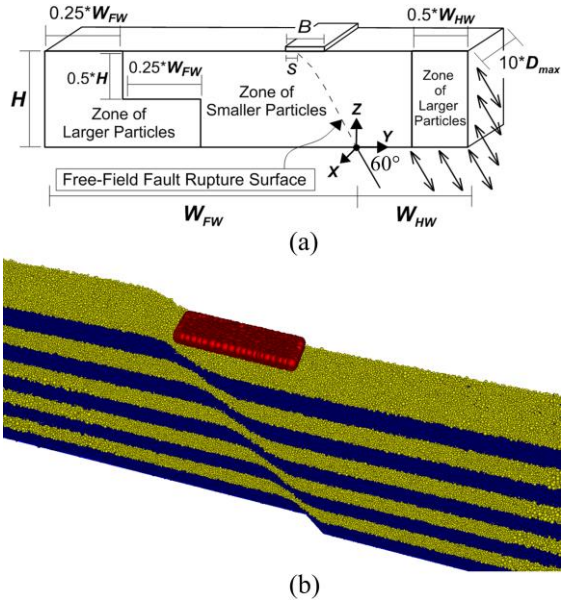

Fig. 6.2. (a) Schematic of earthquake fault rupture-soil-foundation interaction model; (b) foundation sphere-cluster shown in red atop three-dimensional particle assemblage after fault rupture.

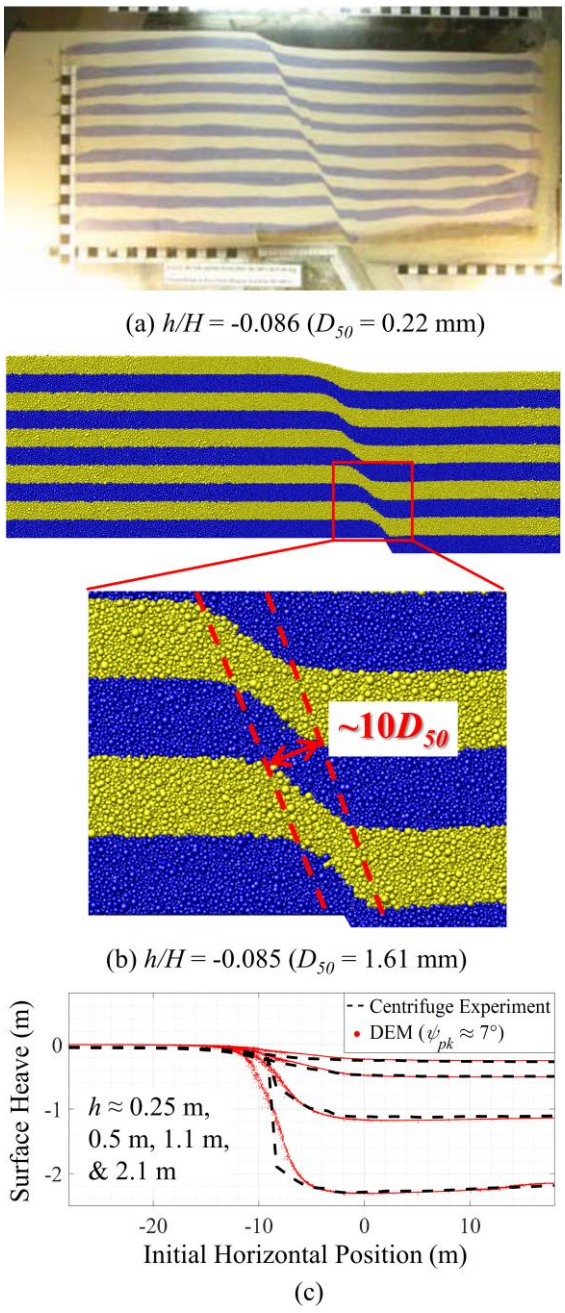

Fig. 6.3. (a) Test 12 centrifuge experiment of Bransby et al. (2008a); (b) DEM simulation of free-field normal fault rupture through 25-m particle assemblage; and (c) free-field surface heave profiles between DEM simulation and Test 12 of Bransby et al. (2008a).

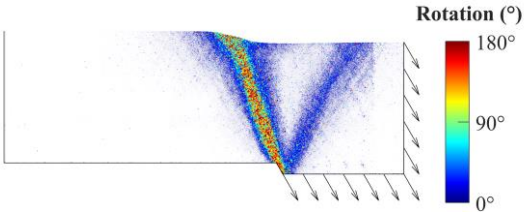

Fig. 6.4. Magnitudes of individual principal-axis particle rotations for the DEM simulation of free-field normal fault rupture through the 25-m particle assemblage (h/H = -0.085).

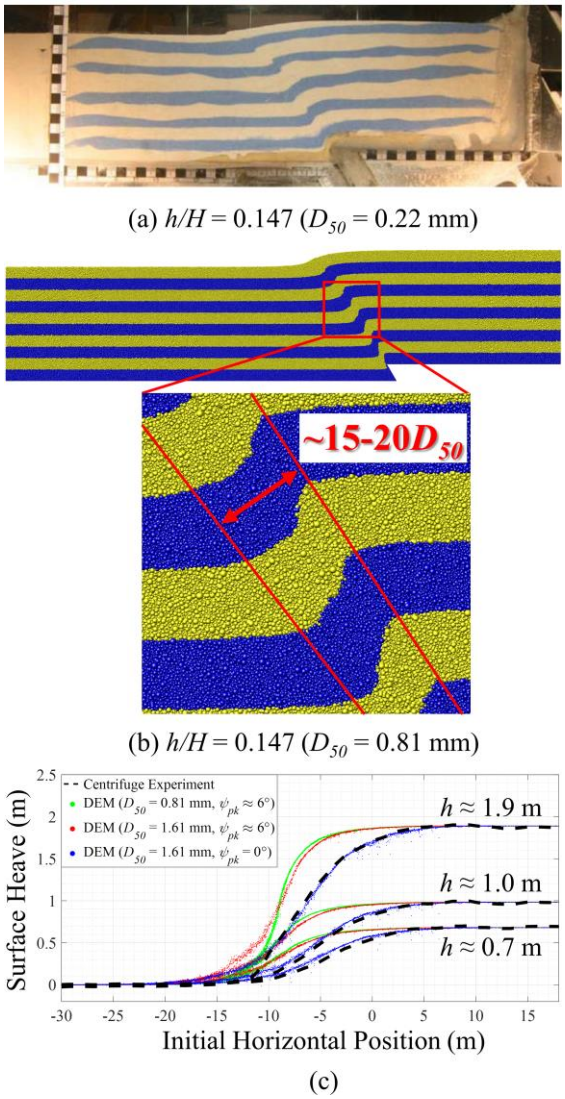

Fig. 6.5. (a) Test 28 of centrifuge experiments from Bransby et al. (2008b); (b) DEM simulation of free-field reverse fault rupture through the 15-m particle assemblage having $\psi_{pk} \approx 6°$ and D_{50} = 0.81 mm; (c) Free-field surface heave profiles between DEM simulations and Test 28 of Bransby et al. (2008b).

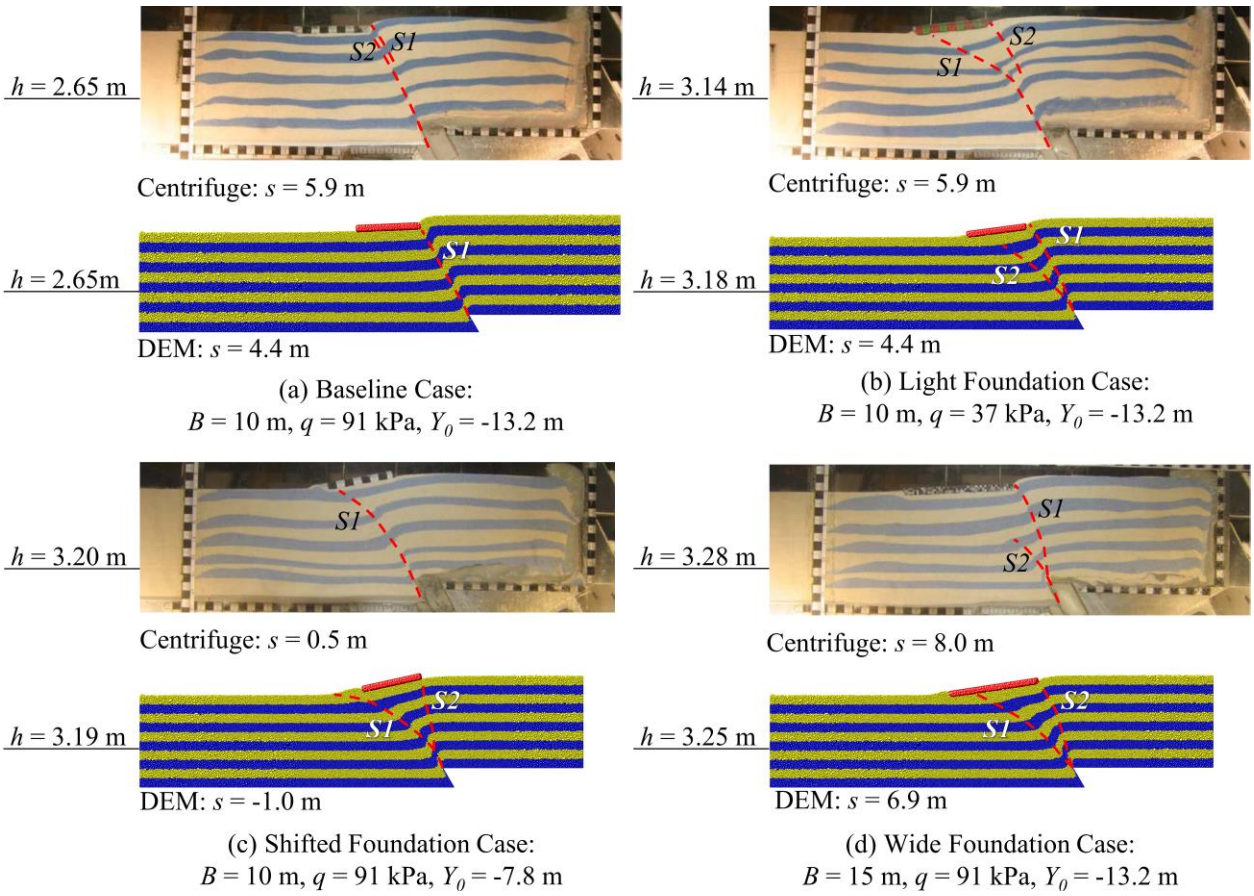

Fig. 6.6. Comparison of reverse fault rupture results of centrifuge experiments presented by Bransby et al. (2008b) and analogous DEM simulations with the 15-m particle assemblage having $\psi_{pk} \approx 6°$ for (a) the baseline case, (b) the light foundation case, (c) the shifted foundation case, and (d) the wide foundation case.

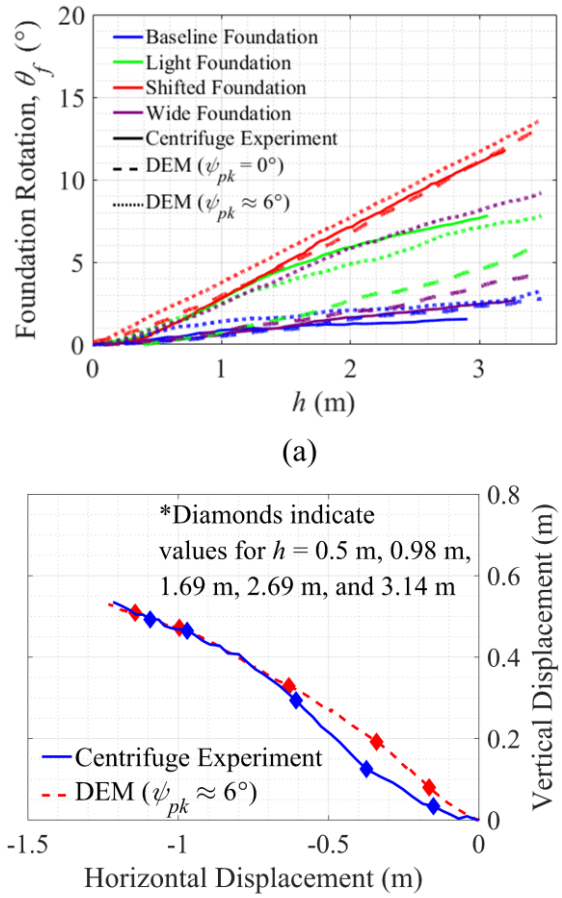

Fig. 6.7. (a) Comparison of foundation rotations between experimental results of Bransby et al. (2008b) and DEM simulation results. (b) Comparison of foundation displacement between the light foundation cases from Bransby et al. (2008b) and the DEM simulation with the 15-m particle assemblage having $\psi_{pk} \approx 6°$.

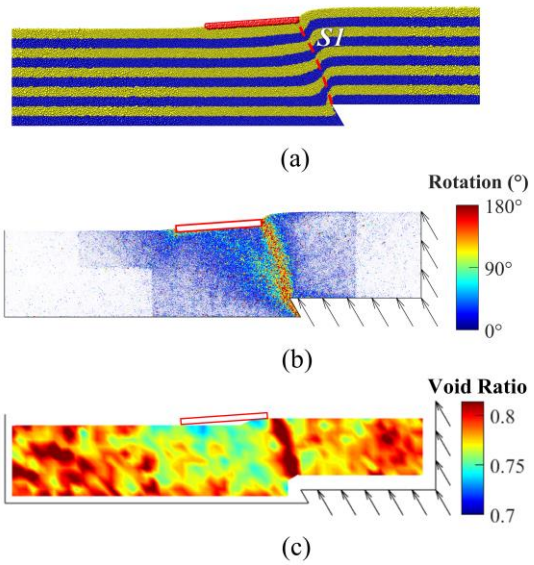

Fig. 6.8. Results for the wide foundation case reverse FR-SFI simulation with the 15-m particle assemblage having zero dilatancy shown through (a) the DEM particle assemblage, (b) individual principal-axis particle rotations, and (c) void ratio distributions.

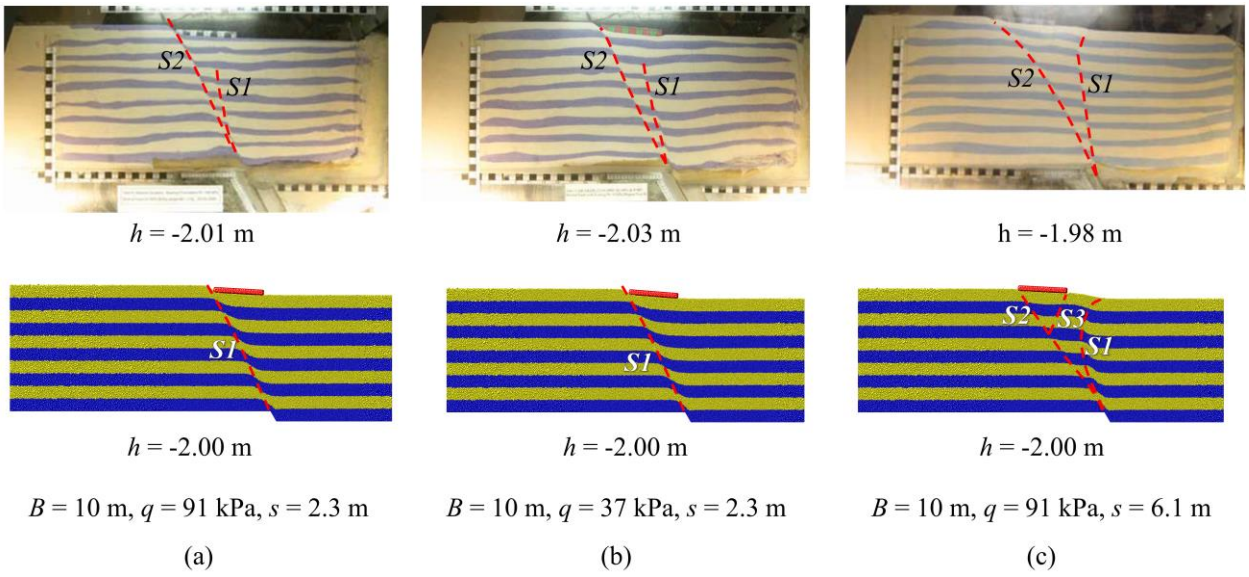

Fig. 6.9. Comparison of normal FR-SFI results from experiments presented by Bransby et al. (2008a) and analogous DEM simulations with the 25-m particle assemblage having $\psi_{pk} \approx 7°$ for (a) the baseline case, (b) the light foundation case, and (c) the shifted foundation case.

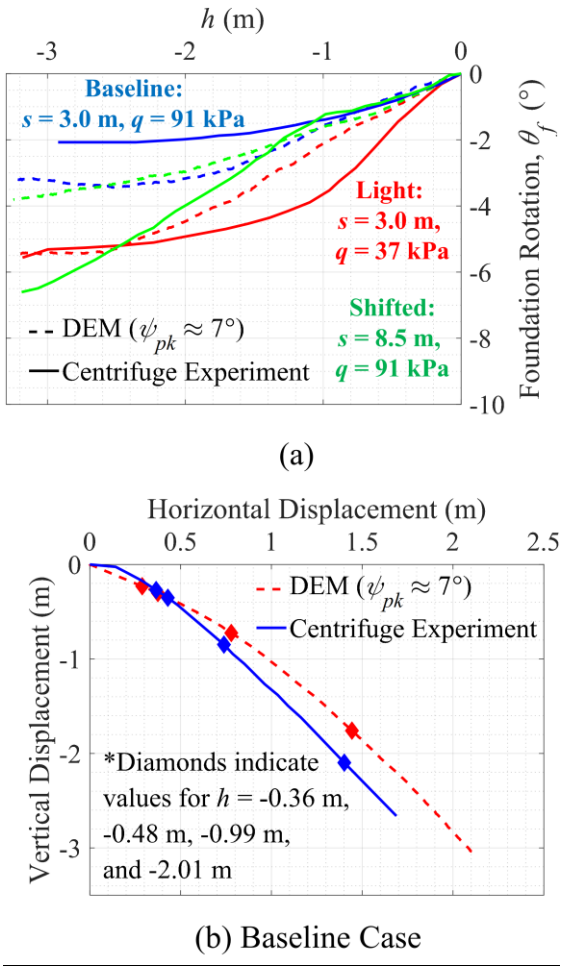

Fig. 6.10. (a) Comparison of foundation rotations between normal FR-SFI experimental results of Bransby et al. (2008a) and DEM simulation results with the 25-m particle assemblage having $\psi_{pk} \approx 7°$. (b) Comparison of foundation displacement between the baseline cases from Bransby et al. (2008b) and the DEM simulation for normal FR-SFI.

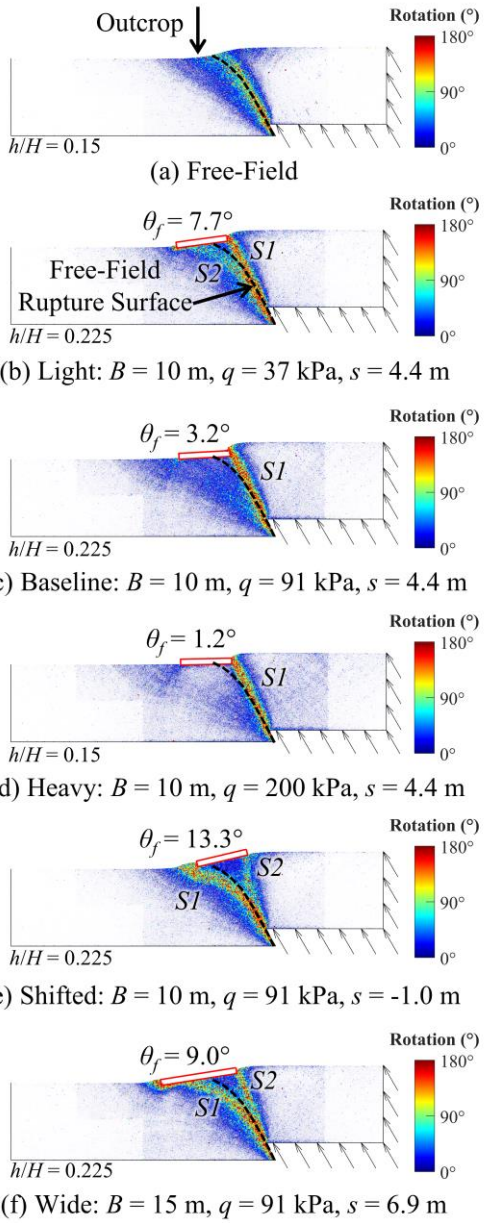

Fig. 6.11. Reverse fault rupture surfaces delineated by principle axis particle rotations for (a) free-field fault rupture, (b) the light foundation case, (c) the baseline case, (d) the heavy foundation case, (e) the shifted foundation case, and (f) the wide foundation case in the 15-m particle assemblage with $\psi_{pk} \approx 6°$.

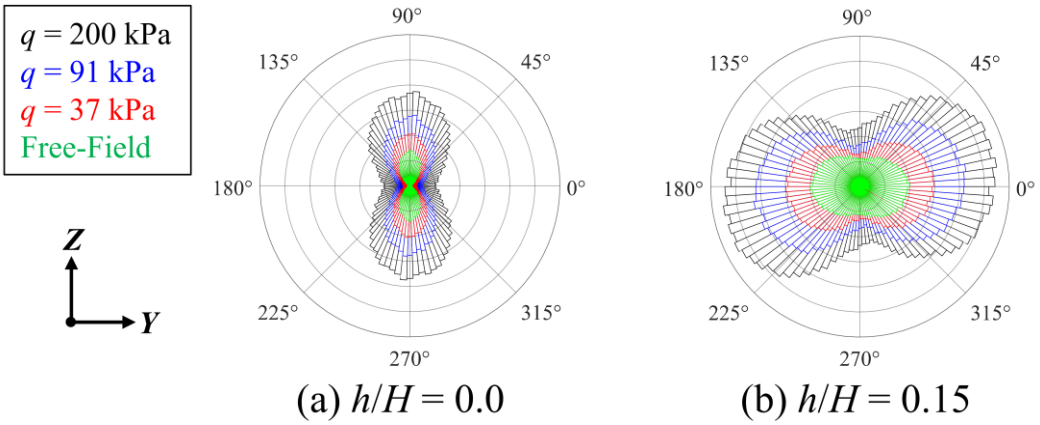

Fig. 6.12. Orientations of normalized strong contact forces (excluding those in boundary zones of larger particles) during reverse fault rupture with the 15-m particle assemblage having $\psi_{pk} \approx 6°$ for the free-field case and for q = 37 kPa, 91 kPa, and 200 kPa at: (a) h/H = 0.0 and (b) h/H = 0.15.

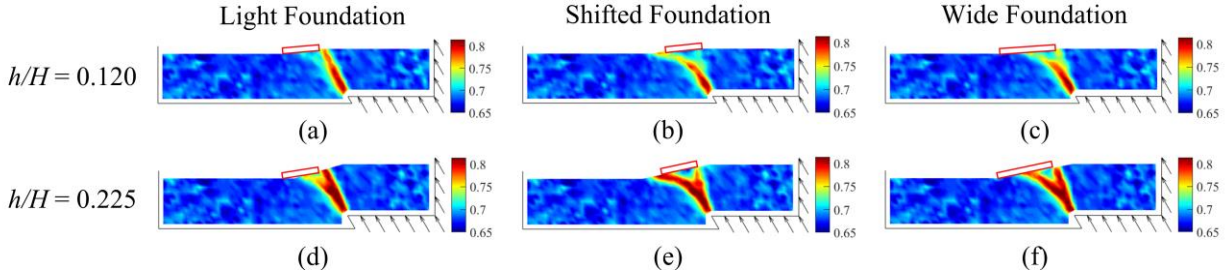

Fig. 6.13. Void ratio distributions at h/H = 0.120 and 0.225 for the (a,d) light foundation, (b,e) shifted foundation, and (c,f) wide foundation cases with the 15-m particle assemblage having $\psi_{pk} \approx 6°$.

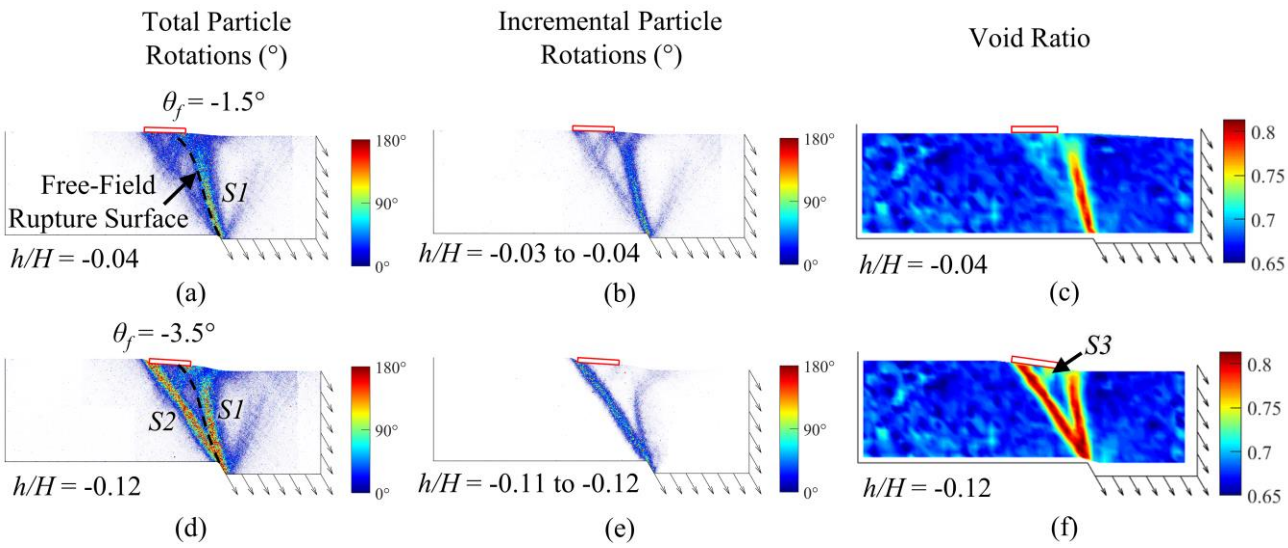

Fig. 6.14. Sequence of shear rupture development for the shifted foundation case during normal FR-SFI with the 25-m particle assemblage having $\psi_{pk} \approx 7°$ shown through (a,d) total particle rotations, (b,e) incremental particle rotations, and (c,f) void ratio distribution at h/H = -0.04 and h/H = -0.12.

CHAPTER 7: CONCLUSION

7.1 Summary

This research used the discrete element method to provide grain-scale insight into the shear rupture process during earthquake surface fault rupture and similar boundary-displacement problems. Earthquake surface fault rupture can potentially cause significant damage to the built environment in near-fault regions, as demonstrated from past earthquakes such as the 1999 Kocaeli and Düzce earthquakes in Turkey and the 1999 Chi-Chi earthquake in Taiwan. More recently, the 2016 Kaikoura, New Zealand, earthquake produced additional striking examples of surface fault-related damage to highways and homes. The significance of the surface fault rupture hazard warrants a complete understanding of its mechanisms through different avenues of research such as field reconnaissance missions, physical experimentation, and computational simulations, the latter of which primarily consist of continuum methods (e.g., FEM and FDM) and discrete methods (e.g., DEM). While both categories of numerical method provide significant quantitative insight into boundary-displacement problems, only discrete methods can capture directly the interactions of individual particles.

Simulations performed in this study initially used the commercial Particle Flow Code (PFC) of Itasca Consulting Group, Inc., on a desktop workstation with up to 8 computing cores in Chapters 3 and 4. Assemblages of non-spherical sphere-clusters consisting of 2 or 3 constituent spheres clumped together as a rigid body were prepared to capture the inherent resistance to rotation of real sand grains in 3D simulations of the direct shear test, anchor pull-out, trapdoor displacement, and surface fault rupture. The direct shear test simulations demonstrated the capability of DEM to capture changes in peak friction angle and angle of dilation due to changes in the void ratio, and hence the relative density, of the particle assemblage. The direct shear test results were consistent with the principles of critical state soil mechanics (Schofield & Wroth 1968) in that they showed higher peak friction angles and angles of dilation at higher relative densities, contractive responses in materials with low relative densities, zero rate of dilation at the critical state, and a consistent critical state friction angle across all relative densities and applied stresses.

The simulations of quasi-static surface fault rupture through dilatant granular media performed with PFC in Chapter 3 used over 175,000 sphere-clusters consisting of over 442,000 constituent spheres. The rupture surfaces in simulations of reverse and normal fault rupture with dip angles ranging from 30° to 90° were delineated through active frictional dissipation at the inter-particle contacts, particle rotations, shear strains, and volumetric strains. The rupture surfaces delineated through particle rotations, in particular, were consistent with those predicted via closed-form solution by Cole & Lade (1984), and the particles within the shear bands tended to rotate predominantly with the sense of shear of the shear band. However, the particles also had significant components of out-of-plane rotations as well.

The distributions of contact forces in Chapter 3 revealed arched patterns of strong inter-particle contact forces consistent with the soil-arching phenomenon in trapdoor experiments (e.g., Terzaghi 1943). The arched patterns of strong contact forces, or stress arching, in shallow normal fault rupture were consistent with the patterns observed in trapdoor simulations, whereas the stress arching in steep normal and reverse fault rupture was one-sided and most similar to the outward half-arches observed in anchor pull-out simulations. Shallow reverse fault rupture tended to show a dense distribution of strong contact forces extending from the hanging wall lateral boundary to

the rupture surface that was consistent with the regional horizontal compression described by Prucha et al. (1965). The distributions of contact forces revealed a mechanism of graben formation in 30°-dip normal fault rupture associated with the progressive collapse of a bridge of strong contact forces at the top of the arched distribution of strong contact forces.

The simulations of free-field surface fault rupture through materials of varying density in Chapter 4 showed how DEM captures directly the influence of void ratio on surface fault rupture through granular soils. Reverse and normal fault rupture simulations that were analogous to the free-field fault rupture experiments of Bransby et al. (2008a,b) showed satisfactory agreement with the experiments in their profiles of vertical surface displacements. The shear rupture surfaces and shear zones were revealed via frictional dissipation, particle rotations, volumetric strains, and displacement contours. Simulations of 60°-dip reverse fault rupture and 30°-dip normal fault rupture with denser materials having lower void ratios showed distinctive, localized rupture surfaces. As the void ratio increased, the rupture surfaces tended to spread over a wider region, and shear rupture occurred in a more ductile manner consistent with observations by Bray et al. (1994a) of local absorption of the bedrock fault displacement in looser soils. The total amount of ground surface displacement on the hanging wall did not change with relative density, because the particles above the hanging wall move relatively uniformly during quasi-static fault rupture. However, the ground surface gradient increased with decreasing void ratio. Since steeper ground surface gradients induced by surface fault rupture are associated with increased structural damage (Bray 2001, 2009), higher-density assemblages that deform in a more brittle manner could potentially be more hazardous to structures during surface fault rupture.

Micro-mechanical analyses of the influence of void ratio in surface fault rupture simulations in Chapter 4 revealed quantitative differences in the nature of the inter-particle contacts. In looser, more contractive assemblages, the coordination numbers tended to increase during reverse fault rupture and eventually reached an asymptotic value. In denser, more dilatant assemblages, the coordination numbers initially increased but then decreased before also reaching an asymptotic value. Since the stress distribution was equivalent in each particle assemblage, the higher void ratio assemblages had fewer total contacts than the lower void ratio assemblages, but the magnitudes of the individual contacts on average were higher in the assemblages with higher void ratios. The higher magnitude contact forces tended to dissipate more energy through frictional slip in looser assemblages than in denser assemblages, and the difference in the amount of frictional dissipation between dense and loose assemblages was more pronounced in shallow normal fault rupture in which two antithetic rupture surfaces developed. In both loose and dense assemblages, the initially vertically oriented contacts tended to reorient towards a diagonal direction during reverse fault rupture but remained predominantly vertical during normal fault rupture.

High-performance computing (HPC) was used to perform even more simulations using higher quantities of particles in a shorter amount of time. HPC facilitated a large parametric study of the direct shear test using the LIGGGHTS DEM code (Kloss et al. 2012) with up to 96 computing cores in Chapter 5. The minimum and maximum void ratios for assemblages with sphere-clusters and with spheres were determined, and direct shear test simulations were performed with a wide range of relative densities that capture the full spectrum of contractive to dilatant behaviors. The large dataset obtained using HPC allowed a linear trend to be fit to the data showing decreasing peak friction angle and angle of dilation with decreasing relative density. However, the effect of stress on the peak strength and dilatancy of the assemblages was not as significant as expected in direct shear tests on real sands. Significant stress dependency was instead

observed in the initial stiffness of the assemblages and in the coordination number at the critical state.

The comparisons of the macroscopic response measured at the boundaries of the simulated direct shear test and the homogenized response within the shear zone of the particle assemblage in Chapter 5 confirmed that the mobilized friction and dilation angles accurately describe the response of the sheared soil with small differences in the magnitudes of the measured friction and dilation angles. The extents of the shear bands in dense assemblages as measured in particle displacement profiles were consistent with the extents of the zones of high-magnitude particle rotations for both spheres and sphere-clusters, and the shear band thicknesses were higher in assemblages of spheres due to their inability to resist rolling. Loose particle assemblages tended to show no distinct shear band formation, as demonstrated through high-magnitude particle rotations all throughout the specimen height in simulations with low relative densities. Analysis of the velocities of the particles in direct shear revealed the fluid-like nature of granular materials in shear, such as the formation of velocity vortex structures within the shear band of densely packed sphere-clusters at the critical state.

The FR-SFI simulations in Chapter 6 ultimately showed that DEM can capture well-documented trends of surface fault rupture interaction with rigid building foundations. HPC facilitated the simulation of approximately 420,000 to 1.7 million sphere-clusters containing approximately 1 million to 4.3 million constituent spheres in reverse fault rupture and over 700,000 sphere-clusters containing over 1.7 million constituent spheres in normal fault rupture. This large number of particles showed great detail in the development of the rupture surfaces during free-field fault rupture and in the presence of the rigid foundations. Finer details such as the inclusion of more particles within the shear band developed when D_{50} = 0.81 mm as opposed to D_{50} = 1.61 mm in reverse fault rupture simulations, but the shape and outcrop location of the reverse fault rupture surfaces were not significantly affected by particle size when the different particle assemblages had equivalent relative densities and hence equivalent angles of dilation. The gradient of the ground surface was slightly higher in the free-field reverse fault simulation with D_{50} = 0.81 mm compared to that with D_{50} = 1.61 mm. The free-field simulations with assemblages having similar angles of dilation as the sand used by Bransby et al. (2008a,b) produced ground surface deformation profiles in close agreement with those of Bransby et al. (2008a) in normal fault rupture but offset by 3-4 m from those in Bransby et al. (2008b) during reverse fault rupture. The offset in reverse fault rupture comparisons is reasonable given the exclusion of particle crushing and fracturing in the DEM simulations. The profiles of surface deformation in a free-field reverse fault rupture simulation with a loose particle assemblage were in better agreement with those of Bransby et al. (2008b), but the contractive nature of the loose particle assemblage is considered inconsistent with the shear rupture mechanisms in materials with a non-zero angle of dilation. The formation of the rupture surfaces and the response of the foundation compared favorably overall with those from the FR-SFI centrifuge experiments of Bransby et al. (2008a,b) with some minor quantitative differences.

The insights into the mechanisms of FR-SFI gained with DEM complement similar findings from experiments and continuum modeling by showing quantitative particle responses and inter-particle interactions. Plots of particle rotation magnitudes from reverse FR-SFI simulations showed that heavier foundations systematically deflect the rupture surface towards the hanging wall side of the foundation, and analysis of the contact forces showed that, as the foundation contact pressure increases, frictional slip becomes more inhibited at the inter-particle contacts. This essentially creates a barrier of strong contacts that resists shear rupture beneath the

foundation, causing forces to continue building up in the horizontal direction and forcing the fault rupture surface to follow the path of lower resistance towards the hanging wall side of the foundation. Analysis of the changing void ratios during fault rupture propagation revealed which rupture surfaces softened first and which reached the ground surface. In normal FR-SFI with the foundation offset towards the footwall, analysis of the changing void ratios and incremental particle rotations revealed a mechanism of fault rupture activity migrating from one rupture path terminating below the hanging wall side of the foundation to a second rupture path outcropping on the footwall side of the foundation. Such analyses of contact forces, void ratio development, and particle rotations are unique to discrete numerical methods, because the granular nature of sand and the void space in between grains are both captured directly and in full quantitative detail. DEM has much potential for in-depth analyses of grain-scale phenomena that control the response of foundations interacting with surface fault rupture at the macroscopic level.

7.2 Principal Findings and Outcomes

The principal findings and outcomes of this research are summarized below:

- This study presents an effective procedure for preparing a 3D soil deposit of analog soil particles using DEM and simulating dip-slip surface fault rupture in the manner of the standard sandbox-style commonly used in physical surface fault rupture experiments.
- DEM simulations performed on a single-node computer with codes such as PFC (Itasca 2014) can provide valuable insight into the shear rupture process. However, the number of particles and thus the level of detail in a simulation are limited by the relatively low number of computing cores used. High-performance computing better facilitates the fast, efficient simulation of orders of magnitude more particles by distributing the computational loads across multiple nodes. Therefore, significantly greater levels of detail may be obtained with high-performance computing simulations.
- The out-of-plane, or along-strike, width of the numerical "sandbox" should be at least $10D_{50}$ to approximate an infinitely long strike and allow full particle movement about all six degrees of freedom.
- The quasi-static increase of gravitational acceleration ultimately produces an at-rest earth pressure coefficient (K_0) of 0.4-0.5, which is consistent with the earth pressure coefficient of normally consolidated or young soil deposits with minimal locked-in stresses.
- The use of larger boundary-particles where shear activity does not occur can significantly reduce the computational costs of a simulation in a manner akin to mesh refinement in the finite element and finite difference methods.
- The rupture surfaces in DEM simulations may be revealed through the particles themselves, particle displacements, particle rotations, frictional dissipation at the contacts, or strains. Particle rotations are judged to provide the most detail.
- The rupture surfaces that develop in normal and reverse fault rupture through dilatant DEM assemblages are consistent with the closed-form predictions of Cole & Lade (1984) for fault dip angles ranging from 30° to 90°. However, the DEM simulations for shallow normal fault rupture and the free-field normal fault experiment of Bransby et al. (2008a) showed less curvature of the primary rupture surface towards the hanging wall than predicted by Cole & Lade (1984). Instead, the primary rupture surface appears more linear in uniform, homogeneous soil deposits. The outcrop location associated with the curvature that Cole &

Lade (1984) predict is more consistent with the lower end of the fault scarp at the ground surface. The secondary rupture surface associated with graben formation emanates from the downward-displaced hanging wall at the distinct bedrock offset location rather than from the stationary footwall.

- The free-field rupture surfaces and distribution of contact forces that develop in 90°-dip normal and reverse fault rupture are mirror images of each other, which shows that, in quasi-static fault rupture, the kinematics of these two scenarios are equivalent.
- The soil-arching phenomenon is associated with an arched distribution of high-magnitude contact forces. The arched patterns of contact forces that develop during trapdoor displacement are also seen in shallow normal fault rupture simulations, which shows that the shear mechanisms in shallow normal fault rupture are similar to those in soil underlain by a subsiding trapdoor. Half-arched contact force patterns emanating in opposite directions develop during anchor pull-out, and similar half-arched patterns develop in steep normal and reverse fault rupture.
- The regional horizontal compression described by Prucha et al. (1965) is evident in shallow reverse fault rupture through strong contact forces emanating from the hanging wall to the fault rupture surface. These strong contact forces appear to "flatten" the rupture surface, making it more linear.
- The mechanism of graben formation in shallow normal fault rupture is associated with the collapse of the arch of strong contact forces when the soil within the developing graben is no longer frictionally supported by the soil bounding the graben. The graben then develops as the material within it moves uniformly downward during quasi-static fault rupture. The uniformity of downward displacement within the graben decreases as the relative density of the soil decreases.
- Although dip-slip fault rupture is a plane-strain phenomenon, particles still exhibit significant out-of-plane movement during it. Particles do tend to rotate in the in-plane sense of shear within the shear band more than in each of the other axes of rotation in a Cartesian coordinate system, even within the secondary, antithetic shear band associated with graben formation. However, although the sense of shear represents the most common direction of rotation, most particles still do rotate in other directions.
- Changing the inter-particle friction coefficient during particle deposition is a viable means of generating particle assemblages with different relative densities. High friction coefficients produce loose particle assemblages and low friction coefficients produce dense particle assemblages during deposition. To obtain a relatively uniform void ratio throughout the soil height, it is recommended that little to no damping be incorporated at the contacts during deposition.
- Dense particle assemblages with low void ratios exhibit brittle deformation characteristics and more distinctive rupture surfaces. The rupture surfaces become less distinctive and the shear zone becomes more widespread as the void ratio increases. Loose, high void ratio particle assemblages tend to absorb into its medium the distinct offset of the underlying bedrock fault as described by Bray et al. (1994a).
- The ground surface gradient increases with decreasing void ratio, suggesting potentially greater structural damage in more brittle granular soils.
- The ground surface displacements atop the hanging wall away from the fault outcrop location are equivalent to those of the bedrock displacements in quasi-static fault rupture, because the soil away from the rupture surface displaces relatively uniformly. When a graben fully or

partially develops in normal fault rupture, the ground surface subsides the most atop the graben in the region bounded by two rupture surfaces.

- Soil dilation is associated with greater numbers of particles decreasing than increasing in coordination number. Contraction is associated with more particles increasing in coordination number. In very dilatant materials, the particles that decrease in coordination number do so after initially increasing in coordination number for a short time period. This initial increase in coordination number reflects initial contraction prior to the onset of dilation.
- Denser soils with lower void space have a greater number of contacts and higher coordination numbers than looser soils. In dense and loose soils with equivalent stress distributions, the individual contact forces are higher on average within the looser soil, because the looser soil has fewer contacts to support the same stresses (i.e. the total force in the system is distributed across fewer contacts).
- Looser particle assemblages tend to dissipate more energy through friction during fault rupture than denser particle assemblages. The higher frictional resistance at the contacts in looser particle assemblages associated with their higher normal forces and the more widespread shear zones contributes to this higher frictional dissipation.
- Prior to fault rupture, the contact normals tend to orient vertically in the direction of gravity loading. This orientation does not significantly change during normal fault rupture, and the number of strong contacts actually tends to decrease during active unloading in normal fault rupture. Reverse fault rupture changes the major principal stress direction more to the horizontal, and the contact normals adjust to this change in the principal stress directions by orienting in line with the major principal stress.
- The direct shear test may appropriately be used as a calibration or characterization tool for materials to be used in surface fault rupture studies. Given that the lateral walls of the direct shear test are frictionless, the trends in the mobilization of strength and dilatancy as measured at the boundaries of the direct shear test accurately reflect their mobilization within the shear zone. The peak strengths and maximum angles of dilation occur at the same amount of shear displacement in boundary-measured values as those within the shear zone, and the critical states occur at the same amount of displacement.
- Given frictionless lateral walls, the peak strengths measured at the boundaries of the direct shear test are close to those that occur within the shear zone and only differ by 1°-2°. The angles of dilation can be as much as 4° lower when measured at the boundaries compared to the angle of dilation within the shear zone, because some dilation is absorbed through small amounts of contraction outside the shear zone.
- The peak friction angle and maximum angle of dilation decrease linearly with decreasing relative density until reaching the critical state friction angle and zero, respectively.
- A shear band begins to develop along the mid-plane at the peak state in the direct shear test and is fully visible by the end of strain softening. Further shearing to the critical state enhances features of the shear band, such as increasing the magnitudes of particle rotations within the shear band. No distinct shear band develops in very loose materials, and shear deformation is distributed across the entire specimen height.
- No standardized procedures are available for determining e_{min} and e_{max} for DEM particle assemblages. e_{max} may appropriately be determined through an air pluviation simulation. e_{min} may be determined via compression under zero inter-particle friction, but inter-particle overlaps must be monitored to ensure that changes in void ratio are resulting from particle rearrangement rather than increased overlaps.

- Sphere-clusters more appropriately capture the inherent resistance to rotation of real sand grains than spheres. Shear bands are thicker in assemblages of spheres than sphere-clusters. In both the direct shear test simulations and in surface fault rupture simulations, the thickness of the shear band is on the order of $10D_{50}$, and shear bands in assemblages of very fine particles may be slightly thicker.
- Sphere-clusters, due to their interlocking capabilities, exhibit higher peak strengths and angles of dilation than spheres at the same relative density, and the critical state strength is significantly higher in assemblages of sphere-clusters. The peak strengths and angles of dilation are also higher in assemblages of sphere-clusters than real sands at similar relative densities, so DEM assemblages of rigid sphere-clusters should be prepared to lower relative densities when using them as an analog for a specific sand with known strength and dilation characteristics.
- Non-crushable DEM particles exhibit negligible stress dependency in their critical state lines in *e-log(p)* space. However, they do exhibit notable stress dependency in their critical state coordination numbers and in their initial stiffness in shear. They exhibit other characteristics consistent with critical state soil mechanics such as a consistent critical state friction angle independent of stress state and relative density, and they exhibit simultaneous peaks in the mobilized strength and angle of dilation. Only explicit particle crushing is recommended to appropriately capture stress-dependency in the critical state void ratio.
- Granular materials in shear exhibit fluid-like characteristics as seen through their velocity flowpaths. These characteristics include uniform flowpaths analogous to laminar flow at low shear displacements and more chaotic flowpaths analogous to turbulent flow at the critical state. The antithetic rolling of contacting spheres produces a more random velocity field than in sphere-clusters. The instability associated with dilatant, strain-softening sphere-cluster assemblages produces scattered vortex patterns in the velocity field within the shear band at the critical state.
- Assemblages of sphere-clusters with effective diameters scaled upward in size by a factor as high as 7.5 can capture key aspects of FR-SFI observed in physical experiments and closely mimic the development of rupture surfaces observed in experiments. Greater refinement of the particle sizes produces more detail in the rupture surfaces.
- While loose assemblages of sphere-clusters may produce foundation responses more consistent with experimental observations in some cases, the contractive nature of loose assemblages is not consistent with more dilatant soils. Therefore, comparisons between DEM assemblages and real sands are most appropriate when the DEM analog assemblage has equivalent dilation characteristics.
- One or two rupture surfaces tend to develop during reverse FR-SFI. Although the rupture surfaces may begin to develop at different hanging wall displacements in reverse FR-SFI, they both tend to remain active at larger displacements.
- While a single rupture surface or two closely-spaced rupture surfaces outcrop on the footwall side of the foundation when it is positioned relatively close to the hanging wall side of the fault outcrop location, a more complex system of rupture surfaces develops when the foundation is positioned further on the footwall side. This latter complex system is associated with the migration of shear rupture activity from an initial path propagating towards the hanging wall side of the foundation to a second rupture path that outcrops on the footwall side of the foundation.

7.3 Suggestions for Future Research

Great strides have been made towards understanding the earthquake surface fault rupture hazard through both physical and numerical means, yet there is much more still to understand. The results of this work open up other potential research opportunities through discrete element modeling. Suggestions for future research via discrete element modeling and other methods to better understand the mechanics of earthquake surface fault rupture and its interactions with the built environment are provided below:

- Soil is rarely ever homogeneous at the scale of interest in Chapters 3, 4, and 6, especially not at the regional scale. Many of the studies of layered systems summarized in Chapter 2 show that strength contrasts can alter the deformation characteristics of surface fault rupture as it traverses through different layers. Moving forward, the effect of layering and other types of inhomogeneities due to changing particle shapes, gradations, void ratios, or strengths should be further explored with 3D DEM simulations.
- Many examples of the effects of strike-slip fault rupture on the built environment are documented through field reconnaissance studies from the 1906 San Francisco earthquake (Lawson 1908), the 1992 Landers earthquake (Lazarte et al. 1994), and the 1999 Kocaeli and Düzce earthquakes (Lettis et al. 2000). A full suite of DEM simulations should be carried out to study free-field strike-slip fault rupture and strike-slip FR-SFI simulations that, as in this study, explore the effect of soil ductility, foundation contact pressure, foundation size, and other relevant parameters.
- High-performance computing allows researchers to simulate greater numbers of particles in shorter amounts of time. The particle sizes in simulations should be further refined until the effective diameters of the analog DEM particles modeling a real sand are the same size as the real sand grains. Then, a full parametric analysis focusing on particle size and characteristic length, such as that of Stone & Wood (1992), may be fulfilled using DEM.
- The effects of relative density were explored through free-field surface fault rupture simulations with materials having different void ratios in Chapter 4 and with direct shear test simulations in Chapter 5. The effects of relative density on FR-SFI should now be explored more thoroughly.
- The direct shear test simulations incorporated most of the recommendations of Shibuya et al. (1997) including frictionless lateral walls, no rotation of the loading platen, and stationary lateral walls of the upper shear box. However, Shibuya et al. (1997) also recommend having a gap of 10-20D_{50} between the upper and lower shear boxes. Such a gap size is prohibitive even with particles of the size used in Chapter 5, but such a gap may be included with simulations having even finer particles in greater quantity. The shear response within the shear zone in direct shear tests that incorporate this gap between the shear boxes should be explored using DEM and compared with the results in Chapter 5 as well as with results from simple shear test simulations such as those performed by Bernhardt et al. (2016). Such a comparison would be useful for evaluating the influence of the test boundaries on the shear zone development at the center of each specimen.
- The shear response in terms of the angle of dilation and the Mohr definition of friction angle should be explored within the shear bands or shear zones in simulations of different laboratory tests including the direct shear, simple shear, biaxial, and triaxial (both true and conventional)

tests. The direct shear test and the true triaxial test are the most convenient computationally for DEM simulations, because implementation of the flexible membranes in the other tests is more complex. If the material characterization obtained through homogenization techniques within the shear zones of direct shear test simulations are equivalent to those in other laboratory test simulations, then researchers in DEM may rely on the direct shear test for the simplest means of material characterization or calibration.

- An efficient method of directly incorporating particle crushing in simulations containing hundreds of thousands or even millions of particles is necessary to have a fully stress-dependent material response. Due to the inability of spheres to interlock, this particle crushing should be incorporated with irregularly-shaped sphere-clusters. Particle crushing thus far has been incorporated in large simulations of spheres (e.g., Hanley et al. 2015) or with only hundreds of sphere-clusters each containing several spheres (e.g., Cheng et al. 2003). Such methods have not yet been evaluated for large-scale simulations of boundary-displacement problems with irregularly shaped sphere-clusters. With an efficient incorporation of particle crushing in a large-scale simulation, the effects of stress distribution, centrifuge scaling, and soil height may be explored more thoroughly with DEM.
- All of the particle assemblages in this study were analogous to dry granular soils. The effects of pore-water pressure were not considered. This effect is negligible during quasi-static surface fault rupture, but pore-water pressure could have an interesting effect on dynamic surface fault rupture, especially if liquefaction does not occur prior to surface fault rupture propagation in loose soils. Surface fault rupture is assumed to not occur through liquefied soil.
- This dissertation focused on cohesionless granular materials, but the shear behavior of natural soils is often significantly influenced by cohesion and cementation. The influences of cohesion and cementation on surface fault rupture have been modeled in-depth using 2D DEM with different types of inter-particle bonding as summarized in Chapter 2, but the influences of these factors warrant further analysis using 3D DEM as well. The effects of grain angularity should also be incorporated with non-spherical particles so that the combined influences of particle interlocking and cementation or cohesion may be fully analyzed.
- The effects of particle shape can be explored more thoroughly with more complex sphere-cluster shapes containing greater quantities of constituent spheres, such as in Ferellec & McDowell (2010). Alternatively, the open-source SparkRocks block mechanics code of Gardner et al. (2017) has potential for shear rupture studies using polyhedral particles, and Level-Set DEM (Kawamoto et al. 2017) is appealing for producing 3D avatars of real sand grain shapes. Furthermore, surface fault rupture experiments with grains having shapes that may be exactly replicated in DEM and with known contact properties would provide valuable data with which to evaluate the capability of DEM to exactly replicate a boundary-displacement experiment. Such one-to-one comparisons were instrumental towards the evaluation of the reproducibility of smaller-scale experiments with DEM in the dissertation of O'Sullivan (2002) and more recently in the direct simple shear test study of Bernhardt et al. (2016).
- The fault rupture simulations can be extended to fault rupture-soil-foundation-structure interaction (FR-SFSI) and fault rupture-soil-structure interaction (FR-SSI). FR-SFSI may be simulated by including a single degree-of-freedom structure atop the mat foundation as was done by El Shamy & Zamani (2012) or by incorporating a truss system atop a foundation. FR-SSI can be simulated by including a tunnel or pipeline within the subsurface.

- Bransby et al. (2008a,b) performed fault rupture experiments with a flexible foundation in addition to the experiments with rigid foundations. Furthermore, Anastasopoulos et al. (2009) analyzed the influence of foundation bending stiffness on the response of the foundation to surface fault rupture, although they found a relatively negligible influence of foundation bending stiffness. Flexible foundations may potentially be simulated in DEM with some combination of contact bonding and rolling resistance to analyze the influence of bending stiffness and foundation flexibility on FR-SFI.
- Fault diversion methods should be analyzed in more detail using DEM. Gazetas et al. (2008) and Oettle & Bray (2013b) analyzed several different methods of altering the path of fault rupture propagation and minimizing the induced structural damage. These and the design recommendations of Bray (2009) should be analyzed using DEM to potentially provide micro-mechanical insight that can further improve these methods and recommendations.
- This study demonstrates the capability of DEM to capture realistic trends of quasi-static fault rupture, but it does not include analyses of dynamic fault rupture as did Oettle et al. (2015). Dynamic DEM simulations should be performed to examine rate effects to ensure that the method can capture realistic trends as shown experimentally by Roth et al. (1981).
- New earthquakes will inevitably and often occur, and the effects of these earthquakes should always be documented where they may provide valuable data for our understanding of the earthquake surface fault rupture hazard. The reconnaissance activities of organizations such as GEER should remain vigilant in their search for understanding of the hazards that affect our livelihoods.

REFERENCES

Abe, S., Van Gent, H., & Urai, J. L. (2011). "DEM simulation of normal faults in cohesive materials." *Tectonophysics*, 512(1-4), 12-21.

Ahmadi, M., Moosavi, M., & Jafari, M. K. (2018a). "Experimental investigation of reverse fault rupture propagation through wet granular soil." *Eng. Geology*, 239, 229-240.

Ahmadi, M., Moosavi, M., & Jafari, M. K. (2018b). "Experimental investigation of reverse fault rupture propagation through cohesive granular soils." *Geomech. for Energy and the Environ.*, 14, 61-65.

Ahmed, W., & Bransby, M. F. (2009). "Interaction of shallow foundations with reverse faults." *J. Geotech. Geoenviron. Eng.*, 135(7), 914-924.

Anastasopoulos, I., & Gazetas, G. (2007a). "Foundation–structure systems over a rupturing normal fault: Part I. Observations after the Kocaeli 1999 earthquake." *Bull. of Earthq. Eng.*, 5(3), 253-275.

Anastasopoulos, I., & Gazetas, G. (2007b). "Foundation–structure systems over a rupturing normal fault: Part II. Analysis of the Kocaeli case histories." *Bull. of Earthq. Eng.*, 5(3), 277-301.

Anastasopoulos, I., Gazetas, G., Bransby, M. F., Davies, M. C. R., and El Nahas, A. (2007). "Fault rupture propagation through sand: Finite element analysis and validation through centrifuge experiments." *J. Geotech. Geoenviron. Eng.*, 133(8), 943-958, https://doi.org/10.1061/(ASCE)1090-0241(2007)133:8(943).

Anastasopoulos, I., Callerio, A., Bransby, M. F., Davies, M. C. R., El Nahas, A., Faccioli, E., Gazetas, G., Masella, A., Paolucci, R., & Rossignol, E. (2008a). "Numerical analyses of fault–foundation interaction." *Bull. of Earthq. Eng.*, 6(4), 645-675.

Anastasopoulos, I., Gerolymos, N., Gazetas, G., & Bransby, M. F. (2008b). "Simplified approach for design of raft foundations against fault rupture. Part I: free-field." *Earthq. Eng. and Eng. Vibration*, 7(2), 147-163.

Anastasopoulos, I., Gerolymos, N., Gazetas, G., & Bransby, M. F. (2008c). "Simplified approach for design of raft foundations against fault rupture. Part II: Soil-structure interaction." *Earthq. Eng. and Eng. Vibration*, 7(2), 165-179.

Anastasopoulos, I., Gazetas, G., Drosos, V., Georgarakos, T., & Kourkoulis, R. (2008d). "Design of bridges against large tectonic deformation." *Earthq. Eng. and Eng. Vibration*, 7(4), 345-368.

Anastasopoulos, I., Gazetas, G., Bransby, M. F., Davies, M. C., & El Nahas, A. (2009). "Normal fault rupture interaction with strip foundations." *J. of Geotech. and Geoenviron. Eng.*, 135(3), 359-370.

Anastasopoulos, I., Antonakos, G., & Gazetas, G. (2010). "Slab foundation subjected to thrust faulting in dry sand: Parametric analysis and simplified design method." *Soil Dyn. and Earthq. Eng.*, 30(10), 912-924.

Anastasopoulos, I., Kourkoulis, R., Gazetas, G., & Tsatsis, A. (2013). "Interaction of piled foundation with a rupturing normal fault." *Géotechnique*, 63(12), 1042-1059.

Anderson, R., Brechwald, D., Hull, A., Lindvall, S., Potter, S., Rockwell, T., Sayre, T., and Schwartz, D. [2016-2017 Advisory Panel] (2018). "Earthquake fault zones: A guide for government agencies, property owners/developers, and geoscience practitioners for assessing fault rupture hazards in California." *California Geological Survey Special Publication 42*, Revision 12.

Ashtiani, M., Ghalandarzadeh, A., & Towhata, I. (2016). "Centrifuge modeling of shallow embedded foundations subjected to reverse fault rupture." *Canadian Geotech. J.*, 53(3), 505-519.

ASTM, D. (2002). "3080, Standard test method for direct shear test of soils under consolidated drained conditions." *ASTM International, West Conshohocken, USA.*

Bardet, J. (1998). "Introduction to computational granular mechanics." In B. Cambou (Ed.), *Behaviour of granular materials*, Number 385 in CISM Courses and Lectures, Wien New York. Springer-Verlag.

Bernhardt, M., Biscontin, G., O'Sullivan, C., 2016. "Experimental Validation Study of 3D Direct Simple Shear DEM Simulations," *Soils and Foundations*, 56(3), 336-347.

Bolton, M. D. (1986). "The strength and dilatancy of sands." *Géotechnique*, 36(1), 65-78.

Botter, C., Cardozo, N., Hardy, S., Lecomte, I., & Escalona, A. (2014). "From mechanical modeling to seismic imaging of faults: A synthetic workflow to study the impact of faults on seismic." *Marine and Petroleum Geology*, 57, 187-207.

Bradley, B.A., Comerio, M., Cubrinovski, M., Dellow, S., Dizhur, D., Elwood, K., Giaretton, M., Green, R., Horspool, N., Hughes, M., Ingham, J., Johnson, L., Massey, C., Seville, E., Simkin, G., Stevenson, J., Wilson, R., and Wotherspoon, L. (2017). "M7.8 Kaikoura, New Zealand Earthquake on November 14, 2016." A QuakeCoRE, GEER, and EERI Earthquake Reconnaissance Report, a product of the EERI Learning From Earthquakes Program, March 2017.

Bransby, M. F., Nahas, E. L., Turner, E., & Davies, M. C. R. (2007). "The interaction of reverse faults with flexible continuous pipelines." *Int. J. of Physical Modelling in Geotechnics*, 7(3), 25-40.

Bransby, M. F., Davies, M. C. R., and El Nahas, A. (2008a). "Centrifuge modeling of normal fault-foundation interaction." *Bull. Earthq. Eng.*, 6(4), 585–605.

Bransby, M. F., Davies, M. C. R., El Nahas, A., and Nagaoka, S. (2008b). "Centrifuge modeling of reverse fault-foundation interaction." *Bull. Earthq. Eng.*, 6(4), 607–628.

Bray, J.D. (1990). "The effects of tectonic movements on stresses and deformations in earth embankments." Thesis. University of California, Berkeley.

Bray, J., Seed, R., & Seed, H. (1993). "1 g small-scale modelling of saturated cohesive soils." *Geotech. Testing J.*, 16(1), 46-53.

Bray, J. D., Seed, R. B., Cluff, L. S., & Seed, H. B. (1994a). "Earthquake fault rupture propagation through soil." *J. Geotech. Eng.*, 120(3), 543-561, https://doi.org/10.1061/(ASCE)0733-9410(1994)120:3(543).

Bray, J. D., Seed, R. B., & Seed, H. B. (1994b). "Analysis of Earthquake Fault Rupture Propagation through Cohesive Soil." *J. Geotech. Eng.*, 120(3), 562-580, https://doi.org/10.1061/(ASCE)0733-9410(1994)120:3(562).

Bray, J. D. (2001). "Developing Mitigation Measures for the Hazards Associated with Earthquake Surface Fault Rupture," in A Workshop on *Seismic Fault-Induced Failures – Possible Remedies for Damage to Urban Facilities*, Research Project 2000 Grant-in-Aid for Scientific Research (No. 12355020), Japan Society for the Promotion of Science, Workshop Leader, Kazuo Konagai, University of Tokyo, Japan, pp. 55-79, January 11-12, 2001 [Invited Paper].

Bray, J. D., & Kelson, K. I. (2006). "Observations of surface fault rupture from the 1906 earthquake in the context of current practice." *Earthq. Spectra*, 22(S2), 69-89.

Bray, J.D. (2009). "Designing buildings to accommodate earthquake surface fault rupture." *Improving the Seismic Performance of Existing and Other Structures*, ASCE, Reston, VA, 1269–1280.

Bray, J., Cohen-Waeber, J., Dawson, T., Kishida, T., and Sitar, N. [Eds.] (2014). "Geotechnical engineering reconnaissance of the August 24, 2014 M6 South Napa earthquake." a report of the NSF-Sponsored GEER Association Team, GEER-037, Ver. 3, 15 September, 2014, https://doi.org/10.13140/2.1.1094.7844.

Brennan, A., Roby, M., Bransby, F., and Nagaoka, S. (2007). "Fault rupture modification by blocky inclusions." In *Proc., 4th International Conference on Earthquake Geotechnical Engineering*. Thessaloniki, Greece. June 25-28, 2007.

Byrne, P.M., Park, S.S., Beaty, M., Sharp, M.K., Gonzalez, L., and Abdoun, T. (2004). "Numerical modeling of liquefaction and comparison with centrifuge tests" *Canadian Geotech. J.,* 41(2), 193–211.

Cardozo, N., Allmendinger, R. W., & Morgan, J. K. (2005). "Influence of mechanical stratigraphy and initial stress state on the formation of two fault propagation folds." *J. of Struct. Geology*, 27(11), 1954-1972.

Chang, Y. Y., Lee, C. J., Huang, W. C., Huang, W. J., Lin, M. L., Hung, W. Y., & Lin, Y. H. (2013). "Use of centrifuge experiments and discrete element analysis to model the reverse fault slip." *Int. J. of Civil Eng.*, 11(2), 79-89.

Cheng, Y. P., Nakata, Y., & Bolton, M. D. (2003). "Discrete element simulation of crushable soil." *Géotechnique*, 53(7), 633-641.

Chevalier, B., Combe, G., & Villard, P. (2012). "Experimental and discrete element modeling studies of the trapdoor problem: influence of the macro-mechanical frictional parameters." *Acta Geotechnica*, 7(1), 15-39.

Christoffersen, J., Mehrabadi, M. M., & Nemat-Nasser, S. (1981). "A micromechanical description of granular material behavior." *J. of App. Mech.*, 48(2), 339-344.

Chu, S. S., Lin, M. L., Huang, W. C., Nien, W. T., Liu, H. C., & Chan, P. C. (2015). "Simulation of growth normal fault sandbox tests using the 2D discrete element method." *Computers & Geosciences*, 74, 1-12.

Ciantia, M., Arroyo Alvarez de Toledo, M., Calvetti, F., & Gens Solé, A. (2015). "An approach to enhance efficiency of DEM modelling of soils with crushable grains." *Géotechnique*, 65(2), 91-110.

Clark, K.J., Nissen, E.K., Howarth, J.D., Hamling, I.J., Mountjoy, J.J., Ries, W.F., Jones, K., Goldstien, S., Cochran, U.A., Villamor, P., Hreinsdóttir, S., Litchfield, N.J., Mueller, C., Berryman, K.R., and Strong, D.T. (2017). "Highly variable coastal deformation in the 2016 Mw7. 8 Kaikōura earthquake reflects rupture complexity along a transpressional plate boundary." *Earth and Planetary Science Letters*, 474, 334-344.

Cohen-Waeber, J., Lanzafame, R., Bray, J., and Sitar, N. (2015). "The performance of structures subjected to surface fault rupture during the Mw 6.0 South Napa earthquake, California, USA." In *Proc. of the 6th International Conf. on Earthquake Engineering*. Christchurch, New Zealand. November 1-4, 2015.

Cole, D. A., Jr., and Lade, P. V. (1984). "Influence zones in alluvium over dip-slip faults." *J. Geotech. Eng*., 110(5), 599-615, https://doi.org/10.1061/(ASCE)0733-9410(1984)110:5(599).

Costa, Y. D., Zornberg, J. G., Bueno, B. S., & Costa, C. L. (2009). "Failure mechanisms in sand over a deep active trapdoor." *J. of Geotech. and Geoenviron. Eng.*, 135(11), 1741-1753.

Cubrinovski, M., and Bray, J.D., [Eds.] (2017). "Geotechnical Reconnaissance of the 2016 M_w7.8 Kaikoura, New Zealand Earthquake," a report of the NSF-Sponsored GEER Association Team, GEER-053, Ver 1., 14 June 2017, https://doi.org/10.18118/G6NK57.

Cui, L. (2002). "Developing a virtual test environment for granular materials using discrete element modelling." Thesis. University College Dublin.

Cui, L., & O'Sullivan, C. (2006). "Exploring the macro-and micro-scale response of an idealised granular material in the direct shear apparatus." *Géotechnique*, 56(7), 455-468.

Cundall, P. A., & Strack, O. D. (1979). "A discrete numerical model for granular assemblies." *Géotechnique*, 29(1), 47-65.

Cundall, P. (1987). Distinct element models of rock and soil structure. In E. Brown (Ed.), *Analytical and Computational Methods in Engineering Rock Mechanics*. Allen and Unwin.

Dean, S. L., Morgan, J. K., & Fournier, T. (2013). "Geometries of frontal fold and thrust belts: Insights from discrete element simulations." *J. of Struct. Geology*, 53, 43-53.

Delfosse-Ribay, E., Djeran-Maigre, I., Cabrillac, R., & Gouvenot, D. (2004). "Shear modulus and damping ratio of grouted sand." *Soil Dyn. Earthq. Eng.*, 24(6), 461-471.

Deluzarche, R., and Cambou, B. (2006). "Discrete numerical modelling of rockfill dams." *Int. J. Numer. Anal. Methods Geomech*., 30(11), 1075–1096.

Deng, C., Gawthorpe, R. L., Finch, E., & Fossen, H. (2017). "Influence of a pre-existing basement weakness on normal fault growth during oblique extension: Insights from discrete element modeling." *J. of Struct. Geology*, 105, 44-61.

Duncan, J.M., Byrne, P., Wong, K.S., and Mabry, P. (1980). "Strength, stress-strain and bulk modulus parameters for finite element analyses of stresses and movements in soil masses." *Report No. UCB/GT/80-01,* University of California, Berkeley, California.

Egholm, D. L. (2007). "A new strategy for discrete element numerical models: 1. Theory." *J. of Geophysical Research: Solid Earth*, 112(B5).

Egholm, D. L., Sandiford, M., Clausen, O. R., & Nielsen, S. B. (2007). "A new strategy for discrete element numerical models: 2. Sandbox applications." *J. of Geophysical Research: Solid Earth*, 112(B5).

Egholm, D. L., Clausen, O. R., Sandiford, M., Kristensen, M. B., & Korstgård, J. A. (2008). "The mechanics of clay smearing along faults." *Geology*, 36(10), 787-790.

El Shamy, U., & Zamani, N. (2012). "Discrete element method simulations of the seismic response of shallow foundations including soil-foundation-structure interaction." *Int. J. for Num. Anal. Meth. in Geomech.*, 36(10), 1303-1329.

Faccioli, E., Anastasopoulos, I., Gazetas, G., Callerio, A., & Paolucci, R. (2008). "Fault rupture–foundation interaction: selected case histories." *Bull. of Earthq. Eng.*, 6(4), 557-583.

Fadaee, M., Anastasopoulos, I., Gazetas, G., Jafari, M. K., & Kamalian, M. (2013). "Soil bentonite wall protects foundation from thrust faulting: analyses and experiment." *Earthq. Eng. and Eng. Vibration*, 12(3), 473-486.

Fadaee, M., Ezzatyazdi, P., Anastasopoulos, I., & Gazetas, G. (2016). "Mitigation of reverse faulting deformation using a soil bentonite wall: Dimensional analysis, parametric study, design implications." *Soil Dyn. and Earthq. Eng.*, 89, 248-261.

Ferellec, J. F., & McDowell, G. R. (2010). "A method to model realistic particle shape and inertia in DEM." *Granular Matter*, 12(5), 459-467.

Finch, E., Hardy, S., & Gawthorpe, R. (2003). "Discrete element modelling of contractional fault-propagation folding above rigid basement fault blocks." *J. Struct. Geology*, 25(4), 515-528.

Finch, E., Hardy, S., & Gawthorpe, R. (2004). "Discrete-element modelling of extensional fault-propagation folding above rigid basement fault blocks." *Basin Research*, 16(4), 467-488.

Finch, E., & Gawthorpe, R. (2017). "Growth and interaction of normal faults and fault network evolution in rifts: insights from three-dimensional discrete element modelling." *Geological Soc., London, Special Publications*, 439, SP439-23.

Fournier, T., & Morgan, J. (2012). "Insights to slip behavior on rough faults using discrete element modeling." *Geophysical Research Letters*, 39(12).

Friedman, D. A., Vignos, R., Walters, M. T., Petteys, C., & Bomba, G. (2012). "The seismic retrofit of UC Berkeley's California Memorial Stadium." *The Struct. Design of Tall and Special Buildings*, 21, 66-80.

Garcia, F.E., & Bray, J.D. (2018a). "Distinct element simulations of shear rupture in dilatant granular media." *Int. J. of Geomech.*, 18(9), 04018111, https://doi.org/10.1061/(ASCE)GM.1943-5622.0001238.

Garcia, F.E., & Bray, J.D. (2018b). "Distinct element simulations of earthquake fault rupture through materials of varying density." *Soils and Foundations*, 58(4), 986-1000, https://doi.org/10.1016/j.sandf.2018.05.009.

Garcia, F.E., & Bray, J.D. (2018c). "High-performance discrete element modeling of free-field surface fault rupture." In *Proc., IS-Atlanta, September 10-12, 2018*, Georgia Institute of Technology, Atlanta, GA.

Garcia, F.E., & Bray, J.D. (2019). "Modeling the shear response of granular materials with discrete element assemblages of sphere-clusters." *Computers and Geotechnics*, 106, 99-107, https://doi.org/10.1016/j.compgeo.2018.10.003.

Gardner, M., Kolb, J., & Sitar, N. (2017). "Parallel and scalable block system generation." *Computers and Geotechnics*, 89, 168-178.

Gaudin, C. (2002). “Experimental and theoretical study of the behaviour of supporting walls: validation of design methods.” Thesis, Laboratoire Central des Ponts et Chaussées, Nantes, France.

Gaudin, C., Schnaid, F., & Garnier, J. (2005). “Sand characterization by combined centrifuge and laboratory tests.” *Int. J. of Physical Modelling in Geotechnics*, 5(1), 42-56.

Gazetas, G., Anastasopoulos, I., & Apostolou, M. (2007). “Shallow and deep foundations under fault rupture or strong seismic shaking.” In K. D. Pitilakis (Ed.), *Earthquake Geotechnical Engineering* (pp. 185-215). Springer, Dordrecht.

Gazetas G., Pecker A., Faccioli E., Paolucci R., and Anastasopoulos I. (2008). “Design recommendations for fault–foundation interaction.” *Bull. of Earthq. Eng.*, 6(4), 677–687.

Gori, S., Falcucci, E., Kayen, R.E., Zimmaro, P., Lingwall, B., Galadini, F., and Stewart, J.P. (2018). “Surface fault rupture from 2016 Central Italy earthquake sequence.” In *Proc. Of the Eleventh U.S. National Conference on Earthquake Engineeirng*. Los Angeles, California, USA. June 25-29, 2018.

Guo, Y., & Morgan, J. K. (2004). “Influence of normal stress and grain shape on granular friction: Results of discrete element simulations.” *J. of Geophysical Research: Solid Earth*, 109(B12).

Guo, Y., & Morgan, J. K. (2007). “Fault gouge evolution and its dependence on normal stress and rock strength—Results of discrete element simulations: Gouge zone properties.” *J. of Geophysical Research: Solid Earth*, 112(B10).

Guo, N., & Zhao, J. (2014). “A coupled FEM/DEM approach for hierarchical multiscale modelling of granular media.” *Int. J. for Num. Methods in Eng.*, 99(11), 789-818.

Guo, N., & Zhao, J. (2016). “3D multiscale modeling of strain localization in granular media.” *Computers and Geotechnics*, 80, 360-372.

Guo, N., & Zhao, J. (2016). “Multiscale insights into classical geomechanics problems.” *Int. J. for Numer. Anal. Meth. in Geomech.*, 40(3), 367-390.

Hanley, K. J., O'Sullivan, C., & Huang, X. (2015). “Particle-scale mechanics of sand crushing in compression and shearing using DEM.” *Soils and Foundations*, 55(5), 1100-1112.

Hardy, S., & Finch, E. (2005). “Discrete-element modelling of detachment folding.” *Basin Research*, 17(4), 507-520.

Hardy, S., & Finch, E. (2006). “Discrete element modelling of the influence of cover strength on basement-involved fault-propagation folding.” *Tectonophysics*, 415(1-4), 225-238.

Hardy, S., & Finch, E. (2007). Mechanical stratigraphy and the transition from trishear to kink-band fault-propagation fold forms above blind basement thrust faults: a discrete-element study.” *Marine and Petroleum Geology*, 24(2), 75-90.

Hardy, S. (2008). “Structural evolution of calderas: Insights from two-dimensional discrete element simulations.” *Geology*, 36(12), 927-930.

Hardy, S., McClay, K., & Munoz, J. A. (2009). “Deformation and fault activity in space and time in high-resolution numerical models of doubly vergent thrust wedges.” *Marine and Petroleum Geology*, 26(2), 232-248.

Hardy, S. (2011). “Cover deformation above steep, basement normal faults: Insights from 2D discrete element modeling.” *Marine and Petroleum Geology*, 28(5), 966-972.

Hardy, S. (2013). “Propagation of blind normal faults to the surface in basaltic sequences: Insights from 2D discrete element modelling.” *Marine and Petroleum Geology*, 48, 149-159.

Härtl, J., & Ooi, J. Y. (2011). “Numerical investigation of particle shape and particle friction on limiting bulk friction in direct shear tests and comparison with experiments.” *Powder Technology*, 212(1), 231-239.

Hashash, Y.M., Tiwari, B., Moss, R.E., Asimaki, D., Clahan, K., Kieffer, D.S., Dreger, D.S., Macdonald, A., Madugo, C.M., Mason, H.B., Pehlivan, M., Rayamajhi, D., Acharya, I., Adhikari, B. (2015). “Geotechnical field reconnaissance: Gorkha (Nepal) earthquake of April 25, 2015 and related shaking sequence.” A report of the NSF-Sponsored GEER Association Team, GEER-040, Ver 1.1, 7 August, 2015, https://doi.org/10.18118/G61591.

Hauksson, E., Jones, L. M., & Hutton, K. (1995). “The 1994 Northridge earthquake sequence in California: Seismological and tectonic aspects.” *J. of Geophysical Research: Solid Earth*, 100(B7), 12335-12355.

Hazeghian, M., & Soroush, A. (2015). “DEM simulation of reverse faulting through sands with the aid of GPU computing.” *Computers and Geotechnics*, 66, 253-263.

Hazeghian, M., & Soroush, A. (2016). “DEM-aided study of shear band formation in dip-slip faulting through granular soils.” *Computers and Geotechnics*, 71, 221-236.

Hazeghian, M., & Soroush, A. (2017). “Numerical modeling of dip-slip faulting through granular soils using DEM.” *Soil Dyn. and Earthq. Eng.*, 97, 155-171.

Hazeghian, M., & Soroush, A. (2018). “DEM simulations to study the effects of the ground surface geometry on dip-slip faulting through granular soils.” *European J. of Environ. and Civil Eng.*, 1-19, https://doi.org/10.1080/19648189.2018.1428225.

Hazzard, J. F., & Mair, K. (2003). “The importance of the third dimension in granular shear.” *Geophysical Research Letters*, 30(13).

Holtz, R.D., & Kovacs, W. D. (1981). Shear Strengths of Sands and Clays. In *An Introduction to Geotechnical Engineering* (pp. 490-664). Prentice-Hall, New Jersey.

Huang, X., O'sullivan, C., Hanley, K. J., & Kwok, C. Y. (2014a). “Discrete-element method analysis of the state parameter.” *Géotechnique*, 64(12), 954-965. http://dx.doi.org/10.1680/geot.14.P.013.

Huang, X., Hanley, K. J., O'Sullivan, C., & Kwok, C. Y. (2014b). “Exploring the influence of interparticle friction on critical state behaviour using DEM.” *Int. J. for Num. Anal. Meth. in Geomech.*, 38(12), 1276-1297.

Iglesia, G. R., Einstein, H. H., & Whitman, R. V. (2013). “Investigation of soil arching with centrifuge tests.” *J. of Geotech. and Geoenviron. Eng.*, 140(2), 04013005.

Imre, B., Räbsamen, S., & Springman, S. M. (2008). “A coefficient of restitution of rock materials.” *Computers & Geosciences*, 34(4), 339-350.

Itasca Consulting Group, Inc. (2014). PFC — Particle Flow Code, Ver. 5.0. Minneapolis: Itasca.

Itasca Consulting Group, Inc. (2016) FLAC — Fast Lagrangian Analysis of Continua, Ver. 8.0. Minneapolis: Itasca.

Iwashita, K., and Oda, M. (1998). “Rolling resistance at contacts in simulation of shear band development by DEM.” *J. Eng. Mech.*, 124(3), 285-292, https://doi.org/10.1061/(ASCE)0733-9399(1998)124:3(285).

Iwashita, K., & Oda, M. (2000). "Micro-deformation mechanism of shear banding process based on modified distinct element method." *Powder Technology,* 109(1), 192-205.

Jewell, R. A. (1989). "Direct shear tests on sand." *Géotechnique,* 39(2), 309-322.

Jiang, M., Z. Shen, and J. Wang (2015). "A novel three-dimensional contact model for granulates incorporating rolling and twisting resistances", *Computers and Geotechnics,* 65, 147-163.

Johansson, J., & Konagai, K. (2006). "Fault induced permanent ground deformations—an experimental comparison of wet and dry soil and implications for buried structures." *Soil Dyn. and Earthq. Eng.*, 26(1), 45-53.

Kawamoto, R., Andò, E., Viggiani, G., & Andrade, J. E. (2016). "Level set discrete element method for three-dimensional computations with triaxial case study." *J. of the Mech. and Physics of Solids,* 91, 1-13.

Kayen, R., Dashti, S., Kokusho, T., Hazarika, H., Franke, K., Oettle, N., Wham, B., Ramirez Calderon, J., Briggs, D., Guillies, S., Cheng, K., Tanoue, Y., Takematsu, K., Matsumoto, D., Morinaga, T., Furuichi, H., Kitano, Y., Tajiri, M, Chaudhary, B., Nishimura, K., and Chu, C. (2016). "Geotechnical Aspects of the 2016 M_w 6.2, M_w 6.0, and M_w 7.0 Kumamoto Earthquakes," a report of the NSF-Sponsored GEER Association Team, GEER-048, Ver. 1, 13 July 2016, https://doi.org/10.18118/ G6JS3M.

Kelson, K.I., Bray, J., Cluff, L., Harder, L., Kieffer, S., Lettis, W., Page, W., Perkins, W., Rix, G., Roblee, C., Sitar, N., Wells, D., Wright, R., Yashinsky, M. (2001). "Fault-related surface deformation." *Earthq. Spectra*, 17(S1), 19-36.

Kloss, C., Goniva, C., Hager, A., Amberger, S., and Pirker, S. (2012). "Models, algorithms and validation for opensource DEM and CFD-DEM." *Progress in Comp. Fluid Dyn., An Inter. J.*, 12(2/3), 140 – 152.

Krumbein, W.C. and Sloss, L.L. (1963). Properties of Sedimentary Rocks. In *Stratigraphy and Sedimentation, Second Edition* (pp. 93-149). W.H. Freeman and Company, San Francisco.

Kulhawy, F. H., & Mayne, P. W. (1990). Manual on estimating soil properties for foundation design (No. EPRI-EL-6800). Electric Power Research Inst., Palo Alto, CA (USA); Cornell Univ., Ithaca, NY (USA). Geotechnical Engineering Group.

Kutter, B. L. (1995). "Recent advances in centrifuge modeling of seismic shaking." *Proc., 3rd International Conference on Recent Advances in Geotechnical Earthquake Engineering & Soil dynamics, April 2-7, 1995,* Volume II, St. Louis, Missouri.

Lade, P. V., Cole Jr, D. A., & Cummings, D. (1984). "Multiple failure surfaces over dip-slip faults." *J. of Geotech. Eng.*, 110(5), 616-627, https://doi.org/10.1061/(ASCE)0733-9410(1984)110:5(616).

Lawson, A. C. (Chairman). (1908). "The California earthquake of April 18, 1906: Report of the California State Earthquake Investigation Commission." Pub. No. 87, Carnegie Institution of Washington, Washington D.C., two volumes and atlas, 451 pp.

Lazarte, C. A, J. D. Bray, A. M. Johnson & Lemmer, R. E. (1994). "Surface Breakage of the 1992 Landers Earthquake and Its Effects on Structures." *Bull. Seismological Soc. of America,* 84(3), 547-561.

Lazarte, C., & Bray, J. (1996). "A study of strike-slip faulting using small-scale models." *Geotech. Testing J.*, 19(2), 118-129.

Lazarte, C. A. (1996). “The response of earth structures to surface fault rupture.” Thesis. University of California, Berkeley.

Lee, K. L., & Seed, H. B. (1967). “Drained strength characteristics of sands.” *Journal of Soil Mechanics & Foundations Div.*, 93(6), 117-141.

Lettis, W., Bachhuber, J., Witter, R., Barka, A., Bray, J., Page, W., Swan, F., Altunel, E., Bardet, J. P., Boulanger, R., Brankman, C., Cakir, Z., Christofferson, S., Cluff, L., Dawson, T., Fumal, T., Güneysu, A. C., Hengesh, J., Kaya, A., Langridge, R., Rathje, E., and Stenner, H. (2000). “Surface fault rupture.” *Earthq. Spectra*, 16(S1), 11–53.

Li, X. S., & Wang, Y. (1998). “Linear representation of steady-state line for sand.” *J. Geotech. Geoenviron. Eng.*, 124(12), 1215-1217.

Li, Y., Xu, Y., & Thornton, C. (2005). “A comparison of discrete element simulations and experiments for ‘sandpiles’ composed of spherical particles.” *Powder Technology*, 160(3), 219-228.

Lin, M. L., Chung, C. F., & Jeng, F. S. (2006). “Deformation of overburden soil induced by thrust fault slip.” *Eng. Geology*, 88(1-2), 70-89.

Loli, M., Anastasopoulos, I., Bransby, M. F., Ahmed, W., & Gazetas, G. (2011). “Caisson foundations subjected to reverse fault rupture: centrifuge testing and numerical analysis.” *J. Geotech. Geoenviron. Eng.*, 137(10), 914-925.

Loli, M., Bransby, M. F., Anastasopoulos, I., & Gazetas, G. (2012). “Interaction of caisson foundations with a seismically rupturing normal fault: centrifuge testing versus numerical simulation.” *Géotechnique*, 62(1), 29.

Loli, M., Anastasopoulos, I., & Gazetas, G. (2015). “Nonlinear analysis of earthquake fault rupture interaction with historic masonry buildings.” *Bull. of Earthq. Eng.*, 13(1), 83-95.

Loli, M., Kourkoulis, R., & Gazetas, G. (2018). “Physical and Numerical Modeling of Hybrid Foundations to Mitigate Seismic Fault Rupture Effects.” *J. of Geotech. and Geoenviron. Eng.*, 144(11), 04018083.

Loukidis, D., Bouckovalas, G.D., and Papadimitriou, A.G. (2009). “Analysis of fault rupture propagation through uniform soil cover.*” Soil Dyn. and Earthq. Eng.*, 29, 1389-1404.

Mindlin, R., and Deresiewicz, H. (1953). “Elastic spheres in contact under varying oblique forces.” *ASME J. of App. Mech.*, 20, 327-344.

Mitchell, J. K., & Soga, K. (2005). Strength and Deformation Behavior. In *Fundamentals of Soil Behavior* (pp. 369-464). John Wiley & Sons, Hoboken, New Jersey, USA.

Morgan, J. K. (1999). “Numerical simulations of granular shear zones using the distinct element method: 2. Effects of particle size distribution and interparticle friction on mechanical behavior.” *J. of Geophysical Research: Solid Earth*, 104(B2), 2721-2732.

Morgan, J. K., & Boettcher, M. S. (1999). “Numerical simulations of granular shear zones using the distinct element method: 1. Shear zone kinematics and the micromechanics of localization.” *J. of Geophysical Research: Solid Earth*, 104(B2), 2703-2719.

Morgan, J. K. (2001). “Distinct element simulations of granular shear zones: Micromechanics of localization and frictional behavior.” In *2nd ACES Workshop Proceedings. APEC Cooperation for Earthquake Simulation* (pp. 83-90).

Morgan, J. K. (2004). “Particle dynamics simulations of rate-and state-dependent frictional sliding of granular fault gouge.” In *Computational Earthquake Science Part I* (pp. 1877-1891). Birkhäuser, Basel.

Morgan, J. K. (2015). “Effects of cohesion on the structural and mechanical evolution of fold and thrust belts and contractional wedges: Discrete element simulations.” *J. of Geophysical Research: Solid Earth*, 120(5), 3870-3896.

Mortazavi Zanjani, M., & Soroush, A. (2017). “Numerical modelling of fault rupture propagation through layered sands.” *European J. of Environ. and Civil Eng.*, 1-17, https://doi.org/10.1080/19648189.2017.1344148.

Moss, R. E. S., & Ross, Z. E. (2011). “Probabilistic fault displacement hazard analysis for reverse faults.” *Bull. Seismological Soc. of America*, 101(4), 1542-1553.

Moss, R. E. S., Stanton, K. V., & Buelna, M. I. (2013). “The impact of material stiffness on the likelihood of fault rupture propagating to the ground surface.” *Seismological Research Letters*, 84(3), 485-488.

Moss, R. E. S., Buelna, M., & Stanton, K. V. (2018). “Physical, Analytical, and Numerical Modeling of Reverse-Fault Displacement through Near-Surface Soils.” *Bull. Seismological Soc. of America*, https://doi.org/10.1785/0120180067.

Mühlhaus, H.B., & Vardoulakis, I. (1987). “The thickness of shear bands in granular materials.” *Géotechnique*, 37(3), 271-283.

Ng, T. T. (2006). “Input parameters of discrete element methods.” *J. Eng. Mech.*, 10.1061/(ASCE)0733-9399(2006)132:7(723).

Ni, Q., Powrie, W., Zhang, X., and Harkness, R. (2000). “Effect of particle properties on soil behaviour: 3-D numerical modelling of shearbox tests.” *Proc., GeoDenver 2000* ‘*Numerical Methods in Geotechnical Engineering*,’ ASCE, Reston, Va., 58–70.

Niccum, M. R., Cluff, L. S., Chamoro, F., & Wylie, L. (1976). “Banco Central de Nicaragua: a case history of a highrise building that survived surface fault rupture.” In *Engineering Geology and Soils Engineering Symposium*, edited by C. B. Humphrey, Vol. 14, Idaho Department of Transportation, Division of Highways, Boise, ID, pp. 133-144.

Nollet, S., Vennekate, G. J. K., Giese, S., Vrolijk, P., Urai, J. L., & Ziegler, M. (2012). “Localization patterns in sandbox-scale numerical experiments above a normal fault in basement.” *J. of Struct. Geology*, 39, 199-209.

Oda, M., & Kazama, H. (1998). “Microstructure of shear bands and its relation to the mechanisms of dilatancy and failure of dense granular soils.” *Géotechnique*, 48(4), 465-481.

Oettle, N.K. (2013). “Earthquake surface fault rupture interaction with building foundations.” Thesis. University of California, Berkeley.

Oettle, N. K., and Bray, J. D. (2013a). “Fault rupture propagation through previously ruptured soil.” *J. Geotech. Geoenviron. Eng.*, 139(10), 1637–1647. https://doi.org/10.1061/(ASCE)GT.1943-5606.0000919.

Oettle, N., and Bray, J. D. (2013b). “Geotechnical mitigation strategies for earthquake surface fault rupture.” *J. Geotech. Geoenviron. Eng.*, 139(11), 1864–1874. https://doi.org/10.1061/(ASCE)GT.1943-5606.0000933.

Oettle, N. K., J. D. Bray, and Dreger, D. S. (2015). “Dynamic effects of surface fault rupture interaction with structures.” *Soil Dyn. Earthq. Eng.* 72, 37–47. https://doi.org/10.1016/j.soildyn.2015.01.019.

Oettle, N. K., & Bray, J. D. (2016). “Numerical Procedures for Simulating Earthquake Fault Rupture Propagation.” *Int. J. of Geomech.*, 17(1), 04016025.

Oettle, N.K., Kayen, R., Franke, K., Dashti, S., Ramirez Calderon, J., and Wham, B.P. (2017). “Observations and finite element modeling of the Aso Caldera depression zone resulting from the 2016 Kumamoto Earthquake.” In *Proc. Of the 6th International Young Geotechnical Engineers’ Conf.* Seoul, Republic of Korea. September 17-22, 2017.

O’Sullivan, C. (2002). “The application of discrete element modelling to finite deformation problems in geomechanics.” Thesis. University of California, Berkeley.

O'Sullivan, C., and Bray, J.D. (2002). “Relating the response of idealized analogue particles and real sands.” *Proc., Numerical Modeling in Micro-Mechanics via Particle Methods*, 1st international PFC symposium, November 2002.

O'Sullivan, C., D Bray, J., & Li, S. (2003). “A new approach for calculating strain for particulate media.” *Int. J. for Num. Anal. Meth. in Geomech.*, 27(10), 859-877.

O’Sullivan, C., and Bray, J. D. (2004). “Selecting a suitable time step for discrete element simulations that use the central difference time integration scheme.” *Eng. Computations*, 21(2–4), 278-303.

O’Sullivan, C., Bray, J. D., & Riemer, M. (2004). “Examination of the response of regularly packed specimens of spherical particles using physical tests and discrete element simulations.” *J. of Eng. Mech.*, 130(10), 1140-1150.

O’Sullivan, C. (2011a). “Particle-based discrete element modeling: geomechanics perspective.” *Int. J. of Geomech.*, 11(6), 449-464.

O'Sullivan, C. (2011b). Particulate discrete element modelling: a geomechanics perspective. CRC Press.

Otsubo, M., O'Sullivan, C., & Shire, T. (2017). “Empirical assessment of the critical time increment in explicit particulate discrete element method simulations.” *Computers and Geotechnics*, 86, 67-79.

Pecker, A. (2008). Foreword. *Bull. Earthquake Eng.*, 6(4), 553-555. https://doi.org/10.1007/s10518-008-9095-0.

Pestana, J. M., & Whittle, A. J. (1995). “Compression model for cohesionless soils.” *Géotechnique*, 45(4), 611-632.

Potyondy, D. O., & Cundall, P. A. (2004). “A bonded-particle model for rock.” *Int. J. of Rock Mech. and Mining Sciences*, 41(8), 1329-1364.

Prucha, J. J., Graham, J. A. and Nickelsen, R. P. (1965). "Basement-Controlled Deformation in Wyoming Province of Rocky Mountains Foreland." *Bull. American Assoc. of Petroleum Geologists*, 49(7), 966-992.

Roscoe, K.H. (1970). “The influence of strains in soil mechanics.” *Géotechnique*, 20(2), 129-170.

Roth, W.H., Scott R.F., and Austin, L. (1981). “Centrifuge modeling of fault propagation through alluvial soils.” *Geophysical Research Letters*, 8(6), 561–564.

Salazar, A., Sáez, E., & Pardo, G. (2015). "Modeling the direct shear test of a coarse sand using the 3D Discrete Element Method with a rolling friction model." *Computers and Geotechnics*, 67, 83-93.

Saltzer, S. D. (1992). "Boundary conditions in sandbox models of crustal extension: an analysis using distinct elements." *Tectonophysics*, 215(3-4), 349-362.

Saltzer, S. D., & Pollard, D. D. (1992). "Distinct element modeling of structures formed in sedimentary overburden by extensional reactivation of basement normal faults." *Tectonics*, 11(1), 165-174.

Santamarina, J.C., Klein, K. and Fam, M. (2001). Characterization of particles and particulate media. In *Soils and Waves* (pp. 25-57). J. Wiley, Chichester, UK.

Sanz, P. F., Borja, R. I., & Pollard, D. D. (2007). "Mechanical aspects of thrust faulting driven by far-field compression and their implications for fold geometry." *Acta Geotechnica*, 2(1), 17-31.

Scarpelli, G., & Wood, D.M. (1982). "Experimental observations of shear patterns in direct shear tests." In *Proc., IUTAM Deformation and Failure of Granular Materials Conference* (pp. 473-483), Delft, 31 August-3 Septemeber, 1982.

Schofield, A., & Wroth, P. (1968). Critical state soil mechanics. McGraw-Hill, London.

Schöpfer, M. P., Childs, C., & Walsh, J. J. (2006). "Localisation of normal faults in multilayer sequences." *J. of Struct. Geology*, 28(5), 816-833.

Schöpfer, M. P., Childs, C., & Walsh, J. J. (2007a). "Two-dimensional distinct element modeling of the structure and growth of normal faults in multilayer sequences: 1. Model calibration, boundary conditions, and selected results." *J. Geophysical Research: Solid Earth*, 112(B10).

Schöpfer, M. P., Childs, C., & Walsh, J. J. (2007b). "Two-dimensional distinct element modeling of the structure and growth of normal faults in multilayer sequences: 2. Impact of confining pressure and strength contrast on fault zone geometry and growth." *J. Geophysical Research: Solid Earth*, 112(B10).

Schöpfer, M. P., Childs, C., & Walsh, J. J. (2009). "Two-dimensional Distinct Element Method (DEM) modeling of tectonic fault growth in mechanically layered sequences." In *Mechanics of Natural Solids* (pp. 127-146). Springer, Berlin, Heidelberg.

Schöpfer, M. P., Childs, C., Walsh, J. J., & Manzocchi, T. (2016). "Evolution of the internal structure of fault zones in three-dimensional numerical models of normal faults." *Tectonophysics*, 666, 158-163.

Schöpfer, M. P., Childs, C., Walsh, J. J., & Manzocchi, T. (2017). "Three-dimensional distinct element method modelling of the growth of normal faults in layered sequences." From Childs, C., Holdsworth, R. E., Jackson, C. A.-L., Manzocchi, T., Walsh, J. J. & Yielding, G. (eds) 2017. *The Geometry and Growth of Normal Faults*. Geological Society, London, Special Publications, 439, 307–332, https://doi.org/10.1144/SP439.17.

Shibuya, S., Mitachi, T., & Tamate, S. (1997). "Interpretation of direct shear box testing of sands as quasi-simple shear." *Géotechnique*, 47(4), 769-790.

Smart, K. J., & Ferrill, D. A. (2018). "Discrete element modeling of extensional fault-related monocline formation." *J. of Struct. Geology*, 115, 82-90.

Šmilauer, V., Catalano, E., Chareyre, B., Dorofeenko, S., Duriez, J., Dyck, N., Elias, J., Er, B., Eulitz, A., Gladky, A., Guo, N., Jakob, C., Kneib, F., Kozicki, J., Marzougui, D., Maurin, R., Modenese, C., Scholtes, L., Sibille, L., Stransky, J., Sweijen, T., Klaus, T., and Yuan, C. (2015). Yade Documentation 2nd ed. The Yade Project. https://doi.org/10.5281/zenodo.34073 (http://yade-dem.org/doc/)

Stirling, M. W., Litchfield, N. J., Villamor, P., Van Dissen, R. J., Nicol, A., Pettinga, J., ... & Mountjoy, J. (2017). "The Mw 7.8 2016 Kaikōura earthquake: Surface fault rupture and seismic hazard context." *Bull. New Zealand Soc. Earthq. Eng*., (2), 73-84.

Stone, K. J., & Wood, D. M. (1992). "Effects of dilatancy and particle size observed in model tests on sand." *Soils and Foundations*, 32(4), 43-57.

Strayer, L. M., & Suppe, J. (2002). "Out-of-plane motion of a thrust sheet during along-strike propagation of a thrust ramp: a distinct-element approach." *J. of Struct. Geology*, 24(4), 637-650.

Strayer, L. M., S. G. Erickson, and Suppe, J. (2004). "Influence of growth strata on the evolution of fault-related folds—Distinct-element models." in K. R. McClay, Ed., *Thrust tectonics and hydrocarbon systems: AAPG Memoir*, 82, p. 413– 437.

Taniyama, H. (2011). "Numerical analysis of overburden soil subjected to strike-slip fault: distinct element analysis of Nojima fault." *Eng. Geology*, 123(3), 194-203.

Taniyama, H. (2017). "Distinct element analysis of overburden subjected to reverse oblique-slip fault." *J. of Struct. Geology*, 96, 90-101.

Tchalenko, J. S. (1970). "Similarities between shear zones of different magnitudes." *Geological Soc. of America Bull.*, 81(6), 1625-1640.

Terzaghi, K. (1936). "Stress distribution in dry and saturated sand above a yielding trap-door." In *Proc., 1st Inter. Conf. on Soil Mechanics and Foundation Engineering*, Graduate School of Engineering, Harvard Univ., Cambridge, MA, 307–311.

Terzaghi, K. (1943). Arching in ideal soils. In *Theoretical Soil Mechanics* (pp. 66-76). John Wiley and Sons, Inc. New York.

Thebian, L., Najjar, S., Sadek, S., & Mabsout, M. (2018). "Numerical investigation of dip-slip fault propagation effects on offshore seabed sediments." *Eng. Geology*, 237, 149-167.

Thomas, P.A. (1997). "Discontinuous deformation analysis of particulate media." Thesis. University of California, Berkeley.

Thomas, P.A. and Bray, J.D. (1999) "Capturing nonspherical shape of granular media with disk clusters." *J. Geotech. and Geoenviron. Eng.*, 125(3), 165-178, https://doi.org/10.1061/(ASCE)1090-0241(1999)125:3(169).

Thornton, C. (2000). "Numerical simulations of deviatoric shear deformation of granular media. *Géotechnique*, 50(1), 43-53.

Thornton, C., & Zhang, L. (2006). "A numerical examination of shear banding and simple shear non-coaxial flow rules." *Philosophical Magazine*, 86(21-22), 3425-3452.

Tolga Yilmaz, M., & Paolucci, R. (2007). "Earthquake fault rupture—shallow foundation interaction in undrained soils: a simplified analytical approach." *Earthq. Eng. & Struct. Dyn.*, 36(1), 101-118.

Tsatsis, A., Anastasopoulos, I., & Gazetas, G. (2015). "Buried pipelines subjected to normal fault: Simulation vs experiment." In *Geotechnical Engineering for Infrastructure and Development-Proceedings of the XVI European Conference on Soil Mechanics and Geotechnical Engineering, ECSMGE* (Vol. 2015, No. 6, pp. 3407-3412).

Wang, L., Leshchinsky, B., Evans, T.M., & Xie, Y. (2017). "Active and passive arching stresses in c′-ϕ′ soils: A sensitivity study using computational limit analysis." *Computers and Geotechnics*, 84, 47-57.

Wells, D. L., and Coppersmith, K. J. (1994). "New empirical relationships among magnitude, rupture length, rupture width, rupture area, and surface displacement." *Bull. Seismological Soc. of America,* 84(4), 974–1002.

Widuliński, L., Tejchman, J., Kozicki, J., & Leśniewska, D. (2011). "Discrete simulations of shear zone patterning in sand in earth pressure problems of a retaining wall." *Int. J. of Solids and Structures*, 48(7-8), 1191-1209.

Wood, D. (2002). "Some observations of volumetric instabilities in soils." *Int. J. of Solids and Structures*, 39(13), 3429-3449.

Wood, D. (2004). Physical modeling. In *Geotechnical modeling* (p. 242-268). E&F Spon, London.

Yan, W. M. (2009). "Fabric evolution in a numerical direct shear test." *Computers and Geotechnics*, 36(4), 597-603.

Yan, W. M., & Dong, J. (2011). "Effect of particle grading on the response of an idealized granular assemblage." *Int. J. of Geomech.,* 11(4), 276-285.

Zhang, J., Morgan, J. K., Gray, G. G., Harkins, N. W., Sanz, P. F., & Chikichev, I. (2013). "Comparative FEM and DEM modeling of basement-involved thrust structures, with application to Sheep Mountain, Greybull area, Wyoming." *Tectonophysics*, 608, 408-417.

Zhao, J., & Guo, N. (2015). "The interplay between anisotropy and strain localisation in granular soils: a multiscale insight." *Géotechnique*, 65(8), 642-656.

Zhou, B., Huang, R., Wang, H., & Wang, J. (2013). "DEM investigation of particle anti-rotation effects on the micromechanical response of granular materials." *Granular Matter*, 15(3), 315-326.

Zimmaro, P., and Stewart, J.P., [Eds.] (2016a). "Engineering reconnaissance following the 2016 M 6.0 Central Italy Earthquake," a report of the NSF- Sponsored GEER Association Team, GEER-050a, Ver. 1, 15 September 2016, https://doi.org/10.18118/G65K5W.

Zimmaro, P., and Stewart, J.P., [Eds.] (2016b). "Engineering Reconnaissance of the 24 August 2016 Central Italy Earthquake," a report of the NSF- Sponsored GEER Association Team, GEER-050b, Ver. 2, 22 November 2016, https://doi.org/10.18118/G61S3Z.

Zimmaro, P., and Stewart, J.P., [Eds.] (2017a). "Engineering Reconnaissance Following the October 2016 Central Italy Earthquakes," a report of the NSF- Sponsored GEER Association Team, GEER-050c, Ver. 1, 9 January 2017, https://doi.org/10.18118/G6S88H.

Zimmaro, P., and Stewart, J.P., [Eds.] (2017b). "Engineering Reconnaissance Following the October 2016 Central Italy Earthquakes," a report of the NSF- Sponsored GEER Association Team, GEER-050d, Ver. 2, 8 May 2017, https://doi.org/10.18118/G6HS39.

APPENDIX A: SENSITIVITY ANALYSIS FOR RATE OF RUPTURE

Select scenarios of free-field fault rupture were simulated using the LIGGGHTS DEM code (Kloss et al. 2012) to assess the sensitivity of simulation results to the rate of rupture. The rate of rupture refers to the vertical component of the speed at which the hanging wall boundaries displace. LIGGGHTS was selected for this research because it is optimized for large-scale, HPC simulations. It is highly modular, making implementation of new features relatively straightforward. Functionalities previously used in the PFC3D simulations of Chapters 3 and 4 were implemented into C++ scripts compiled with LIGGGHTS. The LIGGGHTS code was modified to track unbalanced forces throughout the entire particle assemblage and to calculate the overlap ratio at each inter-particle contact as the ratio of inter-particle contact gap to minimum diameter of the contacting spheres. In addition, local non-viscous damping was implemented (Cundall 1987). This form of damping only acts on accelerating particles by imparting a force on each particle as (Itasca 2014):

$$\boldsymbol{F_d} = -\alpha|F|\frac{\boldsymbol{v}}{|v|} \tag{A.1}$$

where $\boldsymbol{F_d}$ is the damping force, α is the damping coefficient, $\boldsymbol{F}$ is the total force vector acting on the particle, and $\boldsymbol{v}$ is the particle velocity vector. In assemblages of sphere-clusters, this force acts on the centroid of the sphere-cluster so that it does not affect rotational motion. The inclusion of local non-viscous damping effectively reduces high-frequency motion in the system and quickly brings it to equilibrium, which helps facilitate quasi-static motion. The damping factor α is 0.3 in all simulations.

The results of simulations with different rates of rupture are shown below in terms of the ground surface deformations calculated 1 m (prototype scale) below the free surface. All simulations in this appendix section were performed under a gravitational acceleration of 115g and prepared with the method described in Chapter 6. The inter-particle contact properties are also the same as described in Chapters 5 and 6. The timestep in each simulation is 10^{-7} seconds. The model-scale widths of the footwall and hanging wall are 0.45 m and 0.2 m, respectively. The particle assemblages contain the same sphere-cluster shapes and grain size distribution shape as in Chapter 6, but D_{50} = 2.15 mm and no boundary particles are used. The periodic width in the along-strike direction is 0.035 m (model scale) in each simulation.

A dense and a medium-loose particle assemblage were prepared. The dense particle assemblage contains 401,260 sphere-clusters and 1,010,479 constituent spheres. This particle assemblage has a height of 0.143 m (model scale). The medium-loose particle assemblage contains 341,578 sphere-clusters and 860,198 constituent spheres. This particle assemblage has a height of 0.132 m (model scale). Figure A.1 shows the void ratio distributions for the dense and medium-loose particle assemblages. Figures A.2-A.7 show the comparisons of simulations with different rates of rupture in the dense and medium-loose particle assemblages in terms of the ground surface displacements. The horizontal position indicates the position in the Y-direction (perpendicular to the strike), and the distinct bedrock fault initiates at Y = 0 m.

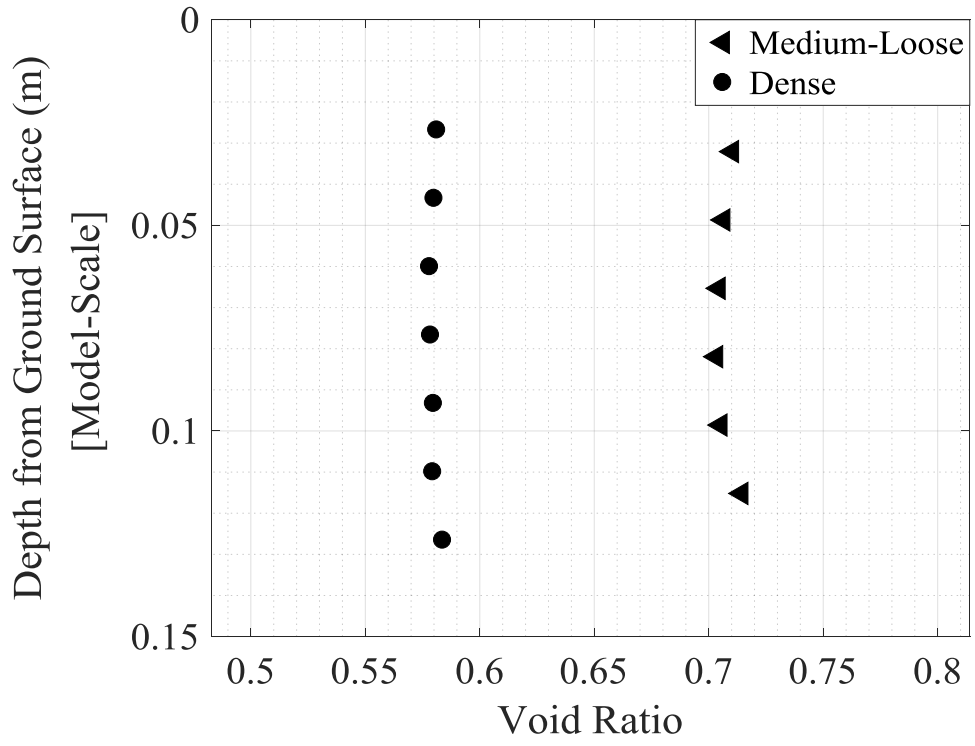

Fig. A.1. Void ratio distributions for the medium-loose and dense particle assemblages.

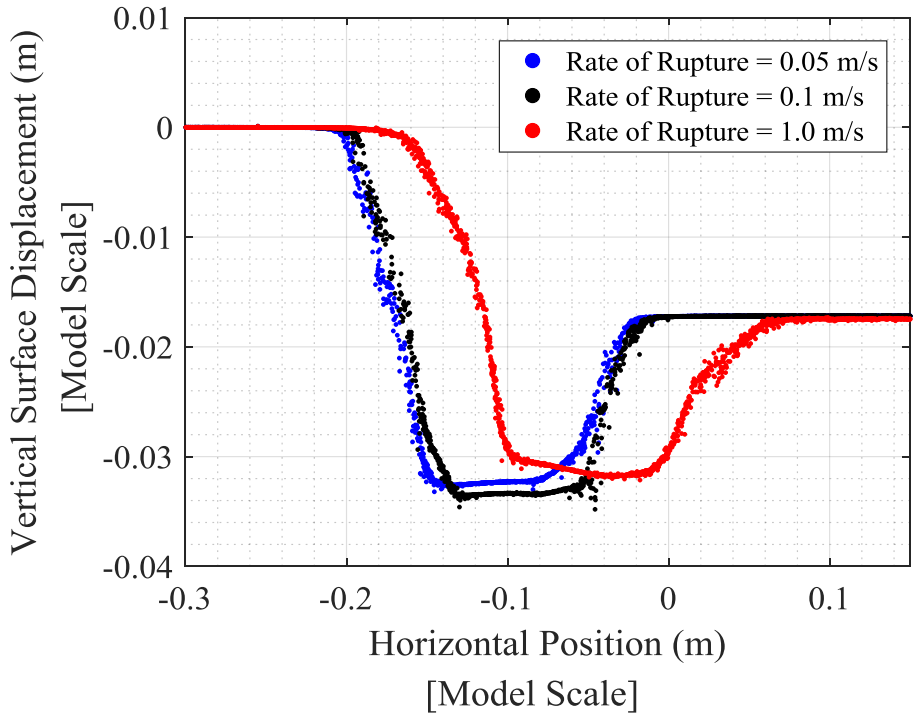

Fig. A.2. 30°-dip normal fault rupture through the dense particle assemblage (*h/H* = -0.12).

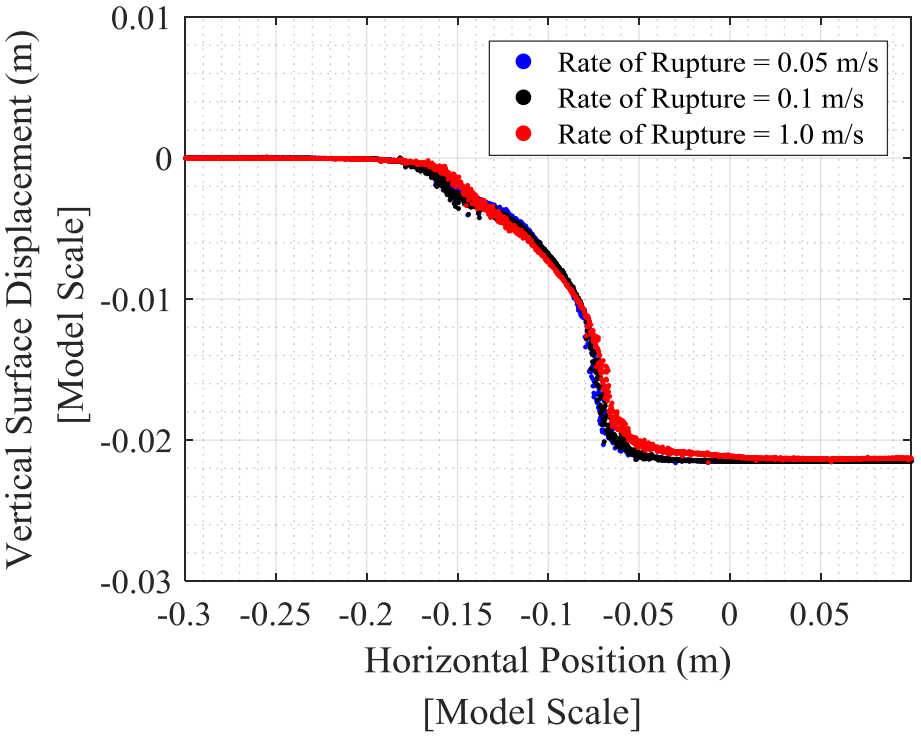

Fig. A.3. 90°-dip normal fault rupture through the dense particle assemblage (*h/H* = -0.15).

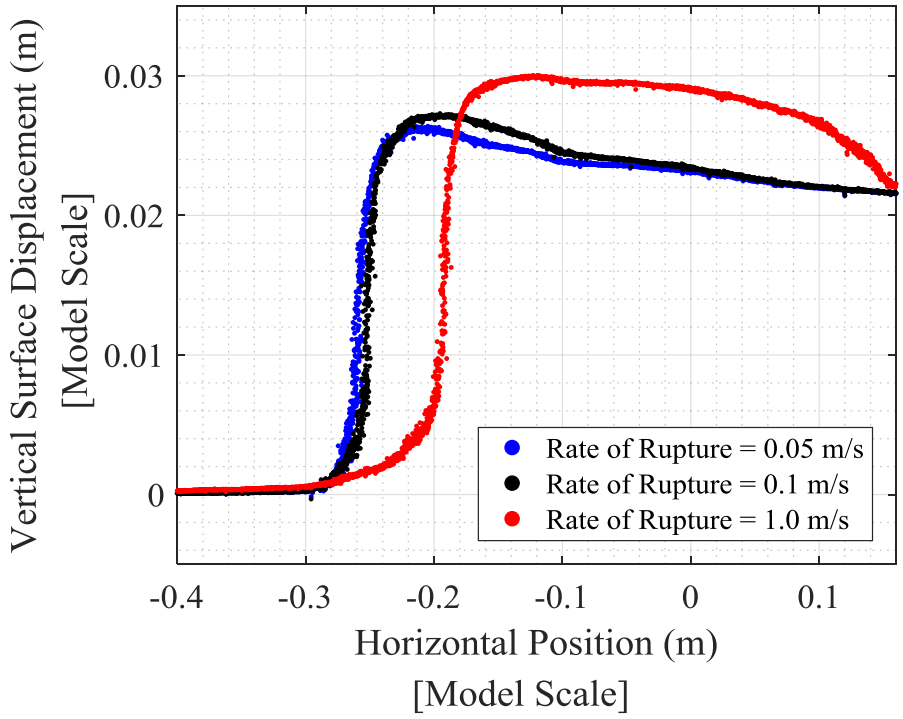

Fig. A.4. 30°-dip reverse fault rupture through the dense particle assemblage (*h/H* = 0.15).

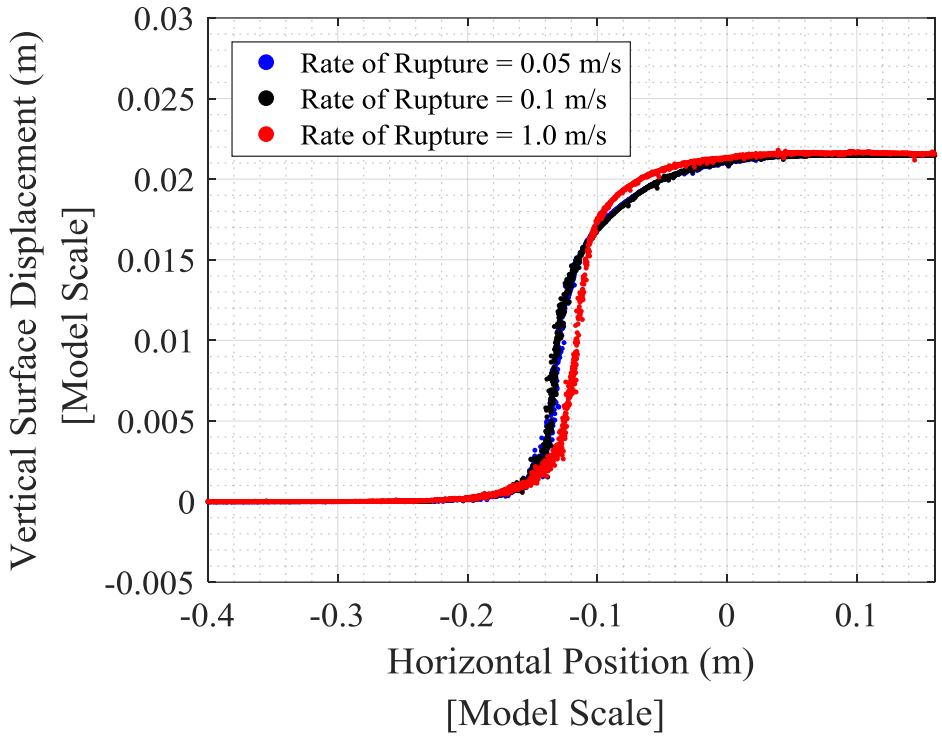

Fig. A.5. 60°-dip reverse fault rupture through the dense particle assemblage (*h*/*H* = 0.15).

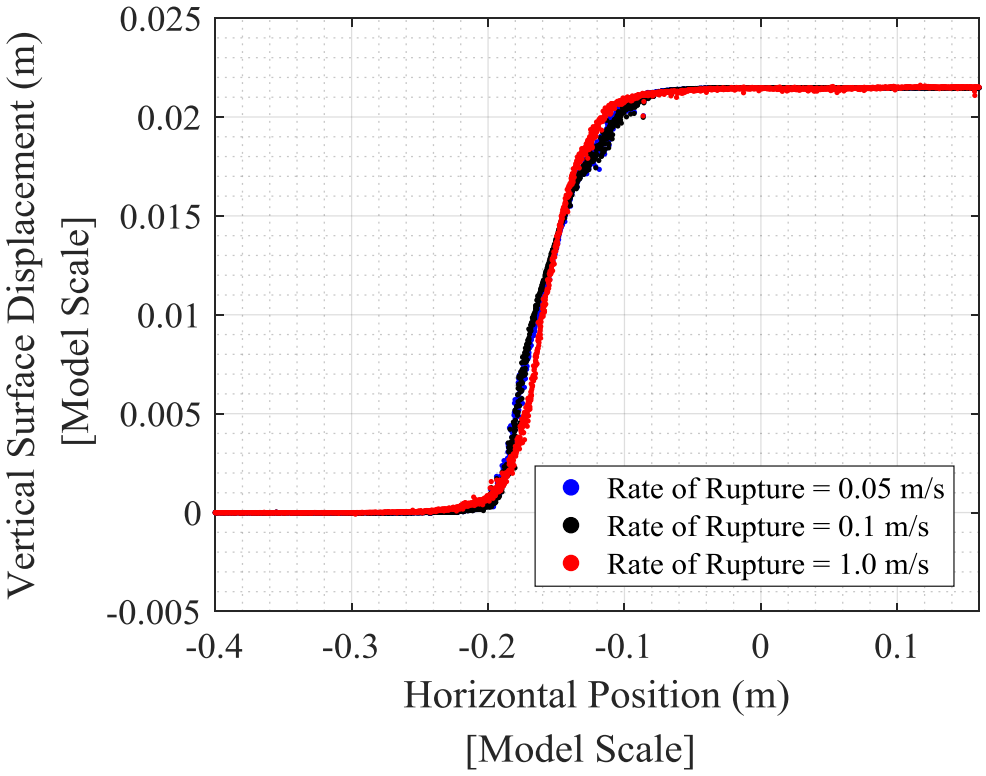

Fig. A.6. 90°-dip reverse fault rupture through the dense particle assemblage (*h/H* = 0.15).

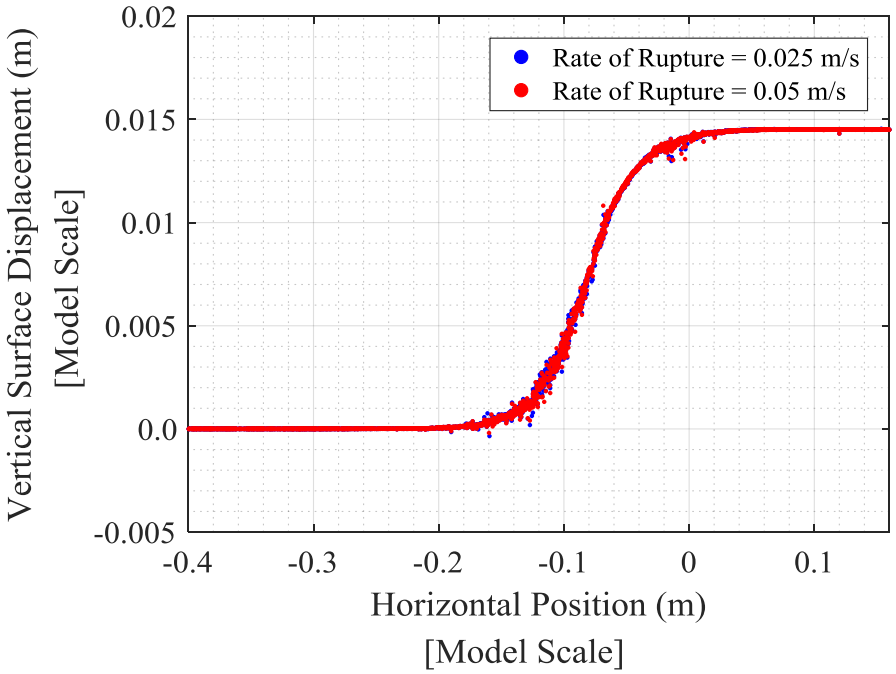

Fig. A.7. 60°-dip reverse fault rupture through the medium-loose particle assemblage (*h/H* = 0.11).

APPENDIX B: COMPARISON OF SURFACE FAULT RUPTURE RESULTS AT VARYING FAULT DIP ANGLES WITH SANDBOX EXPERIMENTS

Simulations of reverse and normal fault rupture were performed with fault dip angles ranging from 30° to 90° in 15° increments using the dense particle assemblage described in Appendix A. The prototype height of this particle assemblage is 16.4 m (0.143 m at model scale), and D_{50} = 2.15 mm with a grain size distribution shape matched to that of Fontainebleau sand with C_u = 1.6 (Delfosse-Ribay et al. 2004). No larger boundary particles are included in this particle assemblage. This dense particle assemblage is estimated to have a peak angle of dilation (ψ_{pk}) of 19° based on its void ratio distribution shown in Fig. A.1 in Appendix A and the numerical direct shear test characterizations in Chapter 5. Figs. B.1-B.10 compare the simulation results using this particle assemblage and different fault dip angles with the closed form solution of Cole & Lade (1984) for the fault rupture surface using ψ_{pk} = 19°. The solution of Cole & Lade (1984), discussed in Chapter 2, is considered representative of physically observed trends for the fault rupture surface in cohesionless, granular soil since Cole & Lade (1984) showed satisfactory comparison of their predicted fault rupture surfaces using their closed-form solution with the fault rupture surfaces observed in sandbox-style experiments with dense sand. The fault rupture surfaces in the simulations are delineated by zones of substantial principal-axis particle rotations, and the Cole & Lade (1984) prediction is indicated by a solid dashed line in Figs. B.1-B.10. Further discussion of these results may be found in Garcia & Bray (2018c).

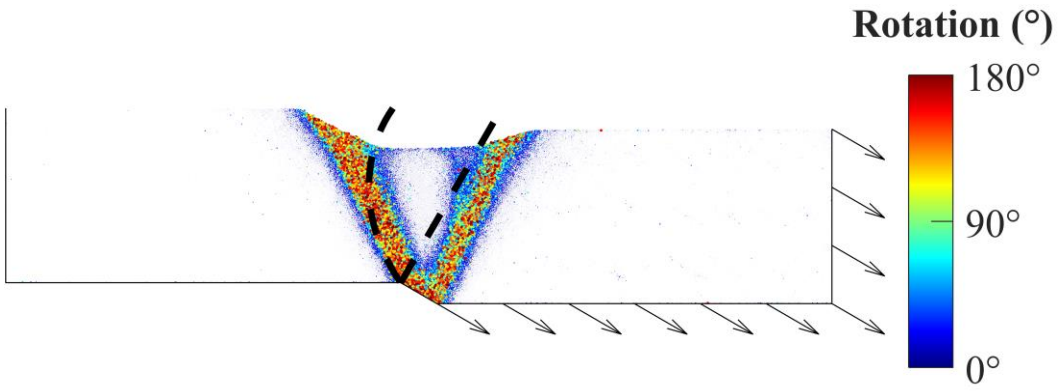

Fig. B.1. 30°-dip normal fault rupture (*h/H* = -0.12).

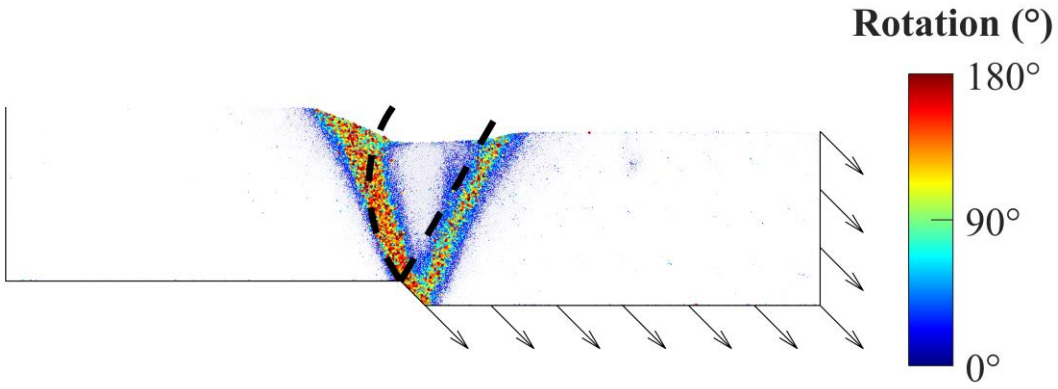

Fig. B.2. 45°-dip normal fault rupture (*h/H* = -0.14).

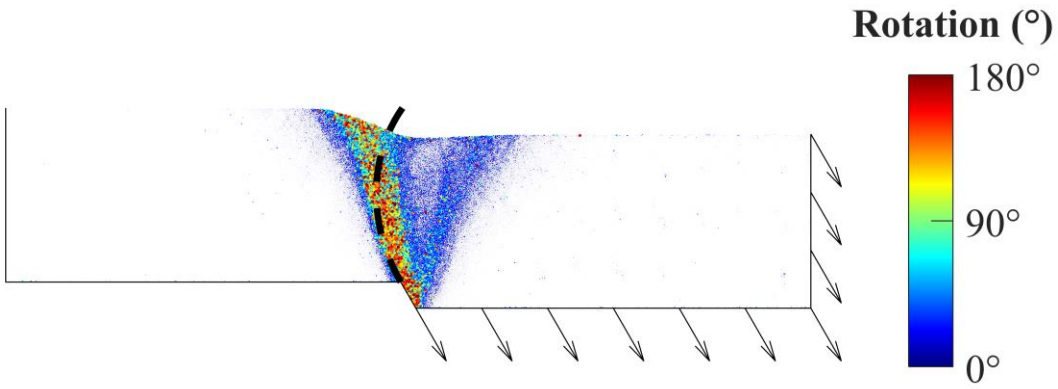

Fig. B.3. 60°-dip normal fault rupture (*h/H* = -0.15).

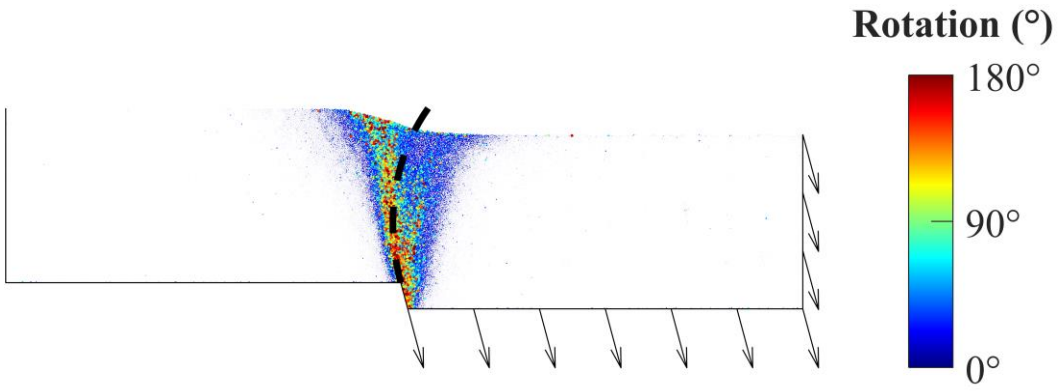

Fig. B.4. 75°-dip normal fault rupture (*h/H* = -0.15).

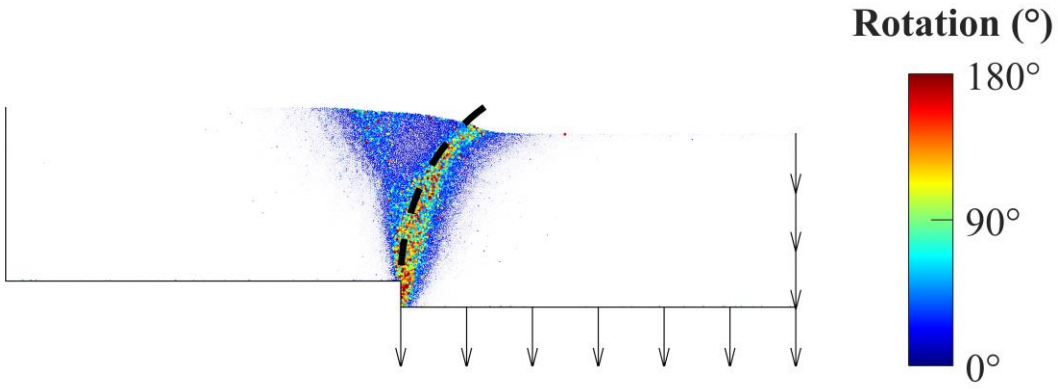

Fig. B.5. 90°-dip normal fault rupture (*h/H* = -0.15).

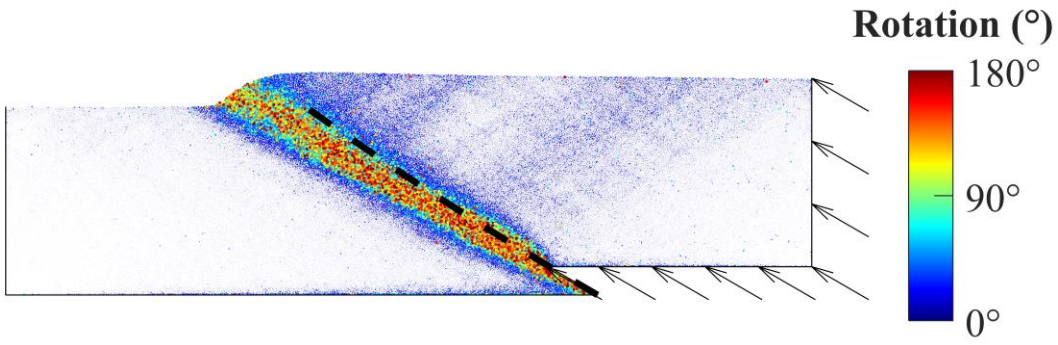

Fig. B.6. 30°-dip reverse fault rupture (*h/H* = 0.15).

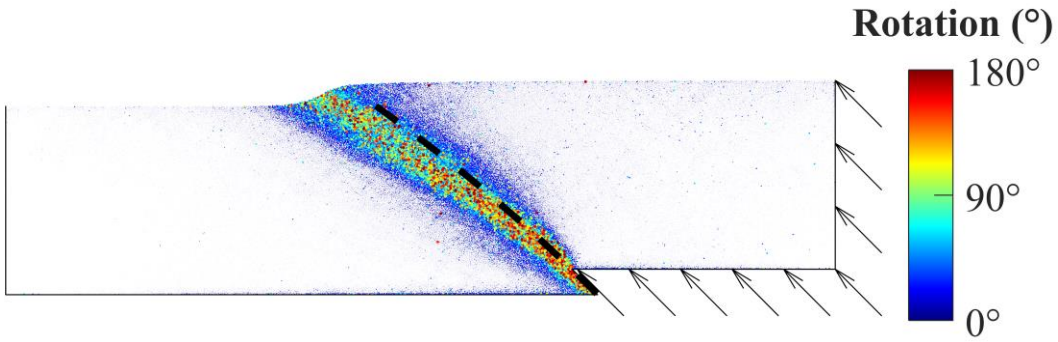

Fig. B.7. 45°-dip reverse fault rupture (*h/H* = 0.135).

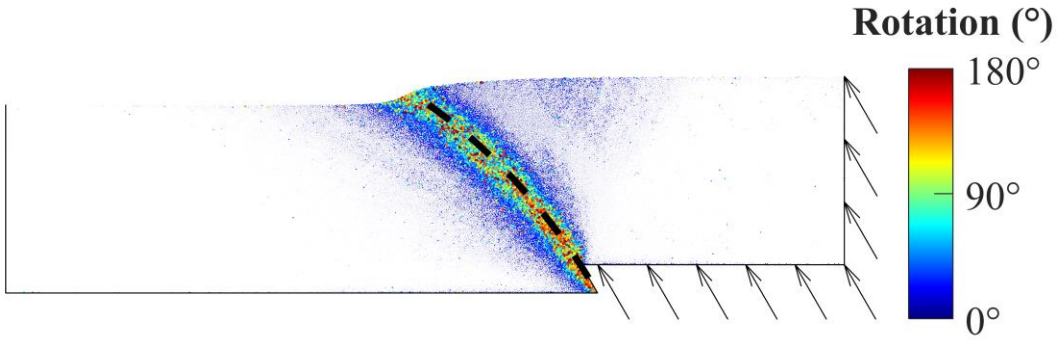

Fig. B.8. 60°-dip reverse fault rupture (*h/H* = 0.15).

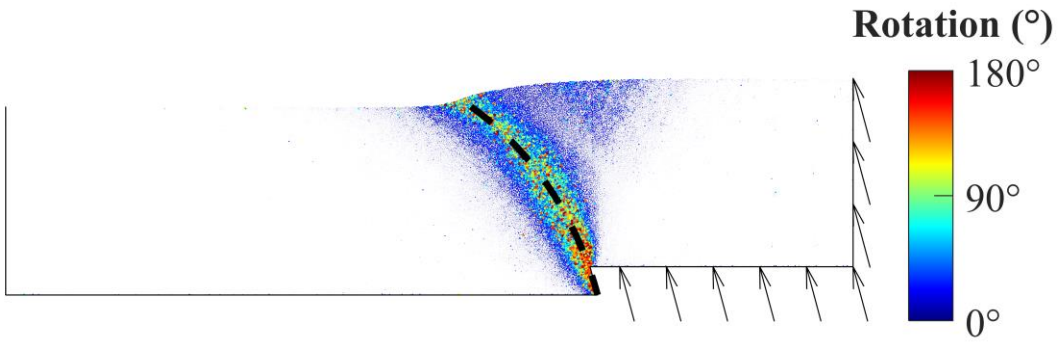

Fig. B.9. 75°-dip reverse fault rupture (*h/H* = 0.15).

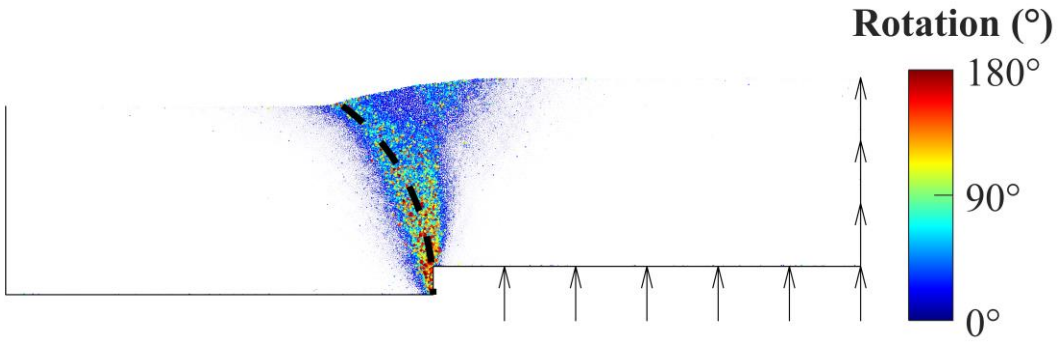

Fig. B.10. 90°-dip reverse fault rupture (*h/H* = 0.15).

APPENDIX C: EFFECT OF PARTICLE SIZE ON SIMULATIONS OF SURFACE FAULT RUPTURE

Surface fault rupture simulations with equivalent relative densities but different particle sizes are compared to assess the influence of particle size on the macroscopic simulation results. The sphere-clusters described in Chapter 6 are used in each simulation. The shape of the grain size distribution of each particle assemblage is matched to that of Fontainebleau sand (C_u = 1.6, Delfosse-Ribay et al 2004) with different values of D_{50}. The periodic length in the along-strike direction is approximately $10D_{max}$ in each simulation. The height of each particle assemblage in these comparisons is 0.132 m in model-scale and 15 m in prototype-scale. The simulated results of surface fault rupture are compared amongst medium-loose, medium, and dense particle assemblages, and the void ratio distributions of these particle assemblages are shown in Fig. C.1.

Figure C.2 shows the ground surface deformations for the medium-loose particle assemblages. The medium-loose particle assemblage with D_{50} = 2.15 mm contains 341,578 sphere-clusters with 860,198 constituent spheres and does not include larger boundary particles. The medium-loose particle assemblage with D_{50} = 1.61 mm contains 418,890 sphere-clusters with 1,054,522 constituent spheres and includes larger boundary particles. The medium-loose particle assemblage with D_{50} = 1.08 mm contains 945,050 sphere-clusters with 2,379,663 constituent spheres and also includes larger boundary particles.

Fig. C.3 shows the ground surface deformations for the medium particle assemblages. The medium particle assemblage with D_{50} = 1.61 mm contains 422,988 sphere-clusters with 1,064,884 constituent spheres. The medium particle assemblage with D_{50} = 0.81 mm contains 1,704,669 sphere-clusters with 4,292,644 constituent spheres. Both of these particle assemblages include larger boundary particles.

Fig. C.4 shows the ground surface deformations for the dense particle assemblages. The dense particle assemblage with D_{50} = 2.15 mm contains 370,497 sphere-clusters with 932,997 constituent spheres and does not include larger boundary particles. The dense particle assemblage with D_{50} = 1.61 mm contains 453,707 sphere-clusters with 1,142,263 constituent spheres and includes larger boundary particles. The dense particle assemblage with D_{50} = 1.08 mm contains 1,025,926 sphere-clusters with 2,583,257 constituent spheres and also includes larger boundary particles. The early flattening towards the upper end of the fault scarp of the dense particle assemblage with D_{50} = 1.08 mm occurs because a second rupture surface develops at a steeper inclination in this simulation. Figs. C.5-C.7 show the magnitudes of individual particle rotations about their principal axes for the dense particle assemblages. These particle assemblages are estimated to have an angle of dilation of 18°-19°, and the predicted rupture surface using the solution of Cole & Lade (1984) with an angle of dilation of 19° is shown in Figs. C.5-C.7. Figs. C.5 and C.6 show that only a single rupture surface develops when D_{50} = 2.15 mm and when D_{50} = 1.61 mm. As seen in Fig. C.7, a second rupture surface develops at a steeper inclination when D_{50} = 1.08 mm. This second rupture surface is a result of the finer particle sizes relative to the characteristic length of the simulation (e.g., Stone & Wood 1992). More details about these simulation results are available in Garcia & Bray (2018c).

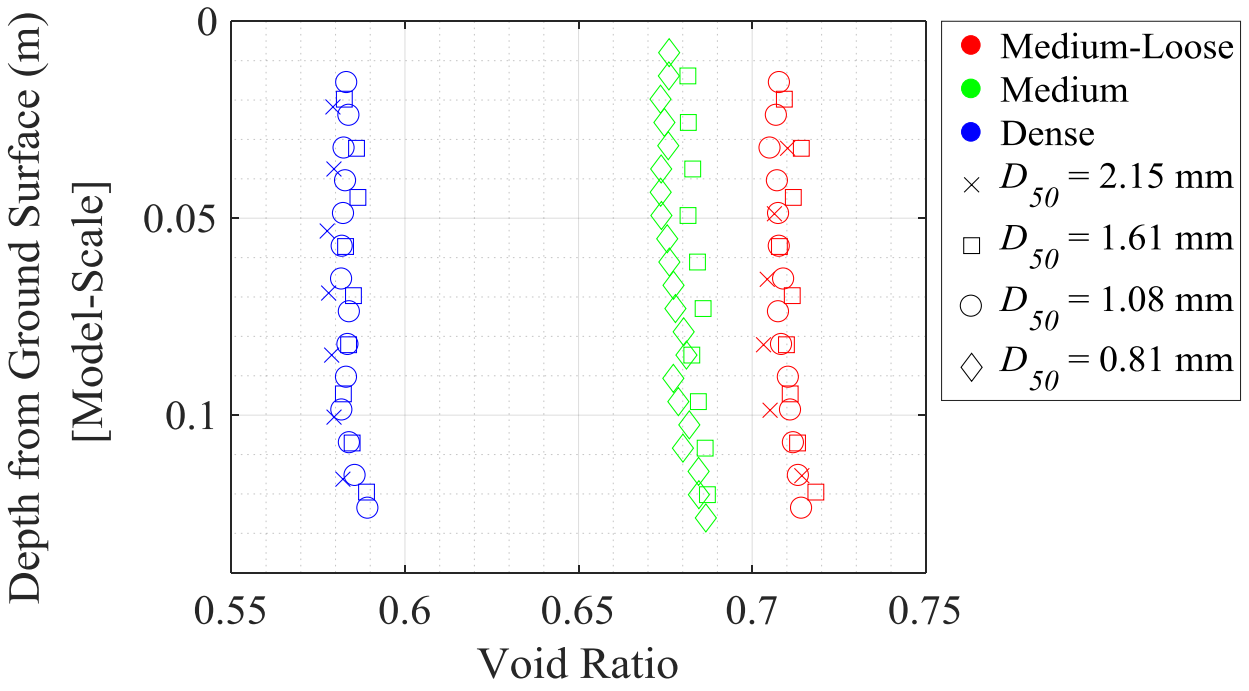

Fig. C.1. Void ratio distributions for the medium-loose, medium, and dense particle assemblages of varying D_{50}. The model height is 132 mm in each assemblage.

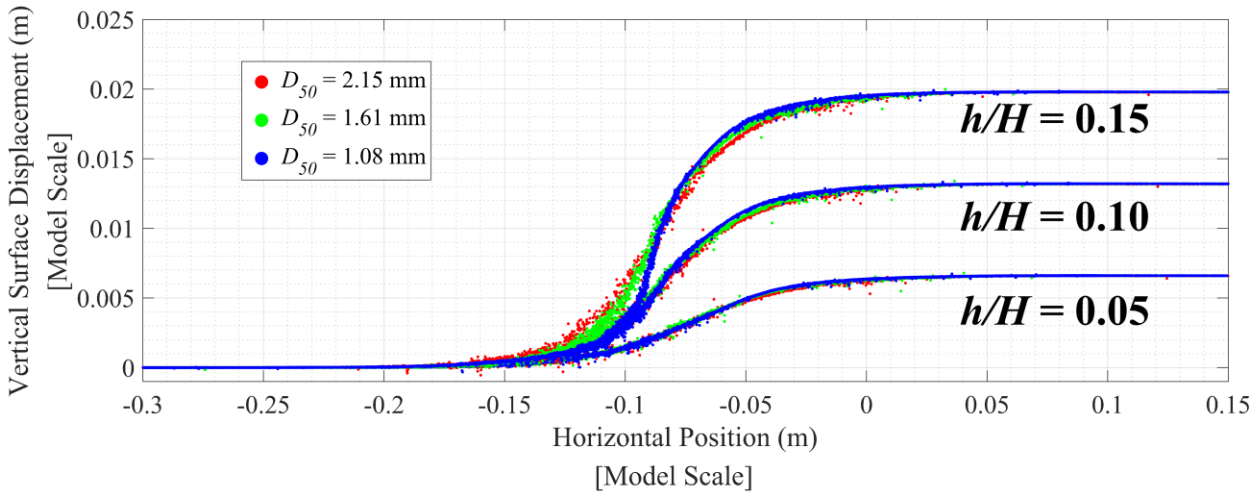

Fig. C.2. Comparison of ground surface deformations for the medium-loose particle assemblages with different particle sizes.

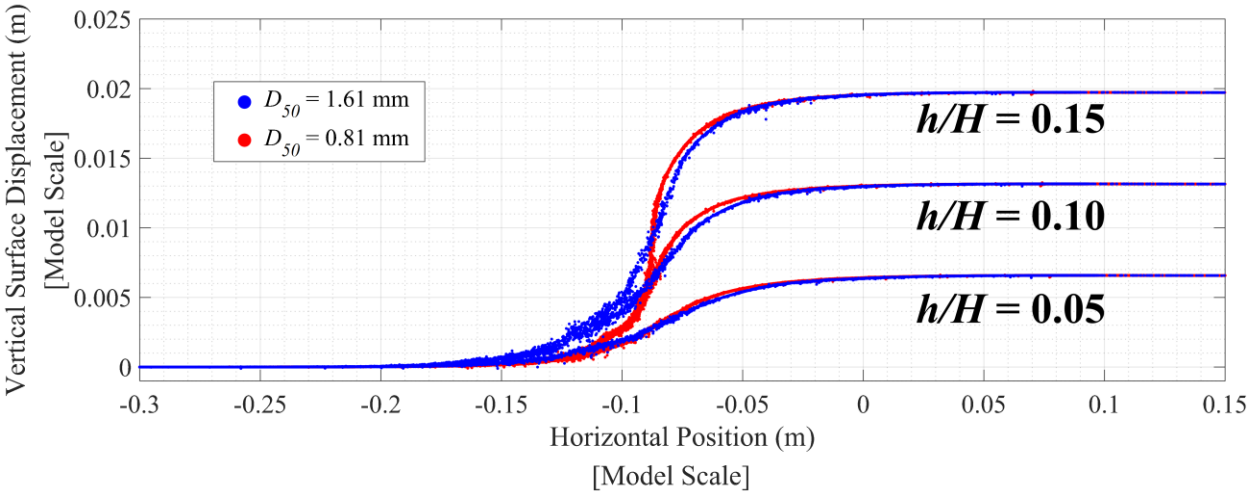

Fig. C.3. Comparison of ground surface deformations for the medium particle assemblages with different particle sizes.

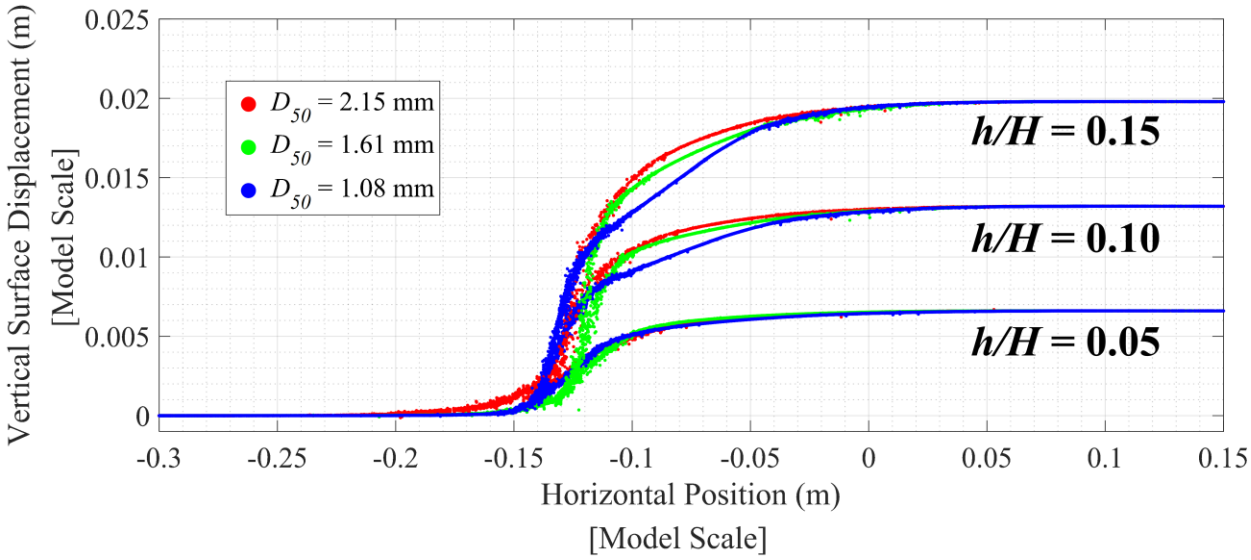

Fig. C.4. Comparison of ground surface deformations for the dense particle assemblages with different particle sizes.

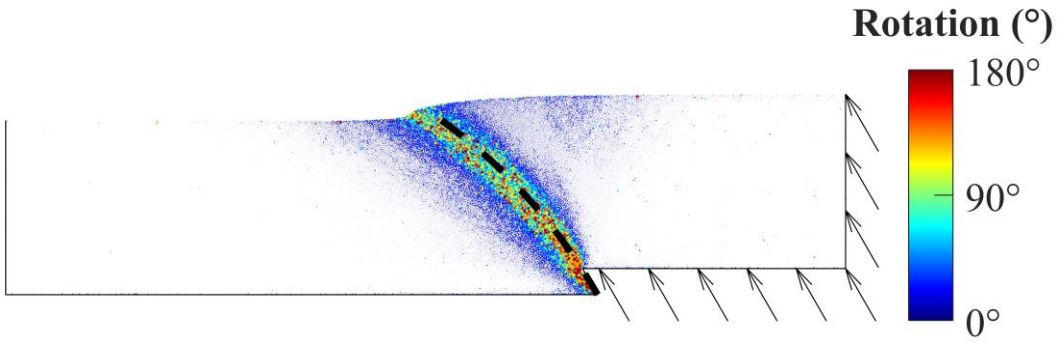

Fig. C.5. Distribution of particle rotations and their magnitudes for the dense particle assemblage with D_{50} = 2.15 mm. The predicted rupture surface of Cole & Lade (1984) using an angle of dilation of 19° is shown as a black dashed line.

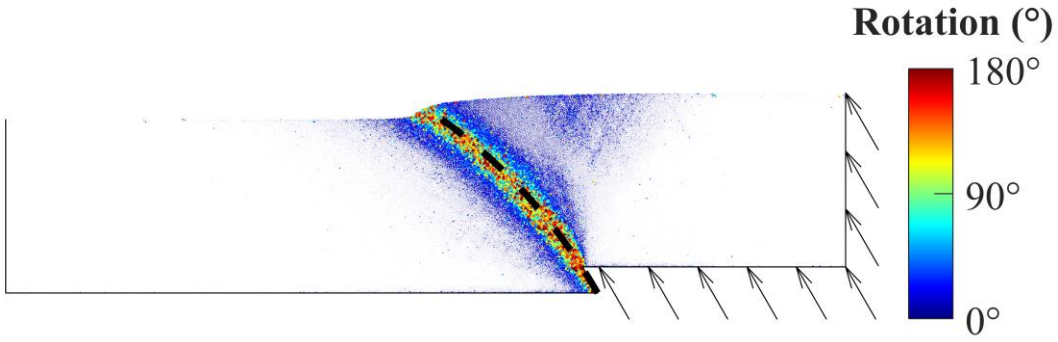

Fig. C.6. Distribution of particle rotations and their magnitudes for the dense particle assemblage with D_{50} = 1.61 mm. The predicted rupture surface of Cole & Lade (1984) using an angle of dilation of 19° is shown as a black dashed line.

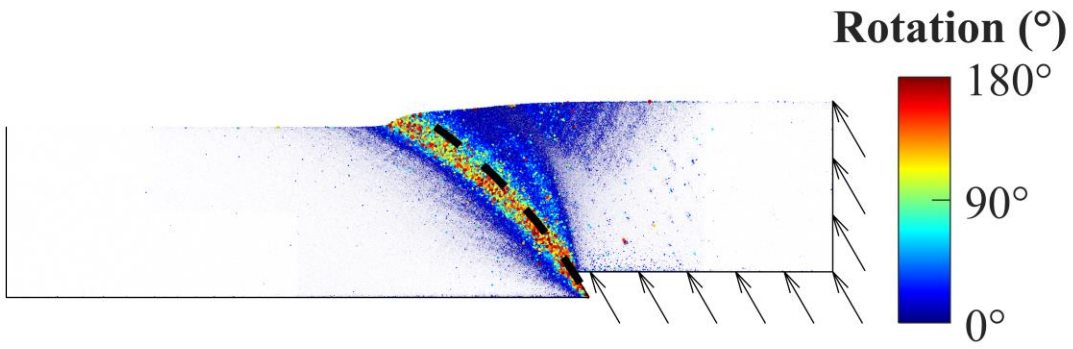

Fig. C.7. Distribution of particle rotations and their magnitudes for the dense particle assemblage with D_{50} = 1.08 mm. The predicted rupture surface of Cole & Lade (1984) using an angle of dilation of 19° is shown as a black dashed line.